STUDY ON FREE VIBRATION BEHAVIOUR OF ROTATING FUNCTIONALLY GRADED MICRO-DISKS

Thesis Submitted
by

Suman Pal

Doctor of Philosophy (Engineering)

Department of Mechanical Engineering
Faculty Council of Engineering & Technology
Jadavpur University
Kolkata, India

2024

INDEX NO. 77/19/E

1. Title of the Thesis:

STUDY ON FREE VIBRATION BEHAVIOUR OF ROTATING FUNCTIONALLY GRADED MICRO-DISKS

2. Name, Designation & Institution of the Supervisor:

Dr. Debabrata Das
Professor
Department of Mechanical Engineering
Jadavpur University, Kolkata - 700032

3. List of Publication:

i. Pal Suman and Das Debabrata, Free vibration behavior of rotating bidirectional functionally-graded micro-disk for flexural and torsional modes in thermal environment. *International Journal of Mechanical Sciences* 2020; 179: 105635.

ii. Pal Suman and Das Debabrata, Free vibration response of bidirectional functionally graded rotating micro-disk under mechanical and thermal loading. *Journal of Strain Analysis for Engineering Design* 2023; 58: 517-537.

iii. Pal Suman and Das Debabrata, Axisymmetric bending vibration analysis of bidirectional functionally graded rotating micro-disk under thermo-mechanical loading. *Journal of Vibration and Control* 2024; 30: 220-236.

4. List of Patents: Nil

5. List of Presentations in National/International/Conferences/Workshops:

i. Pal Suman and Das Debabrata, Free vibration analysis of BFGM rotating micro-disk using modified couple stress theory. *7th International Congress on Computational Mechanics and Simulation (ICCMS)*, IIT Mandi, 2019.

ii. Pal Suman and Das Debabrata, Axisymmetric free vibration behaviour of BFGM rotating micro-disk based on modified couple stress theory. *64th Congress of the Indian Society of Theoretical and Applied Mechanics (ISTAM)*, IIT Bhubaneswar, 2019.

“*This page is intentionally left blank*”

iii. Pal Suman and Das Debabrata, Free vibration response of functionally graded rotating micro-disk under thermal environment. *66th Congress of the Indian Society of Theoretical and Applied Mechanics (ISTAM),* VIT-AP University, Amravati, 2021.

iv. Pal Suman and Das Debabrata, Free Vibration Analysis of variable thickness BFGM rotating micro-disk using modified couple stress theory. *2nd International Conference on Mechanical Engineering (INCOM 24),* Jadavpur University, Kolkata, 2024.

“*This page is intentionally left blank*”

“Statement of Originality”

I **Shri Suman Pal** registered on **10th May 2019** do hereby declare that this thesis entitled “**STUDY ON FREE VIBRATION BEHAVIOUR OF ROTATING FUNCTIONALLY GRADED MICRO-DISKS**” contains literature survey and original research work done by the undersigned candidate as part of Doctoral studies.

All information in this thesis have been obtained and presented in accordance with existing academic rules and ethical conduct. I declare that, as required by these rules and conduct, I have fully cited and referred all materials and results that are not original to this work.

I also declare that I have checked this thesis as per the “Policy on Anti Plagiarism, Jadavpur University, 2019”, and the level of similarity as checked by iThenticate software is **4 %**.

Signature of Candidate: Suman Pal

Date: 29/04/2024

Certified by Supervisor: (Signature with date, seal)

Debabrata Das. 29.04.2024

Professor
Dept. of Mechanical Engineering
Jadavpur University, Kolkata-32

_____

(Dr. Debabrata Das)
Professor
Department of Mechanical Engineering, Jadavpur University
Kolkata - 700032, India

“*This page is intentionally left blank*”

Certificate from the Supervisor

This is to certify that the thesis entitled **"STUDY ON FREE VIBRATION BEHAVIOUR OF ROTATING FUNCTIONALLY GRADED MICRO-DISKS"** submitted by **Shri Suman Pal**, who got his name registered on **10th May, 2019** for the award of Ph.D (Engg.) degree of Jadavpur University is absolutely based upon his own work under the supervision of **Dr. Debabrata Das** and that neither his thesis nor any part of the thesis has been submitted for any degree/diploma or any other academic award anywhere before.

Signature of the Supervisor
and date with Official Seal

Debabrata Das.
29.04.2024

Professor
Dept. of Mechanical Engineering
Jadavpur University, Kolkata-32

_____

(Dr. Debabrata Das**)**
Professor
Department of Mechanical Engg.
Jadavpur University
Kolkata - 700032, India

“*This page is intentionally left blank*”

Acknowledgement

First and foremost, I would like to gratefully acknowledge my Ph.D (Engg.) supervisor, Prof. Debabrata Das, Department of Mechanical Engineering, Jadavpur University. I would like to thank him for inspiring me to pursue excellence. I'm grateful for this opportunity and look forward to continue my interactions with him in future.

I'm happy to be a part of the Applied Mechanics Laboratory, Jadavpur University and my thanks also goes to all laboratory assistants for providing excellent working experience. I would also like to express gratitude to Prof. Amit Karmakar, Department of Mechanical Engineering, Jadavpur University, for his consistent motivation and help for being a research fellow of Applied Mechanics Laboratory.

During my journey of Ph.D (Engg.), I was a Junior Research Fellow (JRF) during 2018-2019 and a Senior Research Fellow (SRF) during 2019-2022 under AICTE Doctoral Fellowship (ADF), formerly known as National Doctoral Fellowship (NDF). I am very much grateful to AICTE-NDF scheme for its financial support to conduct my research work during this tenure. I would like to convey a token of gratitude to Jadavpur University Alumni Association Bombay Branch Trust for the financial support considering the collaborative research project in my Ph.D (Engg.) program. This award was given in memory of Late Amal Kumar Basu, a graduate of 1946 in Chemical Engineering of Jadavpur University and a founder member of the trust.

Most importantly, I'm grateful to my parents (Late Smt. Panna Pal and Sri. Swapan Kr. Pal), brother (Sri. Rahul Pal) and other family members for their love, blessings and support throughout this endeavor. I must thank them for helping me in every step of my life.

Lastly, thanks to my maternal uncle (Sri. Raktim B. Shit and Sri. Bablu Shit) for their motivation and blessings in my whole academic journey.

Thanks to everyone who was associated with me during this journey.

Suman Pal
29/04/2024

(Suman Pal)

Dedicated

to

My Teachers

Abstract

A rotating disk is considered to be a very important machine component due to its wide applications in various fields of engineering and technology. From the perspective of operating performance, durability, reliability and safety, a comprehensive knowledge on free vibration behaviour of rotating disks is essential for design and analysis of machines and instruments involving rotating disks. The coincidence of the free vibration frequency of a rotating disk with its rotational speed marks an important event in the dynamics of rotating systems. In recent times, the reality of miniaturization has shifted the focus of modern scientists and researchers towards the use of micro- and nano-size components in different conventional applications of engineering and technology. The theoretical study of micro-size structural components including rotating disks has become an emerging research area because the experimentation involving micro-size components remain a very costly and complicated affair. Moreover, the research area involving the theoretical study of micro-size components is considered challenging because the classical continuum theories are unable to capture the small-size effect. It is found that the modified couple stress theory (MCST), which is a continuum based non-classical theory, is being extensively explored by the researchers to investigate the mechanical behaviour of various micro-size structural components. Additionally, to have tailor-made material compositions for rotating micro-disks, especially in high-temperature applications, a noble family of composite materials called functionally graded (FG) materials (FGMs) can be used. In FGMs, the continuous variation of the volume fractions of the constituents enables the design engineers and scientists to achieve direction-specific properties. For rotating machineries, especially those involved in power generation in high-thermal environment, increase in the operating temperature is often desirable to increase the thermodynamic efficiency and power density of the system. In those applications, the FGMs are two-phase composites consisting of a metal phase and a ceramic phase. In such FGMs, the metal phase provides the necessary strength and toughness of the overall structure, and the ceramic phase provides the necessary thermal resistance in order to make the structure suitable for high-temperature application.

The research domain to study the free vibration behaviour of rotating micro-disks involving non-classical theories is very new, and has many research gaps. Based on these

research gaps, the present thesis has been thematized to study the free vibration behaviour of rotating bidirectional FGM (BFGM) micro-disks based on the MCST. To be specific, the following four problems have been investigated in the present thesis work: ***First problem*** - *Free vibration behaviour of a BFGM annular clamped–free micro-disk, which is rotating at constant angular speed, and operating in high-temperature environment*; ***Second problem*** - *Free vibration behaviour of a BFGM annular clamped–free micro-disk, which is rotating at constant angular speed, subjected to uniform transverse pressure, and operating in high-temperature environment*; ***Third problem*** - *Free axisymmetric bending vibration behaviour of a BFGM annular clamped–free micro-disk, which is rotating at constant angular speed, subjected to uniform transverse pressure, and operating in high-temperature environment*; ***Fourth problem*** - *Free vibration and static buckling behaviours of a BFGM annular micro-disk under different boundary conditions, which is rotating at constant angular speed, and operating in high-temperature environment.*

The present mathematical model is displacement based. It is formulated using Kirchhoff plate theory coupled with von Kármán nonlinearity for circular plates using polar coordinates. The small size-effect in the micron level is addressed within the framework of the MCST, and assuming linear elastic material behaviour. The micro-disk is assumed to be FG along the radial and thickness directions, and hence it is termed as a BFGM micro-disk. The thermal effect due to high-temperature operating environment has been incorporated into the mathematical model through thermo-elastic constitutive relations. The mechanical properties of the FGM constituents are considered temperature-dependent based on Touloukian model. The effective material properties of the BFGM material are calculated using the rule-of-mixtures (Voigt model). The problem is formulated using two steps. In the first step, the deformed configuration of the BFGM micro-disk under time-invariant centrifugal loading, uniform transverse pressure and thermal loading is determined. The governing equations for this step are derived using the principle of minimum total potential energy. In the second step, the free vibration response of the micro-disk about its deformed configuration is determined. The governing equations for this step are derived using Hamilton's principle. The governing equations for both the steps are discretized following Ritz method with the help of admissible orthogonal functions. The set of governing equations for the first step are nonlinear due to the presence von Kármán type nonlinear relations, and is solved employing Broyden's algorithm. The set of governing equations for the second step constitute an eigenvalue

problem, and is solved using a standard eigen-solver.

A convergence study has been undertaken to decide on the appropriate number of functions, required for the Ritz approximation. The validity of the model has been established successfully through various comparison studies with the available results in the literature. A reasonable volume of numerical results has been generated to investigate the effects of a variety of physical parameters such as rotational speed, applied transverse pressure, thermal loading, size-dependent thickness, material gradation indices, radius ratio and FGM composition. The free vibration response of the BFGM micro-disks has been presented for both axisymmetric and asymmetric bending modes as well as for the torsional mode. The problem is mainly investigated for clamped-free BFGM rotating micro-disks. However, in order to study the effects of different boundary conditions, a separate study has also been undertaken for different boundary conditions namely, simply supported-simply supported, clamped-simply supported, simply supported-clamped and clamped-clamped. While considering different boundary conditions, the critical condition leading to static buckling of the micro-disk, when the vibration frequency becomes zero, has been identified and reported. Four different metal-ceramic FGM compositions namely, Stainless Steel/Silicon Nitride, Stainless Steel/Alumina, Stainless Steel/Zirconia and Titanium Alloy/Zirconia have been considered for presentation of results. Three-dimensional mode-shape plots along with contour plots have also been presented to visualize the axisymmetric and asymmetric bending vibration modes as well as the torsional vibration mode.

The presented formulation is quite general in nature, and can be applied for a wide variety of problems, apart from the specific problems of the thesis, by properly adjusting certain parameters. That the present model successfully solved the four research problems of the thesis clearly justifies the novelty of the model. Additionally, the fact that the model can be employed to solve a wide variety of problems related to mechanical behaviour of micro-disks/plates is a testament of the robustness of the present model. The problem-specific results presented as well as the overall summary of the results are new of its kind. These results and the corresponding findings will definitely serve as benchmark for further study in the domain of dynamics of rotating micro-disks.

“*This page is intentionally left blank*”

Contents

List of Symbols

a	Inner radius of disk
b	Outer radius of disk
b/a	Radius ratio
b/t	Outer radius to thickness ratio
c_j	Undetermined Ritz coefficients
$\{\mathbf{c}\}$	Vector of unknown coefficients c_j
d_j	Undetermined Ritz coefficients for vibration problem
$\{\mathbf{d}\}$	Vector of unknown coefficients d_j
$\{\hat{e}_r,\hat{e}_\theta,\hat{e}_z\}$	Set of unit vectors
k_r	Gradation index along r-direction
k_t	Gradation index along θ-direction
l	Material length scale parameter
$\boldsymbol{m}$	Symmetric couple stress tensor
$m_{rr},m_{\theta\theta},m_{zz},m_{r\theta},m_{\theta r},m_{rz},m_{zr},m_{\theta z},m_{z\theta}$	Components of $\boldsymbol{m}$
n	Number of 2D functions for Ritz approximation
n_ξ, n_μ	Number of 1D functions along ξ- and μ-directions respectively
p	Number of nodal circles
p^*	Non-dimensional transverse pressure
(p,q)	Mode number
q	Number of nodal diameters
q_0	Intensity (per unit area) of applied transverse pressure
(r,θ,z)	Coordinate directions for cylindrical coordinate system

t	Thickness of disk
t/l	Size-dependent thickness
u	Displacement component along r-direction
u_0	Mid-plane displacement component along r-direction
$\vec{\mathbf{u}}$	Displacement vector
v	Displacement component along θ-direction
v_0	Mid-plane displacement component along θ-direction
w	Displacement component along t-direction
w_0	Mid-plane displacement component along t-direction
w^*	Normalized maximum deflection
$w(\rho)$	Weight function used for Gram-Schmidt scheme
A_j, B_j	Coefficients used for Gram-Schmidt scheme
D	Bending stiffness
$E_A, G_A, E_I, G_I, E_{PA}, E_{PI}, E_{TA}, E_C$	Stiffness coefficients
E	Young's modulus
E_c, E_m	Young's moduli of ceramics and metals respectively
E_c^0	Young's modulus of ceramics at T_0
E_f	Effective Young's modulus
G	Shear modulus
G_c, G_m	Shear moduli of ceramics and metals respectively
G_f	Effective shear modulus
$[\mathbf{J}]$	Jacobian matrix
$[\mathbf{K}]$	Tangent stiffness matrix
$[\mathbf{K}^{cl}]$	Classical part of $[\mathbf{K}]$
$[\mathbf{K}^{ncl}]$	Non-classical part of $[\mathbf{K}]$

$[\mathbf{M}]$	Mass matrix
$\{\mathbf{P}\}$	Load vector
$\{\mathbf{P}^r\}$	Restoring load vector
$R_0,\ R_{-1},\ R_1,\ R_2, R_3$	Temperature coefficients for Touloukian model
R_c	Generic material property of ceramics
R_f	Generic effective material property
R_m	Generic material property of metals
$[\mathbf{S}]$	Total stiffness matrix
$[\mathbf{S}^{cl}]$	Classical part of $[\mathbf{S}]$
$[\mathbf{S}^{ncl}]$	Non-classical part of $[\mathbf{S}]$
T	Current temperature of the disk
T_0	Constant stress-free temperature
T_k	Kinetic energy
ΔT	Thermal loading
(T)	Torsional mode
U	Total strain energy
U_{cl}	Classical strain energy
U_n	Approximate displacement field
U_{ncl}	Non-classical strain energy
V	Volume
V_c	Volume fraction of ceramics
V_c^r	Volume fraction of ceramics along r - direction
V_c^t	Volume fraction of ceramics along t - direction
V_m	Volume fraction of metals
W	Work potential
α	Thermal expansion coefficient
α_c, α_m	Thermal expansion coefficient of ceramics and metals respectively

α_f	Effective thermal expansion coefficient
$\boldsymbol{\chi}$	Symmetric curvature tensor
$\chi_{rr}, \chi_{\theta\theta}, \chi_{zz}, \chi_{r\theta}, \chi_{\theta r}, \chi_{rz}, \chi_{zr}, \chi_{\theta z}, \chi_{z\theta}$	Components of $\boldsymbol{\chi}$
δ	Variational operator
$\boldsymbol{\varepsilon}$	Von Kármán strain tensor
$\varepsilon_{rr}, \varepsilon_{\theta\theta}, \varepsilon_{r\theta}, \varepsilon_{\theta r}$	Components of $\boldsymbol{\varepsilon}$
ϕ_0	Ritz function for non-homogeneous boundary condition
ϕ_j	Set of general functions for Ritz approximation
$\left\{\phi_j^u, \phi_j^v, \phi_j^w\right\}$	Sets of Ritz 2D approximation functions
$\left\{\gamma_q^u, \gamma_q^v, \gamma_q^w\right\}$	Sets of Ritz 1D approximation functions along μ-direction
μ	Normalized coordinate along θ-direction
ν	Poisson's ratio
ν_c, ν_m	Poisson's ratio of ceramics and metals respectively
ν_c^0	Poisson's ratio of ceramics at T_0
ν_f	Effective Poisson's ratio
$\vec{\boldsymbol{\theta}}$	Rotation vector
$\theta_r, \theta_\theta, \theta_z$	Components of $\vec{\boldsymbol{\theta}}$
ρ	Mass density/General coordinate for Gram-Schmidt scheme
ρ_c, ρ_m	Mass density of ceramics and metals respectively
ρ_f	Effective mass density
ρ_A, ρ_I	Inertia coefficients
$\boldsymbol{\sigma}$	Cauchy stress tensor
$\sigma_{rr}, \sigma_{\theta\theta}, \sigma_{r\theta}, \sigma_{\theta r}$	Components of $\boldsymbol{\sigma}$
τ	Time
τ_1, τ_2	Initial and final time instants
ω	Frequency of vibration
ω^*	Non-dimensional frequency of vibration

ξ	Normalized coordinate along r-direction
$\left\{\psi_p^u, \psi_p^v, \psi_p^w\right\}$	Sets of Ritz 1D approximation functions along ξ-direction
Π	Total potential energy
Ω	Angular speed of the disk
Ω^*	Non-dimensional angular speed
∇	Delta operator

"*This page is intentionally left blank*"

List of Figures

List of Tables

"*This page is intentionally left blank*"

Chapter 1

INTRODUCTION

1.1 Introduction

A rotating disk is considered to be a very important machine component due to its wide applications in various fields of engineering and technology. Rotating disks are commonly found in different machines and instruments used in mechanical, aerospace, automotive, civil, chemical, marine and bio-medical engineering applications. From the perspective of operating performance, durability, reliability and safety, a comprehensive knowledge on mechanical behaviour of rotating disks is essential for design and analysis of machines and instruments involving rotating disks. The study of mechanical behaviour of rotating disks involves in-depth knowledge of solid mechanics, theory of elasticity, structural vibration and machine dynamics. Hence, this particular topic has become a part of advanced study and research in the discipline of mechanical engineering. The literature review presented in subsequent sections will reveal the fact that the study on mechanical behaviour of rotating disks has been a wide research area for many years. Though the mechanical behaviour broadly involves static, dynamic and buckling responses, the knowledge on dynamic behaviour of rotating disks is of prime importance due to the complicated influence of time-varying forces in presence of rotational motion. Within the ambit of dynamics of rotating disks, study on its free vibration behaviour forms a major part. The present thesis primarily involves free vibration behaviour of rotating disks.

Every structure, having some mass and elasticity, tends to vibrate even with a small disturbance. It is known that disturbances in the form of mass imbalance, pressure differential of working fluid, foundation flexibility etc. are very common to rotating systems. As a result, rotating systems tend to execute free vibration. Hence, for dynamic design of the rotating systems involving rotating disks, having prior knowledge of free vibration behaviour of the rotating disks is essential. The tasks become challenging for micro-size disks, which

supposedly rotate at very high speeds because at high speeds, the effect of the disturbances manifests in a complicated manner. To be specific, the coincidence of the free vibration frequency of a rotating disk with its rotational speed marks an important event in the dynamics of rotating systems. Hence apprehending the complete free vibration behaviour of the micro-size rotating disks, in the frequency domain, is important to prevent its catastrophic failure.

The problem of separation of fiber from matrix of a composite material due to high thermal loading was solved by researchers of Japan in mid-1980s in their hypersonic space plane project (Yamanouchi et al. (1990)). In that project, they required a thermal shield having temperature variation from 2000 K at the outer surface to 1000 K at the inner surface within a thickness of 10 mm. Japanese researchers then came up with a novel material called functionally graded material (FGM). FGMs form noble composite materials, which have material properties that gradually change in the specified direction. In applications with challenging working circumstances, such as heat shields for spacecraft, heat exchanger tubes, biomedical applications, flywheels, plasma facings for fusion reactors etc., FGMs offer a lot of promise. It is possible to implement different combinations of the often-incompatible functionalities to develop novel FGMs. Presently the use of FGMs in various structural applications is on the rise. FGMs are composites that are made of two or more constituent materials in such a way that the volume fractions of the constituents' may be varied smoothly and continuously in desired direction(s) of the volume. Eliminating the interfacial stress discontinuities at the intersection of two separate materials in traditional composites is the main goal of creating FGMs. FGMs are preferred over conventional composites, especially in high-temperature applications. This is because the problem of interfacial stress discontinuity of conventional composites, especially in high-temperature applications, is mitigated in FGMs by smooth and continuation variation of volume fractions. In FGMs, the continuous variation of volume fractions of the constituents enables the design engineers and scientists to achieve direction-specific properties. For rotating machineries, especially those involved in power generation in high-thermal environment, increase in the operating temperature is often desirable to increase the thermodynamic efficiency and power density of the system. In those applications involving high-temperature environment, the FGMs are two-phase composites consisting of a metal phase and a ceramic phase. In such FGMs, the metal phase provides the

necessary strength and toughness of the overall structure and the ceramic phase provides the necessary thermal resistance in order to make the structure suitable for high-temperature application (Reddy and Chin (1998)). An FGM, for which the material gradations are provided in two directions are called bidirectional FGM (BFGM). The rotating disks used in the present thesis for the study of its free vibration are considered to be made of metal-ceramic BFGM.

Usage of micro- and nano-size components has now become a reality due to remarkable advancements in micro- and nano-fabrication technologies over the last few years. The reality of miniaturization has shifted the focus of modern scientists and researchers towards the use of micro- and nano-size components in different conventional applications of engineering and technology. The potential advantages of miniaturization are being considered and explored for micro-CHP (combined heat and power) systems, power-MEMS (micro-electro-mechanical systems), micro-propulsion systems, micro-machining devices, micro-energy harvesters, miniaturized robots, and various other micro-scale distributed generation systems and rotating machineries, where micro-size gas-turbines, steam-turbines, wind-turbines, compressors, pumps etc. are found (Epstein and Senturia (1997); Jacobson and Epstein (2003); Zhang et al. (2013); Schneider et al. (2014); Kim et al. (2015); Kim and Yoon (2016); Amrani et al. (2018); Akour et al. (2018); Giostri et al. (2020); Adamou et al. (2021)). In all these systems, micro-size rotating disks form a major component. The different dimensions of the BFGM rotating disks used in the present thesis are in the order of micrometer.

With the increasing need of miniaturization, scientists and researchers have recently become interested to conduct theoretical investigation on the mechanical behaviour of micro-size components including the rotating disks. The research area involving theoretical study of micro-size structural components is becoming even more demanding as the experimentation involving micro-size components remain a very costly and complicated affair. However, the theoretical study of micro-size components is a challenging and emerging research area because the classical continuum theories are unable to capture the small-size effect. There are experimental evidences (Lam et al. (2003); Liu et al. (2008); Tang and Alici (2011a); Tang and Alici (2011b); Liebold and Muller (2016); Lei et al. (2016); Li et al. (2019)) which show

that the classical continuum theories cannot predict the actual behaviour of micro-size components due to the absence of length scale parameters in those theories. The recent trends of miniaturization have led to the development of different continuum based non-classical theories that contain additional length scale parameter(s) to account for the size-effect. The notable fundamental theories behind the development of these non-classical theories are couple stress theory (Mindlin and Tiersten (1962); Toupin (1962); Koiter (1964)), micro-polar theory (Eringen (1967)), surface elasticity theory (Gurtin and Murdoch (1978)), nonlocal elasticity theory (Eringen (1983)) and strain gradient theory (Fleck et al. (1994); Fleck and Hutchinson (1997); Fleck and Hutchinson (2001)). Based on the couple stress theory, Yang et al. (2002) proposed a modified couple stress theory (MCST) that involves only one material length scale parameter, and thus simplified the treatment of size-effect for micro-size structural elements. The literature survey reveals that the MCST is the mostly used continuum based non-classical theory that is being explored by the researchers to investigate the mechanical behaviour of micro-size structural components. The MCST is popular among other theories because it involves just one material length scale parameter, as contrary to the other theories that include several such parameters. Hence, in the present thesis, the free vibration behaviour of BFGM rotating micro-disks is investigated using MCST.

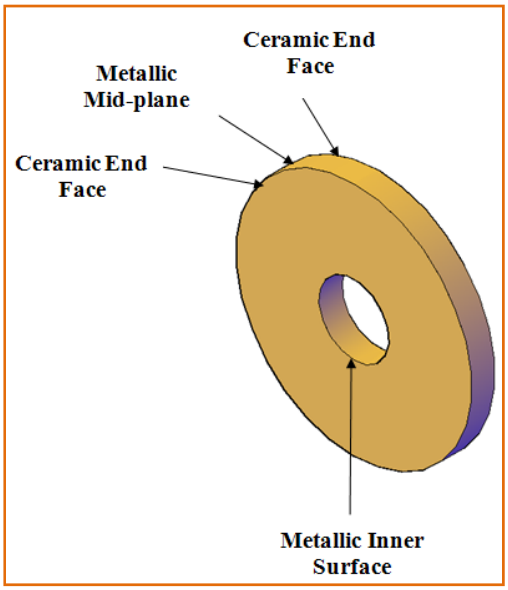

Fig. 1.1: BFGM micro-disk.

The present problem considers a deformable BFGM annular micro-size disk mounted on a rigid shaft. The mathematical model is displacement based. It is formulated using

Kirchhoff plate theory (also called classical plate theory (CPT)) coupled with von Kármán nonlinearity for circular plates using polar coordinates. As already mentioned, the small size-effect in the micron level is addressed within the framework of the MCST, and assuming linear elastic material behaviour. The micro-disk is considered as functionally graded (FG) in the radial and thickness directions, and hence it is termed as a BFGM micro-disk (Fig. 1.1). The disk material is pure metallic at the inner radius, and also at the mid-plane. Further, moving along from the inner radius towards the outer radius, or moving across from the mid-plane towards the top or the bottom surface, the disk material becomes less richer in the metal constituent and more richer in the ceramic constituent. The thermal effect due to high-temperature operating environment has been incorporated into the mathematical model through thermo-elastic constitutive relations. The mechanical properties of the FGM constituents are considered temperature-dependent based on Touloukian model. The effective material properties of the BFGM material are calculated using the rule-of-mixtures (Voigt model). The formulation of the problem is carried out involving two steps. In the first step, the deformed configuration of the BFGM micro-disk under time-invariant centrifugal loading, uniform transverse pressure and thermal loading is determined. The governing equations for this step are derived using the principle of minimum total potential energy. In the second step, the free vibration response of the micro-disk about its deformed configuration is determined. The governing equations for this step are derived employing Hamilton's principle. The governing equations in each of these steps are discretized following Ritz technique with the help of admissible orthogonal functions. The set of governing equations for the first step are nonlinear due to the presence von Kármán type nonlinear relations, and is solved employing Broyden's algorithm. The set of governing equations for the second step constitute an eigenvalue problem, and is solved using a standard eigen-solver. A convergence study has been undertaken to decide on the appropriate number of functions, required for the Ritz approximation. The validity of the model has been established successfully through various comparison studies with the available results in the literature. A reasonable volume of numerical results have been generated to investigate the effects of a variety of practical parameters such as rotational speed, applied transverse pressure, thermal loading, size-dependent thickness, material gradation indices, radius ratio and FGM composition. The free

vibration response of the BFGM micro-disks has been presented for both axisymmetric and asymmetric bending modes as well as for the torsional mode. The problem is mainly investigated for clamped-free BFGM rotating micro-disks. However, in order to study the effects of different boundary conditions, a separate study has also been undertaken for different boundary conditions namely, simply supported-simply supported, clamped-simply supported, simply supported-clamped and clamped-clamped. While considering different boundary conditions, the critical condition leading to static buckling of the micro-disk, when the vibration frequency becomes zero, has been identified and reported.

1.2 Literature Review

The specific research problems of the present thesis have been identified through an extensive survey of the existing literature. As mentioned in the preceding section, the present mathematical model is based on the circular plate theory. Hence, it is understood that the present model is reducible to a conventional circular plate problem. As the present problem involves free vibration of the micro-disk under large transverse deflection due to applied transverse pressure, it is imperative to conduct literature review of circular micro-/nano-plates apart from that of rotating circular disks. The ongoing section on literature review pertaining to static and dynamic analyses is segregated into different sub-sections for homogeneous circular micro-/nano-plates, FGM circular micro-/nano-plates, homogeneous rotating disks, FGM rotating disks, homogeneous rotating micro-/nano-disks and FGM rotating micro-/nano-disks.

1.2.1 Static and Dynamic Behaviours of Homogeneous Circular Micro-/Nano-Plates

Static and dynamic analyses of circular plates have been an important research area among researchers and scientists for many decades. Theoretical studies on homogeneous circular plates (Pardoen (1973); Leissa (1980)) were conducted long before to understand its free vibration behaviour. A significant volume of literature related to mechanical behaviour of homogeneous circular plates is available. But they are not mentioned here to maintain brevity. A nonlocal plate theory was used by Duan and Wang (2007) to investigate the axisymmetric bending of micro-/nano-scale circular plates. They presented qualitative and quantitative analysis of small-scale effects on deflection, radial moment, circumferential moment and

shear force. The MCST was used to conduct a micro-scale vibration analysis of micro-plates by Jomehzadeh et al. (2011). In this work, the influence of the length scale parameter on the natural frequencies of the micro-plates was examined, and numerical findings showed that the material size-dependence led to an increase in the natural frequency. Malekzadeh and Farajpour (2012) studied the axisymmetric free and forced vibration behaviours of elastically supported (Pasternak type) circular nano-plates under in-plane stresses. In this work, the governing equations were formulated by employing Eringen's nonlocal constitutive equations and the CPT. The axisymmetric vibration of a circular nano-plate with clamped edge has been studied by Gheshlaghi and Hasheminejad (2013) in the presence of size-dependent surface dissipation effects. In this work, the numerical examples revealed that the surface dissipation effects increase with increasing mode number.

Using the strain gradient theory and Kirchhoff plate theory, the dynamic pull-in instability and free vibration behaviours of circular micro-plates loaded by hydrostatic and electrostatic forces were studied by Mohammadi et al. (2013). It was found in this work, that raising the dimensionless internal length scale parameter or reducing the applied hydrostatic pressures results in larger pull-in voltage values. Wang et al. (2013) investigated the large amplitude axisymmetric nonlinear free vibration behaviour of size-dependent circular micro-plates based on the MCST and von Kármán nonlinear theory. In this work, the numerical findings show that the MCST-modeled micro-plates create higher stiffness than the classical continuum plate theory. The effects of surface stress on the post-buckling and free vibration behaviours of axisymmetric circular nano-plates with various edge supports were investigated by Ansari et al. (2014). They derived nonlinear equations of motion using Mindlin's plate theory in conjunction with the Gurtin-Murdoch elasticity theory. The axisymmetric vibration characteristics of a circular graphene sheet ingrained in a polymer matrix and subjected to thermo-mechanical stress was discussed by Asemi and Arajpour (2014) considering both surface and nonlocal effects. In this work, the model was developed using Gurtin–Murdoch continuum elasticity in conjunction with the nonlocal elasticity theory, and Galerkin method was used to obtain the vibration frequencies. Thai et al. (2014) carried out a research work involving Eringen's nonlocal elasticity theory and sinusoidal shear deformation theory for

micro-/nano-scale plates. They studied the effects of small scale and shear deformation on the responses of micro-/nano-scale plates.

Using the MCST, the static deflection, pull-in instability and resonant frequency for a circular micro-plate subjected to capillary force were investigated by Kahrobaiyan et al. (2015). This work reveals that when the thickness to length scale parameter ratio of the micro-plate increases, frequency also increases. Vibration analyses of embedded orthotropic circular and elliptical micro-/nano-plates were carried out by Anjomshoa et al. (2015) based on the nonlocal elasticity theory and finite element method (FEM). They showed that, for small dimensions, the natural frequencies depend on the non-locality of the micro-/nano-plates. Based on Eringen's nonlocal elasticity continuum in conjunction with the Gurtin-Murdoch elasticity theory, Sahmani and Bahrami (2015) investigated the dynamic pull-in instability and free vibration behaviour of higher-order shear deformable circular nano-plates under hydrostatic, electrostatic and surface stress effects. Using the continuum model based on the nonlocal elasticity theory Anjomshoa and Tahani (2016) investigated the free vibration responses of ingrained orthotropic thick circular and elliptical nano-plates resting on a Pasternak type elastic support. In this work, the effects on vibration frequencies of the nonlocal parameter, length of nano-plate aspect ratio, mode number, material properties and thickness were reported. A modified Kirchhoff plate model were used by Yan (2016) to examine the size-dependent bending and vibration characteristics of a clamped piezoelectric circular nano-plate. In this work, the effects of flexo-electricity, surface stress and non-local elasticity are considered into the formulation. Nonlinear dynamics and stability behaviour of an electrically actuated circular micro-plate under differential pressure were investigated by Sajadi et al. (2018). This study showed that in presence of a differential pressure, raising the DC or AC voltages assist in stabilizing the motion of the micro-plate.

Yang et al. (2018) studied the bending of nano-plates with consideration of surface effects such as the surface elasticity and surface residual stress. They considered concentrated load at the plate center and uniformly distributed load over the plate surface to develop the results. The buckling and free vibration of a circular tapered nano-plate subjected to in-plane forces were investigated by Zarei et al. (2018a) based on the nonlocal elasticity theory. According to their results, increasing the taper parameter generates an increase in the buckling load and natural frequencies, and their impacts on the clamped boundary condition were

found more than on the simply supported boundary condition. Based on the nonlocal elasticity theory, Zarei et al. (2018b) studied the axisymmetric free vibrational characteristics of a circular nano-plate with variable thickness. They found that the taper parameter had a substantial influence on the non-dimensional frequency. For the bending analysis of micro-plates under an asymmetric load, a Green's function is created, and the MCST was used by Shahrokhi et al. (2019) to predict the behaviour of microstructures with high precision. They reported findings for various asymmetric loads, and concluded that the length scale has a considerable influence on the bending of micro-plates. The small-size effects on the torsional vibration of micro-size rotors for eccentric micro-disks were studied by Jahangiri et al. (2020) using the MCST. The effects of the material length scale parameter on the torsional vibration frequency and super-harmonic resonance were studied in this work. Using the nonlocal elasticity theory, Shishesaz et al. (2020) conducted a research work to explore the small-scale influence on the linear free-field vibration of a nano-circular plate. The Ru's surface stress elasticity theory and the Gurtin-Murdoch surface elasticity theory were used by Benazouz et al. (2022) to explore the nonlinear bending of axisymmetric circular nano-plates. They presented an analytical method to determine static deflections, moments and membrane forces within the purview of circular thin nano-plates.

1.2.2 Static and Dynamic Behaviours of FGM Circular Micro-/Nano-Plates

Employing the MCST, Reddy and Berry (2012) developed mathematical models based on the classical and first-order plate theories for nonlinear axisymmetric bending of FG circular micro-plates. They concluded that the models could be used to develop analytical solutions of bending, buckling, and free vibration responses for axisymmetric formulation of circular mico-plates. Ke et al. (2012) investigated the bending, buckling and free vibration of annular micro-plates made of FGMs using the MCST and the Mindlin plate theory. They studied the effects of the length scale parameter, gradient index and inner-to-outer radius ratio on the bending, buckling and vibration properties of the FGM micro-plates with hinged-hinged and clamped-clamped boundary conditions. The mechanical behaviour of an FGM circular micro-plate exposed to nonlinear electrostatic pressure and mechanical shock was investigated by Sharafkhani et al. (2012). In this work, a step-wise linearization approach and a Galerkin-

based reduced order model were used to investigate the nonlinear static and dynamic problems. Employing Mindlin plate theory, the free vibration behaviour of thick circular FG nano-plates was carried out Hosseini-Hashemi et al. (2013) using Eringen's nonlocal elasticity theory and employing an exact analytical technique. The impacts of several parameters including the radius of the nano-plate, support conditions, material qualities and nonlocal parameter on the natural frequencies were presented in this work. Using the finite difference method, the buckling behaviour of solid circular and annular nano-plates under uniform compression have been studied by Ravari and Shahadi (2013) for a variety of boundary condition combinations. In this work, the effects of nonlocal parameter and plate size have been explored for each set of boundary conditions. Based on the MCST, Mindlin plate theory, and von Kármán geometric nonlinearity, a non-classical micro-plate model was proposed by Ke et al. (2013) for the axisymmetric nonlinear free vibration analysis of annular micro-plates comprised of FGMs. In this work, the impacts of length scale parameter, volume fraction index, inner-to-outer radius ratio, and radius-to-thickness ratio on the nonlinear free vibration response of FGM micro-plates were studied.

Using the MCST, a non-classical model for circular Mindlin plates subjected to axisymmetric loading was investigated by Zhou and Gao (2014). According to the numerical findings, the deflection and rotation angle anticipated by the MCST based model were found lesser compared to the same indicated by the traditional Mindlin plate theory. Based on the MCST, Ahmadi (2015) investigated the free vibration behaviour of annular flexural micro-plates using higher continuity C^2 finite elements. In this work, the sixth-order linear governing differential equation, in polar coordinates, has been solved by using its Galerkin weak form. Ansari et al. (2015) studied a Mindlin micro-plate model based on a modified strain gradient theory to predict axisymmetric bending, buckling, and free vibration properties of circular/annular micro-plates made of FGMs. In this work, the effects of the dimensionless length scale parameter, volume fraction index and radius-to-thickness ratio on the deformation, critical buckling load, and natural frequency of FG circular/annular micro-plates were demonstrated numerically. Eshraghi et. al. (2015) studied the static and dynamic responses of FG circular micro-plates using the MCST and considering the space variation of length scale parameter. They derived the numerical results of the displacement and frequency fields using three distinct plate theories: Kirchhoff plate theory, Mindlin plate theory and

third-order shear deformation theory. In this work, the length scale parameter ratio was shown to have a significant influence on the mechanical behaviour of FG annular and circular micro-plates. Based on the strain gradient theory, Zhang et al. (2015) constructed a size-dependent plate model to study axisymmetric bending, buckling, and free vibration analyses of FG circular and annular micro-plates using a third-order shear deformation theory. They carried out a parametric investigation to evaluate the effects of material length scale, volume fraction index, thickness-to-radius ratio, radii ratio, and support conditions on the mechanical properties of the micro-plate. An isogeometric model was developed by Ansari and Norouzzadeh (2016) to examine the size-dependent buckling behaviours of circular, elliptic, and skew nano-plates composed of FGMs. They used Eringen's nonlocal continuum theory to capture the nonlocal effects, and Mori-Tanaka homogenization technique to analyze the material properties. In this work, the free surface energy was found to have a considerable impact on the buckling configuration of nano-plates at small scale.

Based on the MCST, Ashoori and Vanini (2016a) explored the thermal stability behaviour of circular microstructure-dependent FGM plates supported on an elastic medium. They studied the impacts of the length scale parameter, gradation index, radii ratio, and elastic foundation parameters on the thermal stability properties of FGM plates. Based on MCST, Ashoori and Vanini (2016b) conducted a study on the nonlinear thermal stability of perfect/imperfect circular size-dependent FG plates, with the concurrent objective of studying the snap-through phenomenon in thermally pre-loaded plates under concentrated/uniform lateral loads. They considered two different thermal loadings, namely uniform temperature rise and heat conduction through the thickness, and two boundary conditions namely, clamped and simply supported. Within the context of the nonlocal Mindlin plate theory, Bedroud et al. (2016) investigated the buckling analysis of FG circular/annular nano-plates under uniform in-plane radial compressive force. They explored the impacts of small scales on the maximum buckling load corresponding to the optimal radius of the internal ring support for different parameters such as radius and thickness of the FG nano-plate, boundary conditions, mode numbers and material qualities. Based on the MCST, Eshraghi et al. (2016) investigated the static bending and free vibration responses of thermally loaded FG annular and circular micro-plates. They formulated the problems using three plate theories namely, Kirchhoff

theory, Mindlin theory and third-order shear deformation theory, and demonstrated influences of thermal loading, material and geometric parameters on the static deformation, stress and natural vibration frequencies. Employing the MCST, Reddy et al. (2016) developed finite element formulations based on Kirchhoff and first-order circular plate theories for nonlinear axisymmetric bending of FG micro-plates. They investigated the effects of geometric nonlinearity, power law index and microstructure-dependent constitutive relations on the bending responses for different boundary conditions.

Ji et al. (2017) conducted a comparison study of strain gradient theories and their applications to FG circular micro-plates. In this work, the results showed that considering the strain gradients into account increases plate stiffness, which leads to less deflection, and an increase in the natural frequency. Transverse vibration and thermal buckling of a size-dependent FG circular micro-plate were examined by Ghadiri et al. (2017) using the MCST and CPT for various boundary conditions. They reported the influences of temperature fluctuations, changing boundary conditions, length scale parameter, FG index and buckling stress on the first and second non-dimensional frequencies of vibration. The nonlocal elasticity theory was used by Golmakani and Vahabi (2017) to study the buckling behaviour of FG single-layered annular graphene sheets embedded in a Pasternak elastic medium. They investigated the effects of small-size, gradation parameter, elastic medium, support conditions, buckling mode and geometric parameters on the critical load through a parametric study. The numerical study of thermal stability and free vibration of a temperature-dependent circular FG porous micro-plate subjected to a nonlinear thermal load was performed by Shojaeefard et al. (2017) using the MCST and considering the CPT and FSDT. They represented the critical conditions of the plate for variations of porosity, FG power index, size-dependency, temperature change and geometrical dimensions. Wang et al. (2017) investigated the microstructure-dependent axisymmetric large deflection bending of pressure loaded circular micro-plates made of FGMs using the MCST for different boundary conditions. They presented and analyzed results for the bending deflection of micro-plates with regard to several significant characteristics such as length scale parameter, FGM variation, boundary conditions and symmetrical transverse loadings. Employing the MCST, the size-dependent thermal buckling and post-buckling behaviours of FG circular micro-plates were investigated by Zandekarimi et al. (2018) based on the CPT and von Kármán geometric

nonlinearity under uniform temperature rise and clamped boundary condition. In this work, the effects of the gradation parameter, length scale parameter, and thickness-to-radius ratio on the thermal buckling and post-buckling behaviour were analyzed. The coupled heat conduction equation was used to investigate the thermo-elastic damping of FGM circular micro-plates by Li et al (2018). The results of ceramic-metal composite FGM circular micro-plates were provided to illustrate the impacts of the material gradient index, geometry, vibration mode-shapes and temperature on the thermo-elastic damping.

Norouzzadeh and Ansari (2018) presented a size-dependent investigation of surface elasticity and nonlocal elasticity on the free vibration behaviour of circular and rectangular FGM nano-plates using the Gurtin-Murdoch and Eringen's elasticity theories. Several case studies have been presented to show the effects of surface characteristics and small-scale influences on the vibration behaviour of nano-plates with various boundary conditions. The static and dynamic behaviours of inhomogeneous macro- and nano-plates constructed of FGMs were investigated by Dastjerdi and Akgöz (2018) using the 3D elasticity theory in combination with Eringen's nonlocal theory and considering variation of deflection along the thickness. They investigated the effects of some important parameters such as the size of the plate, loading, FGM parameters and boundary conditions. Mahinzare et al. (2019) investigated the vibration behaviour of circular nano-plates made of functionally graded piezoelectric material (FGPM) subjected to rotational and thermal loading using the strain gradient theory, nonlocal strain gradient theory, Eringen's elasticity theory and considering first order shear deformation theory (FSDT). It was shown that the vibration behaviour of nano-plates was influenced by temperature rise, angular speed, external voltage, FG gradation parameter, material length scale parameter and nonlocal parameter. Analysis of axisymmetric vibrational behaviour of size-dependent circular nano-plates made of FGM using the integral form of the nonlocal strain gradient theory was conducted by Pourabdy et al. (2021). The findings of this study can be considered as a pivotal point in the progress of theoretical results toward better prediction of vibration behaviour of nano-structures. The axisymmetric vibration behaviour of a size-dependent circular nano-plate made of FGM under various boundary conditions was investigated by Shariati et al. (2022). The analysis was carried out using the stress-driven model, strain gradient theory and CPT. The findings indicate that this

methodology is appropriate for the vibration analysis of such components with a high convergence rate.

Based on the nonlocal elasticity theory and FSDT, the nonlinear bending analysis of bilayer orthotropic annular/circular graphene sheets was investigated by Dastjerdi and Jabbarzadeh (2016). Based on the non-local elasticity theory and FSDT, the nonlinear bending analysis of multilayer orthotropic annular/circular graphene sheets under thermal loading was carried out by Dastjerdi and Jabbarzadeh (2017). They investigated the effects of small-scale parameters, the van der Waals interaction between different layers of graphene sheets, different elastic foundation matrix values and load for different nonlocal coefficients. Using FSDT and modified strain gradient theory, Mohammadimehr et al. (2018) studied the bending, vibration and buckling behaviours of micro-composite sandwich circular plates with carbon nanotube (CNT) reinforced composite face-sheets under hydro-thermo-magneto-mechanical loadings. The results were presented to show the influences of the length scale coefficient, thermal and moisture effects, magnetic effect, core-to-facesheet thickness ratios on the deflection, natural frequency and critical load. Arshid et al. (2021) presented the bending and buckling responses of a heterogeneous annular/circular sandwich micro-plates mounted on a Pasternak foundation using the FSDT and MCST. In this work, they investigated and highlighted the effects of different properties and aspect ratio of the plate.

1.2.3 Static and Dynamic Behaviours of Homogeneous Rotating Disks

D'Angelo and Mote (1993) predicted the vibration frequencies of a thin spinning disk, clamped by thick fraction collars. This study showed that friction and slippage significantly affect the disk natural frequency when the disk spins at very high speed. Using Ritz method and employing FEM, Shahab (1993) investigated the vibration behaviours of uniform and variable thickness disks. He also carried out experimentation on this using holographic interferometry. Raman and Mote (1999) investigated the nonlinear response of a circular plate subjected to fixed transverse force and rotating near a critical speed of an asymmetric mode using von Kármán type field equations. They also conducted a simple experiment to confirm the analytical prediction. The transverse vibration behavior of a circular rotating disk was analyzed by Manzione and Nayfeh (2001) when the disk was subjected to a space-fixed linear spring. They studied the stability characteristics of all the possible interactions among four of

the lowest modes. Using Tresca's yield criterion, a static analytical solution is presented by Eraslan and Orcan (2002) for an elastic-plastic rotating solid disk of variable thickness. They reported that the radial stress at the central portion might exceed the circumferential stress, depending on the disk profile. Employing Mindlin plate theory, Eid and Adams (2006) investigated the critical speed and the dynamic response of a spinning disk, which is centrally clamped and subjected to a stationary load. They presented a combined analytical and numerical method to determine the four lowest critical speeds for a clamped-free circular disk for various thickness and clamping ratio. Nonlinearly coupled in-plane and transverse vibrations for a spinning disk have been carried out by Boddur and Zu (2007) using Galerkin method and canonical perturbation approach.

Bauer and Eidel (2007) conducted their research on transverse vibration and stability analyses of rotating circular plates of uniform thickness for various boundary conditions such as clamped, free, guided and simply supported. The dynamic analysis of a rotating annular plate was conducted by Meretic and Glavardanov (2008), and they discussed the impact of mounting overlap on stability of the rotating plate. Basmal et al. (2009) investigated the in-plane free vibration of a circular annular isotropic disk using Rayleigh-Ritz method and presented the mode-shapes to explain the free vibration behaviour of the disk under different boundary conditions. Okuizumi (2009) investigated the vibration behaviour of a rotating circular membrane subjected to a transverse distributed load, considering von Kármán theory and taking into account buckling under rotationally symmetric deformation. The out-of-plane free vibration behaviour of a rotating homogeneous annular disk under uniform transverse pressure loading was studied by Das at al. (2010). They employed energy principle to formulate the governing equations and presented the results in a non-dimensional plane.

The effects of rigid body translational degree-of-freedom on the linear vibration behaviour of a disk were investigated by Khorasany and Hutton (2010). In this work, the disk is constrained by a space-fixed linear spring whereas the inner boundary is free to move along the radial direction. Zhou et al. (2011) conducted a research work on the dynamic behaviour of a thin circular and annular disk using the conservation principle of mixed energy and constructed in a new symplectic space. In this work, three basic support conditions for circular plates and nine basic support conditions for annular plates were studied. Using

piezoelectric actuators, the dynamic behaviour of rotating disk structures due to rotor stator interaction was studied by Presas et al. (2014). Presas et al. (2015a) analyzed the effect of rotation on the natural frequencies and mode-shapes of a disk submerged and confined inside a casing filled with water using analytical, numerical and experimental methods. Presas et al. (2015b) further investigated the vibration frequencies and mode-shapes of a rotating disk from a stationary frame, and showed how frequency and mode-shape changed with the change in medium of fluid inside the casing.

The nonlinear free vibration of a circular rotating thin plate under clamped support condition subjected to a static load in magnetic field was studied by Hu and Wang (2016) using Galerkin integral method. Shahriari et al. (2017) conducted free vibration analysis of variable thickness rotating bladed disks for aircraft gas turbine considering generalized differential quadrature method (DQM). Pei et al. (2018) investigated the dynamic behaviour of rotating flexible annular disks under twenty-five different boundary conditions, and compared their natural frequency, dynamic stability, critical speed and limit speed. Vibration and buckling analyses of a rotating plate were investigated by Yang and Kang (2018) using the Ritz method. In this work, the disk was considered annular with free inner edge and clamped outer edge, and subjected to compressive centrifugal body force. Tang el al. (2021) analyzed the frequency and mode-shape of a rotating-flexible disk-drum structure considering Sander's shell and the Kirchhoff plate theory. Koç et al. (2023) conducted their research on the dynamic behaviour of spinning annular disks for nine different boundary conditions. They employed Galerkin method to solve the governing equations, and investigated the effect of radius ratio and rotational speed on the free vibration frequency.

1.2.4 Static and Dynamic Behaviours of FGM Rotating Disks

Durodola and Attia (2000) investigated the deformation and stress in a rotating hollow and solid disks made up of FGM. In this work, FEM and numerical integration were used to predict the stress and deformation distribution in the disk. The analytical solution for exponential FGM rotating disks with various boundary conditions (Zenkour (2005)) and with rigid casing (Zenkour (2007)) were investigated, where the solution obtained was in terms of Whittker's function. Chen et al. (2007) investigated the three-dimensional analytical solution for a rotating disk made up of FGM, which is transversely isotropic. They showed that the

gradient index has important effect on the elastic deformation. A semi-analytical thermo-elastic solution of an FGM rotating hollow and solid axisymmetric disk was conducted by Kordkheili and Naghdabadi (2007). They presented the effect of radius ratio on stress, strain and displacement components under centrifugal and thermal loading.

Bayat et al. (2008) analyzed the elastic solution of rotating disks with variable thickness for parabolic and hyperbolic profile under free-free and fixed-free boundary conditions. Their results showed that the parabolic concave and hyperbolic convergent thickness could be more efficient than uniform profile. Bending analysis of rotating FGM disks based on the FSDT was conducted by Bayat et al. (2009a), and thermo-elastic analysis of FGM disks with temperature-dependent material properties and thickness variation was carried out by Bayat et al. (2009b). Employing finite element method, Afsar and Go (2010) conducted a thermo-elastic analysis of a thin circular FGM rotating disk which was subjected to a thermal load and centrifugal rotation. The analysis of the results reveals that the thermo-elastic field was influenced by the temperature distribution profile, thickness and angular speed of the disk. A broad analysis regarding thermal stress in FGM rotating annular disks was conducted by Peng and Li (2010). The result was presented graphically showing the effects of temperature difference, rotational speed and thickness of the disk on the distribution of thermal stress.

Asghari and Ghafoori (2010) addressed a three-dimensional elasticity solution for rotating hollow and solid disks made up of FGM. The results showed that there was a substantial difference between three-dimensional and two-dimensional solution for thick rotating disks. Çallioğlu et al. (2011) studied the stress analysis of annular rotating disks made with FGM where the property is varying along the radial direction, and they showed that the radial displacement increased gradually as the material gradation index had been increased. Using Liao's homotopy analysis, Asomina's decomposition method and variational iteration method, a semi-exact elastic solution for a rotating FGM disk with non-uniform thickness and thermal loading was conducted by Hassani et al. (2011) to determine the stress and strain distribution along radial direction. Free vibration analyses of multidirectional FGM circular and annular disks were carried out using the state-space based DQM by Kermani et al. (2012).

Non-dimensional frequencies and mode-shapes were shown for different boundary conditions in this article.

Tutuncu and Temal (2013) investigated the thermo-elastic behaviour of rotating variable thickness disk made up of FGM and subjected to non-uniform temperature rise, using complimentary function method and fifth-order Runge-Kutta method. Thermo-elastic displacements, stresses and strains in a thin rotating circular disk made up of FGM was analyzed by Sharma et al. (2013) using FEM. In this work, the effects of Kibel Number on stresses, strains and displacements have been discussed. Golmakani and Kadkhodayan (2014) studied the axisymmetric bending and stretching behaviour of circular and annular FGM disks of variable thickness under thermo-mechanical loading and different boundary conditions. Bayat et al. (2014) presented a magneto-thermo-mechanical response of FG magneto-elastic material rotating disks with variable thickness for different boundary conditions. The effects of magnetic field and grading index on mechanical and thermal stress were explained in this article. Kermani et al. (2016) investigated the nonlinear behaviour of stability, rotational dynamics and free vibrations of annular spinning disks composed of FGM. The governing equations of motion were developed by applying the CPT and von Kármán nonlinear plate theory. The results showed the effects of the gradation parameter, rotational speed, thickness-to-outer radii ratio, inner-to-outer radii ratio and various support conditions on the vibration frequencies of the disk.

Using elastic-perfectly-plastic material model, Nejad et al. (2014) obtained an exact closed-form solution for deformations and stresses of a rotating FGM disk. The results showed that density variation had a pronounced influence on the distribution of deformation and stress. The stress and displacement for a rotating circular FGM disk with a variable rotational speed was investigated by Dai and Dai (2015) with the help of Runge-Kutta technique and shooting method to solve ordinary differential equations. They showed that the material gradation index and angular speed had major influence on the mechanical behaviour of the rotating disks. A semi-analytical technique was used by Dai and Dai (2016) to determine the displacement and stress fields in a FGM annular disk, revolving with an angular acceleration under varying temperature field. The research results disclose that the values of the FGM index, geometric shape, angular speed, temperature and the boundary condition have prominent effects on the displacement and stress fields. Zheng et al. (2016) performed a

numerical analysis for the stress field in rotating disks made up of FGM with non-uniform thickness and varying angular velocity. The influence of the material gradient index on the stress field was addressed in this work. They also showed that the thickness profile that was a rational function of the radial coordinate produced the best stress field.

Jalali et al. (2018) carried out free vibration study of a spinning annular disk formed of FGM with variable thickness under clamped and free boundary condition using generalized DQM. Bagheri and Jahangiri (2019) used DQM to conduct an in-plane free vibration study of FG spinning disks with varying thickness. The impact of the disk's FG index and geometrical shape on its natural frequencies and critical speed were explained in this article. A rotating porous FG magneto-electro-elastic annular plate with variable thickness in a hygrothermal environment was examined by Dai et al. (2019). They used DQM to construct and solve steady-state heat conduction and nonlinear moisture diffusion equations. Thermo-elastic analysis of axisymmetric bending of FGM rotating disks with and without imperfection was presented by Babamiri et al. (2020). In this work, the impacts of material characteristics, temperature and imperfection on displacement and stress fields with varying support conditions were evaluated numerically. Eldeeb et al. (2021) investigated the influences of angular deceleration on the thermo-elasto-plastic behaviours of non-uniform thickness multilayer FGM disk. They investigated a series of case studies and addressed the effects of many parameters such as the layers and the role of their volume fractions, the deceleration rate, kind of behaviour, the thickness profile, and the disk diameters. The displacements, stresses and strains for a spinning FGM disk with varying thickness was presented by Sharma et al. (2021) using the FEM. Under a power law distribution of material properties, the thermo-elastic behaviour of the disk were studied for different non-homogeneity parameters.

1.2.5 Static and Dynamic Behaviours of Homogeneous Rotating Micro-/Nano-Disks

Pei (2012) modeled a flexible annular rotating micro-disk under thermo-elastic coupling to explore the thermo-elastic damping in spinning micro-disks in micro-drives. In this work, the effects of rotational speed, surface convection and temperature on vibration frequency, frequency shift and thermo-elastic damping were studied. Danesh and Asghari (2014) employed the strain gradient theory of elasticity to examine the mechanical behaviour of

rotating micro-disks using variational approach to generate the governing equations and boundary conditions. Some numerical results were provided to emphasize the benefit of using non-classical theories rather than the classical continuum theory while dealing with micro-rotating disks. Based on the strain gradient theory, the effects of small-size on the mechanical behaviour of micro-rotating disks with angular acceleration were examined by Bagheri et al (2019). They examined the distribution of the displacement and stress components using a numerical case study, and the outcomes were compared with those predicted by the traditional continuum theories. The static inertial-elastic instability of spinning nano-disks was investigated by Guven (2019) using the centrifugal force formulation with radial displacement, considering Eringen's nonlocal theory. In this work, the variations of critical rotation speeds with the nonlocal parameter were demonstrated for different support conditions. Bagheri et al. (2020) investigated the small-scale impacts on the in-plane free vibration of micro-disks using the MCST under diverse boundary conditions. The impacts of the micro-disks' angular speed and the length scale parameter on the stable radial and tangential displacements as well as the natural frequencies were explored in this work. Based on the MCST, the elasticity formulation for the equations of motion of micro-rotating disks were obtained by Bagheri and Asghari (2021) in the presence of angular acceleration for different boundary conditions. They examined the influence of couple stresses on the distribution of stresses and displacements through a numerical case study.

1.2.6 Static and Dynamic Behaviours of FGM Rotating Micro-/Nano-Disks

Employing the strain gradient theory, Baghani et al. (2016) investigated the mechanical response of a micro-/nano-rotating disk made of FGMs with varying thickness. This work demonstrated that non-homogeneity constants had a significant influence on the stress distribution in the FG spinning disk. Based on the strain gradient theory, Hosseini et al. (2016) conducted a study of spinning nano-disks of varied thickness made of FGM. The influence of several characteristics on stresses such as graded index and thickness profile were investigated in this work. The strain gradient theory of elasticity was used by Shishesaz et al. (2017) to investigate the thermo-elastic behaviour of FG nano-disks. This work clearly highlights the differences in stresses generated from the CPT and strain gradient theory. In this work, the effects of external load, material in-homogeneity parameter, rise in temperature

on radial displacement and stress components at the inner and outer radii were thoroughly explored. Based on the FSDT and MCST, the free vibration of a circular rotating nano-plate consisting of bi-directional FG piezo materials was studied by Mahinzare et al. (2018a). They demonstrated that the rotational velocity, external electric voltage, size dependency and power-law index have profound influence on the plate's vibration behaviour. Based on the FSDT and MCST, Mahinzare et al. (2018b) studied the free vibration response of a BFGM spinning circular micro-plate, exposed to thermal load and supported on Winkler-Pasternak foundation. They assessed the effectiveness of the Winkler and Pasternak coefficients, FG gradation parameter, size dependency, rotational speed, temperature variations and thermal environment on the vibration frequencies of the spinning micro-plate using a parametrical analysis.

The free vibration of a rotating variable thickness two-directional FG circular micro-plate was investigated by Shojaeefard et al. (2018a) using the FSDT and MCST. The results reveal that increasing the size-dependency reduces the non-dimensional natural frequency as well as the critical angular velocity. Based on Eringen's nonlocal elasticity theory and the MCST, Shojaeefard et al. (2018b) studied the free vibration behaviour of rotating circular micro-/nano-plates made of FG magneto-elastic material using the FSDT. The work reveals that raising the angular velocity causes a critical point, and the influence of numerous factors such as the size-dependency of non-classical theories and the power law index changes beyond this point. The stress distribution in an FG nano-disk of varying thickness was investigated by Hosseini et al. (2019) using the strain gradient theory while the nano-disk was exposed to thermal and mechanical pressures, and was spinning with a constant angular velocity. They investigated the impacts of rotational speed, material in-homogeneity, thickness profile, mechanical loads and temperature on the total stresses and the radial displacements. The vibrational properties of a laminated composite annular micro-plate covered with a viscoelastic foundation were modeled by Al-Furjan et al. (2021) using the Kelvin-Voight model and MCST. They conducted a parametric study to investigate the effects of the length scale parameter, radial and circumferential modal number, radius ratio, geometry of the laminated layer and support conditions on the frequency characteristics of the annular micro-plate.

Based on the preceding discussion, the summary of the available research contribution pertaining to rotating micro-/nano-disks has been presented in Table 1.1. Also the corresponding research gaps are also presented in Table 1.1.

Table 1.1: Summary of research contribution and research gaps.

Literature	Contribution	Research Gap
• Danesh and Asghari (2014)	• The first work on rotating micro-disk based on strain-gradient theory. • Based on axisymmetric formulation. • Studied static stress analysis.	• Asymmetric formulation was not presented. • Dynamic and buckling behaviour were not studied. • Presented very limited results.
• Hosseini et al. (2016) • Shishesaz et al. (2017) • Hosseini et al. (2019)	• Studied thermo-elastic behaviour of FG nano-disks. • Studied static stress analysis. • Based on axisymmetric formulation.	• Asymmetric formulation was not presented. • Dynamic and buckling behaviour were not studied.
• Mahinzare et al. (2018a) • Mahinzare et al. (2018b) • Shojaeefard et al. (2018a) • Shojaeefard et al. (2018b)	• Studied vibration behaviour of FGM rotating micro-/nano-plates based on the various non-classical theories. • Dealt with solid plates under clamped and hinged boundary conditions at the outer edge of the plates. • Based on axisymmetric formulation.	• Typical clamped-free rotating disk-type problem of FGM micro-disks was not studied. • Annular configurations for different support conditions both at the inner and outer edge were not considered. • Asymmetric formulation was not presented.

1.3 Identification of Research Problems

The literature survey presented in the preceding section reveals that the research works involving mechanical behaviour of homogeneous and FGM rotating disks based on the classical continuum theories are significant in number. It also reveals that there is ample number of research works available, which studied the mechanical behaviour of homogeneous and FGM circular micro-/nano-plates based on different non-classical theories. The literature review further reveals that the number of research works involving mechanical behaviour of rotating micro-/nano-disks based on the non-classical continuum theories is very limited. In fact, the research study involving rotating micro-disks based on a non-classical continuum theory was first reported by Danesh and Asghari (2014) a few years before. After that, though the research studies on the rotating micro-/nano-disks based on the non-classical continuum theories started to come up in open literature, they are limited in number. Hence, the research domain to study the mechanical behaviour of rotating micro-/nano-disks involving non-classical theories is very new, and has many research gaps. The specific problems of the present thesis and the theme of the thesis as a whole are indeed based on those research gaps. In that sense, the problems of the thesis and the presented results are new and reported for the first time through this work and its publications. Beside this novelty, the methodology adopted to formulate the present mathematical model is a novel one, which is reported for the first time through this work. Through a generalized mathematical model, the present work studies four specific problems, which are related to the main theme of the thesis.

From the literature review, it is seen that the studies on the vibration behaviour of FGM rotating micro-/nano-plates based on the various non-classical theories are very limited, and are found in Mahinzare et al. (2018a), Mahinzare et al. (2018b), Shojaeefard et al. (2018a) and Shojaeefard et al. (2018b). In all these works, the rotating plates are assumed to be supported at the outer edge. Hence, the typical clamped-free rotating disk-type problems of FGM micro-disks have not yet been studied by the researchers. Furthermore, only the axisymmetric modes of vibration are considered in the above-mentioned works by Mahinzare et al. (2018a), Mahinzare et al. (2018b), Shojaeefard et al. (2018a) and Shojaeefard et al. (2018b). Hence in the first problem of the present thesis, the free vibration response of clamped-free BFGM rotating micro-disks, operating under high-temperature thermal loading,

have been studied based on the MCST. This particular problem is investigated up to the first six modes of vibration. The modes dealt with are of axisymmetric and asymmetric bending as well as of the torsional vibration.

It is known that understanding of the free vibration behaviour of clamped-free rotating micro-disks subjected to transverse pressure and operating in high-temperature environment has huge significance in industrial applications. However, the literature review finds no such study related to this specific problem. Hence, the second problem of the present thesis studies the free vibration response of the clamped-free BFGM rotating micro-disks subjected to transverse pressure and high-temperature thermal loading, and it is based on the MCST. This particular problem is investigated for the first four modes of vibration, which consists of different combinations of axisymmetric bending, asymmetric bending and torsional modes.

The study of the free vibration behaviour only for the axisymmetric bending/flexural modes of clamped-free rotating disks is of special importance. This is evident from the literature survey where most of the research studies on the free vibration behaviour of rotating disks (of both macro- and micro-size) have been carried out for the asymmetric bending modes. This fact is true for the studies involving both classical and non-classical theories, though the studies involving the non-classical theories are mostly conducted for rotating circular micro-plates supported at their outer edges. Hence, the free axisymmetric bending vibration behaviour of clamped-free rotating micro-disks is not available in the literature. Hence, the third problem of the present thesis studies the free axisymmetric bending vibration response of the clamped-free BFGM rotating micro-disks subjected to transverse pressure, and operating in high-temperature environment. This study is also based on the MCST. This particular problem reports the response for the first four axisymmetric bending vibration modes.

Further, to have a comprehensive understanding of rotating disk dynamics, the effects of different boundary conditions must be studied. The literature survey shows that the free vibration behaviour of BFGM rotating micro-disks have not yet been studied for annular configuration under different boundary conditions. Though studies on FGM rotating micro-size plates are available (Mahinzare et al. (2018a), Mahinzare et al. (2018b), Shojaeefard et al. (2018a) and Shojaeefard et al. (2018b)), they are conducted for solid plates under clamped and hinged boundary conditions at the outer edge of the plates. Because of this research gap, a

problem has been undertaken to study the free vibration behaviour of BFGM rotating annular micro-disks under four different boundary conditions namely, simply supported-simply supported (SS), clamped-simply supported (CS), simply supported-clamped (SC) and clamped-clamped (CC). This is the fourth problem of the thesis. It is noted that 'C', and 'S' stand for clamped and simply supported boundary condition respectively. The first letter of each case corresponds to the inner radius and the second letter corresponds to the outer radius of the annular micro-disk. Furthermore, while considering different boundary conditions, the critical condition leading to static buckling of the micro-disk, when the vibration frequency becomes zero, has been identified and reported.

1.4 Mathematical Background

The following principles/theories/methodologies have been used to formulate the generalized mathematical model for the problems mentioned in the preceding section with an objective to study the free vibration behaviour of BFGM rotating micro-disks: Principle of minimum total potential energy, Hamilton's principle, Ritz method, Gram-Schimdt orthogonalization scheme, Eigenvalue problem and Modified couple stress theory. A brief overview of these standard principles/theories/methodologies is given below:

1.4.1 Principle of Minimum Total Potential Energy

Stress and deformation analysis of structural elements can be carried out using the principle of minimum total potential energy. A constrained structural system (i.e., a structure that is fixed at some part of its boundary) will deform when external forces are applied on it. Deformation of a structural system is the incremental change to the deformed state from the original undeformed state. The displacements are the principal unknown variables in a displacement-based structural analysis, and strains and stresses are the variables which are derived employing the strain-displacement relationships and the constitutive relationships respectively. Therefore, the primary objective is to determine the displacements leading to deformation. Upon application of forces, the deformed state that a structure reaches is the equilibrium state of the system. A structural system, out of the many possible deformations, will only attain a unique deformation state to achieve the equilibrium. According to the

principle of minimum total potential energy, this unique deformation state corresponds to the minimum value of the total potential energy (Π) of the system.

The total potential energy of a structural system is determined as the sum of its strain energy (U) and work potential (W) given as follows:

$$\Pi = U + W. \tag{1.1}$$

Here, the strain energy is defined as the elastic energy induced in the deformed structure; the work potential is the negative value of the mechanical work imposed by the external loads acting on the system. The principle of minimum total potential energy (Shames and Dym (2009); Reddy (2002); Reddy (2008)) states: "For conservative structural systems, of all the kinematically admissible deformations, those corresponding to the equilibrium state extremize (i.e., minimize or maximize) the total potential energy, and if the extremum is a minimum, the equilibrium state is stable." Mathematically, it is written as follows:

$$\delta(\Pi) = \delta(U + W) = 0, \tag{1.2}$$

where, δ is the variational operator. In conservative systems, W is independent of the path taken from the undeformed state to the deformed state. Further, kinematically admissible deformations are those that satisfy the geometric (kinematic) boundary conditions of the structure.

1.4.2 Hamilton's Principle

Hamilton's principle is an important variational principle in structural dynamics. Hamilton's principle (Shames and Dym (2009); Reddy (2002); Reddy (2008)) states: "Of all the paths of admissible configurations that the body can take as it goes from configuration '1' at time τ_1 to configuration '2' at time τ_2, the path that satisfies Newton's law at each instant during the interval (and is thus the actual locus of configurations) is the path that extremizes the time integral of the Lagrangian during the interval." Deformable bodies have an infinite number of degrees of freedom, and occupy continuous regions of space. Consequently, the state of the system is described by using continuous functions of space and time. Hamilton's principle for such bodies is mathematically written as follows:

$$\delta\left(\int_{\tau_1}^{\tau_2}\left(T_k-\Pi\right)d\tau\right)=0, \tag{1.3}$$

where, $\left(T_k-\Pi\right)$ is called the Lagrangian and T_k is the kinetic energy of the body at time τ. Noting that $\Pi=U+W$ is the total potential energy, the following familiar form for Hamilton's principle is obtained:

$$\delta\left(\int_{\tau_1}^{\tau_2}\left(T_k-U-W\right)d\tau\right)=0. \tag{1.4}$$

1.4.3 Ritz Method

One of the most powerful approximate methods originating from variational mathematics is the Ritz method. In this method, an approximate solution is expected with respect to the exact solution of the equation that describes the energy principle. According to this method, an assumed solution is considered in the form of finite linear combinations of unknown coefficients and properly selected functions. As the solution of a continuum problem cannot be obtained by a finite set of functions, an error is introduced and thus making it an approximate solution. With increase in the linearly independent parameters in the assumed solution, error in the solution is reduced, and convergence to the exact solution is achieved.

According to this method (Shames and Dym (2009); Reddy (2002); Reddy (2008)), a dependent unknown (e.g., the displacement) u is approximated by a finite linear combination U_n of the form given below:

$$u\approx U_n=\sum_{i=1}^{n}c_j\phi_j+\phi_0. \tag{1.5}$$

Then the undetermined parameters c_i are determined by considering that the principle of minimum total potential energy holds for this approximate problem. In Eq. (1.5), $\sum c_j\phi_j$ incorporates the homogeneous form of the essential (geometric) boundary conditions, and ϕ_0 incorporates the non-homogeneous form of the essential boundary conditions. To get the solution of the equation that results using Ritz approximation method with minimum error (as the number of parameter n increases), one should choose ϕ_j and ϕ_0 wisely, such that the two

functional requirements of convergence and completeness get satisfied. The lists of requirements needed for convergence of Ritz approximation (Eq. (1.5)) are:

(i) ϕ_j should satisfy the following three conditions:

(a) Each ϕ_j is continuous.

(b) Each ϕ_j satisfies the homogeneous form of the specified essential boundary conditions.

(c) The set $\{\phi_j\}$ is linearly independent and complete.

(ii) ϕ_0 should satisfy the specified essential boundary conditions associated with the variational formulation.

1.4.4 Gram-Schmidt Orthogonalization Scheme

In order to satisfy the requirement of linear independence of ϕ_j, an orthogonal set of functions ϕ_j has been considered in the present work. The complete set of orthogonal functions ϕ_j used in Eq. (1.5) for approximating any displacement field, following the Ritz method, is generated through a numerical implementation of Gram-Schmidt orthogonalization scheme. To cater to the need of the numerical scheme, all the functions are described numerically at some suitably selected Gauss points (Saha et al. (2004)). The algorithm for generation of the functions are given as follows:

Beginning with a polynomial $\phi_0(\rho)$, a set of orthogonal polynomials in the interval $a \le \rho \le b$ is generated as given below:

$$\phi_1(\rho) = (\rho - B_1)\phi_0(\rho), \tag{1.6a}$$

$$\phi_j(\rho) = (\rho - B_j)\phi_{j-1}(\rho) - C_j\phi_{j-2}(\rho), \tag{1.6b}$$

where,

$$B_j = \left(\int_x^b \rho w(\rho)\phi_{j-1}^2(\rho)\,d\rho\right) \Big/ \left(\int_x^b w(\rho)\phi_{j-1}^2(\rho)\,d\rho\right), \tag{1.7a}$$

$$C_j = \left(\int_x^b \rho w(\rho)\phi_{j-1}(\rho)\phi_{j-2}(\rho)\,d\rho\right) \Big/ \left(\int_x^b w(\rho)\phi_{j-2}^2(\rho)\,d\rho\right), \tag{1.7b}$$

with $w(\rho)$ being the weight function. The set of functions $\phi_j(\rho)$, thus generated, satisfy the following orthogonality condition:

$$\int_x^b w(\rho)\phi_i(\rho)\phi_j(\rho)\,d\rho = 0 \text{ if } i \neq j, \tag{1.8a}$$

$$= 1 \text{ if } i = j. \tag{1.8b}$$

Here, the weight function $w(\rho)$ is chosen as unity and the interval of ρ is selected from 0 to 1.

1.4.5 Eigenvalue Problem

Let A and X be a square matrix and column vector respectively of order n as given below:

$$X = \begin{bmatrix} x_1 \\ x_2 \\ \dots \\ x_n \end{bmatrix} \text{ and } A = \begin{bmatrix} a_{11} & a_{12} & \dots. & a_{1n} \\ a_{21} & a_{22} & \dots. & a_{2n} \\ \dots. & \dots. & \dots. & \dots. \\ a_{n1} & a_{n2} & \dots. & a_{nn} \end{bmatrix}. \tag{1.9}$$

The linear transformation $AX = Y$ carries the column vector X into the column vector Y by means of the square-matrix A. In practice, it is often required to find such vectors, which transform into themselves or to a scalar multiple of themselves.

Let X be such a vector, which transforms into λX by means of the above-mentioned transformation, then we can write as follows:

$$\begin{aligned} & AX = \lambda X \\ \Rightarrow\ & AX - \lambda IX = 0 \\ \Rightarrow\ & [A - \lambda I]X = 0. \end{aligned} \tag{1.10}$$

This matrix equation represents *n* homogeneous linear equations of the form given below:

$$\begin{aligned} & (a_{11} - \lambda)x_1 + a_{12}x_2 + \dots. + a_{1n}x_n = 0 \\ & a_{21}x_1 + (a_{22} - \lambda)x_2 + \dots. + a_{2n}x_n = 0 \\ & \dots. \quad \dots. \quad \dots. \quad \dots. \quad \dots. \quad \dots. \\ & a_{n1}x_1 + a_{n2}x_2 + \dots. + (a_{nn} - \lambda)x_n = 0. \end{aligned} \tag{1.11}$$

The set of equations given above will have a non-trivial solution only if the coefficient matrix $\left[A-\lambda I\right]$ is singular, i.e., if

$$\left|A-\lambda I\right|=\begin{vmatrix} a_{11}-\lambda & a_{12} & .... & a_{1n} \\ a_{21} & a_{22}-\lambda & .... & a_{2n} \\ .... & .... & .... & .... \\ a_{n1} & a_{n2} & .... & a_{nn}-\lambda \end{vmatrix}=0. \qquad (1.12)$$

This is called the characteristic equation of the transformation, and is same as the characteristic equation of the matrix A. It has n roots or eigenvalues, which are $\lambda_1,\ \lambda_2,\ .....,\ \lambda_n$. For each eigenvalue $\lambda_i\ \left(i=1,\ 2,....,\ n\right)$, a non-zero solution $X^i=\left[x_1^i,\ x_2^i,.....,x_n^i\right]^T$ can be obtained, which is known as the *eigenvector* or *latent vector* (Shames and Dym (2009); Reddy (2002)).

1.4.6 Modified Couple Stress Theory

The classical theory or conventional mechanics states that a force applied to a material particle produces translation of the particle only, and the force is determined through the observation of the motion or the change in kinetic energy of the particle. The applied loads on the material particle in the classic couple stress theories (CCST) for linear elastic materials comprise (i) a force to translate the material particle and (ii) a couple to drive it to rotate (Fleck and Hutchinson (1997)). Only the classic equilibrium relations between forces and moments (of forces) are required to constrain the force that produces translation. Due to absence of higher order equilibrium relations, the couple is unrestricted. The deformation measure that gives strain energy of any micro-structure are the symmetric stress tensor conjugate to the displacement gradient (or symmetric strain tensor), and the couple stress tensor (both symmetric and asymmetric) conjugate to the rotation gradient (both symmetric and asymmetric). Two curvature tensors coexist because of unconstrained nature of couple vector. For linear elastic materials, there are two independent material length scale parameters $\left(l\right)$ associated with the two curvature tensors in CCST.

Yang et al. (2002) developed couple stress-based strain gradient theory of elasticity, known as modified couple stress theory (MCST), incorporating equilibrium of the moment of couples as an extra equation for the couple stresses. In the MCST, an additional higher order

equilibrium equation for continuum has been introduced that resolves the free-floating nature of the couple vector, and restrict the couple stress tensor and the curvature tensor to be symmetric only. According to the MCST: the classical stress tensor (symmetric) $(\boldsymbol{\sigma})$ is energy conjugate to the classical strain tensor (symmetric) $(\boldsymbol{\varepsilon})$; the deviatoric part of the symmetric couple stress tensor $(\boldsymbol{m})$ is the only energy conjugate to the symmetric curvature tensor $(\boldsymbol{\chi})$. Hence, the deformation energy becomes independent of asymmetric part of the couple stress tensor and the curvature tensor. There is only one independent material length scale parameter l required for linear elastic materials according to the MCST. Earlier for the case of CCST, combination of twisting and bending tests was necessary to determine two different material length scale parameters (l). Now for the MCST, single l can be determined by the twisting test only.

According to the MCST, the total strain energy is the summation of classical (U_{cl}) and non-classical (U_{ncl}) strain energy as given below:

$$U = U_{cl} + U_{ncl} = \frac{1}{2}\int(\boldsymbol{\sigma} : \boldsymbol{\varepsilon})\,dV + \frac{1}{2}\int(\boldsymbol{m} : \boldsymbol{\chi})\,dV. \tag{1.13}$$

In Eq. (1.13), $\boldsymbol{\sigma}$ and $\boldsymbol{\varepsilon}$ are the classical stress and strain tensors respectively, generating the classical strain energy (U_{cl}); $\boldsymbol{m}$ and $\boldsymbol{\chi}$ are the deviatoric part of symmetric couple stress and symmetric curvature tensors respectively, generating the non-classical strain energy (U_{ncl}); V is the volume.

The displacement vector $(\vec{\mathbf{u}})$ and the rotation vector $(\vec{\boldsymbol{\theta}})$ are related using the following relationship (Reddy et al. (2012); Reddy et al. (2016)):

$$\vec{\boldsymbol{\theta}} = \frac{1}{2}(\nabla \times \vec{\mathbf{u}}). \tag{1.14}$$

Here $\nabla \equiv \hat{e}_r \frac{\partial}{\partial r} + \hat{e}_\theta \frac{1}{r}\frac{\partial}{\partial \theta} + \hat{e}_z \frac{\partial}{\partial r}$ is the del operator, where $\{\hat{e}_r, \hat{e}_\theta, \hat{e}_z\}$ is the set of unit vectors along the coordinate directions (r, θ, z). Again, the symmetric curvature tensor $(\boldsymbol{\chi})$ and the

rotation vector $\left(\vec{\theta}\right)$ are related using the following relationship (Reddy et al. (2012); Reddy et al. (2016)):

$$\chi = \frac{1}{2}\left[\nabla\vec{\theta} + \left(\nabla\vec{\theta}\right)^{T}\right]. \tag{1.15}$$

The classical stress (σ) and strain (ε) tensors are related as per the classical stress-strain relationships following Hooke's law. However, accordingly to the MCST, the couple stress (m) and curvature (χ) tensors are related according to the following relationship:

$$\chi = 2Gl^{2}m\,. \tag{1.16}$$

Here l is the material length scale parameter and G is the shear modulus.

1.5 Overview of the Thesis Problems

In this thesis, mainly four problems on BFGM rotating micro-disks have been studied. In Chapter 2, a general mathematical formulation encompassing all the four identified problems has been developed and presented. Subsequently, extensive sets of numerical results have been generated for each of the specific problems to investigate the effects of different practical parameters. The problem-specific description and the corresponding results for the first, second, third and fourth problems of the thesis have been presented and discussed in Chapters 3-6 respectively. The descriptions of the problems and the overview of the presented results are briefly mentioned in the following paragraphs.

In Chapter 2, a generalized mathematical model of BFGM rotating micro-disks subjected to centrifugal loading due to body force of constant angular speed, transverse loading due to uniform transverse pressure and high-temperature thermal loading due to uniform temperature rise has been developed. The metal-ceramic FG micro-disk is assumed to be graded along the radial and thickness directions. Further, the material gradation is assumed to be symmetric along the thickness direction in order to prevent bending of the disk due to centrifugal loading. The mechanical properties of the constituents of the FGM are assumed to be temperature-dependent. The temperature-dependency is addressed employing Touloukian model (Touloukian (1967); Reddy and Chin (1998)), in which any property is a nonlinear function of the temperature (in K). The mathematical formulation is developed within the framework of Kirchhoff plate theory involving von Kármán type nonlinearity, and the small-

size effect is addressed employing the MCST. The formulation is meant to address both axisymmetric and asymmetric behaviour of the micro-disk. The problem is formulated in polar coordinate system using two different but interrelated steps. In the first step, the governing equations to determine the deformed configuration of the micro-disk under centrifugal loading, transverse mechanical loading and thermal loading are formulated using the principle of minimum total potential energy. The governing equations for this step are discretized following Ritz method. For this step, the system of governing equations is geometrically nonlinear, and is solved using Broyden's algorithm, which is a multi-dimensional secant method. In the second step, the governing equations for free vibration of the micro-disk about its deformed configuration are developed using Hamilton's principle. In this step, the tangent stiffness of the deformed micro-disk is used in the formulation to determine the small amplitude free vibration response of the micro-disk in the frequency domain. The governing equations for this step are discretized following Ritz method, and are transformed into a standard eigenvalue problem. The square roots of the eigenvalues represent the frequencies of vibration of the deformed micro-disk, and the eigenvectors represent the related mode-shapes. It is to be mentioned that appropriate admissible orthogonal functions are used for approximating the displacement fields using the Ritz method. The set of orthogonal functions are numerically generated using Gram-Schmidt orthogonalization scheme. Though the mathematical model is developed for an annular micro-disk, it can also be reduced to a solid micro-disk by appropriate transformations. The model is developed for a typical clamped-free (CF) rotating micro-disk where the disk is supported at its inner radius on a rigid shaft while it is free at its outer radius. However, the same model can be used for other classical boundary conditions namely, simply supported-simply supported (SS), clamped-simply supported (CS), simply supported-clamped (SC) and clamped-clamped (CC). In this nomenclature of the boundary conditions, the first letter corresponds to the inner radius while the second letter corresponds to the outer radius of the disk. While considering different boundary conditions, it has been found that the frequency of vibration becomes zero, within the range of speed considered, for certain cases. This definitely signifies the instability condition corresponding to static buckling. Hence, the instability condition leading to static buckling of the micro-disk has been identified and reported. The mathematical model is a

novel one, which considers three different types of loading namely, centrifugal loading due to body force as a result of rotational speed, mechanical loading due to uniform transverse pressure and thermal loading due to uniform temperature rise. The novelty is further established due to consideration of the bi-directional gradation of the material properties. The novelty of the model is further outlined based on the facts that it can address both asymmetric and axisymmetric behaviour, different disk geometry such as annular and solid, and a variety of boundary conditions as mentioned above.

In Chapter 3, the free vibration behaviour of BFGM annular rotating micro-disks is evaluated under centrifugal and thermal loading. In this problem, both axisymmetric and asymmetric behaviour have been studied for clamped-free micro-disks. First of all, a convergence study has been presented to assess the appropriate number of functions required for Ritz approximation. A number of comparison studies with standard available results have been undertaken for some reduced problems to successfully validate the mathematical model. The numerical results, mostly in non-dimensional form, are presented graphically and in tabular form. Up to the first six modes, the effects of rotational speed, thermal loading, size-dependent thickness, material gradation indices, radius ratio and FGM composition on the frequencies of vibration have been discussed. Four different metal-ceramic FGM compositions namely, Stainless Steel/Silicon Nitride (SUS304/Si_3N_4), Stainless Steel/Alumina (SUS304/Al_2O_3), Stainless Steel/Zirconia (SUS304/ZrO_2) and Titanium Alloy/Zirconia (Ti-6Al-4V/ZrO_2) have been considered for presentation of results. Three-dimensional mode-shape plots along with contour plots have also been presented to visualize the axisymmetric and asymmetric bending vibration modes as well as the torsional vibration mode.

In Chapter 4, the free vibration behaviour of BFGM annular rotating micro-disks is studied under centrifugal, transverse and thermal loading. In this problem, both axisymmetric and asymmetric behaviour have been studied for clamped-free micro-disks. The validity of the model is successfully established through a number of comparison studies with standard available results for some reduced problems. The numerical results, mostly in non-dimensional form, are presented graphically and in tabular form. The effects of rotational speed, transverse pressure, thermal loading, size-dependent thickness, material gradation indices, radius ratio and FGM composition on the frequencies of vibration for the first four

modes have been discussed. Four different metal-ceramic FGM compositions namely, Stainless Steel/Silicon Nitride (SUS304/Si_3N_4), Stainless Steel/Alumina (SUS304/Al_2O_3), Stainless Steel/Zirconia (SUS304/ZrO_2) and Titanium Alloy/Zirconia (Ti-6Al-4V/ZrO_2) have been considered for presentation of results. Three-dimensional mode-shape plots along with contour plots have been presented for axisymmetric and asymmetric bending vibration modes as well as for the torsional vibration mode.

In Chapter 5, the free vibration behaviour of axisymmetric bending modes is studied for BFGM annular rotating micro-disks subjected to centrifugal, transverse and thermal loading. In this problem, clamped-free micro-disks have been considered, and first four modes of vibration have been studied. The validity of the model is successfully established by comparison with the available results. The numerical results mostly in non-dimensional form are presented in graphical form and tabular form. The effects of rotational speed, transverse pressure, thermal loading, size-dependent thickness, material gradation indices, radius ratio and FGM composition on the frequencies of vibration for the first four modes have been discussed. Four different metal-ceramic FGM compositions namely, Stainless Steel/Silicon Nitride (SUS304/Si_3N_4), Stainless Steel/Alumina (SUS304/Al_2O_3), Stainless Steel/Zirconia (SUS304/ZrO_2) and Titanium Alloy/Zirconia (Ti-6Al-4V/ZrO_2) have been considered for analysis. Three-dimensional mode-shape plots along with contour plots have been presented for the first four axisymmetric bending vibration modes.

In Chapter 6, the free vibration behaviour of BFGM annular rotating micro-disks subjected to centrifugal and thermal loading has been studied for different boundary conditions. The different boundary conditions that are considered are simply supported-simply supported (SS), clamped-simply supported (CS), simply supported-clamped (SC) and clamped-clamped (CC). Here, the first letter denotes the inner radius while the second letter denotes the outer radius. The model is successfully validated with the available results for different boundary conditions. The numerical results, mostly in non-dimensional form, are presented graphically and in tabular form. The effects of rotational speed, thermal loading, size-dependent thickness, material gradation indices and radius ratio on the frequencies of vibration for the first four modes have been discussed for different boundary conditions. Three-dimensional mode-shape plots along with contour plots for the first four modes have

been presented for a specific boundary condition. Furthermore, the instability condition leading to static buckling of the micro-disk has been identified and reported for different boundary conditions. The influences of size-effect and gradation indices on the critical buckling speed for the fundamental mode have been reported for different boundary conditions.

1.6 Chapter Summary

The thematic background of the present thesis in relation to the current research trends and practical applications has been discussed. An extensive literature review involving studies on homogeneous and FGM rotating macro-/micro-/nano-disks and circular micro-/nano-plates has been presented. Based on the literature review, identifications of specific research problems have been explained. The standard mathematical principles/theories/methodologies that are relevant to the current thesis have been briefly discussed. A very brief overview of the present mathematical model along with its novelty, and the specific problems and its' related results have been provided.

Chapter 2

MATHEMATICAL FORMULATION

2.1 Introduction

In this chapter, a generalized mathematical formulation for the identified research problems will be developed in detail. The sole objective of this study is to investigate the free vibration behaviour of BFGM annular rotating micro-disks made of BFGM for different loadings and boundary conditions. The entire formulation is divided into two steps for the following objectives: (i) Determination of the deformed configuration of the micro-disk under the combined effects of steady or time-invariant centrifugal loading due to constant angular speed, uniform transverse pressure and thermal loading due to uniform temperature rise; (ii) Determination of the free vibration behaviour of the deformed micro-disk in the neighborhood of its deformed configuration in the frequency domain.

For the present study, a metal-ceramic BFGM micro-disk has been modeled where the material is graded along the radial and thickness directions. The gradation is such that it is symmetric through the thickness with reference to the geometrical neutral axis of the disk to avoid bending by the centrifugal force generated due to rotation of the disk. The material properties of the metallic and ceramic phases are considered temperature-dependent following Touloukian model. It must be mentioned that the temperature sensitivity of the material properties of the BFGM constituents must be taken into account in order to consider the effect of thermo-elastic degradation.

The present displacement-based formulation is developed within the framework of Kirchhoff plate theory using the mid plane displacements of the micro-disk. To incorporate the small size-effect, the MCST is used. The classical strain-displacement relationship incorporates von Kármán type nonlinearity to take into the effect of geometric nonlinearity during transverse displacement. Symmetric curvature tensor is developed with the help of

rotational vector, which is again related to the displacement vector. The effect of thermal stress due to the uniform temperature rise of the disk is incorporated employing thermo-elastic constitutive relations.

The governing equations for determining the deformed configuration of the micro-disk under the combination of centrifugal, transverse and thermal loadings were developed using the principle of minimum total potential energy. On the other hand, the governing equations for the free vibration problem were derived using Hamilton's principle with the help of tangent stiffness approach. The Ritz method was used to approximate the displacement fields employing Gram-Schmidt orthogonalization scheme and using orthogonal admissible functions. The solution of the deformed configuration of the micro-disk under the combined effect of different loadings is obtained employing Broyden's algorithm. The free vibration problem was formulated as an eigenvalue problem which is solved using a standard eigen-solver. The solution of the eigenvalue problem yields eigenvalues corresponding to the vibration frequencies of different modes and eigenvectors associated with the mode-shapes. The general formulation embracing all the problems of the thesis is presented such that a reduced model can be obtained by retaining the problem specific relevant terms and neglecting or omitting the out-of-the problem terms, maintaining the base of the considered problem.

An annular micro-size disk is considered with inner radius a, outer radius b and constant thickness t as shown in Fig. 2.1. A cylindrical coordinate system (r, θ, z) is considered, where the origin O lies at the geometric center of the annular disk. Now the disk along with the $(r\text{-}\theta)$ axes is assumed to be rotating with uniform angular speed Ω about the z-axis. The disk is subjected to uniform transverse pressure of intensity q_0. Further the disk is subjected to a thermal loading in the form of a uniform temperature rise $\Delta T = T - T_0$ where T and T_0 denote the present and constant stress-free temperatures respectively. For the development of numerical results, it is assumed that $T_0 = 300\,\mathrm{K}$. The boundary conditions considered for the rotating disk are: clamped-free (CF), simply supported-simply supported (SS), clamped-simply supported (CS), simply supported-clamped (SC) and clamped-clamped (CC), where 'C', 'F' and 'S' stand for clamped, free and simply supported boundary

respectively. The first letter of each boundary condition corresponds to the inner radius and the second letter corresponds to the outer radius.

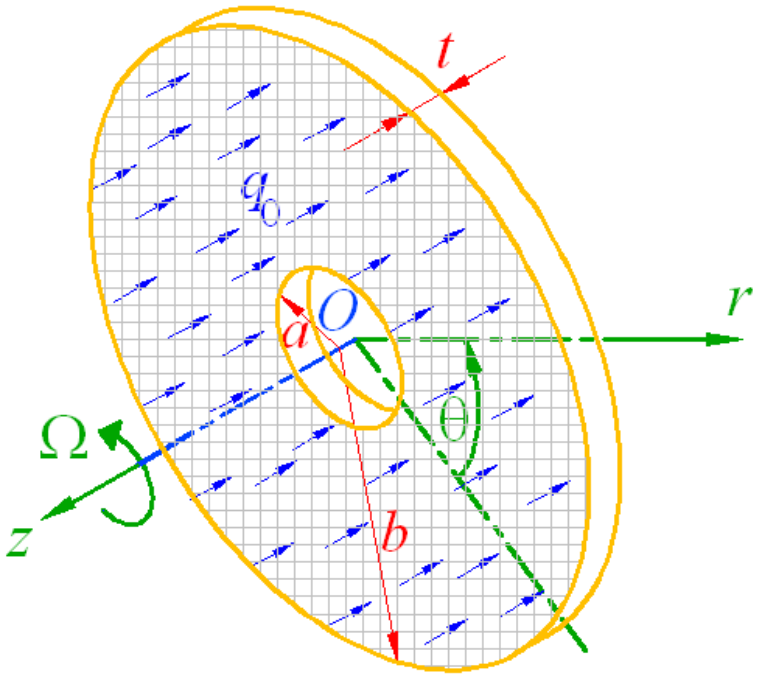

Fig. 2.1: Schematic diagram of a rotating disk.

2.2 Modeling of Bidirectional Functionally Graded Micro-Disk

Different types of FGMs that have been created so far are: chemical composition gradient functionally graded material (CCGFGM), porosity gradient functionally graded material (PGFGM) and microstructure gradient functionally graded material (MGFGM). Numerous studies on the mechanical behaviour of FGM structures such as: beams, plates and shells exist for MGFGM. In those studies, particular mechanical properties are varied using different models namely, power-law model, exponential model, Mori-Tanaka model and sigmoid-law model. The FGM considered for the present thesis is MGFGM type. In the present case, bidirectional functionally gradation of metals and ceramics along the radial and thickness directions has been obtained following power-law model.

By using Voigt's model, also known as the simple rule-of-mixtures, many researchers have calculated the material properties of typical FGMs. According to Voigt's model (Shen

(2004)), any generic effective material property $\left(R_f\right)$ of an FGM is the function of the constituents' material properties $\left(R_m \text{ and } R_c\right)$, and the volume fractions $\left(V_m \text{ and } V_c\right)$ of the constituent materials (metal and ceramic). Here the subscripts '*m*' and '*c*' denote the ceramic and metallic phases respectively. The relation for the rule-of-mixtures is expressed as below:

$$R_f = R_m V_m + R_c V_c . \tag{2.1}$$

As $V_m + V_c = 1$, Eq. (2.1) takes the following form:

$$R_f = R_m + \left(R_c - R_m\right) V_c . \tag{2.2}$$

When the material is graded along the radial direction $\left(r\right)$ and symmetrically through the thickness direction $\left(z\right)$, the variation of the volume fractions of the ceramic phase along the radial $\left(V_c^r\right)$ and thickness $\left(V_c^t\right)$ directions, following the power-law model, are expressed respectively as:

$$V_c^r = \left(\frac{r-a}{b-a}\right)^{k_r} \text{ and } V_c^t = \left|\frac{2z}{t}\right|^{k_t} . \tag{2.3}$$

Here k_r $\left(0 \le k_r \le \infty\right)$ and k_t $\left(0 \le k_t \le \infty\right)$ symbolize the gradation indices along the radial and thickness directions respectively. Hence the combined volume fraction of the ceramic phase becomes,

$$V_c = V_c^r \times V_c^t = \left(\frac{r-a}{b-a}\right)^{k_r} \left|\frac{2z}{t}\right|^{k_t} . \tag{2.4}$$

Using Eq. (2.2) and considering temperature-dependent material property, the generic effective material property of the BFGM disk takes the following form:

$$R_f\left(r,z,T\right) = R_m\left(T\right) + \left\{R_c\left(T\right) - R_m\left(T\right)\right\}\left(\frac{r-a}{b-a}\right)^{k_r} \left|\frac{2z}{t}\right|^{k_t} , \tag{2.5}$$

where T is the temperature in K. The Touloukian model (Touloukian (1967)) which governs the temperature-dependence of the constituents' material properties using a nonlinear relation, is given as follows:

$$R_c\left(T\right) \text{or } R_m\left(T\right) = R_0\left[R_{-1}T^{-1} + 1 + R_1 T + R_2 T^2 + R_3 T^3\right], \tag{2.6}$$

where R_0, R_{-1}, R_1, R_2 and R_3 are phase- and property-specific temperature coefficients.

Table 2.1: Temperature coefficients for different metal and ceramic constituents.

Constituent	Property	R_0	R_{-1}	R_1	R_2	R_3
Stainless Steel (SUS304)	E (Pa)	201.04×10^{9}	0	3.079×10^{-4}	-6.534×10^{-7}	0
	α (1/K)	12.330×10^{-6}	0	8.086×10^{-4}	0	0
	ν	0.3262	0	-2.002×10^{-4}	3.797×10^{-7}	0
Titanium Alloy (Ti-6Al-4V)	E (Pa)	122.56×10^{9}	0	-4.586×10^{-4}	0	0
	α (1/K)	7.5788×10^{-6}	0	6.638×10^{-4}	-3.147×10^{-6}	0
	ν	0.2884	0	1.121×10^{-4}	0	0
Silicon Nitride (Si_3N_4)	E (Pa)	348.43×10^{9}	0	-3.070×10^{-4}	2.160×10^{-7}	-8.946×10^{-11}
	α (1/K)	5.8723×10^{-6}	0	9.095×10^{-4}	0	0
	ν	0.2400	0	0	0	0
Zirconia (ZrO_2)	E (Pa)	244.27×10^{9}	0	-1.371×10^{-3}	1.214×10^{-6}	-3.681×10^{-10}
	α (1/K)	12.766×10^{-6}	0	-1.491×10^{-3}	1.006×10^{-5}	-6.778×10^{-11}
	ν	0.2882	0	1.133×10^{-4}	0	0
Alumina (Al_2O_3)	E (Pa)	349.55×10^{9}	0	-3.853×10^{-4}	4.027×10^{-7}	-1.673×10^{-10}
	α (1/K)	6.8269×10^{-6}	0	1.838×10^{-4}	0	0
	ν	0.2600	0	0	0	0

Eq. (2.5) is used to evaluate the effective material properties such as Young's modulus $\left(E_f\right)$, Poisson's ratio $\left(\nu_f\right)$, thermal expansion coefficient $\left(\alpha_f\right)$ and mass density $\left(\rho_f\right)$. The temperature coefficients for Young's moduli $\left(E_m, E_c\right)$, thermal expansion coefficients

(α_m, α_c) and Poisson's ratios (ν_m, ν_c) for Stainless Steel/Silicon Nitride (SUS304/Si_3N_4), Stainless Steel/Alumina (SUS304/Al_2O_3), Stainless Steel/Zirconia (SUS304/ZrO_2) and Titanium Alloy/Zirconia (Ti-6Al-4 V/ZrO_2) compositions are given in Table 2.1. It is to be noted that mass densities (ρ_m, ρ_c) of these materials are independent of temperature, and their numerical values are provided in Table 2.2.

According to Eq. (2.5), the disk material is pure ceramic (i.e., $R_f = R_c$) when $k_r = k_t = 0$, and pure metallic (i.e., $R_f = R_m$) when $k_r = k_t = \infty$. Furthermore the disk material is pure metallic (i.e., $R_f = R_m$) at the inner radius ($r = a$), and also at the mid-plane ($z = 0$). Hence, at any non-zero finite values of k_r and k_t, moving along from the inner radius towards the outer radius, or moving across from the mid-plane towards the top or the bottom surface, the disk material becomes less richer in the metal constituent and more richer in the ceramic constituent. The presence of metallic core makes it tougher whereas the presence of ceramic-rich outer layers makes it suitable for high-temperature environment as ceramics have high thermal resistance. Eq. (2.5) also shows that the material gradation is symmetric across the thickness. Due to this, the resultant centrifugal force developed along the radial direction due to the rotation of the disk lies at the mid-plane. This avoids bending of the disk as the moment of the centrifugal force about the neutral axis becomes zero.

Table 2.2: Mass density values for different metal and ceramic constituents.

Constituent	Mass Density (kg/m^3)
Stainless Steel (SUS304)	8166
Titanium Alloy (Ti-6Al-4V)	4429
Silicon Nitride (Si_3N_4)	2370
Zirconia (ZrO_2)	3000
Alumina (Al_2O_3)	3750

2.3 Determination of Displacement Fields

The Kirchhoff hypothesis is used in the CPT (Reddy (2007)), which has the following three components:

(i) Before deformation, a straight line perpendicular to the mid surface (i.e., transverse normal) remains straight after deformation.

(ii) A transverse normal does not experience deformation i.e., they are inextensible.

(iii) A transverse normal rotates in such a way that it remains perpendicular to the middle surface after deformation.

The Kirchhoff hypothesis neglects both transverse shear and transverse normal effects, i.e., it considers that the deformation is due to bending and in-plane stretching only.

According to the CPT or Kirchhoff plate theory in cylindrical coordinate system (r,θ,z), the general displacement components $\{u,v,w\}$ of any point Q along the coordinate directions are stated in terms of the mid-plane displacement components $\{u_0,v_0,w_0\}$ as follows:

$$u(r,\theta,z,\tau)=u_0(r,\theta,\tau)-z\frac{\partial w_0(r,\theta,\tau)}{\partial r}, \tag{2.7a}$$

$$v(r,\theta,z,\tau)=v_0(r,\theta,\tau)-\frac{z}{r}\frac{\partial w_0(r,\theta,\tau)}{\partial \theta}, \tag{2.7b}$$

$$w(r,\theta,z,\tau)=w_0(r,\theta,\tau). \tag{2.7c}$$

The displacement fields given by Eqs. (2.7a)-(2.7c) are used for both axisymmetric and asymmetric bending. For axisymmetric bending, Eqs. (2.7a)-(2.7c) take the following form:

$$u(r,z,\tau)=u_0(r,\tau)-z\frac{\partial w_0(r,\tau)}{\partial r}, \tag{2.8a}$$

$$v(r,z,\tau)=0, \tag{2.8b}$$

$$w(r,z,\tau)=w_0(r,\tau). \tag{2.8c}$$

In Eqs. (2.7a)-(2.7c) and Eqs. (2.8a)-(2.8c), the displacement fields $\{u,v,w\}$ and $\{u_0,v_0,w_0\}$ are considered as functions of the space coordinates and also of time coordinate τ.

2.4 Determination of Strain and Stress Fields

Using the general displacement components $\{u, v, w\}$, the components of Green-Lagrange strain tensor (Reddy (2007)) in cylindrical coordinate system for the CPT are given as follows:

$$\varepsilon_{rr} = \frac{\partial u}{\partial r} + \frac{1}{2}\left[\left(\frac{\partial u}{\partial r}\right)^2 + \left(\frac{\partial v}{\partial r}\right)^2 + \left(\frac{\partial w}{\partial r}\right)^2\right], \tag{2.9a}$$

$$\varepsilon_{\theta\theta} = \frac{u}{r} + \frac{1}{r}\frac{\partial v}{\partial \theta} + \frac{1}{2}\left[\left(\frac{1}{r}\frac{\partial u}{\partial \theta}\right)^2 + \left(\frac{1}{r}\frac{\partial v}{\partial \theta}\right)^2 + \left(\frac{1}{r}\frac{\partial w}{\partial \theta}\right)^2\right] + \frac{1}{r^2}\left(2u\frac{\partial v}{\partial \theta} - 2v\frac{\partial u}{\partial \theta} + v^2 + u^2\right), \tag{2.9b}$$

$$\varepsilon_{r\theta} = \varepsilon_{\theta r} = \frac{1}{2}\left[\frac{1}{r}\frac{\partial u}{\partial \theta} + \frac{\partial v}{\partial r} - \frac{v}{r}\right] + \frac{1}{2r}\left(\frac{\partial u}{\partial r}\frac{\partial u}{\partial \theta} + \frac{\partial v}{\partial r}\frac{\partial v}{\partial \theta} + \frac{\partial w}{\partial r}\frac{\partial w}{\partial \theta} + u\frac{\partial v}{\partial r} - v\frac{\partial u}{\partial r}\right). \tag{2.9c}$$

Considering only the von Kármán nonlinearity (i.e., retaining the nonlinear terms involving w), the above set of equations are reduced to the following form:

$$\varepsilon_{rr} = \frac{\partial u}{\partial r} + \frac{1}{2}\left(\frac{\partial w}{\partial r}\right)^2, \tag{2.10a}$$

$$\varepsilon_{\theta\theta} = \frac{u}{r} + \frac{1}{r}\frac{\partial v}{\partial \theta} + \frac{1}{2}\left(\frac{1}{r}\frac{\partial w}{\partial \theta}\right)^2, \tag{2.10b}$$

$$\varepsilon_{r\theta} = \varepsilon_{\theta r} = \frac{1}{2}\left[\frac{1}{r}\frac{\partial u}{\partial \theta} + \frac{\partial v}{\partial r} - \frac{v}{r}\right] + \frac{1}{2r}\left(\frac{\partial w}{\partial r}\frac{\partial w}{\partial \theta}\right). \tag{2.10c}$$

Eqs. (2.10a)-(2.10c) are termed as von Kármán strain tensor. Using the displacement components of the CPT given by Eqs. (2.7a)-(2.7c), the components of the von Kármán strain tensor $(\boldsymbol{\varepsilon})$ can be derived in terms of the mid-plane displacements $\{u_0, v_0, w_0\}$ as given below (Reddy (2007); Reddy et al. (2016)):

$$\varepsilon_{rr} = \left[\frac{\partial u_0}{\partial r} - z\frac{\partial^2 w_0}{\partial r^2} + \frac{1}{2}\left(\frac{\partial w_0}{\partial r}\right)^2\right], \tag{2.11a}$$

$$\varepsilon_{\theta\theta} = \left[\frac{u_0}{r} + \frac{1}{r}\frac{\partial v_0}{\partial \theta} - \frac{z}{r}\frac{\partial w_0}{\partial r} - \frac{z}{r^2}\frac{\partial^2 w_0}{\partial \theta^2} + \frac{1}{2r^2}\left(\frac{\partial w_0}{\partial \theta}\right)^2\right], \tag{2.11b}$$

$$\varepsilon_{r\theta} = \varepsilon_{\theta r} = \frac{1}{2}\left[\frac{1}{r}\frac{\partial u_0}{\partial \theta} + \frac{\partial v_0}{\partial r} - \frac{v_0}{r} + \frac{1}{r}\frac{\partial w_0}{\partial r}\frac{\partial w_0}{\partial \theta} - \frac{2z}{r}\frac{\partial^2 w_0}{\partial r \partial \theta} + \frac{2z}{r^2}\frac{\partial w_0}{\partial \theta}\right]. \tag{2.11c}$$

The last terms in Eqs. (2.11a) and (2.11b) are von Kármán type nonlinear terms. These are included to consider the effect of geometric nonlinearity during transverse displacement.

Assuming linear elastic material behaviour and considering the effect of the thermal strain due to thermal loading ΔT, the components of the Cauchy stress tensor $(\boldsymbol{\sigma})$ and the von Kármán strain tensor $(\boldsymbol{\varepsilon})$ are related as shown below:

$$\sigma_{rr} = \frac{E_f}{1-\left(\nu_f\right)^2}\left(\varepsilon_{rr} + \nu_f \varepsilon_{\theta\theta}\right) - \frac{E_f \alpha_f}{1-\nu_f}\Delta T, \tag{2.12a}$$

$$\sigma_{\theta\theta} = \frac{E_f}{1-\left(\nu_f\right)^2}\left(\varepsilon_{\theta\theta} + \nu_f \varepsilon_{rr}\right) - \frac{E_f \alpha_f}{1-\nu_f}\Delta T, \tag{2.12b}$$

$$\sigma_{r\theta} = \sigma_{\theta r} = 2G_f \varepsilon_{r\theta}. \tag{2.12c}$$

Here $E_f, G_f, \alpha_f, \nu_f$ are effective Young's modulus, effective shear modulus, effective thermal expansion coefficient and effective Poisson's ratio respectively. It is to be noted that the shear modulus (G_f) is obtained using the following relationship: $G_f = E_f / \left\{2\left(1+\nu_f\right)\right\}$.

2.5 Determination of Symmetric Curvature and Couple Stress Fields

Considering $\{\hat{e}_r, \hat{e}_\theta, \hat{e}_z\}$ as the set of unit vectors along the coordinate directions (r, θ, z), the displacement vector for any point $Q(r, \theta, z)$ is given by:

$$\vec{\mathbf{u}} = u\hat{e}_r + v\hat{e}_\theta + w\hat{e}_z \tag{2.13}$$

where $\{u, v, w\}$ are the general components of the displacement field. The relationship between the rotation vector $(\vec{\boldsymbol{\theta}})$ and the displacement vector $(\vec{\mathbf{u}})$ is given by (Yang et al. (2002); Reddy et al. (2016)):

$$\vec{\boldsymbol{\theta}} = \frac{1}{2}\left(\nabla \times \vec{\mathbf{u}}\right). \tag{2.14}$$

Using Eq. (2.14), the complete rotation vector in terms of the displacement components is obtained as follows:

$$\vec{\boldsymbol{\theta}} = \frac{1}{2}\left[\hat{e}_r\left(\frac{1}{r}\frac{\partial w}{\partial \theta} - \frac{\partial v}{\partial z}\right) + \hat{e}_\theta\left(\frac{\partial u}{\partial z} - \frac{\partial w}{\partial r}\right) + \hat{e}_z\left(\frac{\partial v}{\partial r} + \frac{v}{r} - \frac{1}{r}\frac{\partial u}{\partial \theta}\right)\right]. \tag{2.15}$$

In Eq. (2.15), the components of the rotation vector $\left(\vec{\boldsymbol{\theta}}\right)$ are obtained as given below:

$$\theta_r = \frac{1}{2}\left(\frac{1}{r}\frac{\partial w}{\partial \theta} - \frac{\partial v}{\partial z}\right), \tag{2.15a}$$

$$\theta_\theta = \frac{1}{2}\left(\frac{\partial u}{\partial z} - \frac{\partial w}{\partial r}\right), \tag{2.15b}$$

$$\theta_z = \frac{1}{2}\left(\frac{\partial v}{\partial r} + \frac{v}{r} - \frac{1}{r}\frac{\partial u}{\partial \theta}\right). \tag{2.15c}$$

Furthermore, the symmetric curvature tensor $\left(\boldsymbol{\chi}\right)$ is related to the rotation vector $\left(\vec{\boldsymbol{\theta}}\right)$ using the following relationship (Yang et al. (2002); Reddy et al. (2016)):

$$\boldsymbol{\chi} = \frac{1}{2}\left[\nabla\vec{\boldsymbol{\theta}} + \left(\nabla\vec{\boldsymbol{\theta}}\right)^T\right], \tag{2.16}$$

where $\nabla \equiv \hat{e}_r\frac{\partial}{\partial r} + \hat{e}_\theta\frac{1}{r}\frac{\partial}{\partial \theta} + \hat{e}_z\frac{\partial}{\partial r}$ is the del operator in cylindrical coordinate system. The components of the symmetric curvature tensor $\left(\boldsymbol{\chi}\right)$ can be written in matrix form as follows:

$$\boldsymbol{\chi} = \begin{bmatrix} \chi_{rr} & \chi_{r\theta} & \chi_{rz} \\ \chi_{r\theta} & \chi_{\theta\theta} & \chi_{\theta z} \\ \chi_{zr} & \chi_{z\theta} & \chi_{zz} \end{bmatrix}. \tag{2.17}$$

Using Eqs. (2.16) and (2.17), the components of the symmetric curvature tensor $\left(\boldsymbol{\chi}\right)$ are obtained as follows:

$$\chi_{rr} = \frac{\partial \theta_r}{\partial r} = \frac{1}{2}\left(-\frac{1}{r^2}\frac{\partial w}{\partial \theta} + \frac{1}{r}\frac{\partial^2 w}{\partial r \partial \theta} - \frac{\partial^2 v}{\partial r \partial z}\right), \tag{2.18a}$$

$$\chi_{\theta\theta} = \frac{1}{r}\frac{\partial \theta_\theta}{\partial \theta} + \frac{\theta_r}{r} = \frac{1}{2}\left(\frac{1}{r}\frac{\partial^2 u}{\partial \theta \partial z} - \frac{1}{r}\frac{\partial^2 w}{\partial r \partial \theta} + \frac{1}{r^2}\frac{\partial w}{\partial \theta} - \frac{1}{r}\frac{\partial v}{\partial z}\right), \tag{2.18b}$$

$$\chi_{zz} = \frac{\partial \theta_z}{\partial z} = \frac{1}{2}\left(-\frac{1}{r}\frac{\partial^2 u}{\partial \theta \partial z} + \frac{1}{r}\frac{\partial v}{\partial z} + \frac{\partial^2 v}{\partial r \partial z}\right), \tag{2.18c}$$

$$\chi_{r\theta} = \chi_{\theta r} = \frac{1}{2}\left(\frac{1}{r}\frac{\partial \theta_r}{\partial \theta} - \frac{\theta_\theta}{r} + \frac{\partial \theta_\theta}{\partial r}\right)$$
$$= \frac{1}{4}\left(\frac{\partial^2 u}{\partial r \partial z} - \frac{\partial^2 w}{\partial r^2} + \frac{1}{r^2}\frac{\partial^2 w}{\partial \theta^2} - \frac{1}{r}\frac{\partial^2 v}{\partial \theta \partial z} - \frac{1}{r}\frac{\partial u}{\partial z} + \frac{1}{r}\frac{\partial w}{\partial r}\right) \quad (2.18d)$$

$$\chi_{\theta z} = \chi_{z\theta} = \frac{1}{2}\left(\frac{1}{r}\frac{\partial \theta_z}{\partial \theta} + \frac{\partial \theta_\theta}{\partial z}\right)$$
$$= \frac{1}{4}\left(\frac{1}{r}\frac{\partial^2 v}{\partial r \partial \theta} + \frac{1}{r^2}\frac{\partial v}{\partial \theta} - \frac{1}{r^2}\frac{\partial^2 u}{\partial \theta^2} + \frac{\partial^2 u}{\partial z^2} - \frac{\partial^2 w}{\partial r \partial z}\right), \quad (2.18e)$$

$$\chi_{rz} = \chi_{zr} = \frac{1}{2}\left(\frac{\partial \theta_r}{\partial z} + \frac{\partial \theta_z}{\partial r}\right)$$
$$= \frac{1}{4}\left(\frac{\partial^2 v}{\partial r^2} - \frac{v}{r^2} + \frac{1}{r}\frac{\partial v}{\partial r} - \frac{1}{r}\frac{\partial^2 u}{\partial r \partial \theta} + \frac{1}{r^2}\frac{\partial u}{\partial \theta} + \frac{1}{r}\frac{\partial^2 w}{\partial \theta \partial z} - \frac{\partial^2 v}{\partial z^2}\right). \quad (2.18f)$$

Following Eqs. (2.7a)-(2.7c), substituting the mid-plane displacement fields $\{u_0, v_0, w_0\}$ in place of the general displacement fields $\{u, v, w\}$ in Eqs. (2.18a)-(2.18f), the components of the symmetric curvature tensor (χ) are obtained as follows:

$$\chi_{rr} = \left[-\frac{1}{r^2}\frac{\partial w_0}{\partial \theta} + \frac{1}{r}\frac{\partial^2 w_0}{\partial r \partial \theta}\right], \quad (2.19a)$$

$$\chi_{\theta\theta} = \left[\frac{1}{r^2}\frac{\partial w_0}{\partial \theta} - \frac{1}{r}\frac{\partial^2 w_0}{\partial r \partial \theta}\right], \quad (2.19b)$$

$$\chi_{zz} = 0, \quad (2.19c)$$

$$\chi_{r\theta} = \chi_{\theta r} = \frac{1}{2}\left[\frac{1}{r}\frac{\partial w_0}{\partial r} - \frac{\partial^2 w_0}{\partial r^2} + \frac{1}{r^2}\frac{\partial^2 w_0}{\partial \theta^2}\right], \quad (2.19d)$$

$$\chi_{\theta z} = \chi_{z\theta} = \frac{1}{4}\left[-\frac{1}{r^2}\frac{\partial^2 u_0}{\partial \theta^2} + \frac{1}{r^2}\frac{\partial v_0}{\partial \theta} + \frac{1}{r}\frac{\partial^2 v_0}{\partial r \partial \theta}\right], \quad (2.19e)$$

$$\chi_{rz} = \chi_{zr} = \frac{1}{4}\left[\frac{1}{r^2}\frac{\partial u_0}{\partial \theta} - \frac{1}{r}\frac{\partial^2 u_0}{\partial r \partial \theta} - \frac{v_0}{r^2} + \frac{1}{r}\frac{\partial v_0}{\partial r} + \frac{\partial^2 v_0}{\partial r^2}\right]. \quad (2.19f)$$

According to the MCST (Yang et al. (2002)), the components of the deviatoric part of the symmetric couple stress tensor $(\boldsymbol{m})$ are obtained from the corresponding components of the symmetric curvature tensor $(\boldsymbol{\chi})$ as follows:

$$m_{rr} = 2G_f l^2 \chi_{rr}, \tag{2.20a}$$

$$m_{\theta\theta} = 2G_f l^2 \chi_{\theta\theta}, \tag{2.20b}$$

$$m_{zz} = 0, \tag{2.20c}$$

$$m_{r\theta} = m_{\theta r} = 2G_f l^2 \chi_{r\theta}, \tag{2.20d}$$

$$m_{\theta z} = m_{z\theta} = 2G_f l^2 \chi_{\theta z}, \tag{2.20e}$$

$$m_{rz} = m_{zr} = 2G_f l^2 \chi_{rz}. \tag{2.20f}$$

In Eq. (2.20), l is the material length scale parameter. It is noted that the present formulation can be transformed to a classical one (where the size-effect is not considered) by putting l=0.

2.6 Generation of Normalized Computational Domain

The governing equations in terms of the mid-plane displacements $\{u_0, v_0, w_0\}$ will be derived for the middle circular plane $(r, \theta, 0)$. Hence this particular plane is termed as the physical domain of the problem. But to carry out the computation of the equations and other problem parameters, the computational domain should be independent of the physical dimensions. Hence the physical domain $(r, \theta, 0)$ is transformed into a normalized computational domain $(\xi, \mu, 0)$. The normalized coordinates ξ and μ along the r and θ directions respectively are defined as:

$$\xi = (r-a)/(b-a); 0 \le \xi \le 1, \tag{2.21a}$$

$$\mu = \theta/(2\pi);\ 0 \le \mu \le 1. \tag{2.21b}$$

The physical domain and the computational domain are shown in Figs. 2.2(a) and 2.2(b) respectively. The Jacobian matrix $[\mathbf{J}]$ of this transformation between (r, θ) and (ξ, μ) coordinates is given below:

$$[\mathbf{J}] = \begin{bmatrix} \dfrac{\partial r}{\partial \xi} & \dfrac{\partial \theta}{\partial \xi} \\ \dfrac{\partial r}{\partial \mu} & \dfrac{\partial \theta}{\partial \mu} \end{bmatrix} = \begin{bmatrix} (b-a) & 0 \\ 0 & 2\pi \end{bmatrix}. \tag{2.22}$$

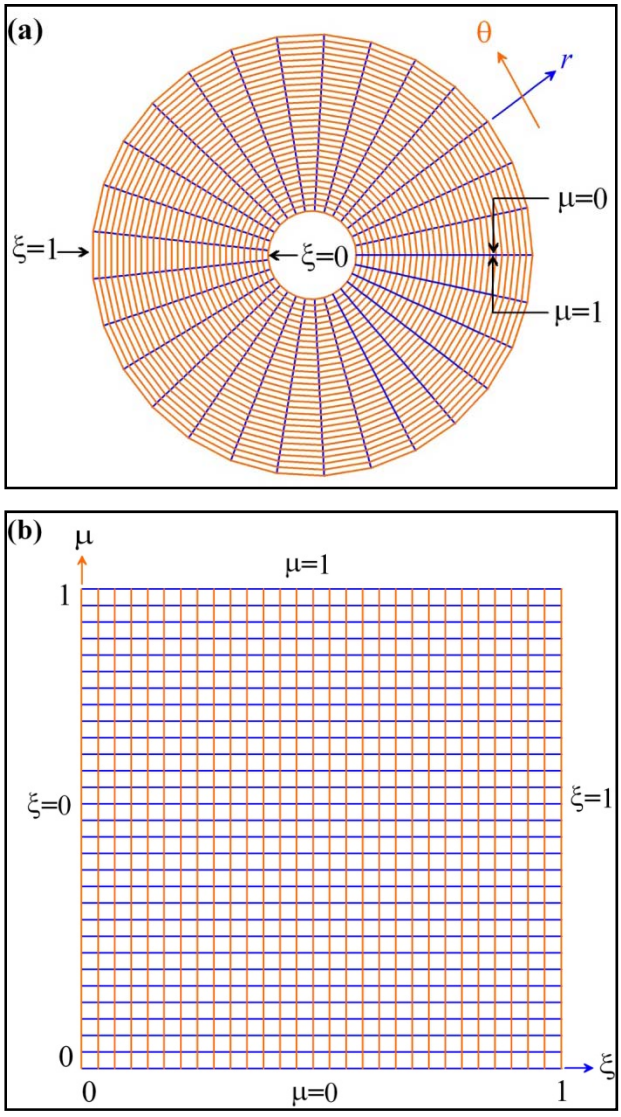

Fig. 2.2: Grid showing domain of the problem: (a) Physical Domain, (b) Computational Domain.

2.7 Determination of Deformed Configuration of Micro-Disk under Different Time-invariant Loadings

This particular objective forms the first step of the problem. The principle of minimum total potential energy is used to determine the deformed configuration of the micro-disk under the combined effects of time-invariant centrifugal loading caused by the constant rotational speed, mechanical loading caused by the uniform transverse pressure and thermal loading caused by the uniform temperature rise. The mathematical form of this principle for the present problem is given as below:

$$\delta\left(U_{cl}+U_{ncl}+W\right)=0, \tag{2.23}$$

where U_{cl} and U_{ncl} are the classical and non-classical strain energies, and W is the potential energy due to the applied loadings. According to the MCST: the Cauchy stress tensor $(\boldsymbol{\sigma})$ is energy conjugate to the von Kármán $(\boldsymbol{\varepsilon})$ strain tensor, and they contribute to form the classical strain energy U_{cl}; the deviatoric portion of the symmetric couple stress tensor $(\boldsymbol{m})$ is the energy conjugate to the symmetric curvature tensor $(\boldsymbol{\chi})$, and they contribute to form the non-classical strain energy U_{ncl}.

Using Eqs. (2.11a)-(2.11c) and Eqs. (2.12a)-(2.12c), the classical strain energy is obtained as follows:

$$U_{cl}=\frac{1}{2}\int_{-t/2}^{+t/2}\int_{0}^{2\pi}\int_{a}^{b}\left(\boldsymbol{\sigma}:\boldsymbol{\varepsilon}\right)\,rdrd\theta dz$$

$$=\frac{1}{2}\int_{-t/2}^{+t/2}\int_{0}^{2\pi}\int_{a}^{b}\left[\sigma_{rr}\left\{\varepsilon_{rr}-\alpha_f\Delta T\right\}+\sigma_{\theta\theta}\left\{\varepsilon_{\theta\theta}-\alpha_f\Delta T\right\}+2\sigma_{r\theta}\varepsilon_{r\theta}\right]rdrd\theta dz$$

$$=\int_{0}^{2\pi}\int_{a}^{b}\left[E_A\left\{\frac{r}{2}\left(\frac{\partial u_0}{\partial r}\right)^2+\frac{u_0^{\,2}}{2r}+\frac{1}{2r}\left(\frac{\partial v_0}{\partial\theta}\right)^2+\frac{r}{8}\left(\frac{\partial w_0}{\partial r}\right)^4+\frac{1}{8r^3}\left(\frac{\partial w_0}{\partial\theta}\right)^4+\frac{u_0}{r}\left(\frac{\partial v_0}{\partial\theta}\right)\right.\right.$$

$$\left.+\frac{r}{2}\frac{\partial u_0}{\partial r}\left(\frac{\partial w_0}{\partial r}\right)^2+\frac{1}{2r^2}u_0\left(\frac{\partial w_0}{\partial\theta}\right)^2+\frac{1}{2r^2}\frac{\partial v_0}{\partial\theta}\left(\frac{\partial w_0}{\partial\theta}\right)^2\right\}$$

$$+G_A\left\{\frac{1}{2r}\left(\frac{\partial u_0}{\partial\theta}\right)^2+\frac{r}{2}\left(\frac{\partial v_0}{\partial r}\right)^2+\frac{v_0^{\,2}}{2r}+\frac{\partial u_0}{\partial\theta}\frac{\partial v_0}{\partial r}-\frac{\partial u_0}{\partial\theta}\frac{v_0}{r}-v_0\frac{\partial v_0}{\partial r}+\frac{1}{r}\frac{\partial u_0}{\partial\theta}\frac{\partial w_0}{\partial r}\frac{\partial w_0}{\partial\theta}\right.$$

$$+\frac{\partial v_0}{\partial r}\frac{\partial w_0}{\partial r}\frac{\partial w_0}{\partial \theta}-\frac{v_0}{r}\frac{\partial w}{\partial r}\frac{\partial w}{\partial \theta}+\frac{1}{2r}\left(\frac{\partial w_0}{\partial r}\right)^2\left(\frac{\partial w_0}{\partial \theta}\right)^2\Bigg\}$$

$$+E_I\left\{\frac{r}{2}\left(\frac{\partial^2 w_0}{\partial r^2}\right)^2+\frac{1}{2r}\left(\frac{\partial w_0}{\partial r}\right)^2+\frac{1}{2r^3}\left(\frac{\partial^2 w_0}{\partial \theta^2}\right)^2+\frac{1}{r^2}\frac{\partial^2 w_0}{\partial \theta^2}\frac{\partial w_0}{\partial r}\right\}$$

$$+G_I\left\{\frac{2}{r}\left(\frac{\partial^2 w_0}{\partial r\partial \theta}\right)^2-\frac{4}{r^2}\frac{\partial^2 w_0}{\partial r\partial \theta}\frac{\partial w_0}{\partial \theta}+\frac{2}{r^3}\left(\frac{\partial w_0}{\partial \theta}\right)^2\right\}$$

$$+E_{PA}\left\{u_0\frac{\partial u_0}{\partial r}+\frac{\partial u_0}{\partial r}\frac{\partial v_0}{\partial \theta}+\frac{u_0}{2}\left(\frac{\partial w_0}{\partial r}\right)^2+\frac{1}{2r}\frac{\partial u_0}{\partial r}\left(\frac{\partial w_0}{\partial \theta}\right)^2+\frac{1}{2}\frac{\partial v_0}{\partial \theta}\left(\frac{\partial w_0}{\partial r}\right)^2+\frac{1}{4r}\left(\frac{\partial w_0}{\partial r}\right)^2\left(\frac{\partial w_0}{\partial \theta}\right)^2\right\}$$

$$+E_{PI}\left\{\frac{\partial w_0}{\partial r}\frac{\partial^2 w_0}{\partial r^2}+\frac{1}{r}\frac{\partial^2 w_0}{\partial r^2}\frac{\partial^2 w_0}{\partial \theta^2}\right\}$$

$$-E_{TA}\left\{u_0+r\frac{\partial u_0}{\partial r}+\frac{\partial v_0}{\partial \theta}+\frac{r}{2}\left(\frac{\partial w_0}{\partial r}\right)^2+\frac{1}{2r}\left(\frac{\partial w_0}{\partial \theta}\right)^2\right\}+rE_C\Bigg]drd\theta. \qquad (2.24)$$

The above equation shows that the classical strain energy is nonlinear due to the presence of cubic and higher order terms of the displacements and its gradients, and this happens due to the presence of von Kármán type nonlinearity in the strain tensor shown in Eqs. (2.11a)-(2.11c).

Using Eqs. (2.19a)-(2.19f) and Eqs. (2.20a)-(2.20f), the non-classical strain energy is obtained as follows:

$$U_{ncl}=\frac{1}{2}\int_{-t/2}^{+t/2}\int_0^{2\pi}\int_a^b(\boldsymbol{m}:\boldsymbol{\chi})\,rdrd\theta dz$$

$$=\frac{1}{2}\int_{-t/2}^{+t/2}\int_0^{2\pi}\int_a^b\left(m_{rr}\chi_{rr}+m_{\theta\theta}\chi_{\theta\theta}+m_{zz}\chi_{zz}+2m_{r\theta}\chi_{r\theta}+2m_{\theta z}\chi_{\theta z}+2m_{rz}\chi_{rz}\right)rdrd\theta dz$$

$$=l^2\int_0^{2\pi}\int_a^b G_A\Bigg[\frac{1}{8r}\left(\frac{\partial^2 u_0}{\partial r\partial \theta}\right)^2+\frac{1}{8r^3}\left(\frac{\partial u_0}{\partial \theta}\right)^2+\frac{1}{8r^3}\left(\frac{\partial^2 u_0}{\partial \theta^2}\right)^2+\frac{r}{8}\left(\frac{\partial^2 v_0}{\partial r^2}\right)^2+\frac{1}{8r}\left(\frac{\partial v_0}{\partial r}\right)^2$$

$$+\frac{1}{8r}\left(\frac{\partial^2 v_0}{\partial r\partial \theta}\right)^2-\frac{v_0^2}{8r^3}+\frac{1}{8r^3}\left(\frac{\partial v_0}{\partial \theta}\right)^2+\frac{r}{2}\left(\frac{\partial^2 w_0}{\partial r^2}\right)^2+\frac{1}{2r}\left(\frac{\partial w_0}{\partial r}\right)^2+\frac{2}{r}\left(\frac{\partial^2 w_0}{\partial r\partial \theta}\right)^2+\frac{2}{r^3}\left(\frac{\partial w_0}{\partial \theta}\right)^2$$

$$+\frac{1}{2r^3}\left(\frac{\partial^2 w_0}{\partial \theta^2}\right)^2-\frac{1}{4r^2}\frac{\partial^2 u_0}{\partial r\partial \theta}\frac{\partial u_0}{\partial \theta}-\frac{1}{4}\frac{\partial^2 u_0}{\partial r\partial \theta}\frac{\partial^2 v_0}{\partial r^2}+\frac{1}{4r}\frac{\partial u_0}{\partial \theta}\frac{\partial^2 v_0}{\partial r^2}-\frac{1}{4r}\frac{\partial^2 u_0}{\partial r\partial \theta}\frac{\partial v_0}{\partial r}$$

$$+\frac{1}{4r^2}\frac{\partial u_0}{\partial\theta}\frac{\partial v_0}{\partial r}-\frac{1}{4r^2}\frac{\partial^2 u_0}{\partial\theta^2}\frac{\partial^2 v_0}{\partial r\partial\theta}+\frac{1}{4r^2}\frac{\partial^2 u_0}{\partial r\partial\theta}v_0-\frac{1}{4r^3}\frac{\partial u_0}{\partial\theta}v_0-\frac{1}{4r^3}\frac{\partial^2 u_0}{\partial\theta^2}\frac{\partial v_0}{\partial\theta}+\frac{1}{4}\frac{\partial v_0}{\partial r}\frac{\partial^2 v_0}{\partial r^2}$$
$$-\frac{v_0}{4r}\frac{\partial^2 v_0}{\partial r^2}-\frac{v_0}{4r^2}\frac{\partial v_0}{\partial r}+\frac{1}{4r^2}\frac{\partial v_0}{\partial\theta}\frac{\partial^2 v_0}{\partial r\partial\theta}-\frac{\partial w_0}{\partial r}\frac{\partial^2 w_0}{\partial r^2}-\frac{1}{r}\frac{\partial^2 w_0}{\partial r^2}\frac{\partial^2 w_0}{\partial\theta^2}+\frac{1}{r^2}\frac{\partial w_0}{\partial r}\frac{\partial^2 w_0}{\partial\theta^2}$$
$$-\frac{4}{r^2}\frac{\partial w_0}{\partial\theta}\frac{\partial^2 w_0}{\partial r\partial\theta}\Bigg]drd\theta. \tag{2.25}$$

The above equation shows that the non-classical strain energy is essentially linear due to absence of any kind of nonlinearity in the symmetric curvature tensor shown in Eqs. (2.19a)-(2.19f).

The work potential due to the centrifugal loading for constant angular speed Ω and due to the uniform transverse pressure of intensity q_0 is derived to the following form:

$$W=-\Omega^2\int_0^{2\pi}\int_a^b\rho_A u_0 r^2 drd\theta-q_0\int_0^{2\pi}\int_a^b w_0 rdrd\theta. \tag{2.26}$$

The set of stiffness coefficients $\{E_A,G_A,E_I,G_I,E_{PA},E_{PI},E_{TA},E_C\}$ used in Eqs. (2.24) and (2.25), and the inertia coefficient ρ_A used in Eq. (2.26) are defined as given below:

$$E_A=\int_{-t/2}^{+t/2}\frac{E_f}{1-\left(\nu_f\right)^2}dz, \tag{2.27a}$$

$$G_A=\int_{-t/2}^{+t/2}G_f dz, \tag{2.27b}$$

$$E_I=\int_{-t/2}^{+t/2}\frac{E_f z^2}{1-\left(\nu_f\right)^2}dz, \tag{2.27c}$$

$$G_I=\int_{-t/2}^{+t/2}G_f z^2 dz, \tag{2.27d}$$

$$E_{PA}=\int_{-t/2}^{+t/2}\frac{E_f\nu_f}{1-\left(\nu_f\right)^2}dz, \tag{2.27e}$$

$$E_{PI}=\int_{-t/2}^{+t/2}\frac{E_f\nu_f z^2}{1-\left(\nu_f\right)^2}dz, \tag{2.27f}$$

$$E_{TA}=\Delta T\int_{-t/2}^{+t/2}\frac{E_f\alpha_f}{1-\nu_f}dz, \tag{2.27g}$$

$$E_C = \left(\Delta T\right)^2 \int_{-t/2}^{+t/2} \frac{E_f \left(\alpha_f\right)^2}{1-\nu_f} dz, \tag{2.27h}$$

$$\rho_A = \int_{-t/2}^{+t/2} \rho_f dz. \tag{2.27i}$$

Also, due to the symmetry of material gradation and of thermal loading through the thickness, the following simplifications are applied to derive Eqs. (2.24) and (2.25): $\int_{-h/2}^{+h/2} \frac{E_f}{1-\left(\nu_f\right)^2} z dz = 0,\ \int_{-h/2}^{+h/2} \frac{E_f \nu_f}{1-\left(\nu_f\right)^2} z dz = 0,\ \int_{-h/2}^{+h/2} G_f z dz = 0,\ \Delta T \int_{-h/2}^{+h/2} \frac{E_f \alpha_f}{1-\nu_f} z dz = 0.$ It is noted that the potential energy due to thermal loading $\left(\Delta T\right)$ has been included in the classical strain energy $\left(U_{cl}\right)$ through thermo-elastic stress-strain relations, and the energy terms in this regard can be seen in the last line of Eq. (2.24).

The variational form of the classical strain energy $\left(U_{cl}\right)$, non-classical strain energy $\left(U_{ncl}\right)$ and work potential $\left(W\right)$ are given as follows:

$$\begin{aligned}
\delta\left(U_{cl}\right) = \int_0^{2\pi}\int_a^b \Bigg[& E_A \Bigg\{ r\left(\frac{\partial u_0}{\partial r}\right)\delta\left(\frac{\partial u_0}{\partial r}\right) + \frac{1}{r}u_0\delta\left(u_0\right) + \frac{1}{r}\left(\frac{\partial v_0}{\partial \theta}\right)\delta\left(\frac{\partial v_0}{\partial \theta}\right) + \frac{r}{2}\left(\frac{\partial w_0}{\partial r}\right)^3 \delta\left(\frac{\partial w_0}{\partial r}\right) \\
& + \frac{1}{2r^3}\left(\frac{\partial w_0}{\partial \theta}\right)^3 \delta\left(\frac{\partial w_0}{\partial \theta}\right) + \frac{1}{r}u_0\delta\left(\frac{\partial v_0}{\partial \theta}\right) + \frac{1}{r}\left(\frac{\partial v_0}{\partial \theta}\right)\delta\left(u_0\right) + \frac{r}{2}\left(\frac{\partial w_0}{\partial r}\right)^2 \delta\left(\frac{\partial u_0}{\partial r}\right) \\
& + r\left(\frac{\partial u_0}{\partial r}\right)\left(\frac{\partial w_0}{\partial r}\right)\delta\left(\frac{\partial w_0}{\partial r}\right) + \frac{1}{2r^2}\left(\frac{\partial w_0}{\partial \theta}\right)^2 \delta\left(u_0\right) + \frac{1}{r^2}u_0\left(\frac{\partial w_0}{\partial \theta}\right)\delta\left(\frac{\partial w_0}{\partial \theta}\right) + \frac{1}{2r^2}\left(\frac{\partial w_0}{\partial \theta}\right)^2 \delta\left(\frac{\partial v_0}{\partial \theta}\right) \\
& + \frac{1}{r^2}\left(\frac{\partial v_0}{\partial \theta}\right)\left(\frac{\partial w_0}{\partial \theta}\right)\delta\left(\frac{\partial w_0}{\partial \theta}\right) \Bigg\} \\
& + G_A \Bigg\{ \frac{1}{r}\left(\frac{\partial u_0}{\partial \theta}\right)\delta\left(\frac{\partial u_0}{\partial \theta}\right) + r\left(\frac{\partial v_0}{\partial r}\right)\delta\left(\frac{\partial v_0}{\partial r}\right) + \frac{1}{r}v_0\delta\left(v_0\right) + \left(\frac{\partial v_0}{\partial r}\right)\delta\left(\frac{\partial u_0}{\partial \theta}\right) \\
& + \left(\frac{\partial u_0}{\partial \theta}\right)\delta\left(\frac{\partial v_0}{\partial r}\right) - \frac{1}{r}v_0\delta\left(\frac{\partial u_0}{\partial \theta}\right) - \frac{1}{r}\left(\frac{\partial u_0}{\partial \theta}\right)\delta\left(v_0\right) - \frac{\partial v_0}{\partial r}\delta\left(v_0\right) - v_0\delta\left(\frac{\partial v_0}{\partial r}\right) \\
& + \frac{1}{r}\left(\frac{\partial w_0}{\partial r}\right)\left(\frac{\partial w_0}{\partial \theta}\right)\delta\left(\frac{\partial u_0}{\partial \theta}\right) + \frac{1}{r}\left(\frac{\partial u_0}{\partial \theta}\right)\left(\frac{\partial w_0}{\partial \theta}\right)\delta\left(\frac{\partial w_0}{\partial r}\right) + \frac{1}{r}\left(\frac{\partial u_0}{\partial \theta}\right)\left(\frac{\partial w_0}{\partial r}\right)\delta\left(\frac{\partial w_0}{\partial \theta}\right)
\end{aligned}$$

$$+\frac{\partial w_0}{\partial r}\frac{\partial w_0}{\partial \theta}\delta\left(\frac{\partial v_0}{\partial r}\right)+\frac{\partial v_0}{\partial r}\frac{\partial w_0}{\partial \theta}\delta\left(\frac{\partial w_0}{\partial r}\right)+\frac{\partial v_0}{\partial r}\frac{\partial w_0}{\partial r}\delta\left(\frac{\partial w_0}{\partial \theta}\right)-\frac{1}{r}\frac{\partial w}{\partial r}\frac{\partial w}{\partial \theta}\delta(v_0)$$

$$-\frac{1}{r}v_0\frac{\partial w}{\partial \theta}\delta\left(\frac{\partial w}{\partial r}\right)-\frac{1}{r}v_0\frac{\partial w}{\partial r}\delta\left(\frac{\partial w}{\partial \theta}\right)+\frac{1}{r}\left(\frac{\partial w_0}{\partial \theta}\right)^2\left(\frac{\partial w_0}{\partial r}\right)\delta\left(\frac{\partial w_0}{\partial r}\right)+\frac{1}{r}\left(\frac{\partial w_0}{\partial r}\right)^2\left(\frac{\partial w_0}{\partial \theta}\right)\delta\left(\frac{\partial w_0}{\partial \theta}\right)\Bigg\}$$

$$+E_I\left\{r\left(\frac{\partial^2 w_0}{\partial r^2}\right)\delta\left(\frac{\partial^2 w_0}{\partial r^2}\right)+\frac{1}{r}\left(\frac{\partial w_0}{\partial r}\right)\delta\left(\frac{\partial w_0}{\partial r}\right)+\frac{1}{r^3}\left(\frac{\partial^2 w_0}{\partial \theta^2}\right)\delta\left(\frac{\partial^2 w_0}{\partial \theta^2}\right)\right.$$

$$\left.+\frac{1}{r^2}\left(\frac{\partial^2 w_0}{\partial \theta^2}\right)\delta\left(\frac{\partial w_0}{\partial r}\right)+\frac{1}{r^2}\left(\frac{\partial w_0}{\partial r}\right)\delta\left(\frac{\partial^2 w_0}{\partial \theta^2}\right)\right\}$$

$$+G_I\left\{\frac{2}{r}\left(\frac{\partial^2 w_0}{\partial r\partial \theta}\right)\delta\left(\frac{\partial^2 w_0}{\partial r\partial \theta}\right)-\frac{4}{r^2}\left(\frac{\partial^2 w_0}{\partial r\partial \theta}\right)\delta\left(\frac{\partial w_0}{\partial \theta}\right)-\frac{4}{r^2}\left(\frac{\partial w_0}{\partial \theta}\right)\delta\left(\frac{\partial^2 w_0}{\partial r\partial \theta}\right)+\frac{4}{r^3}\left(\frac{\partial w_0}{\partial \theta}\right)\delta\left(\frac{\partial w_0}{\partial \theta}\right)\right\}$$

$$+E_{PA}\left\{\left(\frac{\partial u_0}{\partial r}\right)\delta(u_0)+u_0\delta\left(\frac{\partial u_0}{\partial r}\right)+\left(\frac{\partial v_0}{\partial \theta}\right)\delta\left(\frac{\partial u_0}{\partial r}\right)+\left(\frac{\partial u_0}{\partial r}\right)\delta\left(\frac{\partial v_0}{\partial \theta}\right)+\frac{1}{2}\left(\frac{\partial w_0}{\partial r}\right)^2\delta(u_0)\right.$$

$$+u_0\left(\frac{\partial w_0}{\partial r}\right)\delta\left(\frac{\partial w_0}{\partial r}\right)+\frac{1}{2r}\left(\frac{\partial w_0}{\partial \theta}\right)^2\delta\left(\frac{\partial u_0}{\partial r}\right)+\frac{1}{r}\left(\frac{\partial u_0}{\partial r}\right)\left(\frac{\partial w_0}{\partial \theta}\right)\delta\left(\frac{\partial w_0}{\partial \theta}\right)+\frac{1}{2}\left(\frac{\partial w_0}{\partial r}\right)^2\delta\left(\frac{\partial v_0}{\partial \theta}\right)$$

$$\left.+\left(\frac{\partial v_0}{\partial \theta}\right)\left(\frac{\partial w_0}{\partial r}\right)\delta\left(\frac{\partial w_0}{\partial r}\right)+\frac{1}{2r}\left(\frac{\partial w_0}{\partial \theta}\right)^2\left(\frac{\partial w_0}{\partial r}\right)\delta\left(\frac{\partial w_0}{\partial r}\right)+\frac{1}{2r}\left(\frac{\partial w_0}{\partial r}\right)^2\left(\frac{\partial w_0}{\partial \theta}\right)\delta\left(\frac{\partial w_0}{\partial \theta}\right)\right\}$$

$$+E_{PI}\left\{\left(\frac{\partial^2 w_0}{\partial r^2}\right)\delta\left(\frac{\partial w_0}{\partial r}\right)+\left(\frac{\partial w_0}{\partial r}\right)\delta\left(\frac{\partial^2 w_0}{\partial r^2}\right)+\frac{1}{r}\left(\frac{\partial^2 w_0}{\partial \theta^2}\right)\delta\left(\frac{\partial^2 w_0}{\partial r^2}\right)+\frac{1}{r}\left(\frac{\partial^2 w_0}{\partial r^2}\right)\delta\left(\frac{\partial^2 w_0}{\partial \theta^2}\right)\right\}$$

$$-E_{TA}\left\{r\left(\frac{\partial w_0}{\partial r}\right)\delta\left(\frac{\partial w_0}{\partial r}\right)+\frac{1}{r}\left(\frac{\partial w_0}{\partial \theta}\right)\delta\left(\frac{\partial w_0}{\partial \theta}\right)+\delta(u_0)+r\delta\left(\frac{\partial u_0}{\partial r}\right)+\delta\left(\frac{\partial v_0}{\partial \theta}\right)\right]drd\theta, \qquad (2.28)$$

$$\delta(U_{ncl})=l^2\int_0^{2\pi}\int_a^b G_A\left[\frac{1}{4r}\left(\frac{\partial^2 u_0}{\partial r\partial \theta}\right)\delta\left(\frac{\partial^2 u_0}{\partial r\partial \theta}\right)+\frac{1}{4r^3}\left(\frac{\partial u_0}{\partial \theta}\right)\delta\left(\frac{\partial u_0}{\partial \theta}\right)+\frac{1}{4r^3}\left(\frac{\partial^2 u_0}{\partial \theta^2}\right)\delta\left(\frac{\partial^2 u_0}{\partial \theta^2}\right)\right.$$

$$+\frac{r}{4}\left(\frac{\partial^2 v_0}{\partial r^2}\right)\delta\left(\frac{\partial^2 v_0}{\partial r^2}\right)+\frac{1}{4r}\left(\frac{\partial v_0}{\partial r}\right)\delta\left(\frac{\partial v_0}{\partial r}\right)+\frac{1}{4r}\left(\frac{\partial^2 v_0}{\partial r\partial \theta}\right)\delta\left(\frac{\partial^2 v_0}{\partial r\partial \theta}\right)-\frac{1}{4r^3}v_0\delta(v_0)$$

$$+\frac{1}{4r^3}\left(\frac{\partial v_0}{\partial \theta}\right)\delta\left(\frac{\partial v_0}{\partial \theta}\right)+r\left(\frac{\partial^2 w_0}{\partial r^2}\right)\delta\left(\frac{\partial^2 w_0}{\partial r^2}\right)+\frac{1}{r}\left(\frac{\partial w_0}{\partial r}\right)\delta\left(\frac{\partial w_0}{\partial r}\right)+\frac{4}{r}\left(\frac{\partial^2 w_0}{\partial r\partial \theta}\right)\delta\left(\frac{\partial^2 w_0}{\partial r\partial \theta}\right)$$

$$+\frac{4}{r^3}\left(\frac{\partial w_0}{\partial \theta}\right)\delta\left(\frac{\partial w_0}{\partial \theta}\right)+\frac{1}{r^3}\left(\frac{\partial^2 w_0}{\partial \theta^2}\right)\delta\left(\frac{\partial^2 w_0}{\partial \theta^2}\right)-\frac{1}{4r^2}\left(\frac{\partial^2 u_0}{\partial r\partial \theta}\right)\delta\left(\frac{\partial u_0}{\partial \theta}\right)-\frac{1}{4r^2}\left(\frac{\partial u_0}{\partial \theta}\right)\delta\left(\frac{\partial^2 u_0}{\partial r\partial \theta}\right)$$

$$-\frac{1}{4}\left(\frac{\partial^2 v_0}{\partial r^2}\right)\delta\left(\frac{\partial^2 u_0}{\partial r\partial\theta}\right)-\frac{1}{4}\left(\frac{\partial^2 u_0}{\partial r\partial\theta}\right)\delta\left(\frac{\partial^2 v_0}{\partial r^2}\right)+\frac{1}{4r}\left(\frac{\partial^2 v_0}{\partial r^2}\right)\delta\left(\frac{\partial u_0}{\partial\theta}\right)+\frac{1}{4r}\left(\frac{\partial u_0}{\partial\theta}\right)\delta\left(\frac{\partial^2 v_0}{\partial r^2}\right)$$

$$-\frac{1}{4r}\left(\frac{\partial v_0}{\partial r}\right)\delta\left(\frac{\partial^2 u_0}{\partial r\partial\theta}\right)-\frac{1}{4r}\left(\frac{\partial^2 u_0}{\partial r\partial\theta}\right)\delta\left(\frac{\partial v_0}{\partial r}\right)+\frac{1}{4r^2}\left(\frac{\partial v_0}{\partial r}\right)\delta\left(\frac{\partial u_0}{\partial\theta}\right)+\frac{1}{4r^2}\left(\frac{\partial u_0}{\partial\theta}\right)\delta\left(\frac{\partial v_0}{\partial r}\right)$$

$$-\frac{1}{4r^2}\left(\frac{\partial^2 v_0}{\partial r\partial\theta}\right)\delta\left(\frac{\partial^2 u_0}{\partial\theta^2}\right)-\frac{1}{4r^2}\left(\frac{\partial^2 u_0}{\partial\theta^2}\right)\delta\left(\frac{\partial^2 v_0}{\partial r\partial\theta}\right)+\frac{1}{4r^2}v_0\delta\left(\frac{\partial^2 u_0}{\partial r\partial\theta}\right)+\frac{1}{4r^2}\left(\frac{\partial^2 u_0}{\partial r\partial\theta}\right)\delta\left(v_0\right)$$

$$-\frac{1}{4r^3}v_0\delta\left(\frac{\partial u_0}{\partial\theta}\right)-\frac{1}{4r^3}\left(\frac{\partial u_0}{\partial\theta}\right)\delta\left(v_0\right)-\frac{1}{4r^3}\left(\frac{\partial v_0}{\partial\theta}\right)\delta\left(\frac{\partial^2 u_0}{\partial\theta^2}\right)-\frac{1}{4r^3}\left(\frac{\partial^2 u_0}{\partial\theta^2}\right)\delta\left(\frac{\partial v_0}{\partial\theta}\right)$$

$$+\frac{1}{4}\left(\frac{\partial^2 v_0}{\partial r^2}\right)\delta\left(\frac{\partial v_0}{\partial r}\right)+\frac{1}{4}\left(\frac{\partial v_0}{\partial r}\right)\delta\left(\frac{\partial^2 v_0}{\partial r^2}\right)-\frac{1}{4r}\left(\frac{\partial^2 v_0}{\partial r^2}\right)\delta\left(v_0\right)-\frac{1}{4r}v_0\delta\left(\frac{\partial^2 v_0}{\partial r^2}\right)$$

$$-\frac{1}{4r^2}\left(\frac{\partial v_0}{\partial r}\right)\delta\left(v_0\right)-\frac{1}{4r^2}v_0\delta\left(\frac{\partial v_0}{\partial r}\right)+\frac{1}{4r^2}\left(\frac{\partial^2 v_0}{\partial r\partial\theta}\right)\delta\left(\frac{\partial v_0}{\partial\theta}\right)+\frac{1}{4r^2}\left(\frac{\partial v_0}{\partial\theta}\right)\delta\left(\frac{\partial^2 v_0}{\partial r\partial\theta}\right)$$

$$-\left(\frac{\partial^2 w_0}{\partial r^2}\right)\delta\left(\frac{\partial w_0}{\partial r}\right)-\left(\frac{\partial w_0}{\partial r}\right)\delta\left(\frac{\partial^2 w_0}{\partial r^2}\right)-\frac{1}{r}\left(\frac{\partial^2 w_0}{\partial\theta^2}\right)\delta\left(\frac{\partial^2 w_0}{\partial r^2}\right)-\frac{1}{r}\left(\frac{\partial^2 w_0}{\partial r^2}\right)\delta\left(\frac{\partial^2 w_0}{\partial\theta^2}\right)$$

$$+\frac{1}{r^2}\left(\frac{\partial^2 w_0}{\partial\theta^2}\right)\delta\left(\frac{\partial w_0}{\partial r}\right)+\frac{1}{r^2}\left(\frac{\partial w_0}{\partial r}\right)\delta\left(\frac{\partial^2 w_0}{\partial\theta^2}\right)-\frac{4}{r^2}\left(\frac{\partial^2 w_0}{\partial r\partial\theta}\right)\delta\left(\frac{\partial w_0}{\partial\theta}\right)$$

$$-\frac{4}{r^2}\left(\frac{\partial w_0}{\partial\theta}\right)\delta\left(\frac{\partial^2 w_0}{\partial r\partial\theta}\right)\Bigg]drd\theta, \tag{2.29}$$

$$\delta(W)=-\Omega^2\int_0^{2\pi}\int_a^b\rho_A r^2\delta(u_0)drd\theta-q_0\int_0^{2\pi}\int_a^b r\delta(w_0)drd\theta. \tag{2.30}$$

The governing equations are derived and transformed into algebraic form, following Ritz method (Shames and Dym (2009); Reddy (2008)). According to this method, each of the mid-plane displacements $\{u_0, v_0, w_0\}$ are discretized as finite linear combinations of two-dimensional (2D) orthogonal admissible functions $\left\{\phi_j^u, \phi_j^v, \phi_j^w\right\}$ and unknown coefficients c_j as:

$$u_0(\xi,\mu)=\sum_{j=1}^{n}c_j\phi_j^u(\xi,\mu), \tag{2.31a}$$

$$v_0(\xi,\mu)=\sum_{j=1}^{n}c_{n+j}\phi_j^v(\xi,\mu), \tag{2.31b}$$

$$w_0(\xi,\mu)=\sum_{j=1}^{n} c_{2n+j}\phi_j^w(\xi,\mu). \tag{2.31c}$$

Here n is the total number of functions for discretizing each of the displacement fields $\{u_0, v_0, w_0\}$. Each of the functions $\{\phi_j^u, \phi_j^v, \phi_j^w\}$ is defined in the normalized domain (ξ,μ). It is noted that the vector of unknown coefficients $\{\mathbf{c}\}$ is also called vector of generalized coordinates.

Each of the 2D functions $\{\phi_j^u, \phi_j^v, \phi_j^w\}$ is derived by ordered multiplication of the following sets of one-dimensional (1D) functions: $\{\psi_p^u, \psi_p^v, \psi_p^w\}$ and $\{\gamma_q^u, \gamma_q^v, \gamma_q^w\}$. These 1D functions are numerically generated along each direction of the normalized domain (ξ,μ) (Das et al. (2009)). Hence the 2D functions $\{\phi_j^u, \phi_j^v, \phi_j^w\}$ now takes the following form:

$$\phi_j^u(\xi,\mu)=\psi_p^u(\xi)\times\gamma_q^u(\mu), \tag{2.32a}$$

$$\phi_j^v(\xi,\mu)=\psi_p^v(\xi)\times\gamma_q^v(\mu), \tag{2.32b}$$

$$\phi_j^w(\xi,\mu)=\psi_p^w(\xi)\times\gamma_q^w(\mu). \tag{2.32c}$$

Here $p=1,2,...n_\xi$ and $q=1,2,...n_\mu$, where n_ξ and n_μ are the number of functions along the ξ and μ directions respectively, and $j=1,2,...n$ where $n=n_\xi\times n_\mu$. The lowest-order admissible 1D functions $\{\psi_1^u, \psi_1^v, \psi_1^w\}$ for the set $\{\psi_p^u, \psi_p^v, \psi_p^w\}$ are selected considering the boundary conditions of the micro-disk. These 1D functions i.e., $\{\psi_1^u, \psi_1^v, \psi_1^w\}$ for different boundary conditions, namely CF, SS, CS, SC and CC are shown in Table 2.3. The remaining (n_ξ-1) number of functions for $\{\psi_p^u, \psi_p^v, \psi_p^w\}$ are numerically generated employing Gram-Schmidt orthogonalization scheme. On the other hand, the set of functions $\{\gamma_q^u, \gamma_q^v, \gamma_q^w\}$ are selected as follows:

$$\gamma_q^u(\mu)=\gamma_q^v(\mu)=\gamma_q^w(\mu)=\begin{cases}1 & \text{for } q=1\\ \sin\{(q-1)2\pi\mu\} & \text{for } q\geq 2.\end{cases} \tag{2.33}$$

Table 2.3: List of lowest order admissible functions $\left\{\psi_1^u, \psi_1^v, \psi_1^w\right\}$.

Displacement field	Boundary Type	Boundary Conditions	Lowest Order Function
u_0	CF	$u_0\big\|_{r=a} = 0, u_0\big\|_{x=b} \neq 0.$	$\psi_1^u = \xi$
	SS	$u_0\big\|_{r=a} = 0, u_0\big\|_{x=b} = 0.$	$\psi_1^u = \xi\left(1-\xi\right)$
	CS		
	SC		
	CC		
v_0	CF	$v_0\big\|_{r=a} = 0, v_0\big\|_{x=b} \neq 0.$	$\psi_1^v = \xi$
	SS	$v_0\big\|_{r=a} = 0, v_0\big\|_{x=b} = 0.$	$\psi_1^v = \xi\left(1-\xi\right)$
	CS		
	SC		
	CC		
w_0	CF	$w_0\big\|_{r=a} = 0, w_0\big\|_{x=b} \neq 0,$ $\left.\frac{\partial w_0}{\partial \xi}\right\|_{r=a} = 0, \left.\frac{\partial w_0}{\partial \xi}\right\|_{x=b} \neq 0.$	$\psi_1^w\left(\xi\right) = \xi^2$
	SS	$w_0\big\|_{r=a} = 0, w_0\big\|_{x=b} = 0,$ $\left.\frac{\partial^2 w_0}{\partial \xi^2}\right\|_{r=a} = 0, \left.\frac{\partial^2 w_0}{\partial \xi^2}\right\|_{x=b} = 0.$	$\psi_1^w = \sin\left(\pi\xi\right)$
	CS	$w_0\big\|_{r=a} = 0, w_0\big\|_{x=b} = 0,$ $\left.\frac{\partial w_0}{\partial \xi}\right\|_{r=a} = 0, \left.\frac{\partial^2 w_0}{\partial \xi^2}\right\|_{x=b} = 0.$	$\psi_1^w = \xi^2\left(3-5\xi+2\xi^2\right)$
	SC	$w_0\big\|_{r=a} = 0, w_0\big\|_{x=b} = 0,$ $\left.\frac{\partial^2 w_0}{\partial \xi^2}\right\|_{r=a} = 0, \left.\frac{\partial w_0}{\partial \xi}\right\|_{x=b} = 0.$	$\psi_1^w = \xi\left(1-3\xi^2+2\xi^3\right)$
	CC	$w_0\big\|_{r=a} = 0, w_0\big\|_{x=b} = 0,$ $\left.\frac{\partial w_0}{\partial \xi}\right\|_{r=a} = 0, \left.\frac{\partial w_0}{\partial \xi}\right\|_{x=b} = 0.$	$\psi_1^w = \xi^2\left(1-2\xi+\xi^2\right)$

Substituting Eqs. (2.28)-(2.30) into Eq. (2.23), and further substituting the approximate displacement fields given by Eqs. (2.31a)-(2.31c), the set of governing equations are obtained in algebraic form, which in matrix form can be written as follows:

$$\left[\mathbf{S}\right]\left\{\mathbf{c}\right\}=\left\{\mathbf{P}\right\}. \tag{2.34}$$

In the above equation, $\left[\mathbf{S}\right]$ is the total stiffness matrix (of dimension $3n\times 3n$) given by $\left[\mathbf{S}\right]=\left[\mathbf{S}^{cl}\right]+\left[\mathbf{S}^{ncl}\right]$ where $\left[\mathbf{S}^{cl}\right]$ and $\left[\mathbf{S}^{ncl}\right]$ are the classical and non-classical stiffness matrix respectively; $\left\{\mathbf{c}\right\}$ is the vector of unknown coefficients c_j to be determined; $\left\{\mathbf{P}\right\}$ is the load vector. The components of $\left[\mathbf{S}^{cl}\right]$, $\left[\mathbf{S}^{ncl}\right]$ and $\left\{\mathbf{P}\right\}$ are provided in Appendix 2A. Due to the presence von Kármán type nonlinearity in the classical strain tensor, $\left[\mathbf{S}^{cl}\right]$ is nonlinear in nature; whereas in the absence of any type of geometric nonlinear terms in the curvature tensor, $\left[\mathbf{S}^{ncl}\right]$ is essentially linear. To solve the system of nonlinear algebraic equations given by Eq. (2.34), a multi-dimensional secant method, known as Broyden's method (Press et al. (1992); Das et al. (2011)) is employed. This method, though taking significantly longer computation time, provided very stable and accurate solution. The solution of Eq. (2.34) when substituted in Eqs. (2.31a)-(2.31c) determines the displacement fields, and in turn provides the deformed configuration of the micro-disk under combined effects of centrifugal loading, transverse pressure and thermal loading. All the computations up to Eq. (2.34) have been carried out in FORTRAN.

2.8 Determination of Free Vibration Response of Deformed Micro-Disk

This particular objective forms the second step of the problem. If the deformed micro-disk executes free vibration, the vibratory motion will take place about the deformed configuration, which has already been determined in the previous step. It is assumed that the micro-disk will execute small amplitude free vibration about its deformed configuration, and the vibratory motion is essentially linear.

The governing equations for free vibration of the micro-disk about the deformed configuration are derived employing Hamilton's principle, which is given as follows:

$$\delta\left(\int_{\tau_1}^{\tau_2}\left(T_k-U-W\right)d\tau\right)=0. \tag{2.35}$$

Here τ is time, T_k is the kinetic energy, U is the total strain energy, and W is the work potential of the applied load during free vibration. As the present problem involves free vibration, W is equated to zero. Furthermore, U consists of classical $\left(U_{cl}\right)$ and non-classical $\left(U_{ncl}\right)$ parts. Hence Hamilton's principle takes the following form for the present case:

$$\delta\left(\int_{\tau_1}^{\tau_2}\left(T_k - U_{cl} - U_{ncl}\right)d\tau\right) = 0. \tag{2.36}$$

The expression of T_k is derived in terms of the dynamic displacement components $\{u_0, v_0, w_0\}$ as follows:

$$T_k = \frac{1}{2}\int_{-t/2}^{+t/2}\int_0^{2\pi}\int_a^b \frac{\rho_f}{2}\left[\left\{\left(\frac{\partial u}{\partial \tau}\right)^2 + \left(\frac{\partial v}{\partial \tau}\right)^2 + \left(\frac{\partial w}{\partial \tau}\right)^2\right\}\right] r dr d\theta dz$$

$$= \frac{1}{2}\int_{-t/2}^{+t/2}\int_0^{2\pi}\int_a^b \frac{\rho_f}{2}\left[\left\{\frac{\partial\left(u_0 - z\dfrac{\partial w_0}{\partial r}\right)}{\partial \tau}\right\}^2 + \left\{\frac{\partial\left(v_0 - \dfrac{z}{r}\dfrac{\partial w_0}{\partial \theta}\right)^2}{\partial \tau}\right\} + \left\{\frac{\partial w_0}{\partial \tau}\right\}^2\right] r dr d\theta dz$$

$$= \frac{1}{2}\int_{-t/2}^{+t/2}\int_0^{2\pi}\int_a^b \frac{\rho_f}{2}\left[\left(\frac{\partial u_0}{\partial \tau}\right)^2 + \left(\frac{\partial v_0}{\partial \tau}\right)^2 + \left(\frac{\partial w_0}{\partial \tau}\right)^2 - 2zu_0\frac{\partial^2 w_0}{\partial \tau \partial r} - 2z\frac{v_0}{r}\frac{\partial^2 w_0}{\partial \tau \partial \theta}\right.$$

$$\left. + z^2\left(\frac{\partial^2 w_0}{\partial \tau \partial r}\right)^2 + z^2\frac{1}{r^2}\left(\frac{\partial^2 w_0}{\partial \tau \partial \theta}\right)^2\right] r dr d\theta dz$$

$$= \frac{1}{2}\int_0^{2\pi}\int_a^b\left[\rho_A\left\{\left(\frac{\partial u_0}{\partial \tau}\right)^2 + \left(\frac{\partial v_0}{\partial \tau}\right)^2 + \left(\frac{\partial w_0}{\partial \tau}\right)^2\right\} + \rho_I\left\{\left(\frac{\partial^2 w_0}{\partial \tau \partial r}\right)^2 + \frac{1}{r^2}\left(\frac{\partial^2 w_0}{\partial \tau \partial \theta}\right)^2\right\}\right] r dr d\theta \,. \tag{2.37}$$

In Eq. (2.37), $\{\rho_A, \rho_I\}$ is the set of inertia coefficients where ρ_A is already defined in Eq. (2.27i) and ρ_I is defined as:

$$\rho_I = \int_{-t/2}^{+t/2}\rho_f z^2 dz. \tag{2.38}$$

It is noted that the following simplification is used to derive Eq. (2.37) as a result symmetrical material gradation across the thickness: $\int_{-t/2}^{+t/2}\rho_f z dz = 0$. It is further noted that the dynamic

mid-plane displacements $\{u_0, v_0, w_0\}$ for this step of the problem are referenced from the deformed configuration, already determined.

The dynamic displacements $\{u_0, v_0, w_0\}$ are functions of both space and time. It is considered that the space and time parts of $\{u_0, v_0, w_0\}$ are separable. Further the time parts of $\{u_0, v_0, w_0\}$ are assumed harmonic because the present problem involves free vibration of an elastic system. The space parts of the dynamic displacement components are discretized following Ritz method using the same set of functions $\{\phi_j^u, \phi_j^v, \phi_j^w\}$ that are used for determining the deformed configuration of the micro-disk. But the discretization takes place with the combination of a new set of unknown coefficients d_j. The displacement fields in discretized form are given as follows:

$$u_0(\xi, \mu, \tau) = \sum_{j=1}^{n} \left(d_j e^{\mathbf{i}\omega\tau} \right) \phi_j^u (\xi, \mu), \tag{2.39a}$$

$$v_0(\xi, \mu, \tau) = \sum_{j=1}^{n} \left(d_{n+j} e^{\mathbf{i}\omega\tau} \right) \phi_j^v (\xi, \mu), \tag{2.39b}$$

$$w_0(\xi, \mu, \tau) = \sum_{j=1}^{n} \left(d_{2n+j} e^{\mathbf{i}\omega\tau} \right) \phi_j^w (\xi, \mu). \tag{2.39c}$$

In Eqs. (2.39a)-(2.39c), ω is the frequency of vibration and $\mathbf{i}=\sqrt{-1}$. It is noted that the set of unknown coefficients d_j is called the set of generalized coordinates.

As the micro-disk executes small amplitude free vibration about its deformed configuration, its tangent stiffness is responsible for free vibratory motion that would occur in the neighborhood of the deformed configuration. The strain energies involved in Eq. (2.36) would lead to the tangent stiffness matrix $[\mathbf{K}]$ of the deformed disk. It is noted that the tangent stiffness matrix, and the total stiffness matrix used in the previous step (Eq. (2.34)) for determining the deformed configuration of the micro-disk are not same. As the total stiffness of the micro-disk for undergoing time-invariant deformation is already known (i.e., $\{\mathbf{c}\}$ is known for any particular loading) from the previous step, the tangent stiffness can be suitably obtained using it.

At any deformed state given by $\{\mathbf{c}\}$, the components of the tangent stiffness matrix $([\mathbf{K}])$ are determined by taking partial derivative of each of the elements of the restoring force vector $\{\mathbf{P}^r\}$ with respect to each component of $\{\mathbf{c}\}$. The vector of restoring forces $\{\mathbf{P}^r\}$ at any deformed state given by $\{\mathbf{c}\}$ is obtained by the product of the total stiffness matrix $[\mathbf{S}]$ and $\{\mathbf{c}\}$ given as below:

$$\{P_i^r\} = \sum_{j=1}^{3n} [S_{ij}]\{c_j\} \text{ for } i = 1, 2, ..., 3n. \tag{2.40}$$

Hence the components of the tangent stiffness matrix are derived using the following relation (Das (2018)):

$$[K_{ik}] = \frac{\partial\left\{\sum_{j=1}^{3n}[S_{ij}]\{c_j\}\right\}}{\partial c_k} \text{ for } \begin{vmatrix} i = 1, 2, ..., 3n, \\ k = 1, 2, ..., 3n. \end{vmatrix} \tag{2.41}$$

It must be noted that $[\mathbf{K}]$ is contributed by the classical $([\mathbf{K}^{cl}])$ and non-classical $([\mathbf{K}^{ncl}])$ parts. It can be said that the non-classical part of the total and tangent stiffness matrices are both linear and same i.e., $[\mathbf{S}^{ncl}] = [\mathbf{K}^{ncl}]$, owing to the fact that the symmetric curvature tensor (χ) is essentially linear. However the classical part of the tangent stiffness matrix $([\mathbf{K}^{cl}])$ is nonlinear. The derivations of $[\mathbf{K}^{cl}]$ using Eqs. (2.40) and (2.41) are shown in Appendix 2B. The components of $[\mathbf{K}^{cl}]$ are provided in Appendix 2C.

Using Eqs. (2.39a)-(2.39c), substituting Eq. (2.37) into (2.36), and using the components of the tangent stiffness into Eq. (2.36), the governing equations are derived in the following form:

$$\left[[\mathbf{K}] - \omega^2[\mathbf{M}]\right]\{\mathbf{d}\} = 0. \tag{2.42}$$

Here $[\mathbf{M}]$ is the mass matrix and $\{\mathbf{d}\}$ is the set of unknown coefficients representing the dynamic displacements during the free vibration. The components of $[\mathbf{M}]$ are provided in Appendix 2D. It is noted that the nonlinear tangent stiffness matrix $[\mathbf{K}]$ appearing in Eq.

(2.42) is linearized using the solution coefficients $\{\mathbf{c}\}$ of the deformed configuration of the micro-disk to take into the effect of pre-stress induced due to centrifugal loading, transverse pressure and thermal loading. Eq. (2.42) clearly represents an eigenvalue problem. The square roots of the eigenvalues $\left(\omega^2\right)$ signify the frequencies of vibratory motion of the deformed micro-disk, and the eigenvectors i.e., $\{\mathbf{d}\}$ represent the corresponding mode-shapes of vibration. These eigenvectors when used in Eqs. (2.39a)-(2.39c) generate the mode-shapes of vibration. Eq. (2.42) is solved using a standard eigen-solver of MATLAB. All the computations in this section, except the solution of Eq. (2.42), have been carried out in FORTRAN.

2.9 Chapter Summary

The general thematic problem of the thesis as a whole has been defined. The details of FGM modeling of the disk have been explained. The physical and computational domains of the present problem has been identified and discussed. Various components of different tensors, namely von Kármán strain tensor, Cauchy stress tensor, symmetric curvature tensor and deviatoric part of symmetric couple stress tensor have been derived. The governing equations for two different but interrelated parts of the main problem have been derived and solved with the help of Ritz method. The solution methodologies of the governing equations for these two problems have been explained. In nutshell, the generalized mathematical formulation, encompassing all the reduced problems for the subsequent chapters, has been discussed in this chapter.

Appendix 2A

Classical Part of Total Stiffness Matrix

The sub-matrices of $\left[\mathbf{S}^{cl}\right]$, each of dimension $n\times n$, are as follows:

$$\left[\mathbf{S}^{cl}\right]=\begin{bmatrix}\left[\mathbf{S}_{11}^{cl}\right] & \left[\mathbf{S}_{12}^{cl}\right] & \left[\mathbf{S}_{13}^{cl}\right]\\ \left[\mathbf{S}_{21}^{cl}\right] & \left[\mathbf{S}_{22}^{cl}\right] & \left[\mathbf{S}_{23}^{cl}\right]\\ \left[\mathbf{S}_{31}^{cl}\right] & \left[\mathbf{S}_{32}^{cl}\right] & \left[\mathbf{S}_{33}^{cl}\right]\end{bmatrix}. \tag{2A.1}$$

The components of these sub-matrices are given below:

$$\left[\mathbf{S}_{11}^{cl}\right]=\int_0^1\int_0^1\left[E_A\left\{r\frac{\partial\phi_i^u}{\partial r}\frac{\partial\phi_j^u}{\partial r}+\frac{1}{r}\phi_i^u\phi_j^u\right\}+\frac{G_A}{r}\frac{\partial\phi_i^u}{\partial\theta}\frac{\partial\phi_j^u}{\partial\theta}+E_{PA}\left\{\phi_i^u\frac{\partial\phi_j^u}{\partial r}+\frac{\partial\phi_i^u}{\partial r}\phi_j^u\right\}\right]\left|\mathbf{J}\right|d\xi d\mu, \tag{2A.2}$$

$$\left[\mathbf{S}_{12}^{cl}\right]=\int_0^1\int_0^1\left[\frac{E_A}{r}\phi_i^u\frac{\partial\phi_j^v}{\partial\theta}+G_A\left\{\frac{\partial\phi_i^u}{\partial\theta}\frac{\partial\phi_j^v}{\partial r}-\frac{1}{r}\frac{\partial\phi_i^u}{\partial\theta}\phi_j^v\right\}+E_{PA}\frac{\partial\phi_i^u}{\partial r}\frac{\partial\phi_j^v}{\partial\theta}\right]\left|\mathbf{J}\right|d\xi d\mu, \tag{2A.3}$$

$$\left[\mathbf{S}_{13}^{cl}\right]=\int_0^1\int_0^1\left[E_A\left\{\frac{r}{2}\left(\frac{\partial w_0}{\partial r}\right)\frac{\partial\phi_i^u}{\partial r}\frac{\partial\phi_j^w}{\partial r}+\frac{1}{2r^2}\left(\frac{\partial w_0}{\partial\theta}\right)\phi_i^u\frac{\partial\phi_j^w}{\partial\theta}\right\}+G_A\left\{\frac{1}{r}\left(\frac{\partial w_0}{\partial r}\right)\frac{\partial\phi_i^u}{\partial\theta}\frac{\partial\phi_j^w}{\partial\theta}\right\}+E_{PA}\left\{\frac{1}{2}\left(\frac{\partial w_0}{\partial r}\right)\phi_i^u\frac{\partial\phi_j^w}{\partial r}+\frac{1}{2r}\left(\frac{\partial w_0}{\partial\theta}\right)\frac{\partial\phi_i^u}{\partial r}\frac{\partial\phi_j^w}{\partial\theta}\right\}\right]\left|\mathbf{J}\right|d\xi d\mu, \tag{2A.4}$$

$$\left[\mathbf{S}_{21}^{cl}\right]=\int_0^1\int_0^1\left[\frac{E_A}{r}\frac{\partial\phi_i^v}{\partial\theta}\phi_j^u+G_A\left\{\frac{\partial\phi_i^v}{\partial r}\frac{\partial\phi_j^u}{\partial\theta}-\frac{1}{r}\phi_i^v\frac{\partial\phi_j^u}{\partial\theta}\right\}+E_{PA}\frac{\partial\phi_i^v}{\partial\theta}\frac{\partial\phi_j^u}{\partial r}\right]\left|\mathbf{J}\right|d\xi d\mu, \tag{2A.5}$$

$$\left[\mathbf{S}_{22}^{cl}\right]=\int_0^1\int_0^1\left[\frac{E_A}{r}\frac{\partial\phi_i^v}{\partial\theta}\frac{\partial\phi_j^v}{\partial\theta}+G_A\left\{-\phi_i^v\frac{\partial\phi_j^v}{\partial r}-\frac{\partial\phi_i^v}{\partial r}\phi_j^v+r\frac{\partial\phi_i^v}{\partial r}\frac{\partial\phi_j^v}{\partial r}+\frac{\phi_i^v\phi_j^v}{r}\right\}\right]\left|\mathbf{J}\right|d\xi d\mu, \tag{2A.6}$$

$$\left[\mathbf{S}_{23}^{cl}\right]=\int_0^1\int_0^1\left[\frac{E_A}{2r^2}\left(\frac{\partial w_0}{\partial\theta}\right)\frac{\partial\phi_i^v}{\partial\theta}\frac{\partial\phi_j^w}{\partial\theta}+G_A\left\{\left(\frac{\partial w_0}{\partial\theta}\right)\frac{\partial\phi_i^v}{\partial r}\frac{\partial\phi_j^w}{\partial r}-\frac{1}{r}\left(\frac{\partial w_0}{\partial\theta}\right)\phi_i^v\frac{\partial\phi_j^w}{\partial r}\right\}+\frac{E_{PA}}{2}\left(\frac{\partial w_0}{\partial r}\right)\frac{\partial\phi_i^v}{\partial\theta}\frac{\partial\phi_j^w}{\partial r}\right]\left|\mathbf{J}\right|d\xi d\mu, \tag{2A.7}$$

$$\left[\mathbf{S}_{31}^{cl}\right]=0, \tag{2A.8}$$

$$\left[\mathbf{S}_{32}^{cl}\right]=0, \tag{2A.9}$$

$$\left[\mathbf{S}_{33}^{cl}\right]=\int_0^1\int_0^1\Bigg[E_A\Bigg\{r\left(\frac{\partial u_0}{\partial r}\right)\frac{\partial\phi_i^w}{\partial r}\frac{\partial\phi_j^w}{\partial r}+\frac{r}{2}\left(\frac{\partial w_0}{\partial r}\right)^2\frac{\partial\phi_i^w}{\partial r}\frac{\partial\phi_j^w}{\partial r}+\left(\frac{u_0}{r^2}\right)\frac{\partial\phi_i^w}{\partial\theta}\frac{\partial\phi_j^w}{\partial\theta}$$
$$+\frac{1}{r^2}\left(\frac{\partial v_0}{\partial\theta}\right)\frac{\partial\phi_i^w}{\partial\theta}\frac{\partial\phi_j^w}{\partial\theta}+\frac{1}{2r^3}\left(\frac{\partial w_0}{\partial\theta}\right)^2\frac{\partial\phi_i^w}{\partial\theta}\frac{\partial\phi_j^w}{\partial\theta}\Bigg\}$$

$$+G_A\Bigg\{\left(\frac{\partial v_0}{\partial r}\right)\frac{\partial\phi_i^w}{\partial r}\frac{\partial\phi_j^w}{\partial\theta}+\left(\frac{\partial v_0}{\partial r}\right)\frac{\partial\phi_i^w}{\partial\theta}\frac{\partial\phi_j^w}{\partial r}-\frac{v_0}{r}\frac{\partial\phi_i^w}{\partial r}\frac{\partial\phi_j^w}{\partial\theta}-\frac{v_0}{r}\frac{\partial\phi_i^w}{\partial\theta}\frac{\partial\phi_j^w}{\partial r}+\frac{1}{r}\left(\frac{\partial u_0}{\partial\theta}\right)\frac{\partial\phi_i^w}{\partial r}\frac{\partial\phi_j^w}{\partial\theta}$$
$$+\frac{1}{r}\left(\frac{\partial u_0}{\partial\theta}\right)\frac{\partial\phi_i^w}{\partial\theta}\frac{\partial\phi_j^w}{\partial r}+\frac{1}{r}\left(\frac{\partial w_0}{\partial r}\right)^2\frac{\partial\phi_i^w}{\partial\theta}\frac{\partial\phi_j^w}{\partial\theta}+\frac{1}{r}\left(\frac{\partial w_0}{\partial\theta}\right)^2\frac{\partial\phi_i^w}{\partial r}\frac{\partial\phi_j^w}{\partial r}\Bigg\}$$

$$+E_I\left\{r\frac{\partial^2\phi_i^w}{\partial r^2}\frac{\partial^2\phi_j^w}{\partial r^2}+\frac{1}{r}\frac{\partial\phi_i^w}{\partial r}\frac{\partial\phi_j^w}{\partial r}+\frac{1}{r^2}\frac{\partial\phi_i^w}{\partial r}\frac{\partial^2\phi_j^w}{\partial\theta^2}+\frac{1}{r^2}\frac{\partial^2\phi_i^w}{\partial\theta^2}\frac{\partial\phi_j^w}{\partial r}+\frac{1}{r^3}\frac{\partial^2\phi_i^w}{\partial\theta^2}\frac{\partial^2\phi_j^w}{\partial\theta^2}\right\}$$

$$+G_I\left\{\frac{4}{r}\frac{\partial^2\phi_i^w}{\partial r\partial\theta}\frac{\partial^2\phi_j^w}{\partial r\partial\theta}-\frac{4}{r^2}\frac{\partial\phi_i^w}{\partial\theta}\frac{\partial^2\phi_j^w}{\partial r\partial\theta}-\frac{4}{r^2}\frac{\partial^2\phi_i^w}{\partial r\partial\theta}\frac{\partial\phi_j^w}{\partial\theta}+\frac{4}{r^3}\frac{\partial\phi_i^w}{\partial\theta}\frac{\partial\phi_j^w}{\partial\theta}\right\}$$

$$+E_{PA}\Bigg\{(u_0)\frac{\partial\phi_i^w}{\partial r}\frac{\partial\phi_j^w}{\partial r}+\left(\frac{\partial v_0}{\partial\theta}\right)\frac{\partial\phi_i^w}{\partial r}\frac{\partial\phi_j^w}{\partial r}+\frac{1}{r}\left(\frac{\partial u_0}{\partial r}\right)\frac{\partial\phi_i^w}{\partial\theta}\frac{\partial\phi_j^w}{\partial\theta}+\frac{1}{2r}\left(\frac{\partial w_0}{\partial\theta}\right)^2\frac{\partial\phi_i^w}{\partial r}\frac{\partial\phi_j^w}{\partial r}$$
$$+\frac{1}{2r}\left(\frac{\partial w_0}{\partial r}\right)^2\frac{\partial\phi_i^w}{\partial\theta}\frac{\partial\phi_j^w}{\partial\theta}\Bigg\}$$

$$+E_{PI}\left\{\frac{\partial\phi_i^w}{\partial r}\frac{\partial^2\phi_j^w}{\partial r^2}+\frac{\partial^2\phi_i^w}{\partial r^2}\frac{\partial\phi_j^w}{\partial r}+\frac{1}{r}\frac{\partial^2\phi_i^w}{\partial r^2}\frac{\partial^2\phi_j^w}{\partial\theta^2}+\frac{1}{r}\frac{\partial^2\phi_i^w}{\partial\theta^2}\frac{\partial^2\phi_j^w}{\partial r^2}\right\}$$
$$-E_{TA}\left\{r\frac{\partial\phi_i^w}{\partial r}\frac{\partial\phi_j^w}{\partial r}+\frac{1}{r}\frac{\partial\phi_i^w}{\partial\theta}\frac{\partial\phi_j^w}{\partial\theta}\right\}\Bigg]|\mathbf{J}|\,d\xi\,d\mu. \tag{2A.10}$$

<u>Non-classical Part of Total Stiffness Matrix</u>

The sub-matrices of $\left[\mathbf{S}^{ncl}\right]$, each of dimension $n\times n$, are as follows:

$$\left[\mathbf{S}^{ncl}\right]=\begin{bmatrix}\left[\mathbf{S}_{11}^{ncl}\right] & \left[\mathbf{S}_{12}^{ncl}\right] & \left[\mathbf{S}_{13}^{ncl}\right]\\ \left[\mathbf{S}_{21}^{ncl}\right] & \left[\mathbf{S}_{22}^{ncl}\right] & \left[\mathbf{S}_{23}^{ncl}\right]\\ \left[\mathbf{S}_{31}^{ncl}\right] & \left[\mathbf{S}_{32}^{cl}\right] & \left[\mathbf{S}_{33}^{ncl}\right]\end{bmatrix}. \tag{2A.11}$$

The components of these sub-matrices are given below:

$$\left[\mathbf{S}_{11}^{ncl}\right]=l^2\int_0^1\int_0^1 G_A\left[\frac{1}{4r}\frac{\partial^2\phi_i^u}{\partial r\partial\theta}\frac{\partial^2\phi_j^u}{\partial r\partial\theta}-\frac{1}{4r^2}\frac{\partial\phi_i^u}{\partial\theta}\frac{\partial^2\phi_j^u}{\partial r\partial\theta}-\frac{1}{4r^2}\frac{\partial^2\phi_i^u}{\partial r\partial\theta}\frac{\partial\phi_j^u}{\partial\theta}+\frac{1}{4r^3}\frac{\partial\phi_i^u}{\partial\theta}\frac{\partial\phi_j^u}{\partial\theta}+\frac{1}{4r^3}\frac{\partial^2\phi_i^u}{\partial\theta^2}\frac{\partial^2\phi_j^u}{\partial\theta^2}\right]|\mathbf{J}|\,d\xi\,d\mu, \tag{2A.12}$$

$$\left[\mathbf{S}_{12}^{ncl}\right]=l^2\int_0^1\int_0^1 G_A\left[-\frac{1}{4}\frac{\partial^2\phi_i^u}{\partial r\partial\theta}\frac{\partial^2\phi_j^v}{\partial r^2}+\frac{1}{4r}\frac{\partial\phi_i^u}{\partial\theta}\frac{\partial^2\phi_j^v}{\partial r^2}-\frac{1}{4r}\frac{\partial^2\phi_i^u}{\partial r\partial\theta}\frac{\partial\phi_j^v}{\partial r}+\frac{1}{4r^2}\frac{\partial\phi_i^u}{\partial\theta}\frac{\partial\phi_j^v}{\partial r}+\frac{1}{4r^2}\frac{\partial^2\phi_i^u}{\partial r\partial\theta}\phi_j^v-\frac{1}{4r^2}\frac{\partial^2\phi_i^u}{\partial\theta^2}\frac{\partial^2\phi_j^v}{\partial r\partial\theta}-\frac{1}{4r^3}\frac{\partial\phi_i^u}{\partial\theta}\phi_j^v-\frac{1}{4r^3}\frac{\partial^2\phi_i^u}{\partial\theta^2}\frac{\partial\phi_j^v}{\partial\theta}\right]|\mathbf{J}|\,d\xi\,d\mu, \tag{2A.13}$$

$$\left[\mathbf{S}_{13}^{ncl}\right]=0, \tag{2A.14}$$

$$\left[\mathbf{S}_{21}^{ncl}\right]=l^2\int_0^1\int_0^1 G_A\left[-\frac{1}{4}\frac{\partial^2\phi_i^v}{\partial r^2}\frac{\partial^2\phi_j^u}{\partial r\partial\theta}+\frac{1}{4r}\frac{\partial^2\phi_i^v}{\partial r^2}\frac{\partial\phi_j^u}{\partial\theta}-\frac{1}{4r}\frac{\partial\phi_i^v}{\partial r}\frac{\partial^2\phi_j^u}{\partial r\partial\theta}+\frac{1}{4r^2}\frac{\partial\phi_i^v}{\partial r}\frac{\partial\phi_j^u}{\partial\theta}+\frac{1}{4r^2}\phi_i^v\frac{\partial^2\phi_j^u}{\partial r\partial\theta}-\frac{1}{4r^2}\frac{\partial^2\phi_i^v}{\partial r\partial\theta}\frac{\partial^2\phi_j^u}{\partial\theta^2}-\frac{1}{4r^3}\phi_i^v\frac{\partial\phi_j^u}{\partial\theta}-\frac{1}{4r^3}\frac{\partial\phi_i^v}{\partial\theta}\frac{\partial^2\phi_j^u}{\partial\theta^2}\right]|\mathbf{J}|\,d\xi\,d\mu, \tag{2A.15}$$

$$\left[\mathbf{S}_{22}^{ncl}\right]=l^2\int_0^1\int_0^1 G_A\left[\frac{1}{4}\frac{\partial\phi_i^v}{\partial r}\frac{\partial^2\phi_j^v}{\partial r^2}+\frac{1}{4}\frac{\partial^2\phi_i^v}{\partial r^2}\frac{\partial\phi_j^v}{\partial r}+\frac{r}{4}\frac{\partial^2\phi_i^v}{\partial r^2}\frac{\partial^2\phi_j^v}{\partial r^2}-\frac{1}{4r}\phi_i^v\frac{\partial^2\phi_j^v}{\partial r^2}-\frac{1}{4r}\frac{\partial^2\phi_i^v}{\partial r^2}\phi_j^v+\frac{1}{4r}\frac{\partial\phi_i^v}{\partial r}\frac{\partial\phi_j^v}{\partial r}+\frac{1}{4r}\frac{\partial^2\phi_i^v}{\partial r\partial\theta}\frac{\partial^2\phi_j^v}{\partial r\partial\theta}-\frac{1}{4r^2}\phi_i^v\frac{\partial\phi_j^v}{\partial r}-\frac{1}{4r^2}\frac{\partial\phi_i^v}{\partial r}\phi_j^v+\frac{1}{4r^2}\frac{\partial\phi_i^v}{\partial\theta}\frac{\partial^2\phi_j^v}{\partial r\partial\theta}+\frac{1}{4r^2}\frac{\partial^2\phi_i^v}{\partial r\partial\theta}\frac{\partial\phi_j^v}{\partial\theta}-\frac{1}{4r^3}\phi_i^v\phi_j^v+\frac{1}{4r^3}\frac{\partial\phi_i^v}{\partial\theta}\frac{\partial\phi_j^v}{\partial\theta}\right]|\mathbf{J}|\,d\xi\,d\mu, \tag{2A.16}$$

$$\left[\mathbf{S}_{23}^{ncl}\right]=0, \tag{2A.17}$$

$$\left[\mathbf{S}_{31}^{ncl}\right]=0, \tag{2A.18}$$

$$\left[\mathbf{S}_{32}^{ncl}\right]=0, \tag{2A.19}$$

$$\left[\mathbf{S}_{33}^{ncl}\right] = l^2 \int_0^1 \int_0^1 G_A \left[-\frac{\partial \phi_i^w}{\partial r}\frac{\partial^2 \phi_j^w}{\partial r^2} - \frac{\partial^2 \phi_i^w}{\partial r^2}\frac{\partial \phi_j^w}{\partial r} + r\frac{\partial^2 \phi_i^w}{\partial r^2}\frac{\partial^2 \phi_j^w}{\partial r^2} + \frac{1}{r}\frac{\partial \phi_i^w}{\partial r}\frac{\partial \phi_j^w}{\partial r} \right.$$
$$-\frac{1}{r}\frac{\partial^2 \phi_i^w}{\partial r^2}\frac{\partial^2 \phi_j^w}{\partial \theta^2} - \frac{1}{r}\frac{\partial^2 \phi_i^w}{\partial \theta^2}\frac{\partial^2 \phi_j^w}{\partial r^2} + \frac{4}{r}\frac{\partial^2 \phi_i^w}{\partial r \partial \theta}\frac{\partial^2 \phi_j^w}{\partial r \partial \theta} + \frac{1}{r^2}\frac{\partial \phi_i^w}{\partial r}\frac{\partial^2 \phi_j^w}{\partial \theta^2}$$
$$+\frac{1}{r^2}\frac{\partial^2 \phi_i^w}{\partial \theta^2}\frac{\partial \phi_j^w}{\partial r} - \frac{4}{r^2}\frac{\partial \phi_i^w}{\partial \theta}\frac{\partial^2 \phi_j^w}{\partial r \partial \theta} - \frac{4}{r^2}\frac{\partial^2 \phi_i^w}{\partial r \partial \theta}\frac{\partial \phi_j^w}{\partial \theta}$$
$$\left. +\frac{4}{r^3}\frac{\partial \phi_i^w}{\partial \theta}\frac{\partial \phi_j^w}{\partial \theta} + \frac{1}{r^3}\frac{\partial^2 \phi_i^w}{\partial \theta^2}\frac{\partial^2 \phi_j^w}{\partial \theta^2} \right] |\mathbf{J}|\, d\xi\, d\mu. \tag{2A.20}$$

Elements of Load Vector

The sub-vectors of $[\mathbf{P}]$, each of dimension $n \times 1$, are as follows:

$$\{\mathbf{P}\} = \begin{Bmatrix} \{\mathbf{P}_1\} \\ \{\mathbf{P}_2\} \\ \{\mathbf{P}_3\} \end{Bmatrix}. \tag{2A.21}$$

The components of these sub-vectors are given below:

$$\{\mathbf{P}_1\} = \Omega^2 \int_0^1 \int_0^1 \rho_A r^2 \phi_i^u |\mathbf{J}|\, d\xi\, d\mu + \int_0^1 \int_0^1 E_{TA} \left[\phi_i^u + r\frac{\partial \phi_i^u}{\partial r} \right] |\mathbf{J}|\, d\xi\, d\mu, \tag{2A.22}$$

$$\{\mathbf{P}_2\} = \int_0^1 \int_0^1 E_{TA} \frac{\partial \phi_i^v}{\partial \theta} |\mathbf{J}|\, d\xi\, d\mu, \tag{2A.23}$$

$$\{\mathbf{P}_3\} = q_0 \int_0^1 \int_0^1 r \phi_i^w |\mathbf{J}|\, d\xi\, d\mu. \tag{2A.24}$$

Appendix 2B

If the elements of the total stiffness matrix $[\mathbf{S}]$ are linear (i.e., independent of the generalized coordinates $\{c_j\}$), then the corresponding elements of the tangent stiffness matrix $[\mathbf{K}]$ are also linear. This makes the corresponding elements of the total and tangent stiffness matrices identical. This can be shown, employing Eqs. (2.40) and (2.41) as follows:

$$[K_{ik}] = \frac{\partial}{\partial c_k}\{P_i^r\} = \frac{\partial}{\partial c_k}\{[S_{ij}]\{c_j\}\} = [S_{ij}] \quad \text{for possible} \begin{vmatrix} i = 1, 2, ..., 3n, \\ k = 1, 2, ..., 3n, \\ j = 1, 2, ..., 3n. \end{vmatrix} \qquad \text{(2B.1)}$$

The components of the classical part $\left([\mathbf{S}^{cl}]\right)$ of the total stiffness matrix, given by Eqs. (2A.2), (2A.3), (2A.5) and (2A.6), and also all the elements of the non-classical part $\left([\mathbf{S}^{ncl}]\right)$ of the total stiffness matrix given by Eqs. (2A.12)-(2A.20) are linear.

On the other hand, if the elements of the total stiffness matrix $[\mathbf{S}]$ are nonlinear (i.e., dependent on the displacement fields, and in turn on the generalized coordinates $\{c_j\}$), then the corresponding elements of the tangent stiffness matrix $[\mathbf{K}]$ are nonlinear and distinct from $[\mathbf{S}]$. It can be seen from Appendix 2A that the elements of $[\mathbf{S}]$, represented by Eqs. (2A.4), (2A.7) and (2A.10) are nonlinear. As an illustration, the derivation of the particular elements of $[\mathbf{K}]$ corresponding to the elements of $[\mathbf{S}]$, given by Eq. (2A.7), is shown below:

$$[K_{ik}]_{\substack{i=n+1,2n \\ k=2n+1,3n}} = \frac{\partial}{\partial c_k}\{P_i^r\} = \frac{\partial}{\partial c_k}\{[S_{ij}]\{c_j\}\}_{j=2n+1,3n}$$

$$= \frac{\partial}{\partial c_k}\left\{\int_0^1\int_0^1\left[\frac{E_A}{2r^2}\left(\frac{\partial w_0}{\partial \theta}\right)\frac{\partial \phi_{i-n}^v}{\partial \theta}\left(c_j\frac{\partial \phi_{j-2n}^w}{\partial \theta}\right) + \frac{E_{PA}}{2}\left(\frac{\partial w_0}{\partial r}\right)\frac{\partial \phi_{i-n}^v}{\partial \theta}\left(c_j\frac{\partial \phi_{j-2n}^w}{\partial r}\right)\right.\right.$$

$$\left.\left. + G_A\left\{-\frac{1}{r}\left(\frac{\partial w_0}{\partial \theta}\right)\phi_{i-n}^v\left(c_j\frac{\partial \phi_{j-2n}^w}{\partial r}\right) + \left(\frac{\partial w_0}{\partial \theta}\right)\frac{\partial \phi_{i-n}^v}{\partial r}\left(c_j\frac{\partial \phi_{j-2n}^w}{\partial r}\right)\right\}\right]|\mathbf{J}|\,d\xi\,d\eta\right\}_{j=2n+1,3n}$$

$$= \frac{\partial}{\partial c_k}\left\{\int_0^1\int_0^1\left[\frac{E_A}{2r^2}\frac{\partial\phi_{i-n}^{v}}{\partial\theta}\left(c_j\frac{\partial\phi_{j-2n}^{w}}{\partial\theta}\right)^2+\frac{E_{PA}}{2}\frac{\partial\phi_{i-n}^{v}}{\partial\theta}\left(c_j\frac{\partial\phi_{j-2n}^{w}}{\partial\theta}\right)^2\right.\right.$$

$$\left.\left.+G_A\left\{-\frac{1}{r}\phi_{i-n}^{v}\left(c_j\frac{\partial\phi_{j-2n}^{w}}{\partial\theta}\right)\left(c_j\frac{\partial\phi_{j-2n}^{w}}{\partial r}\right)+\frac{\partial\phi_{i-n}^{v}}{\partial r}\left(c_j\frac{\partial\phi_{j-2n}^{w}}{\partial\theta}\right)\left(c_j\frac{\partial\phi_{j-2n}^{w}}{\partial r}\right)\right\}\right]|\mathbf{J}|\,d\xi d\eta\right\}_{j=2n+1,3n}$$

$$= \int_0^1\int_0^1\left[\frac{E_A}{r^2}\frac{\partial\phi_{i-n}^{v}}{\partial\theta}\left(c_j\frac{\partial\phi_{j-2n}^{w}}{\partial\theta}\right)\frac{\partial\phi_{j-2n}^{w}}{\partial\theta}+E_{PA}\frac{\partial\phi_{i-n}^{v}}{\partial\theta}\left(c_j\frac{\partial\phi_{j-2n}^{w}}{\partial r}\right)\frac{\partial\phi_{j-2n}^{w}}{\partial r}\right.$$

$$+G_A\left\{-\frac{1}{r}\phi_{i-n}^{v}\left(c_j\frac{\partial\phi_{j-2n}^{w}}{\partial\theta}\right)\frac{\partial\phi_{j-2n}^{w}}{\partial r}-\frac{1}{r}\phi_{i-n}^{v}\left(c_j\frac{\partial\phi_{j-2n}^{w}}{\partial r}\right)\frac{\partial\phi_{j-2n}^{w}}{\partial\theta}\right.$$

$$\left.\left.+\frac{\partial\phi_{i-n}^{v}}{\partial r}\left(c_j\frac{\partial\phi_{j-2n}^{w}}{\partial\theta}\right)\frac{\partial\phi_{j-2n}^{w}}{\partial r}+\frac{\partial\phi_{i-n}^{v}}{\partial r}\left(c_j\frac{\partial\phi_{j-2n}^{w}}{\partial r}\right)\frac{\partial\phi_{j-2n}^{w}}{\partial\theta}\right\}\right]|\mathbf{J}|\,d\xi d\eta_{j=2n+1,3n}$$

$$= \int_0^1\int_0^1\left[\frac{E_A}{r^2}\left(\frac{\partial w_0}{\partial\theta}\right)\frac{\partial\phi_{i-n}^{v}}{\partial\theta}\frac{\partial\phi_{j-2n}^{w}}{\partial\theta}+E_{PA}\left(\frac{\partial w_0}{\partial r}\right)\frac{\partial\phi_{i-n}^{v}}{\partial\theta}\frac{\partial\phi_{j-2n}^{w}}{\partial r}+G_A\left\{-\frac{1}{r}\left(\frac{\partial w_0}{\partial\theta}\right)\phi_{i-n}^{v}\frac{\partial\phi_{j-2n}^{w}}{\partial r}\right.\right.$$

$$\left.\left.-\frac{1}{r}\left(\frac{\partial w_0}{\partial r}\right)\phi_{i-n}^{v}\frac{\partial\phi_{j-2n}^{w}}{\partial\theta}+\left(\frac{\partial w_0}{\partial\theta}\right)\frac{\partial\phi_{i-n}^{v}}{\partial r}\frac{\partial\phi_{j-2n}^{w}}{\partial r}+\left(\frac{\partial w_0}{\partial r}\right)\frac{\partial\phi_{i-n}^{v}}{\partial r}\frac{\partial\phi_{j-2n}^{w}}{\partial\theta}\right\}\right]|\mathbf{J}|\,d\xi d\eta. \qquad \text{(2B.2)}$$

Appendix 2C

Classical Part of Tangent Stiffness Matrix

The sub-matrices of $\left[\mathbf{K}^{cl}\right]$, each of dimension $n\times n$, are as follows:

$$\left[\mathbf{K}^{cl}\right]=\begin{bmatrix}\left[\mathbf{K}_{11}^{cl}\right] & \left[\mathbf{K}_{12}^{cl}\right] & \left[\mathbf{K}_{13}^{cl}\right]\\ \left[\mathbf{K}_{21}^{cl}\right] & \left[\mathbf{K}_{22}^{cl}\right] & \left[\mathbf{K}_{23}^{cl}\right]\\ \left[\mathbf{K}_{31}^{cl}\right] & \left[\mathbf{K}_{32}^{cl}\right] & \left[\mathbf{K}_{33}^{cl}\right]\end{bmatrix}. \tag{2C.1}$$

The components of these sub-matrices are given below:

$$\begin{aligned}\left[\mathbf{K}_{11}^{cl}\right]=\int_0^1\int_0^1\Bigg[& E_A\left\{r\frac{\partial\phi_i^u}{\partial r}\frac{\partial\phi_k^u}{\partial r}+\frac{1}{r}\phi_i^u\phi_k^u\right\}+\frac{G_A}{r}\frac{\partial\phi_i^u}{\partial\theta}\frac{\partial\phi_k^u}{\partial\theta}\\ & +E_{PA}\left\{\phi_i^u\frac{\partial\phi_k^u}{\partial r}+\frac{\partial\phi_i^u}{\partial r}\phi_k^u\right\}\Bigg]\left|\mathbf{J}\right|d\xi d\mu,\end{aligned} \tag{2C.2}$$

$$\left[\mathbf{K}_{12}^{cl}\right]=\int_0^1\int_0^1\left[\frac{E_A}{r}\phi_i^u\frac{\partial\phi_k^v}{\partial\theta}+G_A\left\{\frac{\partial\phi_i^u}{\partial\theta}\frac{\partial\phi_k^v}{\partial r}-\frac{1}{r}\frac{\partial\phi_i^u}{\partial\theta}\phi_k^v\right\}+E_{PA}\frac{\partial\phi_i^u}{\partial r}\frac{\partial\phi_k^v}{\partial\theta}\right]\left|\mathbf{J}\right|d\xi d\mu, \tag{2C.3}$$

$$\begin{aligned}\left[\mathbf{K}_{13}^{cl}\right]=\int_0^1\int_0^1\Bigg[& E_A\left\{r\left(\frac{\partial w_0}{\partial r}\right)\frac{\partial\phi_i^u}{\partial r}\frac{\partial\phi_k^w}{\partial r}+\frac{1}{r^2}\left(\frac{\partial w_0}{\partial\theta}\right)\phi_i^u\frac{\partial\phi_k^w}{\partial\theta}\right\}\\ & +G_A\left\{\frac{1}{r}\left(\frac{\partial w_0}{\partial r}\right)\frac{\partial\phi_i^u}{\partial\theta}\frac{\partial\phi_k^w}{\partial\theta}+\frac{1}{r}\left(\frac{\partial w_0}{\partial\theta}\right)\frac{\partial\phi_i^u}{\partial\theta}\frac{\partial\phi_k^w}{\partial r}\right\}\\ & +E_{PA}\left\{\left(\frac{\partial w_0}{\partial r}\right)\phi_i^u\frac{\partial\phi_k^w}{\partial r}+\frac{1}{r}\left(\frac{\partial w_0}{\partial\theta}\right)\frac{\partial\phi_i^u}{\partial r}\frac{\partial\phi_k^w}{\partial\theta}\right\}\Bigg]\left|\mathbf{J}\right|d\xi d\mu,\end{aligned} \tag{2C.4}$$

$$\left[\mathbf{K}_{21}^{cl}\right]=\int_0^1\int_0^1\left[\frac{E_A}{r}\frac{\partial\phi_i^v}{\partial\theta}\phi_k^u+G_A\left\{\frac{\partial\phi_i^v}{\partial r}\frac{\partial\phi_k^u}{\partial\theta}-\frac{1}{r}\phi_i^v\frac{\partial\phi_k^u}{\partial\theta}\right\}+E_{PA}\frac{\partial\phi_i^v}{\partial\theta}\frac{\partial\phi_k^u}{\partial r}\right]\left|\mathbf{J}\right|d\xi d\mu, \tag{2C.5}$$

$$\left[\mathbf{K}_{22}^{cl}\right]=\int_0^1\int_0^1\left[\frac{E_A}{r}\frac{\partial\phi_i^v}{\partial\theta}\frac{\partial\phi_k^v}{\partial\theta}+G_A\left\{-\phi_i^v\frac{\partial\phi_k^v}{\partial r}-\frac{\partial\phi_i^v}{\partial r}\phi_k^v+r\frac{\partial\phi_i^v}{\partial r}\frac{\partial\phi_k^v}{\partial r}+\frac{\phi_i^v\phi_k^v}{r}\right\}\right]\left|\mathbf{J}\right|d\xi d\mu, \tag{2C.6}$$

$$\left[\mathbf{K}_{23}^{cl}\right]=\int_0^1\int_0^1\Bigg[\frac{E_A}{r^2}\left(\frac{\partial w_0}{\partial\theta}\right)\frac{\partial\phi_i^v}{\partial\theta}\frac{\partial\phi_k^w}{\partial\theta}$$
$$+G_A\left\{\left(\frac{\partial w_0}{\partial\theta}\right)\frac{\partial\phi_i^v}{\partial r}\frac{\partial\phi_k^w}{\partial r}+\left(\frac{\partial w_0}{\partial r}\right)\frac{\partial\phi_i^v}{\partial r}\frac{\partial\phi_k^w}{\partial\theta}-\frac{1}{r}\left(\frac{\partial w_0}{\partial\theta}\right)\phi_i^v\frac{\partial\phi_k^w}{\partial r}\right. \tag{2C.7}$$
$$\left.-\frac{1}{r}\left(\frac{\partial w_0}{\partial r}\right)\phi_i^v\frac{\partial\phi_k^w}{\partial\theta}+E_{PA}\left(\frac{\partial w_0}{\partial r}\right)\frac{\partial\phi_i^v}{\partial\theta}\frac{\partial\phi_k^w}{\partial r}\right]|\mathbf{J}|\,d\xi\,d\mu,$$

$$\left[\mathbf{K}_{31}^{cl}\right]=\int_0^1\int_0^1\Bigg[E_A\left\{r\left(\frac{\partial w_0}{\partial r}\right)\frac{\partial\phi_i^w}{\partial r}\frac{\partial\phi_k^u}{\partial r}+\frac{1}{r^2}\left(\frac{\partial w_0}{\partial\theta}\right)\frac{\partial\phi_i^w}{\partial\theta}\phi_k^u\right\}$$
$$+G_A\left\{\frac{1}{r}\left(\frac{\partial w_0}{\partial\theta}\right)\frac{\partial\phi_i^w}{\partial r}\frac{\partial\phi_k^u}{\partial\theta}+\frac{1}{r}\left(\frac{\partial w_0}{\partial r}\right)\frac{\partial\phi_i^w}{\partial\theta}\frac{\partial\phi_k^u}{\partial\theta}\right\} \tag{2C.8}$$
$$\left.+E_{PA}\left\{\left(\frac{\partial w_0}{\partial r}\right)\frac{\partial\phi_i^w}{\partial r}\phi_k^u+\frac{1}{r}\left(\frac{\partial w_0}{\partial\theta}\right)\frac{\partial\phi_i^w}{\partial\theta}\frac{\partial\phi_k^u}{\partial r}\right\}\right]|\mathbf{J}|\,d\xi\,d\mu,$$

$$\left[\mathbf{K}_{32}^{cl}\right]=\int_0^1\int_0^1\Bigg[\frac{E_A}{r^2}\left(\frac{\partial w_0}{\partial\theta}\right)\frac{\partial\phi_i^w}{\partial\theta}\frac{\partial\phi_k^v}{\partial\theta}$$
$$+G_A\left\{\left(\frac{\partial w_0}{\partial r}\right)\frac{\partial\phi_i^w}{\partial\theta}\frac{\partial\phi_k^v}{\partial r}+\left(\frac{\partial w_0}{\partial\theta}\right)\frac{\partial\phi_i^w}{\partial r}\frac{\partial\phi_k^v}{\partial r}-\frac{1}{r}\left(\frac{\partial w_0}{\partial r}\right)\frac{\partial\phi_i^w}{\partial\theta}\phi_k^v\right. \tag{2C.9}$$
$$\left.-\frac{1}{r}\left(\frac{\partial w_0}{\partial\theta}\right)\frac{\partial\phi_i^w}{\partial r}\phi_k^v+E_{PA}\left(\frac{\partial w_0}{\partial r}\right)\frac{\partial\phi_i^w}{\partial r}\frac{\partial\phi_k^v}{\partial\theta}\right]|\mathbf{J}|\,d\xi\,d\mu,$$

$$\left[\mathbf{K}_{33}^{cl}\right]=\int_0^1\int_0^1\Bigg[E_A\left\{r\left(\frac{\partial u_0}{\partial r}\right)\frac{\partial\phi_i^w}{\partial r}\frac{\partial\phi_k^w}{\partial r}+\frac{3r}{2}\left(\frac{\partial w_0}{\partial r}\right)^2\frac{\partial\phi_i^w}{\partial r}\frac{\partial\phi_k^w}{\partial r}+\left(\frac{u_0}{r^2}\right)\frac{\partial\phi_i^w}{\partial\theta}\frac{\partial\phi_k^w}{\partial\theta}\right.$$
$$\left.+\frac{1}{r^2}\left(\frac{\partial v_0}{\partial\theta}\right)\frac{\partial\phi_i^w}{\partial\theta}\frac{\partial\phi_k^w}{\partial\theta}+\frac{3}{2r^3}\left(\frac{\partial w_0}{\partial\theta}\right)^2\frac{\partial\phi_i^w}{\partial\theta}\frac{\partial\phi_k^w}{\partial\theta}\right\}$$

$$+G_A\left\{\left(\frac{\partial v_0}{\partial r}\right)\frac{\partial\phi_i^w}{\partial r}\frac{\partial\phi_k^w}{\partial\theta}+\left(\frac{\partial v_0}{\partial r}\right)\frac{\partial\phi_i^w}{\partial\theta}\frac{\partial\phi_k^w}{\partial r}+\frac{1}{r}\left(\frac{\partial u_0}{\partial\theta}\right)\frac{\partial\phi_i^w}{\partial r}\frac{\partial\phi_k^w}{\partial\theta}+\frac{1}{r}\left(\frac{\partial u_0}{\partial\theta}\right)\frac{\partial\phi_i^w}{\partial\theta}\frac{\partial\phi_k^w}{\partial r}\right.$$
$$-\frac{v_0}{r}\frac{\partial\phi_i^w}{\partial r}\frac{\partial\phi_k^w}{\partial\theta}-\frac{v_0}{r}\frac{\partial\phi_i^w}{\partial\theta}\frac{\partial\phi_k^w}{\partial r}+\frac{1}{r}\left(\frac{\partial w_0}{\partial r}\right)^2\frac{\partial\phi_i^w}{\partial\theta}\frac{\partial\phi_k^w}{\partial\theta}+\frac{1}{r}\left(\frac{\partial w_0}{\partial\theta}\right)^2\frac{\partial\phi_i^w}{\partial r}\frac{\partial\phi_k^w}{\partial r}$$
$$\left.+\frac{2}{r}\left(\frac{\partial w_0}{\partial r}\right)\left(\frac{\partial w_0}{\partial\theta}\right)\frac{\partial\phi_i^w}{\partial\theta}\frac{\partial\phi_k^w}{\partial r}+\frac{2}{r}\left(\frac{\partial w_0}{\partial r}\right)\left(\frac{\partial w_0}{\partial\theta}\right)\frac{\partial\phi_i^w}{\partial r}\frac{\partial\phi_k^w}{\partial\theta}\right\}$$

$$+E_I\left\{r\frac{\partial^2\phi_i^w}{\partial r^2}\frac{\partial^2\phi_k^w}{\partial r^2}+\frac{1}{r}\frac{\partial\phi_i^w}{\partial r}\frac{\partial\phi_k^w}{\partial r}+\frac{1}{r^2}\frac{\partial\phi_i^w}{\partial r}\frac{\partial^2\phi_k^w}{\partial\theta^2}+\frac{1}{r^2}\frac{\partial^2\phi_i^w}{\partial\theta^2}\frac{\partial\phi_k^w}{\partial r}+\frac{1}{r^3}\frac{\partial^2\phi_i^w}{\partial\theta^2}\frac{\partial^2\phi_k^w}{\partial\theta^2}\right\}$$

$$+G_I\left\{\frac{4}{r}\frac{\partial^2\phi_i^w}{\partial r\partial\theta}\frac{\partial^2\phi_k^w}{\partial r\partial\theta}-\frac{4}{r^2}\frac{\partial\phi_i^w}{\partial\theta}\frac{\partial^2\phi_k^w}{\partial r\partial\theta}-\frac{4}{r^2}\frac{\partial^2\phi_i^w}{\partial r\partial\theta}\frac{\partial\phi_k^w}{\partial\theta}+\frac{4}{r^3}\frac{\partial\phi_i^w}{\partial\theta}\frac{\partial\phi_k^w}{\partial\theta}\right\}$$

$$+E_{PA}\left\{(u_0)\frac{\partial\phi_i^w}{\partial r}\frac{\partial\phi_k^w}{\partial r}+\left(\frac{\partial v_0}{\partial\theta}\right)\frac{\partial\phi_i^w}{\partial r}\frac{\partial\phi_k^w}{\partial r}+\frac{1}{r}\left(\frac{\partial u_0}{\partial r}\right)\frac{\partial\phi_i^w}{\partial\theta}\frac{\partial\phi_k^w}{\partial\theta}+\frac{1}{2r}\left(\frac{\partial w_0}{\partial r}\right)^2\frac{\partial\phi_i^w}{\partial\theta}\frac{\partial\phi_k^w}{\partial\theta}\right.$$
$$\left.+\frac{1}{2r}\left(\frac{\partial w_0}{\partial\theta}\right)^2\frac{\partial\phi_i^w}{\partial r}\frac{\partial\phi_k^w}{\partial r}+\frac{1}{r}\left(\frac{\partial w_0}{\partial r}\right)\left(\frac{\partial w_0}{\partial\theta}\right)\frac{\partial\phi_i^w}{\partial r}\frac{\partial\phi_k^w}{\partial\theta}+\frac{1}{r}\left(\frac{\partial w_0}{\partial r}\right)\left(\frac{\partial w_0}{\partial\theta}\right)\frac{\partial\phi_i^w}{\partial\theta}\frac{\partial\phi_k^w}{\partial r}\right\}$$

$$+E_{PI}\left\{\frac{\partial\phi_i^w}{\partial r}\frac{\partial^2\phi_k^w}{\partial r^2}+\frac{\partial^2\phi_i^w}{\partial r^2}\frac{\partial\phi_k^w}{\partial r}+\frac{1}{r}\frac{\partial^2\phi_i^w}{\partial r^2}\frac{\partial^2\phi_k^w}{\partial\theta^2}+\frac{1}{r}\frac{\partial^2\phi_i^w}{\partial\theta^2}\frac{\partial^2\phi_k^w}{\partial r^2}\right\}$$

$$\left.-E_{TA}\left\{r\frac{\partial\phi_i^w}{\partial r}\frac{\partial\phi_k^w}{\partial r}+\frac{1}{r}\frac{\partial\phi_i^w}{\partial\theta}\frac{\partial\phi_k^w}{\partial\theta}\right\}\right]|\mathbf{J}|\,d\xi\,d\mu. \qquad (2C.10)$$

Appendix 2D

Mass Matrix

The sub-matrices of $[\mathbf{M}]$, each of dimension $n \times n$, are as follows:

$$[\mathbf{M}] = \begin{bmatrix} [\mathbf{M}_{11}] & \mathbf{0} & \mathbf{0} \\ \mathbf{0} & [\mathbf{M}_{22}] & \mathbf{0} \\ \mathbf{0} & \mathbf{0} & [\mathbf{M}_{33}] \end{bmatrix}. \tag{2D.1}$$

The components of these sub-matrices are given below:

$$[\mathbf{M}_{11}] = \int_0^1 \int_0^1 \left[\rho_A r \phi_i^u \phi_k^u \right] |\mathbf{J}| \, d\xi \, d\mu, \tag{2D.2}$$

$$[\mathbf{M}_{22}] = \int_0^1 \int_0^1 \left[\rho_A r \phi_i^v \phi_k^v \right] |\mathbf{J}| \, d\xi \, d\mu, \tag{2D.3}$$

$$[\mathbf{M}_{33}] = \int_0^1 \int_0^1 \left[\rho_A r \phi_i^w \phi_k^w + \rho_I \left(r \frac{\partial \phi_i^w}{\partial r} \frac{\partial \phi_k^w}{\partial r} + \frac{1}{r} \frac{\partial \phi_i^w}{\partial \theta} \frac{\partial \phi_k^w}{\partial \theta} \right) \right] |\mathbf{J}| \, d\xi \, d\mu. \tag{2D.4}$$

Chapter 3

FREE VIBRATION BEHAVIOUR OF BFGM ROTATING MICRO-DISKS UNDER HIGH-TEMPERATURE THERMAL LOADING

3.1 Introduction

From the literature review, it is seen that the studies on the vibration behaviour of FGM rotating micro-/nano-plates based on various non-classical theories are very limited, and are found in Mahinzare et al. (2018a), Mahinzare et al. (2018b), Shojaeefard et al. (2018a) and Shojaeefard et al. (2018b). In all these works, the rotating plates are assumed to be supported at the outer edge. Hence, the typical clamped-free rotating disk-type problem of FGM micro-disks has not yet been studied. Furthermore, only the axisymmetric modes of vibration are considered in the above-mentioned works. In this chapter, the free vibration behaviour of clamped-free BFGM annular rotating micro-disks subjected to centrifugal loading due to constant rotational speed and thermal loading due to high-temperature operating environment has been studied. The effect of transverse pressure has been considered to be zero in this case. The mathematical model is developed based on the Kirchhoff plate theory and the MCST, and the governing equations are derived employing the principle of minimum total potential energy and Hamilton's principle. The governing equations are solved after discretization of the mid-plane displacements following Ritz method. In this problem, both axisymmetric and asymmetric behaviours have been studied for clamped-free micro-disks. After developing the model, a convergence study has been presented to assess the number of functions required for Ritz approximation. A number of comparison studies with standard available results have been undertaken for some reduced problems to successfully validate the mathematical model for this particular problem. The numerical results mostly in non-dimensional plane are presented in graphical and tabular form. The effects of rotational speed, thermal loading, size-dependent thickness, material gradation indices, radius ratio and FGM composition on the frequencies of vibration have been discussed. Four different metal-ceramic FGM

compositions namely, Stainless Steel/Silicon Nitride (SUS304/Si_3N_4), Stainless Steel/Alumina (SUS304/Al_2O_3), Stainless Steel/Zirconia (SUS304/ZrO_2) and Titanium Alloy/Zirconia (Ti-6Al-4V/ZrO_2) have been considered for presentation of results. Three-dimensional mode shape plots along with contour plots have also been presented to visualize the axisymmetric and asymmetric bending vibration modes as well as the torsional vibration mode.

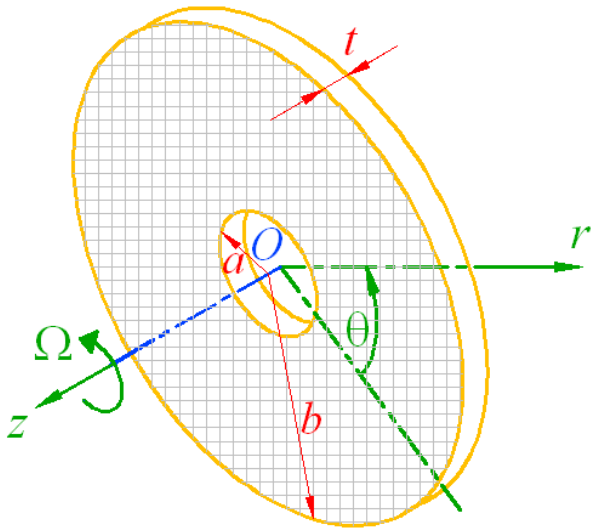

Fig. 3.1: Schematic diagram of a rotating disk.

3.2 Mathematical Background

A general mathematical model has already been presented in the preceding chapter. The present model can be obtained from the generalized mathematical model. The outline of the mathematical formulation has been provided here, to have better understanding of the subsequent sections of the present chapter.

A rotating micro-disk having inner radius a, outer radius b and constant thickness t is considered as shown in Fig. 3.1. The micro-size disk is made of metal-ceramic BFGM, which is graded along the radial and transverse directions, following Voigt rule involving power law. The parameters k_r and k_t symbolize the gradation indices along the radial and thickness directions respectively. The problem has been formulated using two steps. In the first step, the deformed configuration of the micro-disk under centrifugal loading due to constant rotational speed (Ω) and thermal loading $(\Delta T = T - T_0)$ due to uniform temperature

rise has been determined, where T and $T_0\left(=300\,\mathrm{K}\right)$ denote the present and constant stress-free temperatures respectively. In the second step, the free vibration response of the deformed micro-disk about its deformed configuration has been determined.

Using the Kirchhoff plate theory and the MCST, employing the principle of minimum total potential energy, and discretizing the mid-plane displacement fields following Ritz method, the governing equations for the first step have already been derived as Eq. (2.34), which is again given below:

$$\left[\mathbf{S}\right]\left\{\mathbf{c}\right\}=\left\{\mathbf{P}\right\}. \tag{3.1}$$

In Eq. (3.1), $\left[\mathbf{S}\right]$ is the total stiffness matrix (of dimension $3n\times 3n$, where n is the number of functions to discretize each of the displacement fields $\left\{u_0, v_0, w_0\right\}$) having classical $\left(\left[\mathbf{S}^{cl}\right]\right)$ and non-classical $\left(\left[\mathbf{S}^{ncl}\right]\right)$ parts; $\left\{\mathbf{c}\right\}$ is the vector of unknown coefficients c_j to be determined with reference to Eqs. (2.31a)-(2.31c); $\left\{\mathbf{P}\right\}$ is the load vector. The components of $\left[\mathbf{S}^{cl}\right]$ and $\left[\mathbf{S}^{ncl}\right]$ remain same as given in Appendix 2A. However, due to the absence of uniform transverse pressure, the components of the load vector $\left\{\mathbf{P}\right\}=\left\{\left\{\mathbf{P}_1\right\}\ \left\{\mathbf{P}_2\right\}\ \left\{\mathbf{P}_3\right\}\right\}^T$ for the present problem are reduced to the following form:

$$\left\{\mathbf{P}_1\right\}=\Omega^2\int_0^1\int_0^1\rho_A r^2\phi_i^u\left|\mathbf{J}\right|d\xi\, d\mu+\int_0^1\int_0^1 E_{TA}\left[\phi_i^u+r\frac{\partial\phi_i^u}{\partial r}\right]\left|\mathbf{J}\right|d\xi\, d\mu, \tag{3.2a}$$

$$\left\{\mathbf{P}_2\right\}=\int_0^1\int_0^1 E_{TA}\frac{\partial\phi_i^v}{\partial\theta}\left|\mathbf{J}\right|d\xi\, d\mu, \tag{3.2b}$$

$$\left\{\mathbf{P}_3\right\}=0. \tag{3.2c}$$

Eq. (3.1) provides a set of non-linear algebraic equations, which is solved employing Broyden's algorithm. It is to be mentioned that, for Ritz approximation, the functions, given for a CF disk in Table 2.3, is to be used for the present problem.

Employing Hamilton's principle, assuming harmonic vibration for the elastic system, and discretizing the space part of the displacement fields following Ritz method, the

governing equations for the second step have already been derived as Eq. (2.42), which is again given below:

$$\left[\left[\mathbf{K}\right]-\omega^2\left[\mathbf{M}\right]\right]\{\mathbf{d}\}=0. \tag{3.3}$$

Here $[\mathbf{K}]$ is the tangent stiffness matrix, the components of which are given in Appendix 2C; $[\mathbf{M}]$ is the mass matrix, the components of which are given in Appendix 2D; $\{\mathbf{d}\}$ is the set of unknown coefficients representing the dynamic displacements during the free vibration. The set of equations given by Eq. (3.3) is non-linear, which is linearized using the solution parameters $\{\mathbf{c}\}$ of the previous step to take into the effect of pre-stress induced due to centrifugal and thermal loading. For the eigenvalue problem given by Eq. (3.3), the square roots of the eigenvalues (ω^2) signify the frequencies of vibration of the deformed micro-disk, and the eigenvectors i.e., $\{\mathbf{d}\}$ represent the corresponding mode-shapes of vibration. The mode-shapes are obtained by appropriately substituting $\{\mathbf{d}\}$ into Eqs. (2.39a)-(2.39c).

Table 3.1: Material properties of the ceramic constituents at T_0 = 300 K.

Material Property	Silicon Nitride (Si_3N_4)	Zirconia (ZrO_2)	Alumina (Al_2O_3)
E_c^0 (GPa)	322.27	168.06	320.24
ν_c^0	0.240	0.298	0.260
ρ_c (kg/m^3)	2370	3000	3750

3.3 Results and Discussion

The non-dimensional speed (Ω^*) and frequency of vibration (ω^*) for the present problem are defined as follows (Das et al. (2010); Kermani et al. (2016); Shojaeefard et al. (2018b)):

$$\Omega^*=\Omega b^2\sqrt{\rho_c t/D}, \tag{3.4a}$$

$$\omega^*=\omega b^2\sqrt{\rho_c t/D}, \tag{3.4b}$$

where $D = E_c^0 t^3 \Big/ \left\{12\left(1-\left(\nu_c^0\right)^2\right)\right\}$.It is noted that the non-dimensional parameters are defined with reference to the property values of the ceramic phase of the FGM composition at $T_0\left(=300\,\mathrm{K}\right)$, which are calculated using the Touloukian model given by Eq. (2.6) and employing the temperature coefficients provided in Table 2.1. For the ceramic constituents, the mass density values, which are independent of temperature, are already listed in Table 2.2. However, the mass density $\left(\rho_c\right)$ values along with the values of the Young's modulus $\left(E_c^0\right)$ and Poisson's ratio $\left(\nu_c^0\right)$ for different ceramic constituents at T_0 used in the present analysis are provided in Table 3.1.

The bending or flexural mode shape is denoted by mode number (p,q), in which p represents the number of nodal circles and q represents the number of nodal diameters. The torsional mode is denoted by (T) which is contributed by v_0, the displacement field along the θ direction. It is to be noted that $(p,0)$ denotes an axisymmetric bending mode indicating the absence of nodal diameter (i.e., $q=0$). Further, the presence of one or more nodal diameters gives an asymmetric bending mode $(q\neq 0)$. For example, (1,1) implies an asymmetric bending mode with one nodal circle ($p=1$) and one nodal diameter ($q=1$). Further (1,0) implies an axisymmetric bending mode with one nodal circle ($p=1$) and without the presence any nodal diameter ($q=0$).

The present formulation is quite general in nature, and can be applied for a wide variety of problems by properly adjusting certain parameters as follows: the present model can be reduced to a plate model under non-rotating condition by putting the rotational speed Ω =0; the size-independent behaviour, which is applicable for a macro-size rotating disk, can be investigated by putting $l=0$; the problem of solid micro-plate clamped at the outer edge can be investigated by putting a =0, $\Omega=0$ and considering $\psi_1^u=\psi_1^v=\left(1-\xi\right);\ \psi_1^w=\left(1-\xi\right)^2$ as the lowest order admissible function for Ritz discretization; a radial-FG micro-disk/plate is obtained by putting $k_t=0$; a thickness-FG micro-disk/plate is obtained by putting $k_r=0$.

Unless otherwise specified, the numerical results for this chapter are represented for a Stainless Steel/Silicon Nitride BFGM micro-disk for the following values: l=17.6×10^{-6} m, $t/l=1, b/t=50$, $b/a=5$, $k_r=1$, $k_t=1$ and $\Delta T=300$. All the results are associated with the corresponding mode numbers.

Table 3.2: Non-dimensional frequency values for different number of functions.

$n=n_\xi \times n_\mu$							
3×3	4×4	5×5	6×6	7×7	8×8	9×9	10×10
6.403 (0,0)	6.360 (0,0)	6.356 (0,0)	6.355 (0,0)	6.355 (0,0)	6.354 (0,0)	6.354 (0,0)	6.354 (0,0)
8.061 (0,1)	7.986 (0,1)	7.974 (0,1)	7.971 (0,1)	7.970 (0,1)	7.970 (0,1)	7.970 (0,1)	7.970 (0,1)
12.764 (0,2)	12.687 (0,2)	12.666 (0,2)	12.658 (0,2)	12.656 (0,2)	12.654 (0,2)	12.654 (0,2)	12.654 (0,2)
30.776 (T)	21.733 (0,3)	21.722 (0,3)	21.715 (0,3)	21.712 (0,3)	21.711 (0,3)	21.711 (0,3)	21.711 (0,3)
36.047 (1,0)	30.560 (T)	30.507 (T)	30.496 (T)	30.494 (T)	30.494 (T)	30.493 (T)	30.493 (T)
40.531 (1,1)	35.462 (1,0)	34.701 (0,4)	34.696 (0,4)	34.695 (0,4)	34.694 (0,4)	34.693 (0,4)	34.693 (0,4)

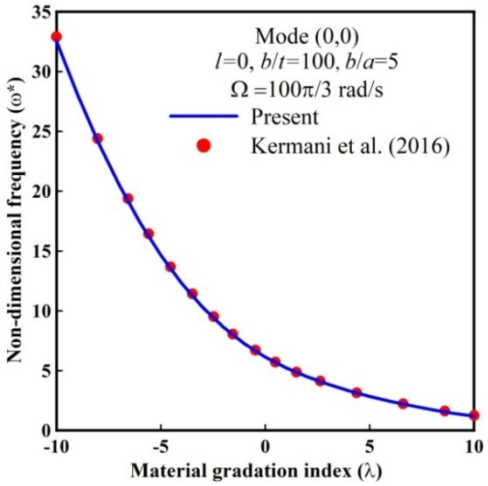

Fig. 3.2: Comparison of the variation of fundamental natural frequency with material gradation index for a radial-FG annular rotating disk based on the classical theory.

3.3.1 Convergence Study

As the governing equations are discretized following Ritz method, it is essential to decide the number of functions to be employed for generation of results. In this regard, a convergence

study has been conducted for the BFGM rotating annular micro-disk for the following values: l=17.6 μm (Lam et al. (2003); Park and Gao (2006)), $t/l=1, b/t=50$, $b/a=5$, $k_r=1$, $k_t=1$, $\Delta T=300$. Accordingly, the dimensions of the BFGM rotating annular micro-disk become: t =17.6 μm, b= 880 μm, a= 176 μm. Table 3.2 presents the results of the convergence study which are the non-dimensional frequencies of vibration for the first six modes for different values of $n\left(=n_\xi \times n_\mu\right)$. It can be seen from Eqs. (2.31a)-(2.31c) and Eqs. (2.32a)-(2.32c) that n is the total number of functions used to discretize each of the displacement fields $\{u_0, v_0, w_0\}$, and n_ξ and n_μ are the number of functions along ξ and μ directions respectively. Table 3.2 shows that a converged set of results are obtained for $n=8\times 8$ and above. Hence, this particular value of n has been used for generation of results.

3.3.2 Validation Study

The variation of fundamental natural frequency $\left(\omega^*\right)$ with material gradation index (λ) for a clamped-free radial-FG annular rotating disk is shown in Fig. 3.2based on the classical theory $(l=0)$. This figure shows a good matching between the present result and the result from Kermani et al.(2016). The plot is generated by considering dimensional speed $\Omega=100\pi/3$ rad/s, and the following property values: $E_f=3800e^{\lambda r/b}$ GPa, $\rho_f=380e^{\lambda r/b}$ kg/m^3, $\nu_f=0.3$ (constant).

Table 3.3: Comparison of the first two axisymmetric and asymmetric non-dimensional free vibration frequencies for a radial-FG (λ=1) annular non-rotating disk $(\Omega=0)$ based on the classical theory $(l=0)$ with $b/t=100$ and $b/a=5$.

Type	Mode	Present	Kermani et al. (2016)
Axisymmetric	(0,0)	4.23	4.24
	(1,0)	30.00	30.10
Asymmetric	(0,1)	3.81	3.81
	(1,1)	32.52	32.56

Another comparison with Kermani et al. (2016) is shown in Table 3.3 for the first two axisymmetric and asymmetric free vibration frequencies for the same disk (used for Fig. 3.2)under non-rotating condition $(\Omega = 0)$ and having λ=1. It also demonstrates excellent matching of the results.

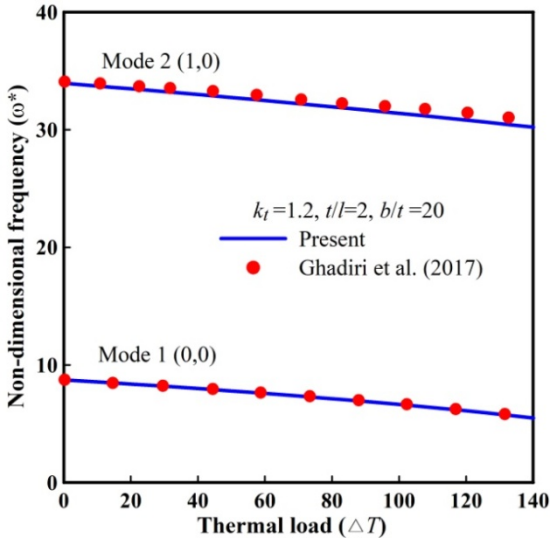

Fig. 3.3: Comparison of the first two axisymmetric free vibration frequencies under different thermal loadings for a thickness-FG solid circular clamped micro-plate.

The variation of the first two axisymmetric free vibration frequencies with thermal loading under uniform temperature rise is compared with that of Ghadiri et al. (2017) in Fig. 3.3 to validate the size-effect for a clamped (outer edge) thickness-FG $(k_t = 1.2)$ solid $(a = 0)$ micro-plate $(t/l = 2)$. The functional gradation is asymmetric all through the plate thickness and the plate is clamped at the outer circular edge $(r = b)$. The asymmetric gradation through the plate thickness is modeled by replacing $\left|\frac{2z}{t}\right|^{k_t}$ by $\left(\frac{z}{t}+\frac{1}{2}\right)^{k_t}$ and putting $k_r = 0$ in Eq. (2.5). Fig. 3.3 shows good matching of the results. Thus, the validity of the present model is established through the above comparisons.

3.3.3 Numerical Results for Different Parameters

Tables 3.4-3.19 illustrate the first four free vibration frequencies for various size-dependent thickness (t/l) values including that for a classical $(l = 0)$ rotating clamped-free micro-disk.

Each of these tables presents results for both $\Delta T = 0$ and 300. Tables 3.4-3.19 present the results for different rotational speed Ω^* and these values are: 0, 1, 2, 3, 4, 5, 6, 7, 8, 9, 10, 11, 12, 13, 14 and 15 respectively. The size-dependent thickness (t/l) is considered to study the effect of small-size. Smaller value of (t/l) signifies enhanced effect of small-size, and as the value of t/l increases, small-size effect diminishes. The collective observation from Tables 3.4 to 3.19 demonstrates a constant trend of increasing flexural vibration frequencies with the increase of speed due to centrifugal stiffening while all other parameters are kept constant. It should be noted that the stretching-flexural coupling involving von Kármán type non-linearity is used to introduce the centrifugal stiffening effect into the free vibration behaviour. However, it appears that the torsional vibration frequencies, which are manifested by the circumferential displacement field v_0, are independent of the rotational speed, and the reason is the lack of stretching-torsional coupling (i.e., coupling of axial-tangential displacements). The torsional vibration modes are evolved gradually at higher rotational speed. Additionally, each table shows a notable rise in the flexural vibration frequencies with decrease in t/l values because of the enhanced size-dependent stiffening effect when the disk thickness approaches the material length scale parameter (l) value. For the lower flexural modes, the size-effect decreases or nearly disappears as t/l approaches 10. The torsional vibration frequencies which appeared as the fourth mode as shown in Table 3.19 are observed to be mostly unaffected by the parameter t/l. The effect of thermal loading (ΔT) for the first mode is shown to be negligible, but for the higher modes, it becomes progressively relevant. The frequency values for the first two flexural modes are found to be lower at $\Delta T = 0$ and higher at $\Delta T = 300$. But for the higher flexural modes and the torsional mode, the frequency values are found to be higher at $\Delta T = 0$ and lower at $\Delta T = 300$, indicating prominent effect of thermo-elastic material degradation. Further, mode-switching is observed to occur between different sets of consecutive modes at higher speed ranges depending on the specific t/l values and thermal loading condition, although it is found absent in lower and medium speed ranges. For example, at speed $\Omega^* = 15$, as shown in Table 3.19, for $t/l = 5$, mode-switching takes place for the fourth mode where the flexural mode (0,3) is switched to the torsional mode as the

thermal loading changes from $\Delta T = 0$ to 300 K. Table 3.4-3.19 clearly indicates the role of the torsional mode in properly understanding the dynamic behaviour of rotating micro-disks, especially at higher rotational speeds and thermal loading condition.

Table 3.4: First four non-dimensional free vibration frequencies for different size-dependent thicknesses at $\Delta T = 0$ and 300, and $\Omega^* = 0$.

t/l	ΔT	Mode 1	Mode 2	Mode 3	Mode 4
1	0	4.04 (0,0)	5.79 (0,1)	10.51 (0,2)	19.97 (0,3)
	300	3.99 (0,0)	5.65 (0,1)	10.00 (0,2)	19.06 (0,3)
2	0	3.39 (0,0)	3.69 (0,1)	6.31 (0,2)	12.41 (0,3)
	300	3.45 (0,0)	3.71 (0,1)	5.96 (0,2)	11.81 (0,3)
5	0	2.83(0,1)	2.98(0,0)	4.26(0,2)	8.63(0,3)
	300	2.94 (0,1)	3.15 (0,0)	4.00 (0,2)	8.25 (0,3)
10	0	2.69 (0,1)	2.90(0,0)	3.84(0,2)	7.81(0,3)
	300	2.81 (0,1)	3.09 (0,0)	3.60 (0,2)	7.50 (0,3)
l=0 (classical)	0	2.64 (0,1)	2.87(0,0)	3.68(0,2)	7.49(0,3)
	300	2.76 (0,1)	3.06 (0,0)	3.46 (0,2)	7.22 (0,3)

Table 3.5: First four non-dimensional free vibration frequencies for different size-dependent thicknesses at $\Delta T = 0$ and 300, and $\Omega^* = 1.0$.

t/l	ΔT	Mode 1	Mode 2	Mode 3	Mode 4
1	0	4.16 (0,1)	5.89 (0,0)	10.62 (0,2)	20.07 (0,3)
	300	4.11 (0,0)	5.76 (0,1)	10.11 (0,2)	19.18 (0,3)
2	0	3.53 (0,0)	3.86 (0,1)	6.50 (0,2)	12.58 (0,3)
	300	3.59 (0,0)	3.88 (0,1)	6.15 (0,2)	11.99 (0,3)
5	0	3.05 (0,1)	3.13 (0,0)	4.53 (0,2)	8.87 (0,3)
	300	3.14 (0,1)	3.29 (0,0)	4.29 (0,2)	8.50 (0,3)
10	0	2.91 (0,1)	3.05 (0,0)	4.13 (0,2)	8.06 (0,3)
	300	3.02 (0,1)	3.23 (0,0)	3.92 (0,2)	7.77 (0,3)
l=0 (classical)	0	2.86 (0,1)	3.01 (0,0)	3.99 (0,2)	7.76 (0,3)
	300	2.98 (0,0)	3.21(0,1)	3.78(0,2)	7.50(0,3)

Table 3.6: First four non-dimensional free vibration frequencies for different size-dependent thicknesses at $\Delta T = 0$ and 300, and $\Omega^* = 2.0$.

t/l	ΔT	Mode 1	Mode 2	Mode 3	Mode 4
1	0	4.50 (0,0)	6.21 (0,1)	10.96 (0,2)	20.39 (0,3)
	300	4.46 (0,0)	6.08 (0,1)	10.47 (0,2)	19.51 (0,3)
2	0	3.90 (0,0)	4.32 (0,1)	7.03 (0,2)	13.08 (0,3)
	300	3.97 (0,0)	4.34 (0,1)	6.71 (0,2)	12.51 (0,3)
5	0	3.53 (0,0)	3.61 (0,1)	5.26 (0,2)	9.54 (0,3)
	300	3.69 (0,0)	3.70 (0,1)	5.05 (0,2)	9.21 (0,3)
10	0	3.45 (0,0)	3.50 (0,1)	4.92 (0,2)	8.80 (0,3)
	300	3.60 (0,1)	3.63 (0,0)	4.74 (0,2)	8.54 (0,3)
$l = 0$ (classical)	0	3.42 (0,0)	3.46 (0,1)	4.80 (0,2)	8.52 (0,3)
	300	3.56 (0,1)	3.61 (0,0)	4.63 (0,2)	8.29 (0,3)

Table 3.7: First four non-dimensional free vibration frequencies for different size-dependent thicknesses at $\Delta T = 0$ and 300 and $\Omega^* = 3.0$.

t/l	ΔT	Mode 1	Mode 2	Mode 3	Mode 4
1	0	5.02 (0,0)	6.70 (0,1)	11.49 (0,2)	20.91(0,3)
	300	4.98 (0,0)	6.58 (0,1)	11.03 (0,2)	20.06 (0,3)
2	0	4.44 (0,0)	5.00 (0,1)	7.83 (0,2)	13.86(0,3)
	300	4.52 (0,0)	5.01 (0,1)	7.55 (0,2)	13.34(0,3)
5	0	4.10 (0,0)	4.39 (0,1)	6.29 (0,2)	10.57(0,3)
	300	4.26(0,0)	4.47(0,1)	6.12(0,2)	10.29(0,3)
10	0	4.02 (0,0)	4.30 (0,1)	6.01 (0,2)	9.90 (0,3)
	300	4.21 (0,0)	4.39 (0,1)	5.86(0,2)	9.68 (0,3)
l=0 (classical)	0	4.00 (0,0)	4.27 (0,1)	5.91 (0,2)	9.66(0,3)
	300	4.19 (0,0)	4.36 (0,1)	5.77 (0,2)	9.46 (0,3)

Table 3.8: First four non-dimensional free vibration frequencies for different size-dependent thicknesses at $\Delta T = 0$ and 300, and $\Omega^* = 4.0$.

t/l	ΔT	Mode 1	Mode 2	Mode 3	Mode 4
1	0	5.65 (0,0)	7.33 (0,1)	12.20 (0,2)	21.62(0,3)
	300	5.63 (0,0)	7.22 (0,1)	11.77 (0,2)	20.80 (0,3)
2	0	5.10 (0,0)	5.81 (0,1)	8.84 (0,2)	14.90(0,3)
	300	5.18 (0,0)	5.83 (0,1)	8.59 (0,2)	14.41 (0,3)
5	0	4.77 (0,0)	5.29 (0,1)	7.50 (0,2)	11.87(0,3)
	300	4.93 (0,0)	5.36 (0,1)	7.35 (0,2)	11.62 (0,3)
10	0	4.70 (0,0)	5.21 (0,1)	7.26 (0,2)	11.27(0,3)
	300	4.89 (0,0)	5.29 (0,1)	7.14 (0,2)	11.09 (0,3)
$l = 0$ (classical)	0	4.68 (0,0)	5.18(0,1)	7.18 (0,2)	11.05(0,3)
	300	4.87 (0,0)	5.27 (0,1)	7.07 (0,2)	10.89 (0,3)

Table 3.9: First four non-dimensional free vibration frequencies for different size-dependent thicknesses at $\Delta T = 0$ and 300, and $\Omega^* = 5.0$.

t/l	ΔT	Mode 1	Mode 2	Mode 3	Mode 4
1	0	6.37 (0,0)	8.06 (0,1)	13.06 (0,2)	22.50 (0,3)
	300	6.35 (0,0)	7.97 (0,1)	12.65 (0,2)	21.71 (0,3)
2	0	5.83 (0,0)	6.71 (0,1)	9.98 (0,2)	16.12(0,3)
	300	5.91 (0,0)	6.72 (0,1)	9.76 (0,2)	15.68(0,3)
5	0	5.51 (0,0)	6.25 (0,1)	8.81 (0,2)	13.34(0,3)
	300	5.67 (0,0)	6.32 (0,1)	8.69 (0,2)	13.14(0,3)
10	0	5.44 (0,0)	6.19 (0,1)	8.61 (0,2)	12.81(0,3)
	300	5.62 (0,0)	6.26(0,1)	8.51(0,2)	12.66(0,3)
l=0 (classical)	0	5.42 (0,0)	6.16 (0,1)	8.54 (0,2)	12.61(0,3)
	300	5.61 (0,0)	6.24 (0,1)	8.44 (0,2)	12.49 (0,3)

Table 3.10: First four non-dimensional free vibration frequencies for different size-dependent thicknesses at $\Delta T = 0$ and 300, and $\Omega^* = 6.0$.

t/l	ΔT	Mode 1	Mode 2	Mode 3	Mode 4
1	0	7.13 (0,0)	8.88 (0,1)	14.04 (0,2)	23.53 (0,3)
	300	7.13 (0,0)	8.79 (0,1)	13.66 (0,2)	22.78 (0,3)
2	0	6.59 (0,0)	7.66 (0,1)	11.22 (0,2)	17.49 (0,3)
	300	6.69 (0,0)	7.67 (0,1)	11.03 (0,2)	17.10 (0,3)
5	0	6.28 (0,0)	7.25 (0,1)	10.18 (0,2)	14.95 (0,3)
	300	6.44 (0,0)	7.31 (0,1)	10.08 (0,2)	14.78 (0,3)
10	0	6.21 (0,0)	7.19 (0,1)	10.01 (0,2)	14.47 (0,3)
	300	6.39 (0,0)	7.26 (0,1)	9.92 (0,2)	14.35 (0,3)
$l = 0$ (classical)	0	6.20 (0,0)	7.17 (0,1)	9.95 (0,2)	14.30 (0,3)
	300	6.38 (0,0)	7.24 (0,1)	9.87 (0,2)	14.19 (0,3)

Table 3.11: First four non-dimensional free vibration frequencies for different size-dependent thicknesses at $\Delta T = 0$ and 300, and $\Omega^* = 7.0$.

t/l	ΔT	Mode 1	Mode 2	Mode 3	Mode 4
1	0	7.93 (0,0)	9.75 (0,1)	15.11 (0,2)	24.68(0,3)
	300	7.94 (0,0)	9.68 (0,1)	14.76 (0,2)	23.97 (0,3)
2	0	7.39 (0,0)	8.64(0,1)	12.52 (0,2)	18.99(0,3)
	300	7.48 (0,0)	8.66 (0,1)	12.35 (0,2)	18.64(0,3)
5	0	7.07 (0,0)	8.28 (0,1)	11.60 (0,2)	16.65(0,3)
	300	7.23 (0,0)	8.33 (0,1)	11.51 (0,2)	16.50 (0,3)
10	0	7.01 (0,0)	8.22(0,1)	11.45 (0,2)	16.21(0,3)
	300	7.19 (0,0)	8.28(0,1)	11.37(0,2)	16.11(0,3)
$l = 0$ (classical)	0	6.99 (0,0)	8.20 (0,1)	11.40 (0,2)	16.05 (0,3)
	300	7.17 (0,0)	8.27 (0,1)	11.32 (0,2)	15.97 (0,3)

Table 3.12: First four non-dimensional free vibration frequencies for different size-dependent thicknesses at $\Delta T = 0$ and 300, and $\Omega^* = 8.0$.

t/l	ΔT	Mode 1	Mode 2	Mode 3	Mode 4
1	0	8.75 (0,0)	10.67 (0,1)	16.26 (0,2)	25.95(0,3)
	300	8.76 (0,0)	10.60 (0,1)	15.94 (0,2)	25.28 (0,3)
2	0	8.19 (0,0)	9.65(0,1)	13.88 (0,2)	20.58(0,3)
	300	8.29 (0,0)	9.67 (0,1)	13.72 (0,2)	20.26 (0,3)
5	0	7.88 (0,0)	9.31 (0,1)	13.05(0,2)	18.41(0,3)
	300	8.03 (0,0)	9.36 (0,1)	12.96 (0,2)	18.28 (0,3)
10	0	7.81 (0,0)	9.26 (0,1)	12.91 (0,2)	18.01(0,3)
	300	7.99(0,0)	9.32 (0,1)	12.84 (0,2)	17.93 (0,3)
$l = 0$ (classical)	0	7.80 (0,0)	9.25 (0,1)	12.87 (0,2)	17.87(0,3)
	300	7.97 (0,0)	9.30 (0,1)	12.80 (0,2)	17.80 (0,3)

Table 3.13: First four non-dimensional free vibration frequencies for different size-dependent thicknesses at $\Delta T = 0$ and 300, and $\Omega^* = 9.0$.

t/l	ΔT	Mode 1	Mode 2	Mode 3	Mode 4
1	0	9.59 (0,0)	11.62 (0,1)	17.47 (0,2)	27.32 (0,3)
	300	9.60 (0,0)	11.56 (0,1)	17.17 (0,2)	26.68 (0,3)
2	0	9.01 (0,0)	10.67 (0,1)	15.27 (0,2)	2.24 (0,3)
	300	9.10 (0,0)	10.69 (0,1)	15.13 (0,2)	21.95 (0,3)
5	0	8.69 (0,0)	10.36 (0,1)	14.51 (0,2)	20.23 (0,3)
	300	8.85 (0,0)	10.41 (0,1)	14.43 (0,2)	20.11 (0,3)
10	0	8.63 (0,0)	10.31 (0,1)	14.39 (0,2)	19.86 (0,3)
	300	8.80 (0,0)	10.36(0,1)	14.32 (0,2)	19.78 (0,3)
$l = 0$ (classical)	0	8.61 (0,0)	10.30 (0,1)	14.35 (0,2)	19.73 (0,3)
	300	8.78 (0,0)	10.35 (0,1)	14.28 (0,2)	19.66 (0,3)

Table 3.14: First four non-dimensional free vibration frequencies for different size-dependent thicknesses at $\Delta T = 0$ and 300, and $\Omega^* = 10.0$.

t/l	ΔT	Mode 1	Mode 2	Mode 3	Mode 4
1	0	10.43 (0,0)	12.60 (0,1)	18.73 (0,2)	28.77(0,3)
	300	10.44 (0,0)	12.53 (0,1)	18.45 (0,2)	28.16 (0,3)
2	0	9.83 (0,0)	11.71 (0,1)	16.68 (0,2)	23.96 (0,3)
	300	9.93 (0,0)	11.72 (0,1)	16.55 (0,2)	23.69 (0,3)
5	0	9.51 (0,0)	11.41 (0,1)	15.99 (0,2)	22.07 (0,3)
	300	9.66 (0,0)	11.46 (0,1)	15.92 (0,2)	21.97 (0,3)
10	0	9.46 (0,0)	11.37 (0,1)	15.88 (0,2)	21.73 (0,3)
	300	9.62 (0,0)	11.42 (0,1)	15.81 (0,2)	21.67 (0,3)
l=0	0	9.44 (0,0)	11.35 (0,1)	15.84 (0,2)	21.61 (0,3)
(classical)	300	9.60 (0,0)	11.40 (0,1)	15.78 (0,2)	21.56 (0,3)

Table 3.15: First four non-dimensional free vibration frequencies for different size-dependent thicknesses at $\Delta T = 0$ and 300, and $\Omega^* = 11.0$.

t/l	ΔT	Mode 1	Mode 2	Mode 3	Mode 4
1	0	11.27 (0,0)	13.58 (0,1)	20.03 (0,2)	30.28 (0,3)
	300	11.29 (0,0)	13.53 (0,1)	19.77 (0,2)	29.71 (0,3)
2	0	10.66 (0,0)	12.75 (0,1)	18.12 (0,2)	25.73 (0,3)
	300	10.75 (0,0)	12.76 (0,1)	18.00 (0,2)	25.48 (0,3)
5	0	10.34 (0,0)	12.47 (0,1)	17.48 (0,2)	23.95 (0,3)
	300	10.48 (0,0)	12.51 (0,1)	17.41 (0,2)	23.86 (0,3)
10	0	10.28 (0,0)	12.43 (0,1)	17.37 (0,2)	23.63 (0,3)
	300	10.44 (0,0)	12.47 (0,1)	17.31 (0,2)	23.57 (0,3)
l= 0	0	10.26 (0,0)	12.41 (0,1)	17.34 (0,2)	23.52 (0,3)
(classical	300	10.42 (0,0)	12.46 (0,1)	17.28 (0,2)	23.47 (0,3)

Table 3.16: First four non-dimensional free vibration frequencies for different size-dependent thicknesses at $\Delta T = 0$ and 300, and $\Omega^* = 12.0$.

t/l	ΔT	Mode 1	Mode 2	Mode 3	Mode 4
1	0	12.12 (0,0)	14.59 (0,1)	21.36 (0,2)	31.86 (0,3)
	300	12.14 (0,0)	14.53 (0,1)	21.11 (0,2)	30.49 (T)
2	0	11.49 (0,0)	13.80 (0,1)	19.57 (0,2)	27.52 (0,3)
	300	11.58 (0,0)	13.81 (0,1)	19.46 (0,2)	27.29 (0,3)
5	0	11.17 (0,0)	13.53 (0,1)	18.97 (0,2)	25.85 (0,3)
	300	11.31 (0,0)	13.57 (0,1)	18.91 (0,2)	25.76 (0,3)
10	0	11.11 (0,0)	13.49 (0,1)	18.87 (0,2)	25.55 (0,3)
	300	11.26 (0,0)	13.53 (0,1)	18.82 (0,2)	25.49 (0,3)
$l = 0$ (classical)	0	11.09 (0,0)	13.48 (0,1)	18.84 (0,2)	25.44 (0,3)
	300	11.24 (0,0)	13.52 (0,1)	18.79 (0,2)	25.40 (0,3)

Table 3.17: First four non-dimensional free vibration frequencies for different size-dependent thicknesses at $\Delta T = 0$ and 300, and $\Omega^* = 13.0$.

t/l	ΔT	Mode 1	Mode 2	Mode 3	Mode 4
1	0	12.97 (0,0)	15.61 (0,1)	22.72 (0,2)	31.92 (T)
	300	12.98 (0,0)	15.56 (0,1)	22.49 (0,2)	30.49 (T)
2	0	12.32 (0,0)	14.85 (0,1)	21.03 (0,2)	29.35 (0,3)
	300	12.41 (0,0)	14.86 (0,1)	20.93 (0,2)	29.14 (0,3)
5	0	12.00 (0,0)	14.60 (0,1)	20.47 (0,2)	27.76 (0,3)
	300	12.13 (0,0)	14.63 (0,1)	20.41 (0,2)	27.68 (0,3)
10	0	11.94 (0,0)	14.56 (0,1)	20.38 (0,2)	27.48 (0,3)
	300	12.09 (0,0)	14.59 (0,1)	20.33 (0,2)	27.43 (0,3)
$l = 0$ (classical)	0	11.92 (0,0)	14.54 (0,1)	20.35 (0,2)	27.38 (0,3)
	300	12.07 (0,0)	14.58 (0,1)	20.30 (0,2)	12.07 (0,0)

Table 3.18: First four non-dimensional free vibration frequencies for different size-dependent thicknesses at $\Delta T = 0$ and 300, and $\Omega^* = 14.0$.

t/l	ΔT	Mode 1	Mode 2	Mode 3	Mode 4
1	0	13.81 (0,0)	16.63 (0,1)	24.10 (0,2)	31.92 (T)
	300	13.83 (0,0)	16.59 (0,1)	23.88 (0,2)	30.49 (T)
2	0	13.15 (0,0)	15.91 (0,1)	22.51 (0,2)	31.20 (0,3)
	300	13.24 (0,0)	15.92 (0,1)	22.41 (0,2)	30.52 (0,3)
5	0	12.83 (0,0)	15.66 (0,1)	21.98 (0,2)	29.69 (0,3)
	300	12.96 (0,0)	15.69 (0,1)	21.92 (0,2)	29.62 (0,3)
10	0	12.78 (0,0)	15.62 (0,1)	21.89 (0,2)	29.42 (0,3)
	300	12.91 (0,0)	15.66 (0,1)	21.84 (0,2)	29.37 (0,3)
$l = 0$ (classical)	0	12.76 (0,0)	15.61 (0,1)	21.86 (0,2)	29.33 (0,3)
	300	12.90 (0,0)	15.65 (0,1)	21.82 (0,2)	29.29 (0,3)

Table 3.19 First four non-dimensional free vibration frequencies for different size-dependent thicknesses at $\Delta T = 0$ and 300, and $\Omega^* = 15.0$.

t/l	ΔT	Mode 1	Mode 2	Mode 3	Mode 4
1	0	14.66 (0,0)	17.66 (0,1)	25.50 (0,2)	31.92 (0,3)
	300	14.68 (0,0)	17.62 (0,1)	25.29 (0,2)	30.49 (T)
2	0	13.98 (0,0)	16.97 (0,1)	23.99 (0,2)	31.95 (T)
	300	14.07 (0,0)	16.98 (0,1)	23.89 (0,2)	30.52 (T)
5	0	13.67 (0,0)	16.73 (0,1)	23.49 (0,2)	31.63 (0,3)
	300	13.79 (0,0)	16.76 (0,1)	23.43 (0,2)	30.53 (T)
10	0	13.61 (0,0)	16.69 (0,1)	23.41 (0,2)	31.38 (0,3)
	300	13.74 (0,0)	16.73 (0,1)	23.36 (0,2)	30.53 (T)
l=0 (classical)	0	13.59 (0,0)	16.68 (0,1)	23.38 (0,2)	31.29 (0,3)
	300	13.73 (0,0)	16.71 (0,1)	23.33 (0,2)	30.53 (T)

The mode shape and the corresponding contour plots for the first four modes are displayed in Figs. 3.4(a)-(d) and Figs. 3.5(a)-(d) for two different speeds $\Omega^*=12$ and $\Omega^*=15$ respectively for $t/l=2$. In Fig. 3.4, one symmetric mode and three different asymmetric modes are depicted, whereas in Fig. 3.5, one symmetric mode, two different asymmetric modes and the torsional mode are depicted. It is observed that the fourth mode changes from third asymmetric bending mode to the torsional mode (T) as the speed increases from 12 to 15.

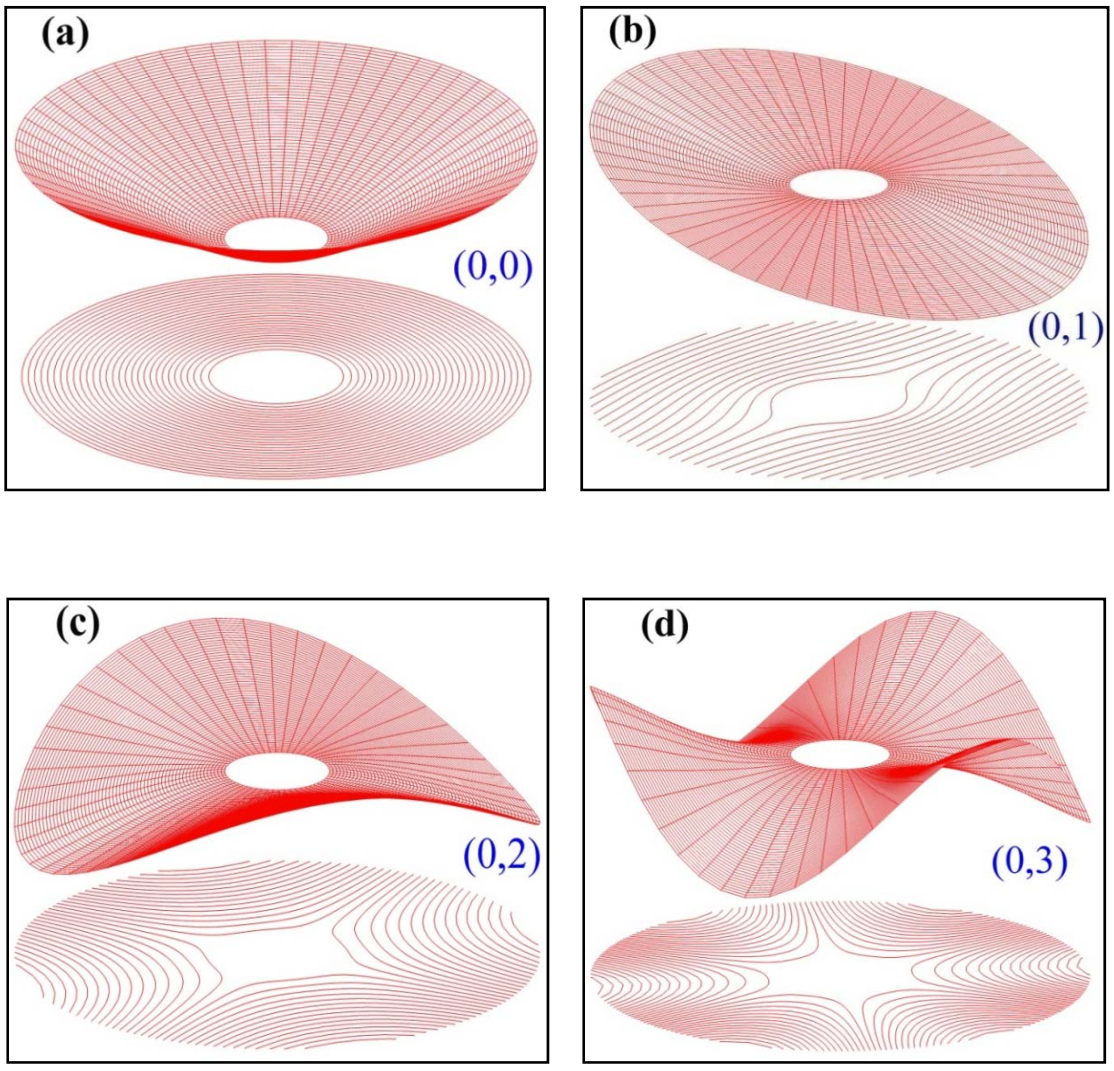

Fig. 3.4: Mode shape and contour plots for the first four modes for $t/l=2$ at $\Omega^*=12$: (a) Mode (0,0), (b) Mode (0,1), (c) Mode (0,2), (d) Mode (0,3).

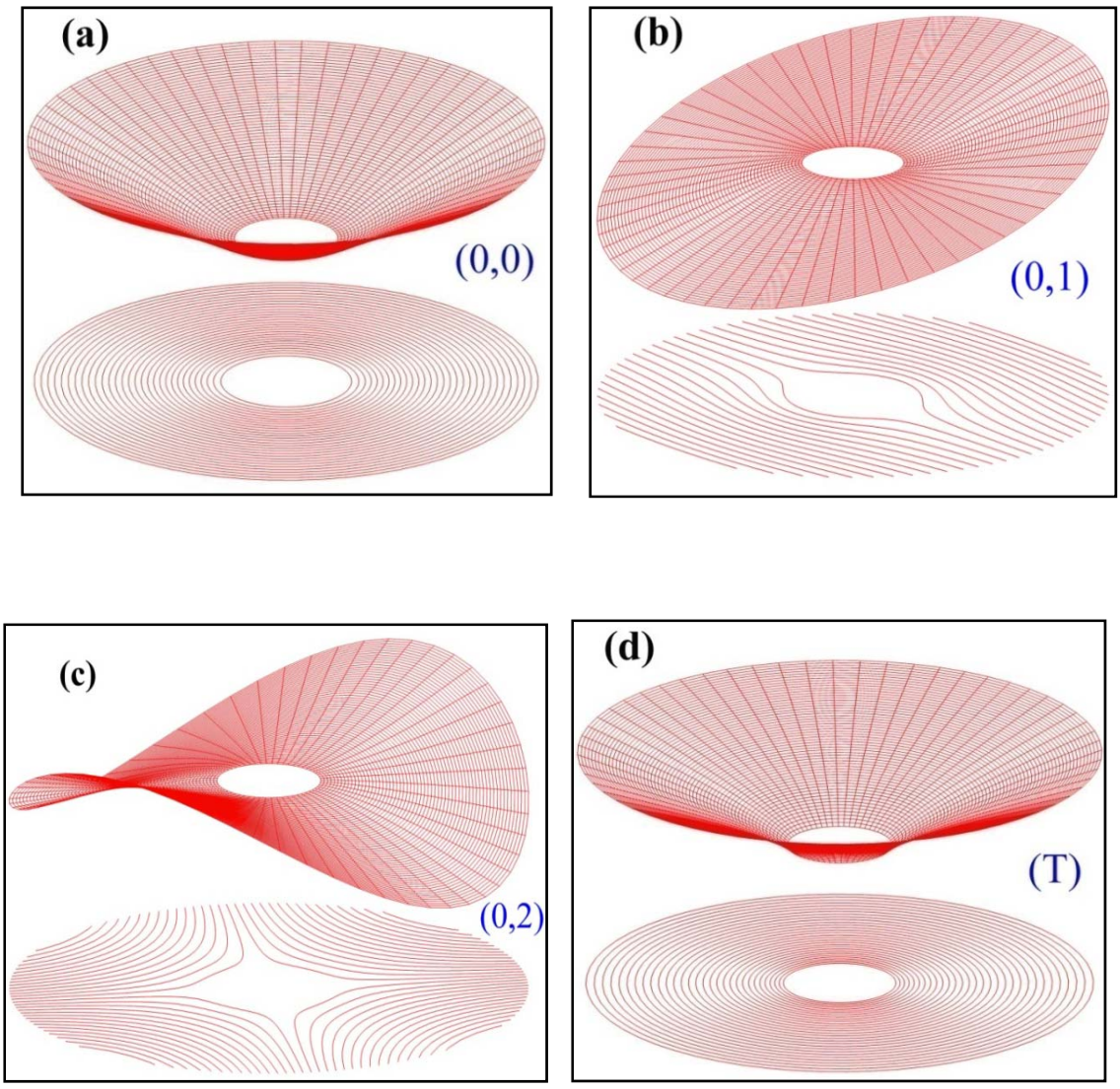

Fig. 3.5: Mode shape and contour plots for the first four modes for t/l=2 at $\Omega^* = 15$: (a) Mode (0,0), (b) Mode (0,1), (c) Mode (0,2), (d) Mode (T).

For the first four flexural vibration modes and the torsional mode, the non-dimensional speed-frequency behaviour is shown in Figs. 3.6(a)-(d) for various radial gradation indices (k_r), and in Figs. 3.7(a)-(d) for various thickness gradation indices (k_t). The constant

frequency values of the torsional modes, which are engaged in mode-switching with the preceding flexural modes, are also displayed in the relevant figures. The amount of metal volume fraction in the disk increases as either k_r or k_t or both are increased. Increasing k_r or k_t results in a drop in the frequency values for both the flexural and torsional modes as shown in the figures. This is because the metal (Stainless Steel) used in the current FGM composition is less elastically stiffer and heavier than its ceramic equivalent (Silicon Nitride). However, this effect becomes more and more predominant as the mode number becomes higher and higher. On the other hand, when the mode number increases, this impact of gradation indices gets more and more pronounced.

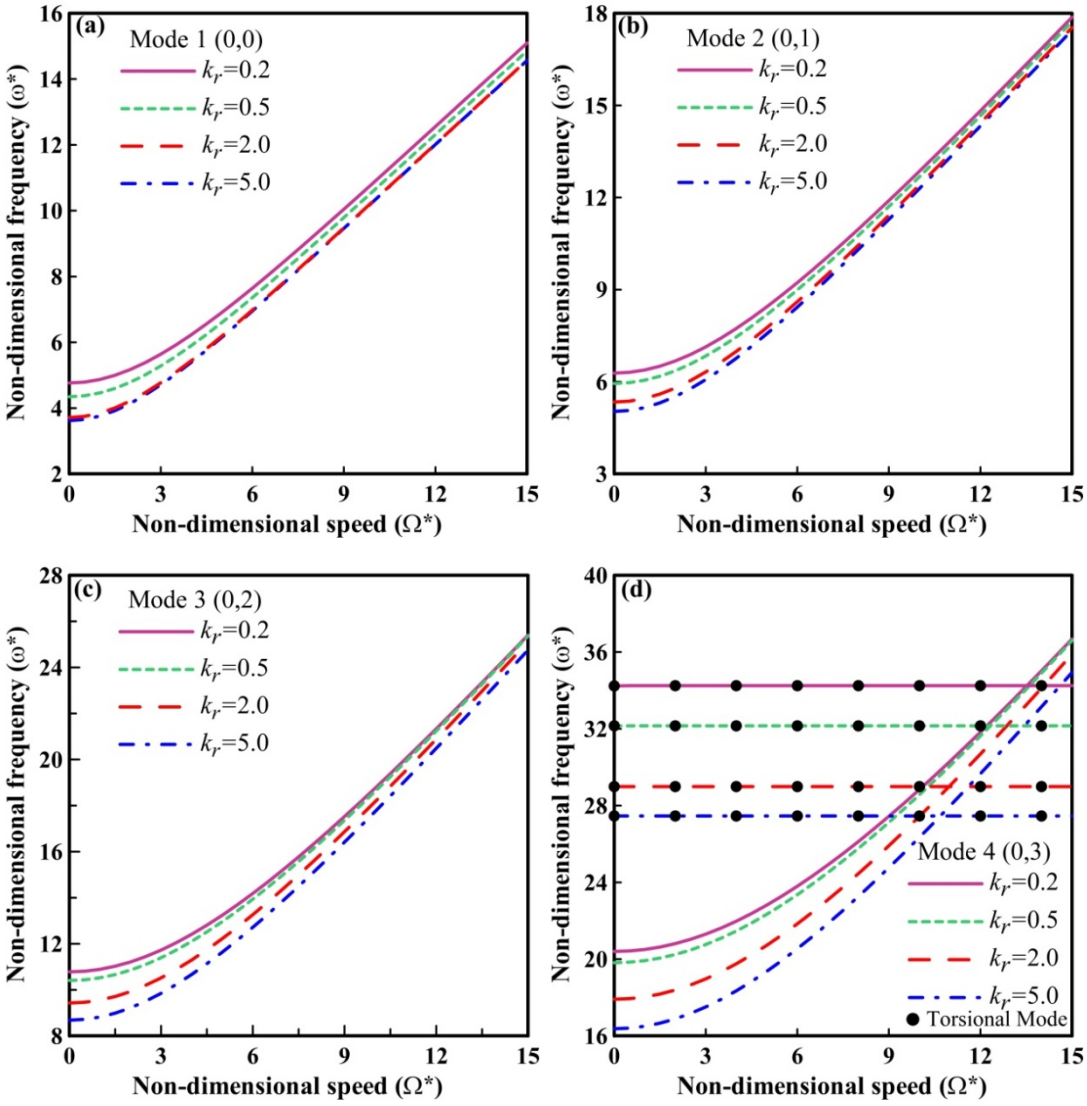

Fig.3.6: Effect of radial gradation index on the speed-frequency behaviour for the flexural modes and the torsional mode: (a) Mode 1, (b) Mode 2, (c) Mode 3, (d) Mode 4.

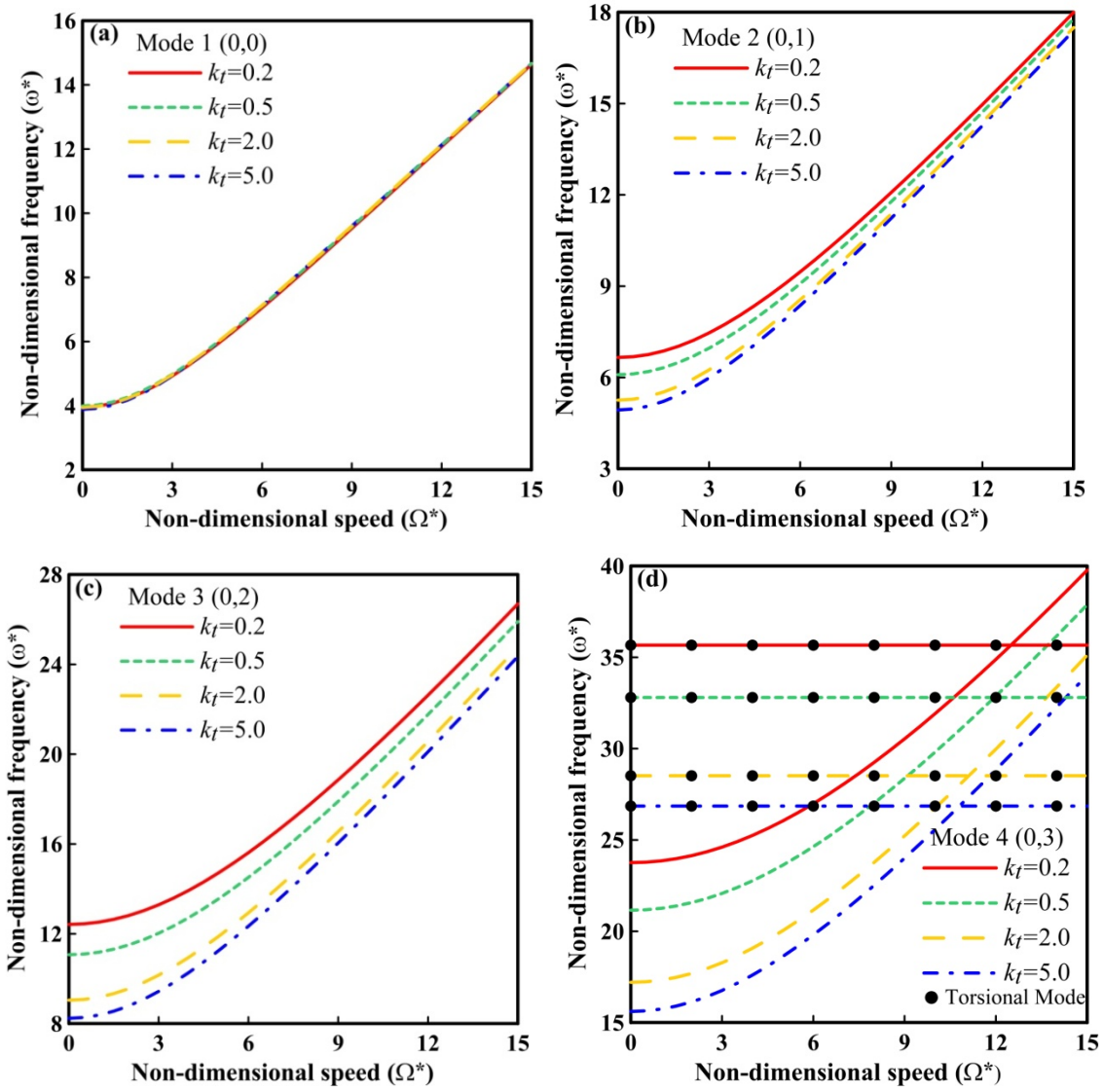

Fig.3.7: Effect of thickness gradation index on the speed-frequency behaviour for the flexural modes and the torsional mode: (a) Mode 1, (b) Mode 2, (c) Mode 3, (d) Mode 4.

The effect of radius ratio (b/a) is shown in Figs. 3.8(a)-(d) for the first four modes respectively. The torsional mode is also shown in Figs. 3.8(b) and (c) to depict its mode switching with the first (0,1) and second (0,2) asymmetric modes at different levels of speeds. Smaller annular dimensions are indicated by a decreasing b/a value, which makes the disk stiffer. As a result, for the first three modes (first axisymmetric and first two asymmetric

modes), a rise in the frequency is seen with a decrease in the b/a value. This tendency reverses for the fourth mode at higher value of b/a, which shows that the reduction of b/a relaxes the stiffening effect.

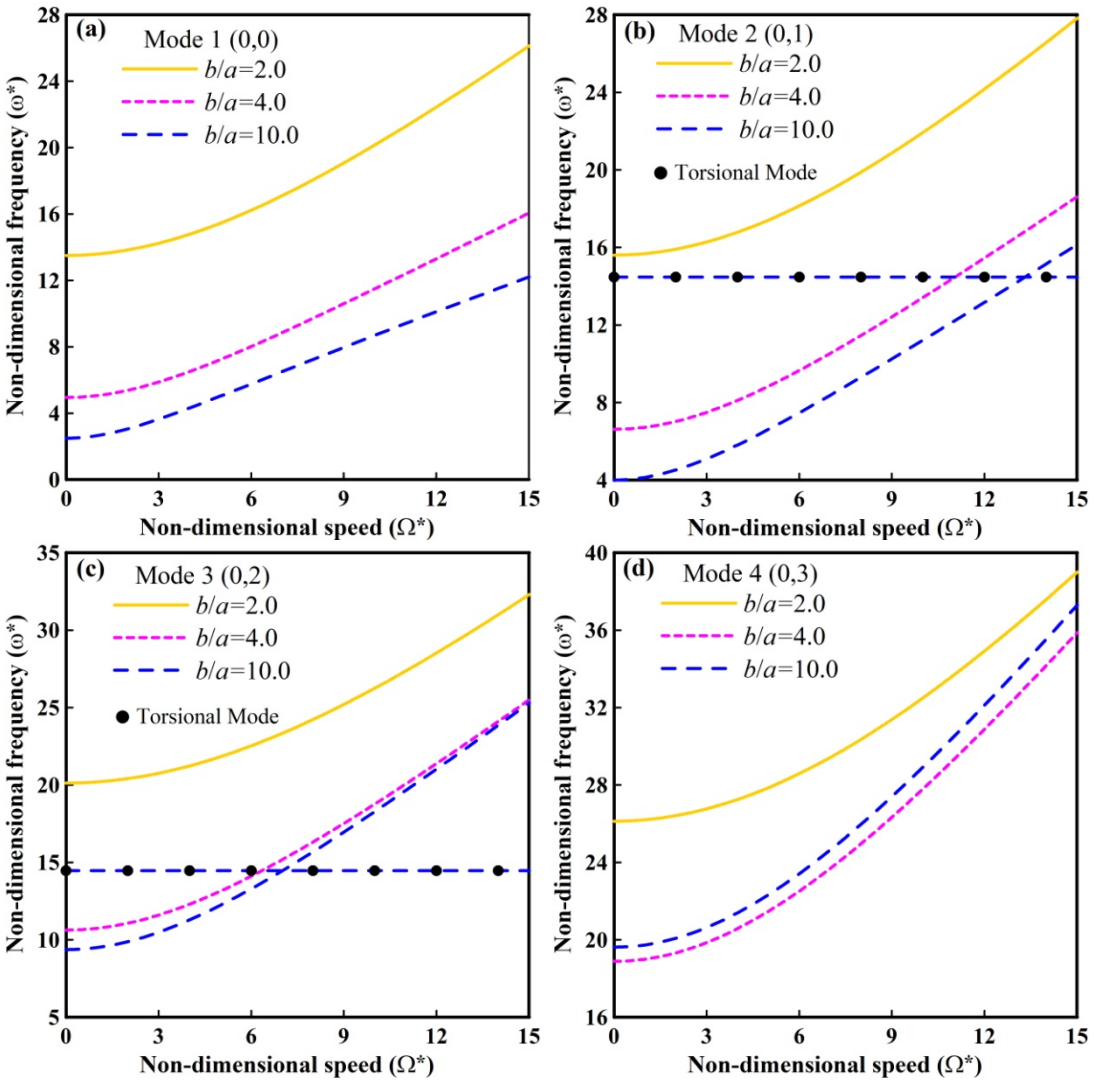

Fig.3.8: Effect of radius ratio on the speed-frequency behaviour for the flexural modes and the torsional mode: (a) Mode 1, (b) Mode 2, (c) Mode 3, (d) Mode 4.

The effect of thermal loading (ΔT) is shown in Figs. 3.9(a)-(d) for the first four flexural modes respectively and also for the torsional mode. For the first two modes, the impact of thermal loading is shown to be negligible, but for the higher modes, it becomes progressively relevant. However, the thermal effect has a major impact on the torsional mode, which is found to switch modes with the asymmetric (0,3) mode. That the frequency values

decrease as thermal loading rises, indicate to a significant role of thermo-elastic material degradation.

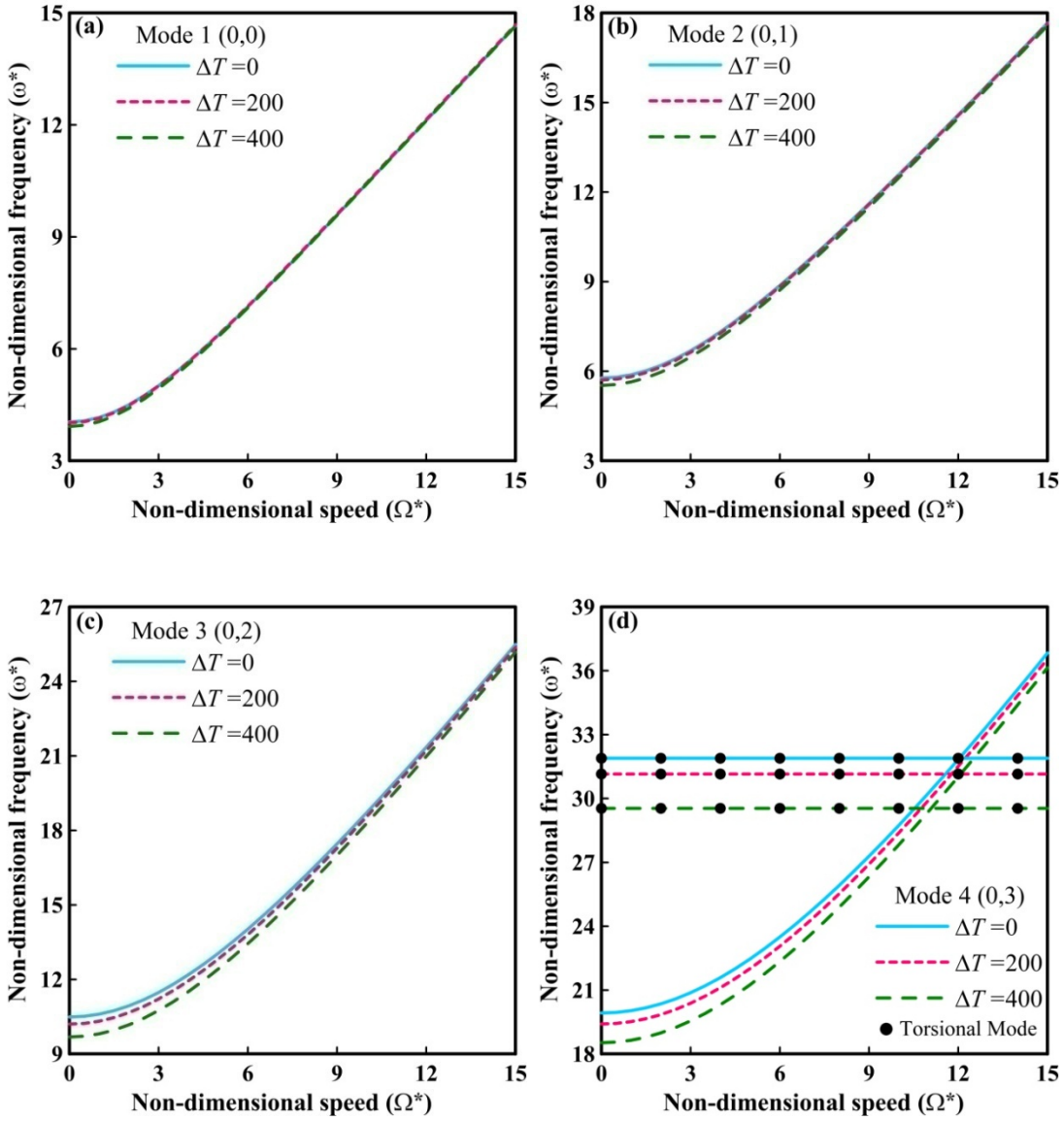

Fig.3.9: Effect of thermal loading on the speed-frequency behaviour for the flexural modes and the torsional mode: (a) Mode 1, (b) Mode 2, (c) Mode 3, (d) Mode 4.

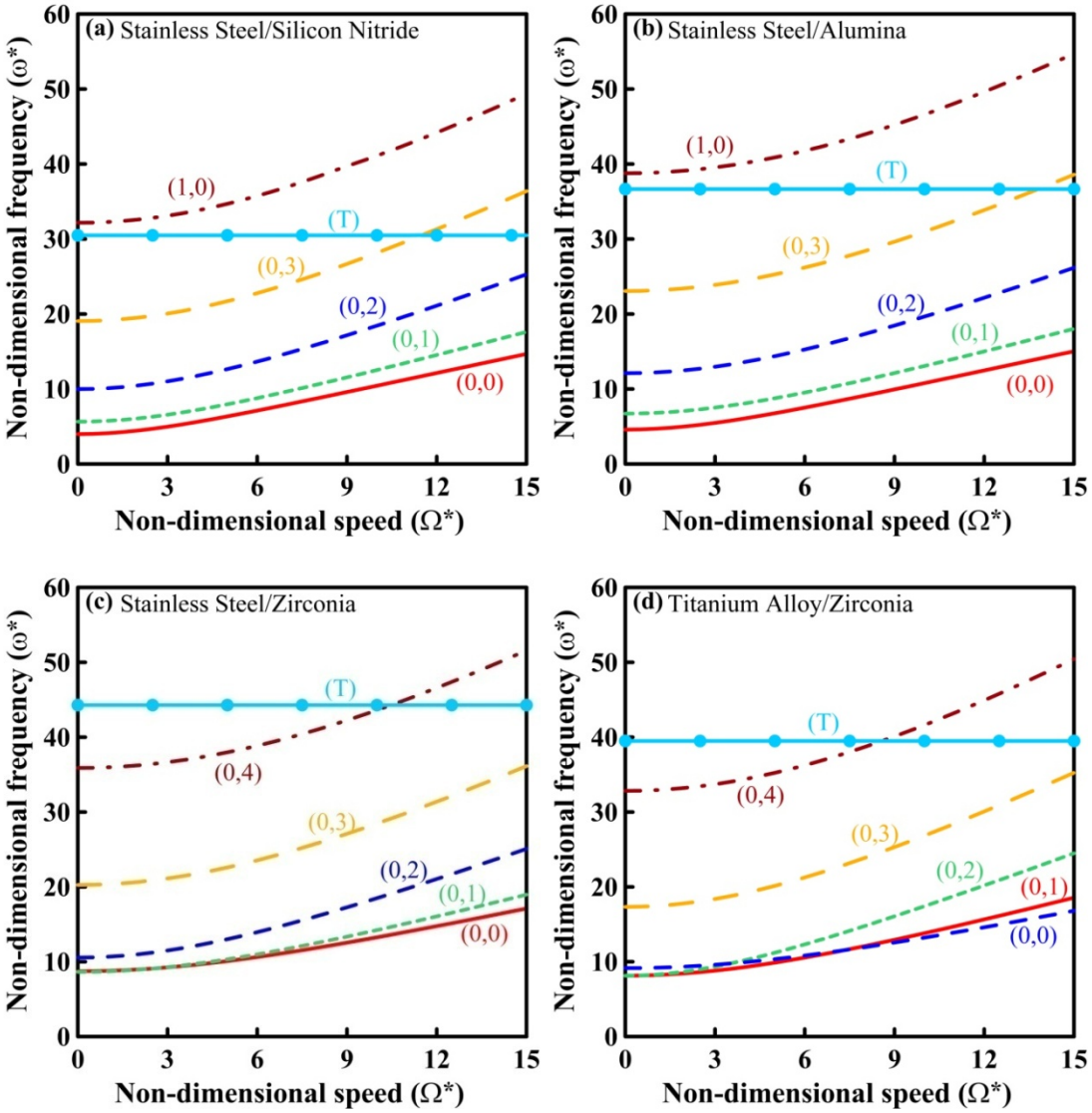

Fig. 3.10: Speed-frequency behaviour for the first five flexural modes and the torsional mode: (a) Stainless Steel/Silicon Nitride, (b) Stainless Steel/Alumina, (c) Stainless Steel/Zirconia, (d) Titanium Alloy/Zirconia.

The previous results are all presented for Stainless Steel/Silicon Nitride composition. To demonstrate the effect of different FGM compositions, Figs. 3.10(a)-(d) are presented for Stainless Steel/Silicon Nitride, Stainless Steel/Alumina, Stainless Steel/Zirconia and Titanium Alloy/Zirconia compositions respectively, each for the first five flexural modes and the torsional mode. Fig. 3.10 shows that the trends of the mode-specific speed-frequency behaviour for Stainless Steel/Silicon Nitride and Stainless Steel/Alumina compositions are similar, but they differ in the relative values. The behaviour of Stainless Steel/Zirconia and

Titanium Alloy/Zirconia compositions are different than the other two compositions. For Stainless Steel/Zirconia, mode-switching occurs between the first two flexural modes (modes (0,1) and (0,0)) at very low rotational speeds. For Titanium Alloy/Zirconia, mode-switching occurs between the first two asymmetric modes (modes (0,1) and (0,2)) at low rotational speeds, and then between the first axisymmetric and asymmetric modes (modes (0,0) and (0,1)) at slightly higher speed.

3.4 Chapter Summary

The free flexural and torsional vibration behaviour of a BFGM rotating annular micro-disk operating in a high-temperature environment is investigated. Using Kirchhoff plate theory and Ritz technique, an energy-based formulation is developed to address the size-effect while taking into account the MCST. The mathematical framework captures both the axisymmetric and asymmetric vibration behaviour for the BFGM rotating micro-disk problem. The non-dimensional speed-frequency behaviours are presented to investigate the effects of size-dependent thickness, radial and thickness gradation indices, radius ratio, thermal loading and FGM composition, for a wide range of parametric values. A few mode-shape plots along with their contour have been presented for visualization of the axisymmetric and asymmetric bending, and the torsional modes. The mathematical model is new of its kind. The results that are being presented are the first of their kind, and will act as a standard for further research in this domain. The key findings of this chapter are summarized below:

- Due to centrifugal stiffening, the flexural vibration frequencies increase with speed, but the torsional vibration frequency is found to be indifferent with the change of speed.
- Although it has a minor influence on the torsional mode, the size-dependent thickness has a significant stiffening effect on the flexural vibration frequencies.
- The flexural and torsional vibration frequencies are significantly influenced by the radial and thickness gradation indices, with the effects being more pronounced for the higher flexural modes. The vibration frequencies decrease with increase in the gradation indices.

- The vibration frequencies for the flexural modes are found to increase with decrease in the radius ratio for the first three modes, but this trend is reversed for the fourth bending mode for higher values of the radius ratio.
- The speed-frequency behaviour is found to be significantly affected by the high operating temperature only for the higher modes.

Chapter 4

FREE VIBRATION BEHAVIOUR OF BFGM ROTATING MICRO-DISKS SUBJECTED TO TRANSVERSE PRESSURE UNDER HIGH-TEMPERATURE THERMAL LOADING

4.1 Introduction

The preceding chapter studied the free vibration behaviour of BFGM annular rotating micro-disks subjected to centrifugal loading under high-temperature environment. A rotating disk may have to operate under high pressure and high temperature environment. To have basic understanding of the dynamic behaviour of the rotating disks under such situation, the free vibration behaviour of BFGM rotating annular disks subjected to uniform transverse pressure and operating at high-temperature environment needs to be studied. However, the literature review finds no such study related to this specific problem. Hence, in this chapter, the free vibration response of the clamped-free BFGM rotating micro-disks under transverse pressure and high-temperature thermal loading has been investigated. The mathematical model has been developed based on the Kirchhoff plate theory and the MCST. The governing equations are formulated employing the principle of minimum total potential energy and Hamilton's principle, and are solved after discretization of the mid-plane displacements following Ritz method. In this problem, both axisymmetric and asymmetric modes as well as the torsional mode has been studied for a clamped-free micro-disk. The validity of the mathematical model for this particular problem has been established through a number of comparison studies with some standard available results. The numerical results are presented as graphs and tables. The effects of rotational speed, transverse pressure, thermal loading, size-dependent thickness, material gradation indices, radius ratio and FGM composition on the frequencies of vibration have been discussed. Four different metal-ceramic FGM compositions namely, Stainless Steel/Silicon Nitride (SUS304/Si_3N_4), Stainless Steel/Alumina (SUS304/Al_2O_3), Stainless

Steel/Zirconia (SUS304/ZrO_2) and Titanium Alloy/Zirconia (Ti-6Al-4V/ZrO_2) have been considered for presentation of results. Three-dimensional mode shape plots along with contour plots have also been presented.

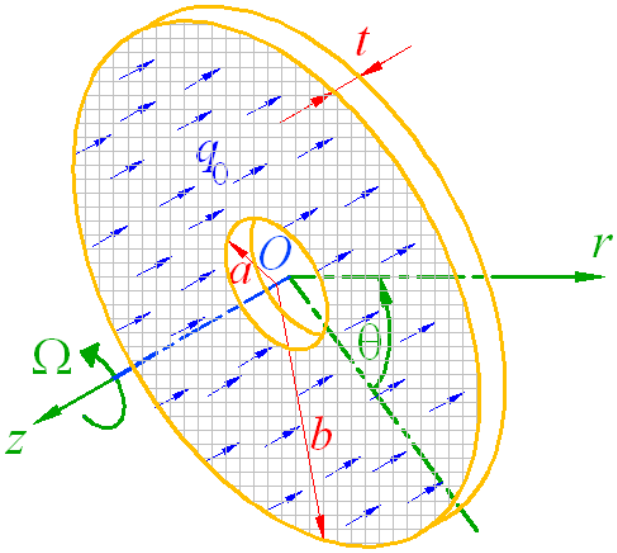

Fig. 4.1: Schematic diagram of a rotating disk under uniform transverse pressure.

4.2 Mathematical Background

The general mathematical model has already been presented in the second chapter. To address the present problem, no simplification is needed with regard to the model presented in the second chapter, because the generalized mathematical model fully describes the present problem. Hence the entire generalized formulation is applicable for the present problem. However, to have better understanding of the subsequent sections of the present chapter, the outline of the mathematical formulation has been provided here.

A rotating micro-disk having inner radius a, outer radius b and constant thickness t is considered as shown in Fig. 4.1. The disk is made of metal-ceramic BFGM, which is graded along the radial and transverse directions, following Voigt rule involving power law. The parameters k_r and k_t symbolize the gradation indices along the radial and thickness directions respectively. The micro-disk is assumed to be rotating with uniform angular speed Ω, and subjected to uniform transverse pressure of intensity q_0 and thermal loading in the form of a uniform temperature rise $\Delta T = T - T_0$, where T and $T_0\,(=300\,\mathrm{K})$ denote the present and constant stress-free temperatures respectively. The problem has been formulated using two

steps. In the first step, the configuration of the micro-disk under centrifugal loading, uniform transverse pressure and high-temperature environment has been determined. In the second step, the free vibration response of the deformed micro-disk about its deformed configuration has been determined in the frequency domain.

Using Kirchhoff plate theory and the MCST, employing the principle of minimum total potential energy, and discretizing the mid-plane displacement fields following Ritz method, the governing equations for the first step have already been derived as Eq. (2.34), which is again given below:

$$[\mathbf{S}]\{\mathbf{c}\} = \{\mathbf{P}\}. \tag{4.1}$$

In Eq. (4.1), $[\mathbf{S}]\left(=\left[\mathbf{S}^{cl}\right]+\left[\mathbf{S}^{ncl}\right]\right)$ is the total stiffness matrix (of dimension $3n\times 3n$, where n is the number of functions to discretize each of the mid-plane displacement fields $\{u_0, v_0, w_0\}$) ; $\left[\mathbf{S}^{cl}\right]$ and $\left[\mathbf{S}^{ncl}\right]$ are the classical and non-classical parts of $[\mathbf{S}]$; $\{\mathbf{c}\}$ is the vector of unknown coefficients c_j to be determined with reference to Eqs. (2.31a)-(2.31c); $\{\mathbf{P}\}$ is the load vector. The components of $\left[\mathbf{S}^{cl}\right]$, $\left[\mathbf{S}^{ncl}\right]$ and $\{\mathbf{P}\}$ remain same as given in Appendix 2A. Eq. (4.1) presents a set of non-linear algebraic equations, which is solved employing Broyden's method. For Ritz discretization, the functions given for CF disks as given in Table 2.3, is to be used for the present problem.

Employing Hamilton's principle, assuming harmonic vibration for the elastic system, and discretizing the space part of the displacement fields following Ritz method, the governing equations for the second step have already been derived as Eq. (2.42), which is again given below:

$$\left[[\mathbf{K}]-\omega^2[\mathbf{M}]\right]\{\mathbf{d}\} = 0. \tag{4.2}$$

Here $[\mathbf{K}]$ is the tangent stiffness matrix, the components of which are given in Appendix 2C; $[\mathbf{M}]$ is the mass matrix, the components of which are given in Appendix 2D; $\{\mathbf{d}\}$ is the set of unknown coefficients representing the dynamic displacements during the free vibration. Eq. (4.2) represents an eigenvalue problem, which is solved using a standard eigen-solver. Eq. (4.2) is non-linear but is linearized using the solution parameters $\{\mathbf{c}\}$ of the previous step to

take into the effect of pre-stress induced due to centrifugal, transverse pressure and thermal loading. The square roots of the eigenvalues $\left(\omega^2\right)$ signify the frequencies of vibration of the deformed micro-disk, and the eigenvectors i.e., $\{\mathbf{d}\}$ represent the corresponding mode-shapes of vibration. The mode-shapes are obtained by appropriately substituting $\{\mathbf{d}\}$ into Eqs. (2.39a)-(2.39c).

4.3 Results and Discussion

The non-dimensional speed $\left(\Omega^*\right)$, pressure $\left(p^*\right)$ and frequency of vibration $\left(\omega^*\right)$ for the present problem are defined as follows (Das et al. (2010); Kermani et al. (2016); Shojaeefard et al. (2018b)):

$$\Omega^* = \Omega b^2 \sqrt{\rho_c t / D}, \tag{4.3a}$$

$$p^* = q_0 b^4 / \left(E_c^0 t^4\right), \tag{4.3b}$$

$$\omega^* = \omega b^2 \sqrt{\rho_c t / D}, \tag{4.3c}$$

where $D = E_c^0 t^3 \Big/ \left\{12\left(1-\left(\nu_c^0\right)^2\right)\right\}$. It is noted that the non-dimensional parameters, defined in Eqs. (4.3a)-(4.3c) are defined with reference to the property values of the ceramic phase of the FGM composition at $T_0\left(=300\,\mathrm{K}\right)$. These property values are calculated using the Touloukian model given by Eq. (2.6),and employing the temperature coefficients provided in Table 2.1. The values of the Young's modulus $\left(E_c^0\right)$, Poisson's ratio $\left(\nu_c^0\right)$ and mass density $\left(\rho_c\right)$ for different ceramic constituents at T_0 used in the present analysis are provided in Table 4.1. It is noted that the mass density is independent of temperature.

The bending or flexural mode-shape is denoted by mode number $\left(p,q\right)$ in which p represents the number of nodal circles and q represents the number of nodal diameters. The torsional mode is denoted by (T) which is contributed by v_0 which is the mid-plane displacement field along the θ direction. It is to be noted that $\left(p,0\right)$ denotes an axisymmetric

bending mode indicating the absence of nodal diameter(s). Further, the presence of one or more nodal diameters generates an asymmetric bending mode $(q \neq 0)$.

Table 4.1: Material properties of the ceramic constituents at T_0 = 300 K.

Material Property	Silicon Nitride (Si_3N_4)	Zirconia (ZrO_2)	Alumina (Al_2O_3)
E_c^0 (GPa)	322.27	168.06	320.24
ν_c^0	0.240	0.298	0.260
ρ_c (kg/m^3)	2370	3000	3750

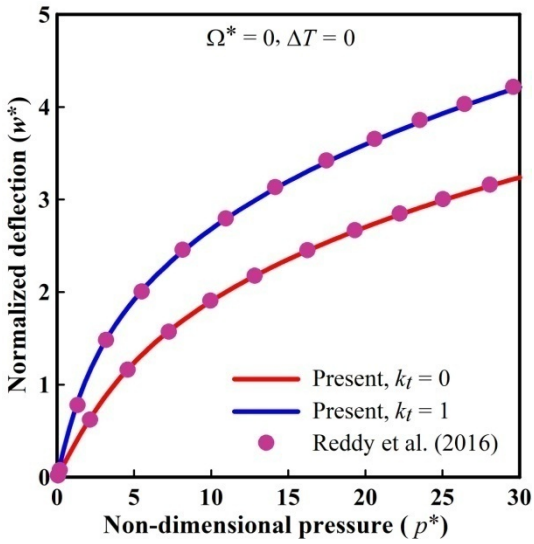

Fig. 4.2: Comparison of non-dimensional pressure versus deflection behaviour of a thickness-FG annular clamped-free micro-plate.

The present formulation is quite general in nature and can be applied for a wide variety of problems by properly adjusting certain parameters as follows: the present model can be reduced to a plate model under non-rotating condition by putting the rotational speed $\Omega = 0$; the size-independent behaviour, which is applicable for a macro-size rotating disk, can be investigated by putting $l = 0$; the problem of solid micro-plate clamped at the outer edge can be investigated by putting a =0, $\Omega = 0$ and considering $\psi_1^u = \psi_1^v = (1-\xi)$; $\psi_1^w = (1-\xi)^2$ as the lowest order admissible function for Ritz discretization; a radial-FG micro-disk/plate is obtained by putting $k_t = 0$; a thickness-FG micro-disk/plate is obtained by putting $k_r = 0$.

Unless otherwise mentioned, the numerical results for this chapter are generated for a Stainless Steel/Silicon Nitride BFGM micro-disk using the following values of the parameters: l =17.6×10^{-6} m (Lam et al. (2003); Park and Gao (2006)), t/l =1, b/t = 40, b/a =7.5, $k_r = k_t = 1$, Ω^* =10, p^* =5 and ΔT =300.Accordingly, the dimensions of the BFGM rotating annular micro-disk become: t =17.6 μm, b =704 μm, a =93.87 μm. Based on the convergence study reported in Table 3.2, the number of functions for Ritz approximation has been taken as $n = 8 \times 8$ for generation of results.

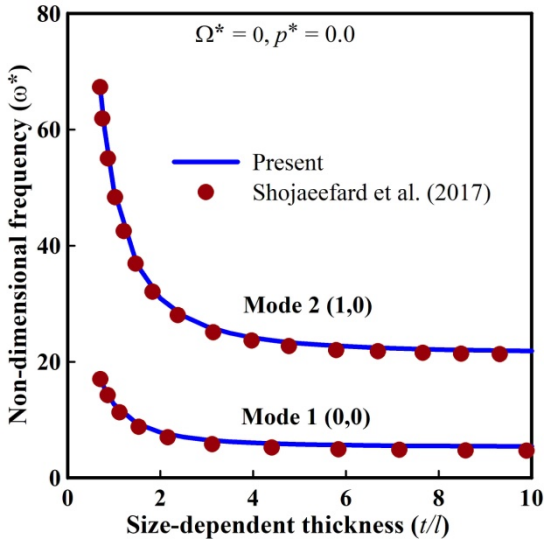

Fig. 4.3: Comparison showing variation of non-dimensional vibration frequency with size-dependent thickness under thermal loading for the first two axisymmetric modes of a thickness-FG solid circular clamped micro-plate.

4.3.1 Validation Study

The load-deflection behaviour of a thickness-FG $(k_r = 0)$ annular and clamped-free micro-plate under uniform transverse pressure has been compared with Reddy et al. (2016) in Fig. 4.2 for different values of k_t, where the normalized deflection (w^*) is given by $w^* = w_{max}/t$. The results for this comparison are generated considering the following relation: $E_f(z) = E_2 + (E_1 - E_2)\left(\frac{z}{t} + \frac{1}{2}\right)$, and with the following values: E_1=10^6 N/m^2, E_2=10^5 N/m^2, ν_f =0.25, t =0.1×10^{-6} m, l/t = 0.6, b/t = 10, b/a = 4, Ω^* = 0 and ΔT = 0. The results exhibit excellent conformity.

The variation of vibration frequency for the first two axisymmetric modes with size-dependent thickness (t/l) of a thickness-FG $(k_r=0, k_t=2)$ solid circular $(a=0)$ clamped micro-plate has been compared with Shojaeefard et al. (2017) in Fig. 4.3. The results in Fig. 4.3 correspond to Stainless Steel/Silicon Nitride plate under non-linear through-thickness temperature variation given by: $T(z)=300+40\left(\frac{z}{t}+\frac{1}{2}\right)^{0.9}$ K. The results of Fig. 4.3 are generated considering asymmetric functional gradation, by using the following in Eq. (2.5): $R_f(z,T)=R_m(T)+\{R_c(T)-R_m(T)\}\left(\frac{z}{t}+\frac{1}{2}\right)^{k_t}$, and with the following values: $l=17.6\times10^{-6}$ m, $b/t=20$, $\Omega^*=0$, $p^*=0$. Fig. 4.3 also shows excellent matching of the results.

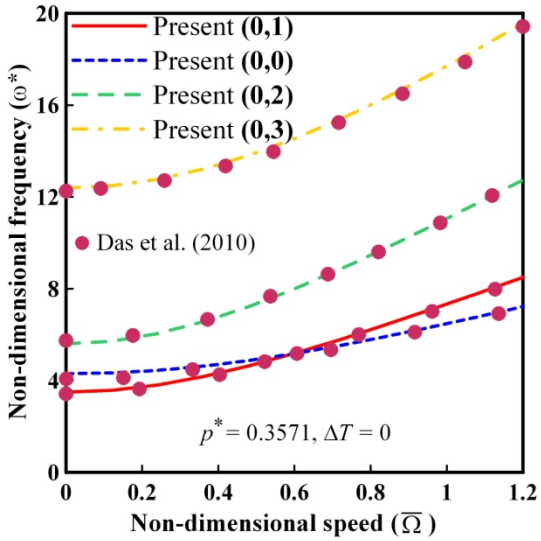

Fig. 4.4: Comparison of non-dimensional speed versus frequency behaviour under uniform transverse pressure for the first four modes of a homogeneous annular rotating disk.

The variation in vibration frequency with rotational speed for the first four modes of a classical $(l=0)$ homogeneous $(k_r=0, k_t=0)$ annular rotating disk, subjected to uniform transverse pressure, has been compared with Das et al. (2010). The comparison is shown in Fig. 4.4. The non-dimensional speed $\overline{\Omega}$ in Fig. 4.4 is defined as $\overline{\Omega}=\Omega b\sqrt{\rho/\sigma_y}$, and the results are generated with the following values: $l=0$, $E=210\times10^9$ N/m^2, $\nu=0.3$, $\rho=7850$

kg/m^3, σ_y=300×10^6 N/m^2, t=0.006 m, b/t= 50, b/a=12, p^*=0.3571 and ΔT=0. The comparison shows great matching for both the axisymmetric and asymmetries modes. Figs. 4.2-4.4 clearly validate the accuracy of the present mathematical model.

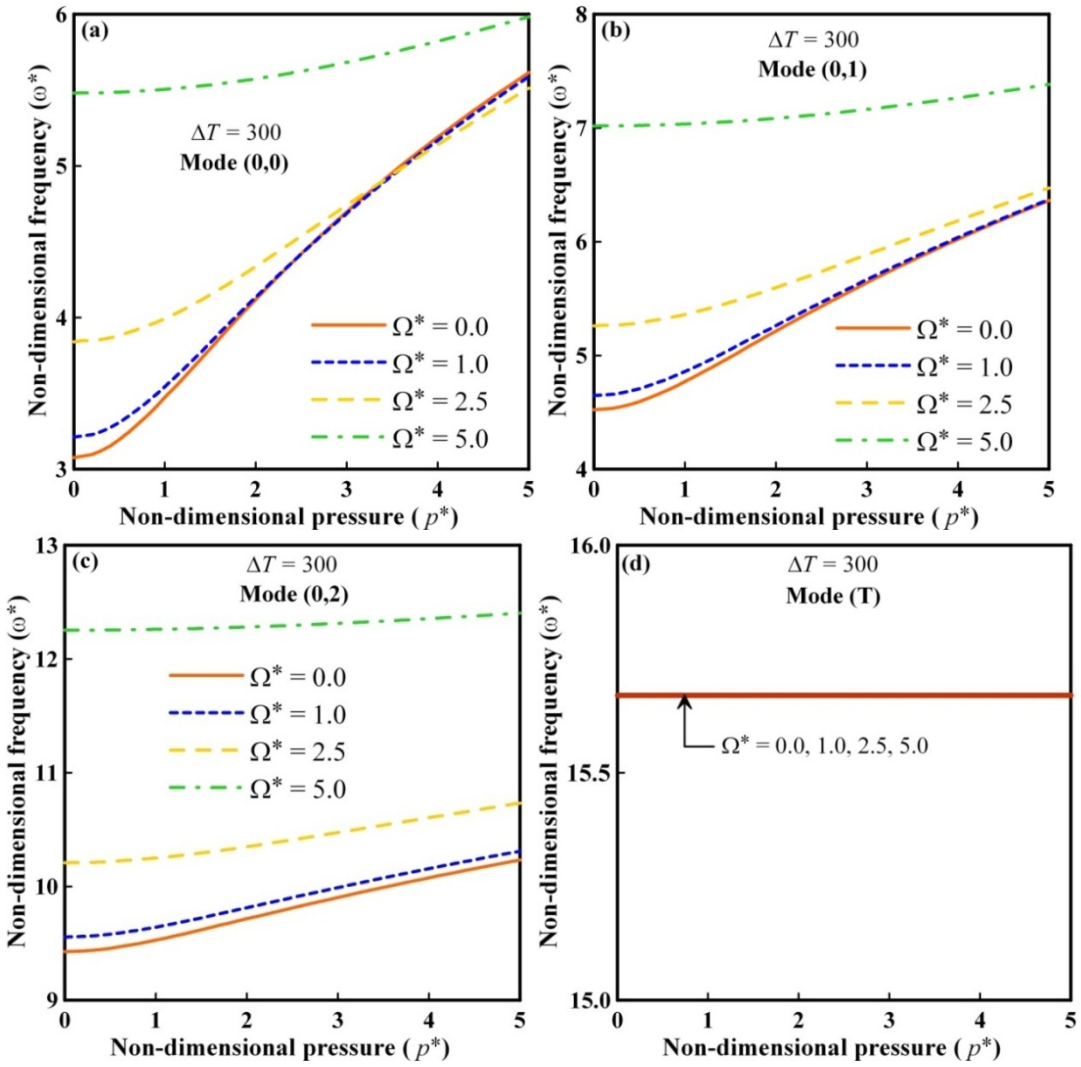

Fig. 4.5: Variation of vibration frequency with transverse pressure for different rotational speed under constant thermal loading: (a) Mode 1, (b) Mode 2, (c) Mode 3, (d) Mode 4.

4.3.2 Numerical Results for Different Parameters

Figs. 4.5(a)-(d) present the variation of vibration frequency with transverse pressure in high-temperature environment for the first four modes, each for different rotational speeds. The first mode is an axisymmetric bending mode, the second and third modes are asymmetric bending modes, and the fourth mode is a torsional mode, as can be observed from Figs. 4.5(a)-(d). The geometric stiffening caused by non-linear transverse deformation is observed

to cause the bending frequencies to increase with pressure, and this effect is more prominent at lower rotational speeds, and also for the lower modes. It is observed that the pressure and rotational speed have no effect on the vibration frequency for the torsional mode. This implies that neither the centrifugal stiffening caused by the rotational speed nor the geometric stiffening caused by the transverse pressure have an impact on the torsional mode. It is noted that the torsional mode is contributed by the in-plane displacement θ along circumferential direction.

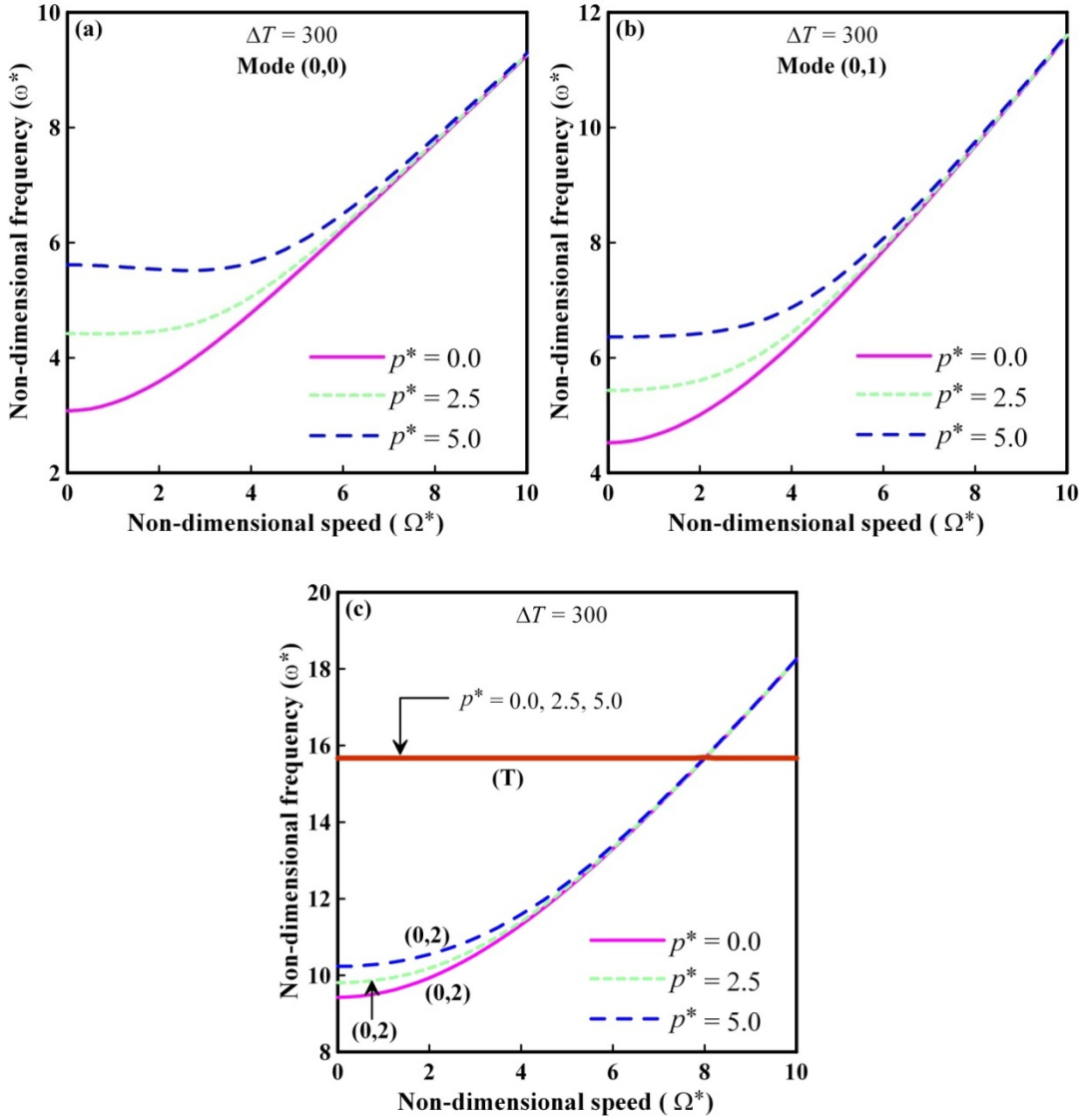

Fig. 4.6: Variation of vibration frequency with rotational speed for different transverse pressure under constant thermal loading: (a) Mode 1, (b) Mode 2, (c) Modes 3 & 4.

Table 4.2: Effect of size-dependent thickness (t/l) on vibration frequency (ω^*) for different rotational speed at transverse pressure $p^* = 0$.

Ω^*	t/l	Mode 1	Mode 2	Mode 3	Mode 4
1	1	3.21 (0,0)	4.65 (0,1)	9.56 (0,2)	15.67 (T)
	2	2.78 (0,0)	3.08 (0,1)	6.06 (0,2)	12.48 (0,3)
	5	2.46 (0,1)	2.47 (0,0)	4.44 (0,2)	9.15 (0,3)
	10	2.36 (0,1)	2.40 (0,0)	4.13 (0,2)	8.46 (0,3)
	$l = 0$ (classical)	2.32 (0,1)	2.38 (0,0)	4.01 (0,2)	8.20 (0,3)
5	1	5.48 (0,0)	7.02 (0,1)	12.25 (0,2)	15.67 (T)
	2	5.07 (0,0)	6.08 (0,1)	9.74 (0,2)	15.75 (T)
	5	4.80 (0,0)	5.78 (0,1)	8.80 (0,2)	13.67 (0,3)
	10	4.75 (0,0)	5.73 (0,1)	8.64 (0,2)	13.19 (0,3)
	$l = 0$ (classical)	4.73 (0,0)	5.72 (0,1)	8.59 (0,2)	13.02 (0,3)
10	1	9.25 (0,0)	11.60 (0,1)	15.67 (T)	18.25 (0,2)
	2	8.68 (0,0)	11.00 (0,1)	15.75 (T)	16.61 (0,2)
	5	8.39 (0,0)	10.81 (0,1)	15.77 (T)	16.04 (0,2)
	10	8.34 (0,0)	10.78 0,1)	15.77 (T)	15.95 (0,2)
	$l = 0$ (classical)	8.32 (0,0)	10.77 (0,1)	15.78 (T)	18.25 (0,2)

Figs. 4.6(a)-(c) show the variation of vibration frequency with rotational speed in high-temperature environment for the first four modes, each for different values of transverse pressure. Due to centrifugal stiffening, it is observed that the vibration frequencies of the bending modes increase with speed. However, there is an exception to this trend for the first and second modes (Figs. 4.6(a) and (b)) in the lower speed ranges, and for moderate to higher pressure values, in which the frequency remains constant or slightly declines with speed. The influence of transverse pressure is less at higher bending modes, and it also vanishes at higher rotational speeds, as shown in Fig. 4.6. Mode switching between the third bending mode and the torsional mode at very high speed is clearly visible in 4.6(c).

Table 4.3: Effect of size-dependent thickness (t/l) on vibration frequency (ω^*) for different rotational speed at transverse pressure $p^* = 2.5$.

Ω^*	t/l	Mode 1	Mode 2	Mode 3	Mode 4
1	1	4.42 (0,0)	5.47 (0,1)	9.90 (0,2)	15.67 (T)
	2	4.32 (0,0)	4.40 (0,1)	6.52 (0,2)	12.26 (0,3)
	5	4.14 (0,1)	4.30 (0,0)	4.96 (0,2)	8.60 (0,3)
	10	4.11 (0,1)	4.31 (0,0)	4.66 (0,2)	7.80 (0,3)
	$l = 0$ (classical)	4.10 (0,1)	4.31 (0,0)	4.55 (0,2)	15.67 (T)
5	1	5.63 (0,0)	7.12 (0,1)	12.30 (0,2)	15.67 (T)
	2	5.24 (0,0)	6.21 (0,1)	9.78 (0,2)	15.75 (T)
	5	5.02 (0,0)	5.94 (0,1)	8.83 (0,2)	13.59 (0,3)
	10	4.98 (0,0)	5.90 (0,1)	8.67 (0,2)	13.10 (0,3)
	$l = 0$ (classical)	4.96 (0,0)	5.88 (0,1)	8.61 (0,2)	12.93 (0,3)
10	1	9.26 (0,0)	11.60 (0,1)	15.67 (T)	18.25 (0,2)
	2	8.70 (0,0)	11.01 (0,1)	15.75 (T)	16.61 (0,2)
	5	8.40 (0,0)	10.81 (0,1)	15.77 (T)	16.04 (0,2)
	10	8.35 (0,0)	10.78 (0,1)	15.77 (T)	15.95 (0,2)
	$l = 0$ (classical)	8.33 (0,0)	10.77 (0,1)	15.78 (T)	15.92 (0,2)

The size-effect has been presented in Tables 4.2-4.4, where the vibration frequencies in high-temperature environment are listed for the first four modes considering different size-dependent thickness (t/l) values including the classical one (l=0). Tables 4.2-4.4 correspond to different non-dimensional transverse pressure such as p^* = 0, 2.5 and 5 respectively, and each case corresponds to Ω^*=1, 5 and 10. It is observed that the bending vibration frequencies are strongly influenced by the size-effect. They are diminished significantly as t/l values rise, and become closer to those predicted by the classical theory. It shows that the frequency values for the bending modes would be significantly underestimated if the size-effect are ignored. For each of Tables 4.2-4.4, the torsional vibration modes are prominent for higher rotational speed. Moreover, the torsional vibration frequency is seen to be almost unaffected

by the size-effect where it increases marginally with t/l. The tabulated results also demonstrate that the sequence in which different vibrational modes occur is determined by the size-dependent thickness together with the magnitude of rotational speed and transverse pressure. As a result, it causes mode switching between different modes. For example, considering Table 4.4 for Ω^*=1, the first four modes for t/l=1 are (0,0), (0,1), (0,2) and (T) respectively, whereas, they are: (0,1), (0,0), (0,2) and (0,3) respectively for t/l=2, and (0,1), (0,2), (0,0) and (0,3) respectively for t/l=5 . Tables 4.2 to 4.4 show same pattern of mode-shapes which are (0,0), (0,1), (T) and (0,2) for the first four modes respectively at Ω^*=10. In this case, mode-shape is not influenced by the size effect and transverse pressure. As an illustration, the mode shapes along with their contour have been shown in Figs. 4.7(a)-(d) for the first four modes respectively for t/l=1 at p^*=5.0 and Ω^*=10.

Table 4.4: Effect of size-dependent thickness (t/l) on vibration frequency (ω^*) for different rotational speed at transverse pressure $p^* = 5.0$.

Ω^*	t/l	Mode 1	Mode 2	Mode 3	Mode 4
1	1	5.59 (0,0)	6.37 (0,1)	10.31 (0,2)	15.67 (T)
	2	5.49 (0,1)	5.51 (0,0)	6.94 (0,2)	11.95 (0,3)
	5	5.27 (0,1)	5.34 (0,2)	5.51 (0,0)	7.94 (0,3)
	10	5.03 (0,2)	5.24 (0,1)	5.52 (0,0)	7.03 (0,3)
	l= 0 (classical)	4.92 (0,2)	5.23 (0,1)	5.52 (0,0)	6.68 (0,3)
5	1	5.99 (0,0)	7.39 (0,1)	12.41 (0,2)	15.67 (T)
	2	5.67 (0,0)	6.54 (0,1)	9.88 (0,2)	15.75 (T)
	5	5.52 (0,0)	6.30 (0,1)	8.90 (0,2)	13.39 (0,3)
	10	5.49 (0,0)	6.27 (0,1)	8.74 (0,2)	12.89 (0,3)
	l= 0 (classical)	5.48 (0,0)	6.26 (0,1)	8.68 (0,2)	12.70 (0,3)
10	1	9.29 (0,0)	11.62 (0,1)	15.67 (T)	18.26 (0,2)
	2	8.73 (0,0)	11.03 (0,1)	15.75 (T)	16.61 (0,2)
	5	8.45 (0,0)	10.84 (0,1)	15.77 (T)	16.04 (0,2)
	10	8.40 (0,0)	10.81 (0,1)	15.77 (T)	15.95 (0,2)
	l= 0 (classical)	8.38 (0,0)	10.80 (0,1)	15.78 (T)	15.92 (0,2)

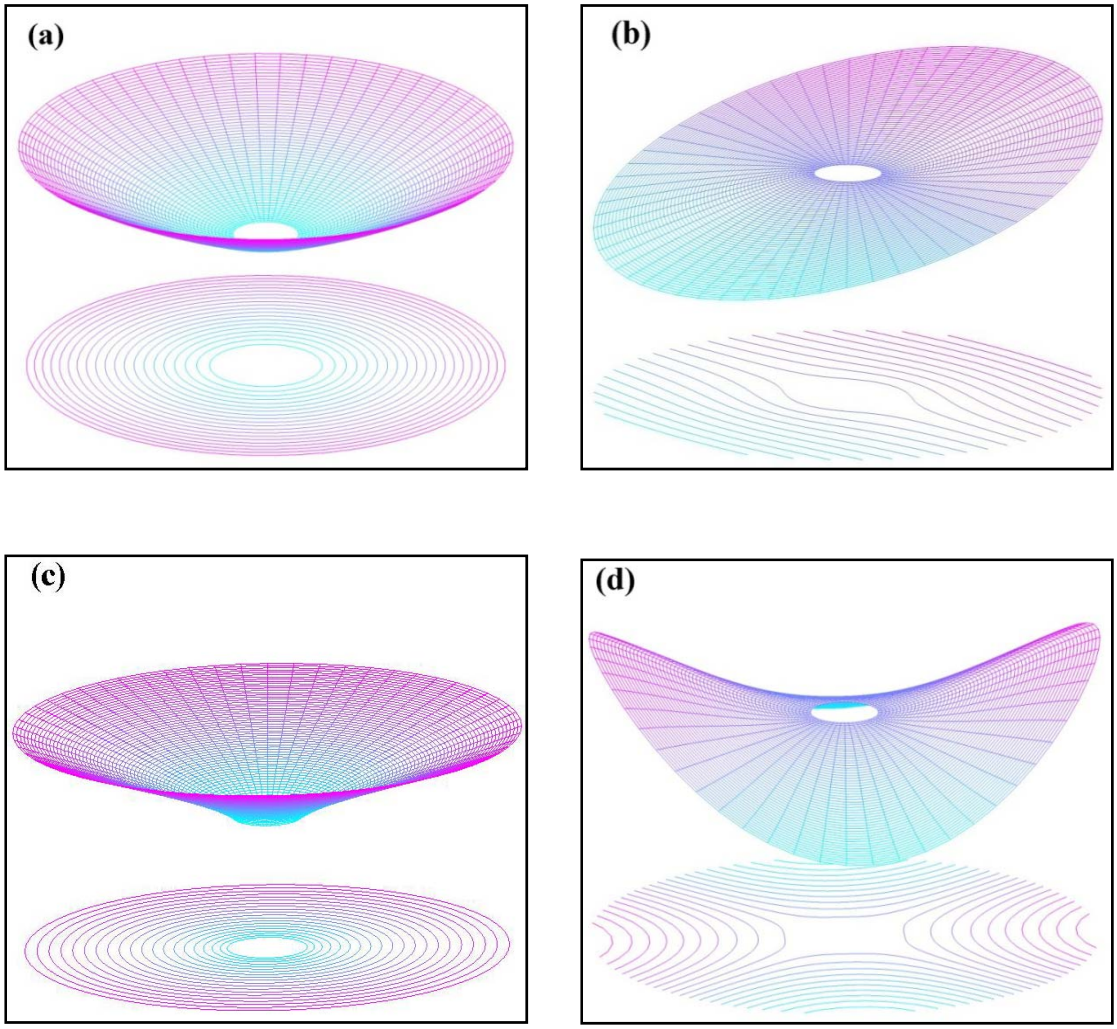

Fig. 4.7 Mode shape and contour plots for t/l=1 at p^*=5.0 and Ω^*=10: (a) Mode 1 (0,0), (b) Mode 2 (0,1), (c) Mode 3 (T), (d) Mode 4 (0,2).

Figs. 4.8(a)-(d) depict the behaviour of vibration frequency for the first four modes respectively with rotational speed in a high-temperature environment at p^*=5.0 and ΔT=300 K for different values of the gradation indices (k_r, k_t). Eq. (2.5) states that when one or both the gradation indices rises, the ceramic (Silicon Nitride) percentage of the micro-disk declines, leading to an increase in the metallic portion (Stainless Steel). Since the ceramic phase is indeed lighter and more elastic than the metallic phase, a rise in the gradation index values results in a reduction in the vibration frequency for the bending modes and the torsional mode, as seen from Figs. 4.8(a)-(d). For the entire range of rotational speeds, this

explanation is valid. Both at lower levels of the rotational speed and lower values of the gradation indices, it is observed that the impact of these parameters is more prominent. Figs. 4.8(c) and (d) show mode switching at larger rotational speeds between the third bending mode (0,2) and the torsional mode for $k_r = k_t = 0.75$ and higher values. The speed at which mode switching occurs decreases with increase in the values of k_r and k_t.

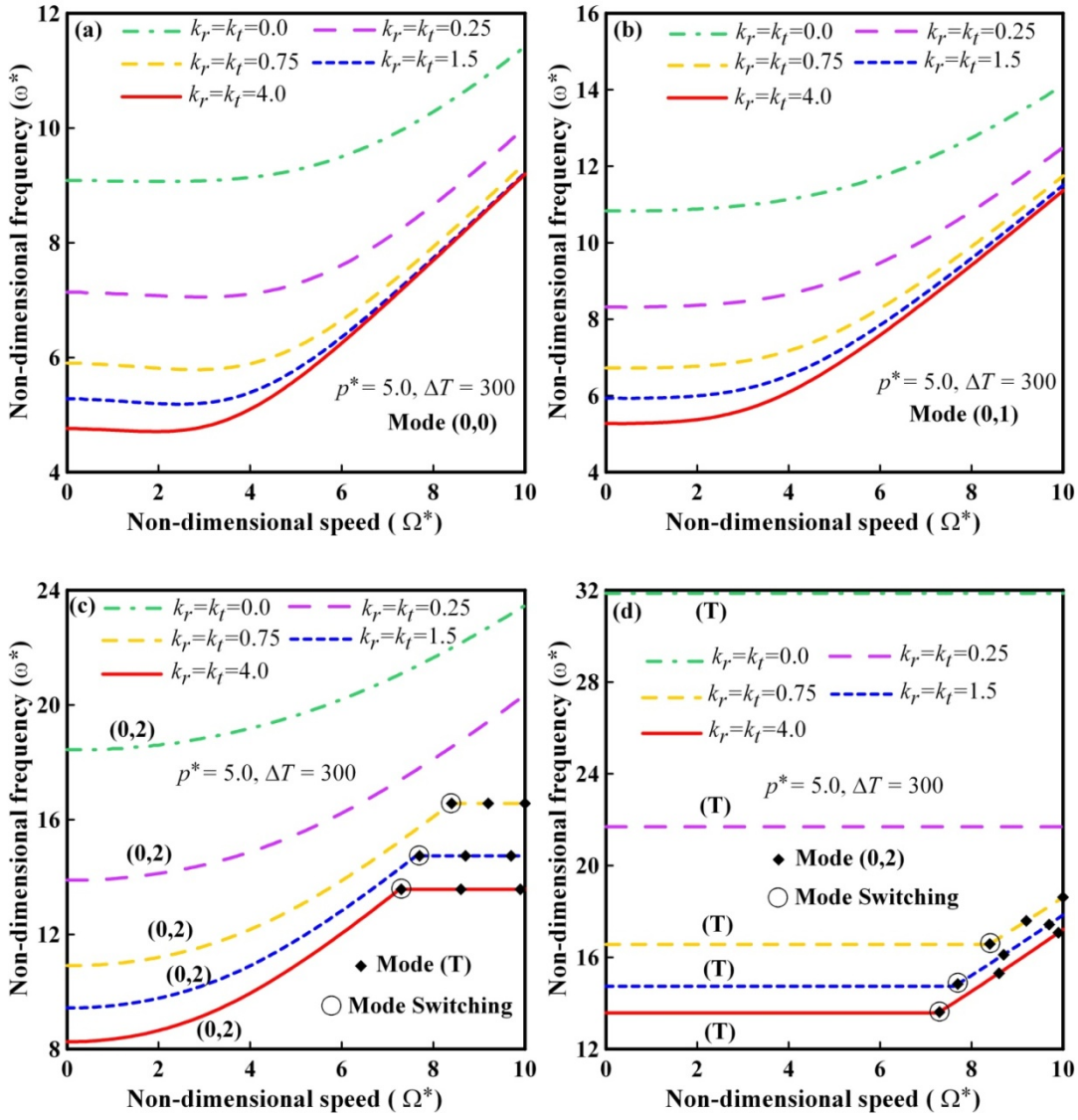

Fig. 4.8: Variation of vibration frequency with rotational speed for different gradation indices under constant transverse pressure and thermal loading: (a) Mode 1, (b) Mode 2, (c) Mode 3, (d) Mode 4.

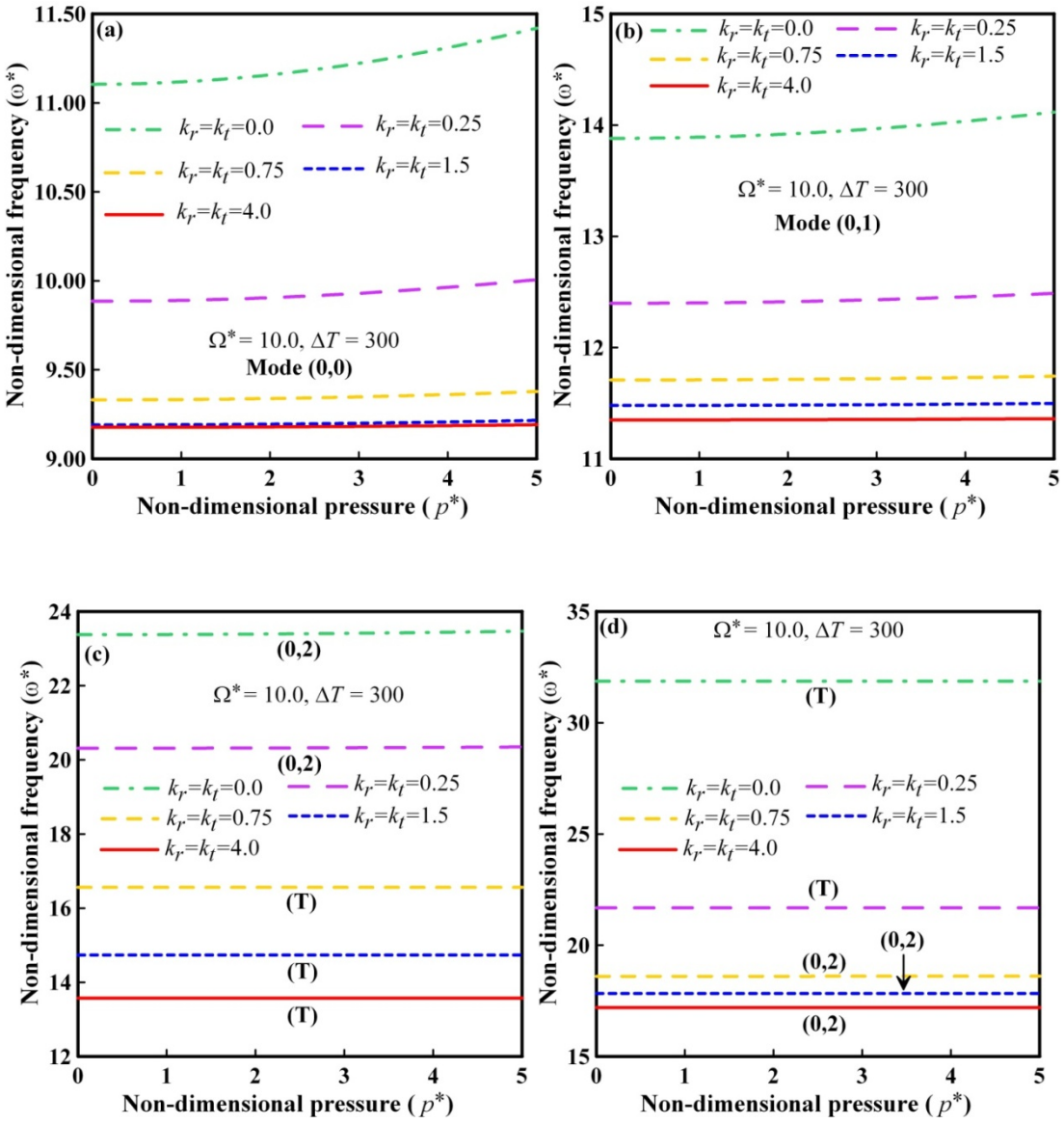

Fig. 4.9: Variation of vibration frequency with transverse pressure for different gradation indices under constant rotational speed and thermal loading: (a) Mode 1, (b) Mode 2, (c) Mode 3, (d) Mode 4.

Figs. 4.9(a)-(d) depict the variation of vibration frequency with transverse pressure in high-temperature environment at Ω^* =10.0 for the first four modes, each for various values of gradation indices (k_r , k_t). The increase in the gradation index values leads to significant decrease in the vibration frequency values. The effect of gradation indices remains true for the bending modes as well as for the torsional mode across the whole range of transverse pressure

values. For the first two modes, the frequency is slightly incremental in nature with pressure for $k_r = k_t =$ 0.0 and 0.25. For other values of k_r and k_t, and for the third and the fourth modes, the frequency values do not change much with transverse pressure. Figs. 4.9(c) and (d) reveal that the third and the fourth modes are (0,2) and (T) respectively for lower values of k_r and k_t ($k_r = k_t =$ 0.0 and 0.25). On the other hand, they are (T) and (0,2) respectively for the higher values of k_r and k_t ($k_r = k_t =$ 0.75, 1.5 and 4.0). It may therefore be concluded that the gradation indices significantly affect the free vibration behaviour of a BFGM rotating micro-disk under transverse pressure.

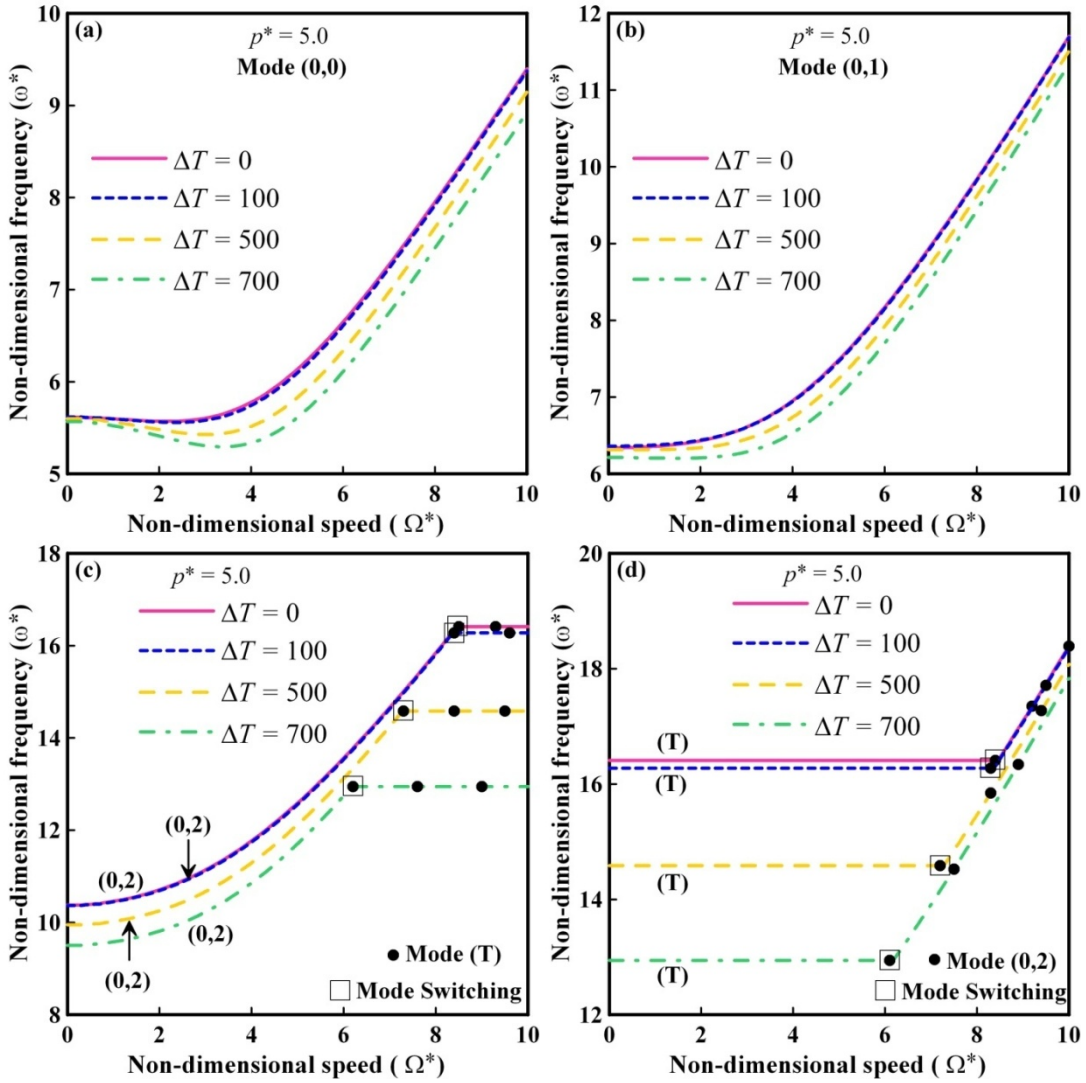

Fig. 4.10: Variation of vibration frequency with rotational speed for different thermal loading under constant transverse pressure: (a) Mode 1, (b) Mode 2, (c) Mode 3, (d) Mode 4.

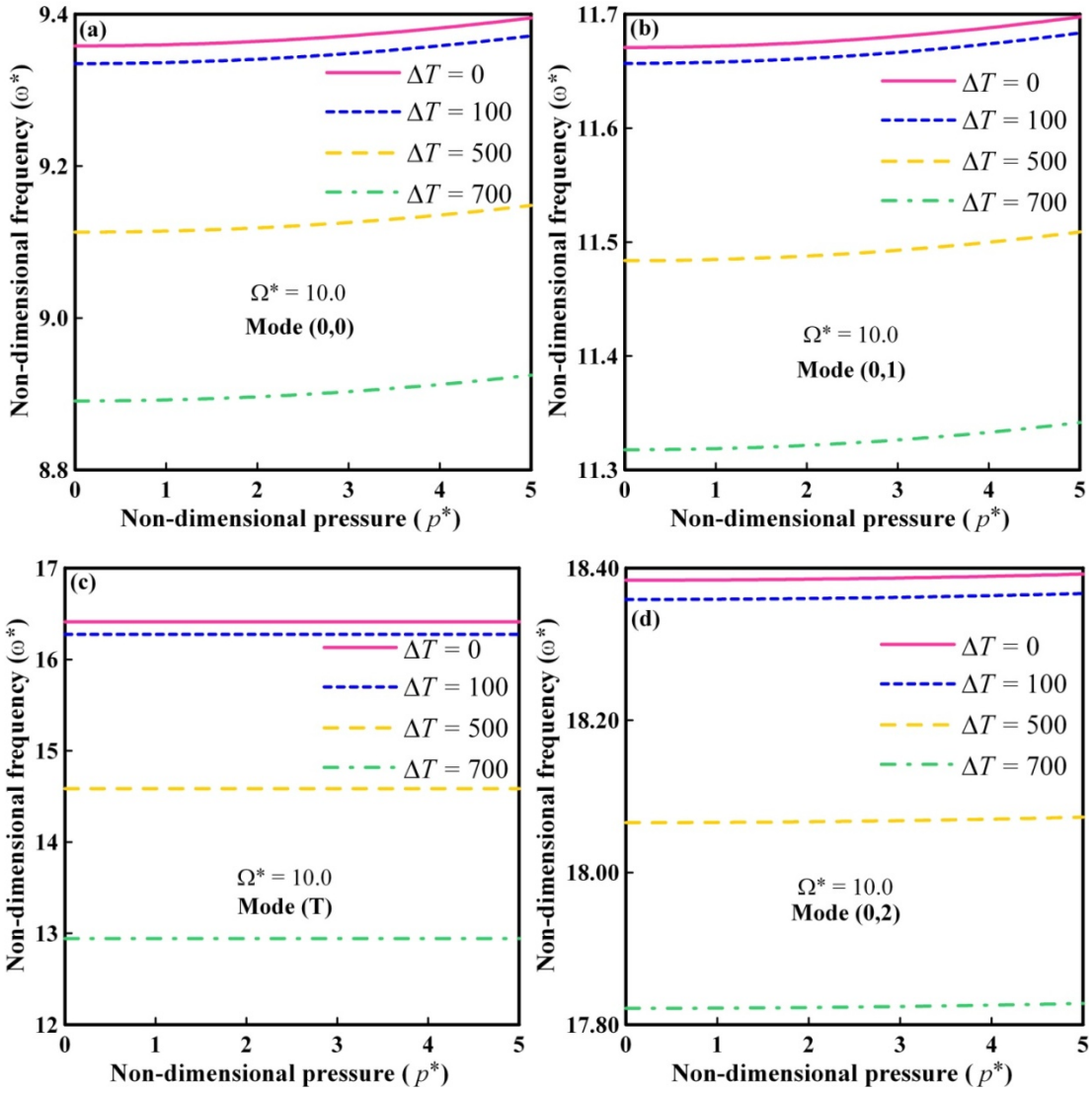

Fig. 4.11: Variation of vibration frequency with transverse pressure for different thermal loading under constant rotational speed: (a) Mode 1, (b) Mode 2, (c) Mode 3, (d) Mode 4.

The variation of vibration frequency with rotational speed at $p^* = 5.0$ for the first four modes, each for different magnitude of thermal loading, is shown in Figs. 4.10(a)-(d). For both bending modes and the torsional mode, the vibration frequencies decrease as temperature increases, and this effect is more prominent for larger thermal loading values. This influence of temperature is found to be uniform for the entire range of speed, with the exception at lower values of rotational speed for the first and second modes. Figs. 4.10(c) and (d) show

mode switching at larger rotational speeds between the third bending mode (0,2) and the torsional mode for all the values of thermal loading. The speed, at which mode switching occurs, decreases with increase in the values of thermal loading. Figs. 4.10(a)-(d) reveal that the change in frequency values with temperature is more pronounced for the torsional mode compared to the bending modes throughout the entire range of rotational speed.

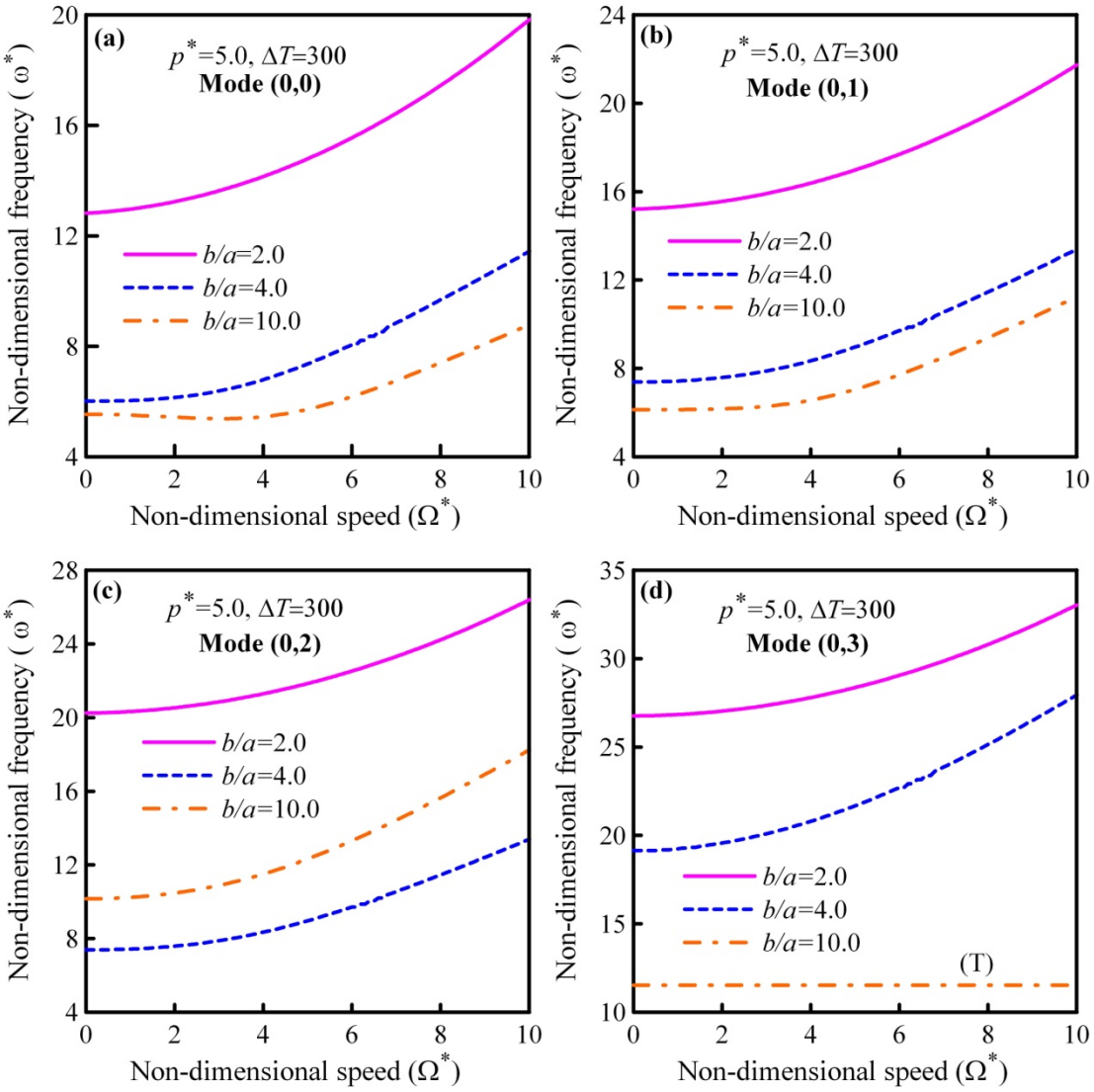

Fig. 4.12: Variation of vibration frequency with rotational speed for different radius ratio under constant transverse pressure and thermal loading: (a) Mode 1, (b) Mode 2, (c) Mode 3, (d) Mode 4.

Figs. 4.11(a)-(d) show the variation of vibration frequency with transverse pressure at $\Omega^* = 10.0$ for the first four modes, each for different values of thermal loading. Over the entire range of transverse pressure, the vibration frequencies decrease with temperature for all the four modes. Also, the impact of temperature continues to be almost entirely independent of transverse pressure for all modes considered. It is observed from Figs. 4.11(a)–(d) that the change in frequency values with temperature is more pronounced for the torsional mode compared to the bending modes throughout the entire range of transverse pressure.

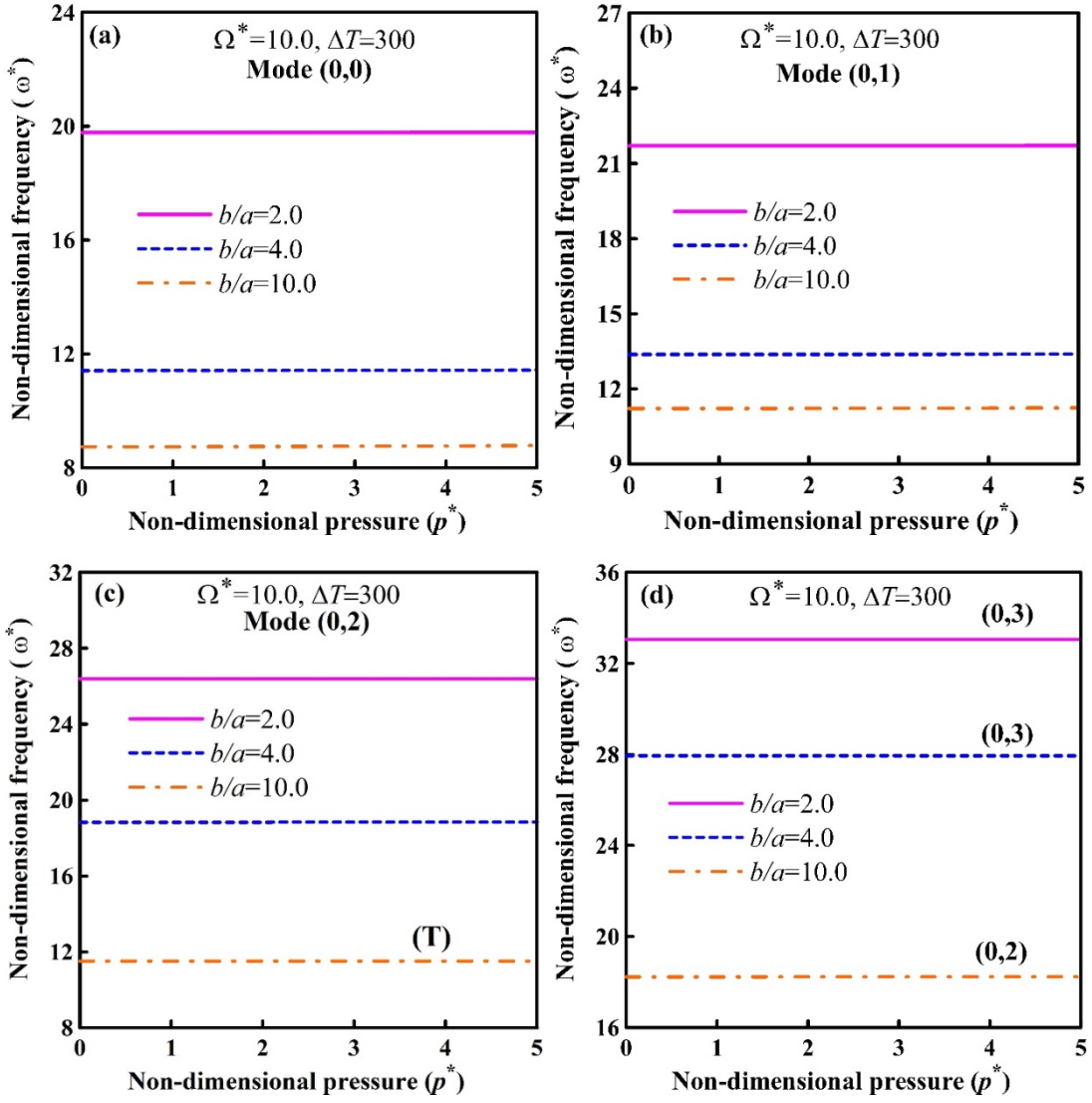

Fig. 4.13: Variation of vibration frequency with transverse pressure for different radius ratio under constant rotational speed and thermal loading: (a) Mode 1, (b) Mode 2, (c) Mode 3, (d) Mode 4.

The variation of vibration frequency with speed for different radius ratio (b/a) is shown in Figs. 4.12(a)-(d) for the first four modes respectively at Ω^* = 10.0 and p^* =5.0. Higher annular dimensions are indicated by an increased value b/a . Hence an increasing b/a value signifies decreasing bending stiffness. As a result, for the first two modes, a decrease in frequency values is seen with increasing b/a values. This trend changes for the third mode for higher values of b/a , which shows that an increase of annular dimension (i.e., increasing b/a value) stiffens the disk, leading to increased frequency values. Figs. 4.12(c) and (d) show mode switching between the third bending mode (0,2) and the torsional mode (T) for b/a =10.0. Figs. 4.12(a) and (b) show that, for b/a =10.0 at low-speed range, frequency decreases slightly as rotational speed increases indicating a softening effect, and this effect vanishes at higher rotational speed. The variation of vibration frequency with non-dimensional pressure for different radius ratio (b/a) is shown in Figs. 4.13(a)-(d) for the first four modes respectively. From Figs. 4.13(a), (b) and (d), a rise in the frequency values is seen with a decrease in b/a values for the first, second and the fourth modes. But for the third mode, as shown in Figs. 4.13(c), the frequency becomes maximum for b/a =4.0, and decreases slightly for b/a =2.0.

The previous results are all presented for Stainless Steel/Silicon Nitride composition. To illustrate the impact of various FGM compositions on the speed-frequency behaviour, Figs. 4.14(a)-(d) are presented for Stainless Steel/Silicon Nitride, Stainless Steel/Alumina, Stainless Steel/Zirconia and Titanium Alloy/Zirconia compositions respectively, each for the first four modes under constant pressure and thermal loading. Figs. 4.14(a) and (b)show that the trends of the mode-specific speed-frequency behaviour for Stainless Steel/Silicon Nitride and Stainless Steel/Alumina compositions are identical, and they differ in the relative values. The effect of softening is clearly visible for the first mode for these two material compositions (Stainless Steel/Silicon Nitride and Stainless Steel/Alumina) at low-speed range, where the frequency is slightly decreasing in nature while speed is increasing. For higher modes, this effect ceases to exist. The behaviour of Stainless Steel/Zirconia and Titanium Alloy/Zirconia compositions are different than the other two compositions. For Stainless Steel/Zirconia, one axisymmetric, two asymmetric and a torsional mode is depicted. For Titanium Alloy/Zirconia,

mode-switching occurs between the first two asymmetric modes (modes (0,1) and (0,2)) at slightly higher speed.

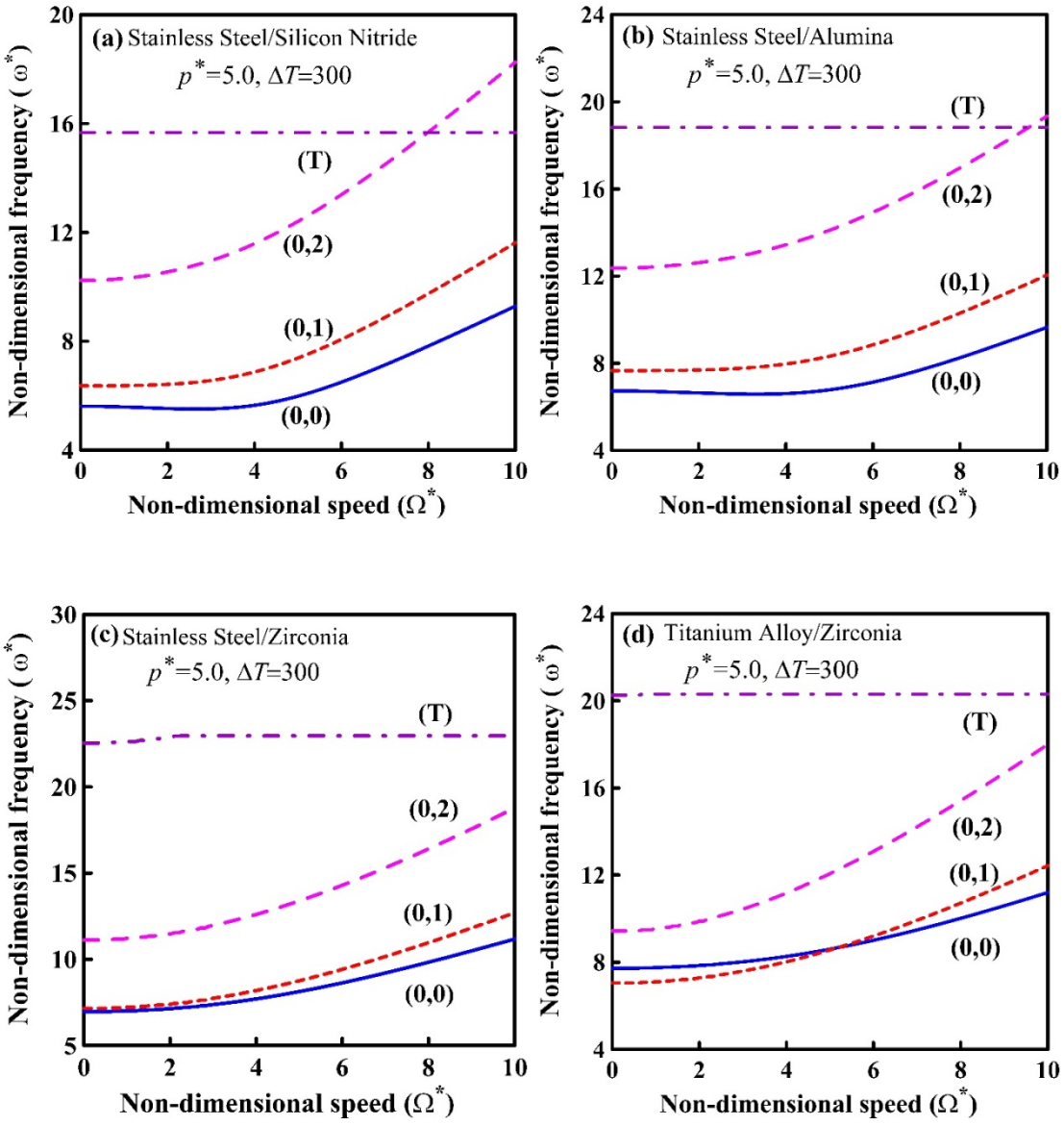

Fig. 4.14: Variation of vibration frequency with rotational speed under constant transverse pressure and thermal loading: (a) Stainless Steel/Silicon Nitride, (b) Stainless Steel/Alumina, (c) Stainless Steel/Zirconia, (d) Titanium Alloy/Zirconia.

Variation of vibration frequency with transverse pressure for different material compositions under constant rotational speed and thermal loading is shown in Figs. 4.15(a)-(d). Figs. 4.15(a) and (b) show that the trend of the mode-specific pressure-frequency behaviour for Stainless Steel/Silicon Nitride and Stainless Steel/Alumina compositions are identical, and differs in the relative values, whereas similar trend is observed for Stainless Steel/Zirconia and Titanium Alloy/Zirconia compositions as shown in Figs. 4.15(c) and (d).

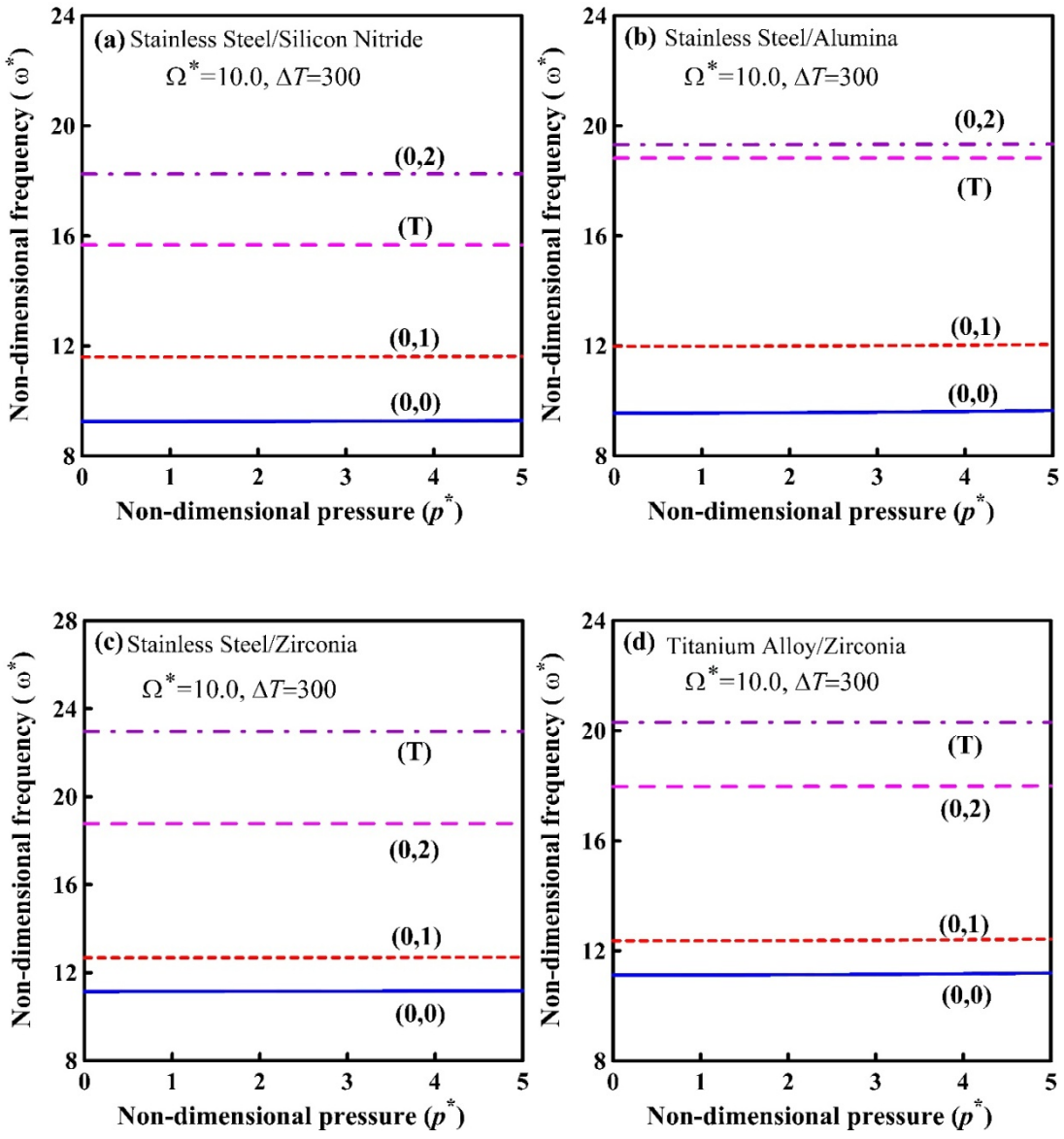

Fig. 4.15: Variation of vibration frequency with transverse pressure for different material combination under constant rotational speed and thermal loading: (a) Stainless Steel/Silicon Nitride, (b) Stainless Steel/Alumina, (c) Stainless Steel/Zirconia, (d) Titanium Alloy/Zirconia.

4.4 Chapter Summary

With the objective of studying the free vibration behaviour of rotating micro-size disks operating in high-pressure and high-temperature environment, the free flexural and torsional vibration behaviour of a BFGM rotating annular micro-disk operating in high-temperature environment and subjected to uniform transverse pressure has been investigated in the frequency domain. Using the Kirchhoff plate theory and the MCST, an energy-based mathematical model is developed. The model studies both axisymmetric and asymmetric bending modes, and also the torsional mode of vibration. The mathematical model is successfully compared against several simplified problems, demonstrating that it can be used to solve a variety of related problems. For a wide range of parametric values, the effects of speed, transverse pressure, thermal loading, size-dependent thickness, radial and thickness gradation indices, radius ratio and FGM composition on the frequencies of vibration of the first four modes have been discussed through extensive sets of numerical results. A few mode-shape plots along with their contour have been presented for visualization of the axisymmetric, asymmetric and torsional modes. The mathematical model is a novel one and the results that have been presented are the first of their kind, and will act as a standard for further research in this domain. The key findings of this chapter are summarized below:

- The small-size shows significant stiffening effect on both the axisymmetric and asymmetric bending modes of vibration, whereas the torsional mode is not significantly affected by small-size of the micro-disk.
- The transverse pressure only affects the bending modes within low to moderate speed ranges. However the rotational speed has a substantial impact on the bending vibration frequencies over the entire range of pressure values. In this instance, the torsional mode is found to be independent of the rotational speed and transverse pressure.
- For the entire ranges of speed and pressure loadings, the thermal loading significantly reduces frequencies for both the bending modes and the torsional mode. However, the effect of thermal loading is found more pronounced on the torsional mode compared to the bending modes.

- The bending vibration frequencies and the torsional vibration frequency are significantly reduced with the gradation indices for the entire ranges of speed and pressure loadings.
- The radius ratio has significant influence on the vibration frequencies for the bending modes and the torsional mode for the entire range of speed but it exhibits minute effect with the variation of pressure loading.
- Different FGM compositions exhibit different extent of influence on the speed-frequency and pressure-frequency behaviours.

Chapter 5

AXISYMMETRIC FREE VIBRATION BEHAVIOUR OF BFGM ROTATING MICRO-DISKS SUBJECTED TO TRANSVERSE PRESSURE UNDER HIGH-TEMPERATURE THERMAL LOADING

5.1 Introduction

The preceding chapter studied the free vibration behaviour of BFGM rotating micro-disks, considering both axisymmetric and asymmetric behaviour. For that study, the results were presented for the first four modes, and within the first four modes, only a single mode appeared for symmetric bending vibration. That symmetric mode of bending vibration is the first of the many such modes that the micro-disks can exhibit. It is known that the free vibration behaviour of the symmetric modes is often useful for mechanical and aerodynamic design of rotating disks. So, it essential to study the free vibration behaviour involving symmetric bending of rotating micro-disks at least for the first few modes. Most of the research works discussed in section 1.2.6 investigated the free axisymmetric bending vibration behaviour. This clearly indicates the significance of the axisymmetric modes as far as the dynamics of rotating disks are concerned. But at the same time, it must be mentioned that those works are mainly involved in the vibration behaviour of rotating plates that are supported at the outer edge. Hence the free axisymmetric bending vibration behaviour of typical clamped-free rotating micro-disks has not yet been studied. With this objective, the present chapter investigates the free vibration behaviour of BFGM rotating clamped-free micro-disks for axisymmtric modes, which is subjected to transverse pressure and high-temperature thermal loading.

The general mathematical model has already been presented in detail in the second chapter. In the following section, to maintain brevity, only the salient features and equations

are briefly discussed and provided for the present problem of axisymmetric bending vibration of BFGM rotating micro-disks.

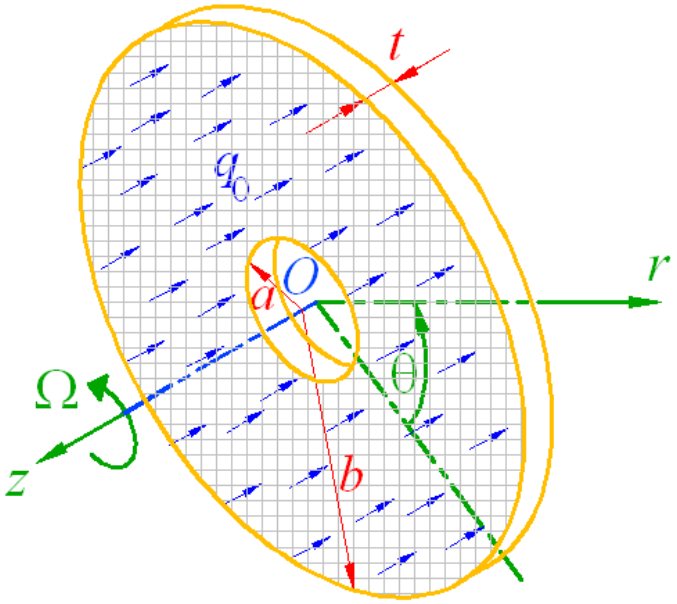

Fig. 5.1: Schematic diagram of a rotating disk for axisymmetric vibration.

5.2 Mathematical Background

A rotating micro-disk having inner radius a, outer radius b and constant thickness t is considered as shown in Fig. 5.1. The disk is made of metal-ceramic BFGM, which is graded along the radial and transverse directions, following Voigt rule involving power law. The parameters k_r and k_t symbolize the gradation indices along the radial and thickness directions respectively. The material properties are determined using Eq. (2.5). The micro-disk is assumed to be rotating with uniform angular speed Ω, and subjected to uniform transverse pressure of intensity q_0 and thermal loading in the form of uniform temperature rise $\Delta T = T - T_0$, where T and $T_0\,(=300\,\mathrm{K})$ denote the present and constant stress-free temperatures respectively.

Considering an arbitrary point $Q(r,\theta,z)$ on the disk, the displacement vector $\vec{\mathbf{u}}$ is given by,

$$\vec{\mathbf{u}} = u\hat{e}_r + v\hat{e}_\theta + w\hat{e}_z \quad . \tag{5.1}$$

According to Kirchhoff plate theory for axisymmetric bending, the displacement components $\{u,v,w\}$ are stated in terms of the mid-plane displacement components $\{u_0,v_0,w_0\}$ of the disk as follows:

$$u(r,z)=u_0(r)-z\frac{\partial w_0(r,\tau)}{\partial r}, \tag{5.2a}$$

$$v(r,z,\tau)=0, \tag{5.2b}$$

$$w(r,z,\tau)=w_0(r,\tau), \tag{5.2c}$$

where τ denotes time. Incorporating von Kármán type non-linearity, the classical strain tensor $(\boldsymbol{\varepsilon})$ can be derived as given below:

$$\varepsilon_{rr}=\left[\frac{\partial u_0}{\partial r}-z\frac{\partial^2 w_0}{\partial r^2}+\frac{1}{2}\left(\frac{\partial w_0}{\partial r}\right)^2\right], \tag{5.3a}$$

$$\varepsilon_{\theta\theta}=\left[\frac{u_0}{r}-\frac{z}{r}\frac{\partial w_0}{\partial r}\right], \tag{5.3b}$$

$$\varepsilon_{r\theta}=\varepsilon_{\theta r}=0. \tag{5.3c}$$

Considering the effect of thermal strain due to thermal loading ΔT, the components of the Cauchy stress tensor $(\boldsymbol{\sigma})$ are obtained using the von Kármán strain tensor $(\boldsymbol{\varepsilon})$ as follows:

$$\sigma_{rr}=\frac{E_f}{1-\left(\nu_f\right)^2}\left(\varepsilon_{rr}+\nu_f\varepsilon_{\theta\theta}\right)-\frac{E_f\alpha_f}{1-\nu_f}\Delta T, \tag{5.4a}$$

$$\sigma_{\theta\theta}=\frac{E_f}{1-\left(\nu_f\right)^2}\left(\varepsilon_{\theta\theta}+\nu_f\varepsilon_{rr}\right)-\frac{E_f\alpha_f}{1-\nu_f}\Delta T, \tag{5.4b}$$

$$\sigma_{r\theta}=\sigma_{\theta r}=0. \tag{5.4c}$$

According to the MCST, for any point $Q(r,\theta,z)$, the components of the rotation vector $(\vec{\theta})$ and the symmetric curvature tensor (χ) are obtained as given below:

$$\theta_\theta=\frac{1}{2}\left(\frac{\partial u}{\partial z}-\frac{\partial w}{\partial r}\right), \tag{5.5a}$$

$$\theta_r=\theta_z=0, \tag{5.5b}$$

$$\chi_{r\theta} = \chi_{\theta r} = \frac{1}{2}\left[\frac{1}{r}\frac{\partial w_0}{\partial r} - \frac{\partial^2 w_0}{\partial r^2}\right], \tag{5.6a}$$

$$\chi_{rr} = \chi_{\theta\theta} = \chi_{zz} = \chi_{\theta z} = \chi_{z\theta} = \chi_{rz} = \chi_{zr} = 0. \tag{5.6b}$$

In deriving the above components, the following form of del operator is considered:

$$\nabla = \hat{n}_r \frac{\partial}{\partial r} + \hat{n}_z \frac{\partial}{\partial z}. \tag{5.7}$$

The deviatoric part of the symmetric couple stress tensor $(\boldsymbol{m})$ is obtained from the corresponding components of the symmetric curvature tensor $(\boldsymbol{\chi})$ as follows:

$$m_{r\theta} = m_{\theta r} = 2G_f l^2 \chi_{r\theta}, \tag{5.8a}$$

$$m_{rr} = m_{\theta\theta} = m_{\theta z} = m_{z\theta} = m_{rz} = m_{zr} = 0. \tag{5.8b}$$

In Eq. (5.8a), l is the material length scale parameter. It is noted that the present formulation can be transformed to a classical one by putting l =0.

The problem is formulated using two different steps. In the first step, the configuration of the micro-disk as a result of the combined effects of time-invariant centrifugal loading, transverse pressure and uniform thermal loading is determined. The second step involves determination of the free vibration behaviour about the micro disk's deformed configuration.

5.2.1 Determination of Deformed Configuration of Micro-Disk under Different Time-invariant Loadings

The principle of minimum total potential energy is used to determine the deformed configuration of the micro-disk under the combined effects of time-invariant loadings mentioned above. The principle of minimum total potential energy is given as follows:

$$\delta\left(U_{cl} + U_{ncl} + W\right) = 0, \tag{5.9}$$

where U_{cl} and U_{ncl} are the classical and non-classical strain energies; W is the potential energy due to the applied loadings. According to the MCST, the expressions of U_{cl}, U_{ncl} and W can be derived to the following form as given below:

$$U_{cl} = \frac{1}{2}\int_{-t/2}^{+t/2}\int_{0}^{2\pi}\int_{a}^{b}\left(\boldsymbol{\sigma} : \boldsymbol{\varepsilon}\right) r dr d\theta dz$$

$$= \frac{1}{2}\int_{-t/2}^{+t/2}\int_{0}^{2\pi}\int_{a}^{b}\left[\sigma_{rr}\left\{\varepsilon_{rr}-\alpha_f\Delta T\right\}+\sigma_{\theta\theta}\left\{\varepsilon_{\theta\theta}-\alpha_f\Delta T\right\}\right]rdrd\theta dz$$

$$= 2\pi\int_{a}^{b}\left[E_A\left\{\frac{r}{2}\left(\frac{\partial u_0}{\partial r}\right)^2+\frac{{u_0}^2}{2r}+\frac{r}{8}\left(\frac{\partial w_0}{\partial r}\right)^4+\frac{r}{2}\frac{\partial u_0}{\partial r}\left(\frac{\partial w_0}{\partial r}\right)^2\right\}\right.$$

$$+E_I\left\{\frac{r}{2}\left(\frac{\partial^2 w_0}{\partial r^2}\right)^2+\frac{1}{2r}\left(\frac{\partial w_0}{\partial r}\right)^2\right\}+E_{PA}\left\{u_0\frac{\partial u_0}{\partial r}+\frac{u_0}{2}\left(\frac{\partial w_0}{\partial r}\right)^2\right\}+E_{PI}\frac{\partial w_0}{\partial r}\frac{\partial^2 w_0}{\partial r^2}$$

$$\left.-E_{TA}\left\{u_0+r\frac{\partial u_0}{\partial r}+\frac{r}{2}\left(\frac{\partial w_0}{\partial r}\right)^2\right\}+rE_C\right]dr, \tag{5.10}$$

$$U_{ncl} = \frac{1}{2}\int_{-t/2}^{+t/2}\int_{0}^{2\pi}\int_{a}^{b}\left(\boldsymbol{m}:\boldsymbol{\chi}\right)rdrd\theta dz$$

$$= \frac{1}{2}\int_{-t/2}^{+t/2}\int_{0}^{2\pi}\int_{a}^{b}\left(2m_{r\theta}\chi_{r\theta}\right)rdrd\theta dz$$

$$= 2\pi l^2\int_{a}^{b}G_A\left[\frac{r}{2}\left(\frac{\partial^2 w_0}{\partial r^2}\right)^2+\frac{1}{2r}\left(\frac{\partial w_0}{\partial r}\right)^2-\frac{\partial w_0}{\partial r}\frac{\partial^2 w_0}{\partial r^2}\right]dr, \tag{5.11}$$

$$W = -2\pi\left[\Omega^2\int_{a}^{b}\rho_A u_0 r^2 dr+q_0\int_{a}^{b}w_0 rdr\right]. \tag{5.12}$$

The set of stiffness coefficients $\left\{E_A, G_A, E_I, E_{PA}, E_{PI}, E_{TA}, E_C\right\}$ used in Eqs. (5.10) and (5.11), and the inertia coefficient ρ_A used in Eq. (5.12) are defined in Eqs. (2.27a)-(2.27i).

In this problem, the physical domain $(r,0,0)$ is transformed into a normalized computational domain $(\xi,0,0)$, where the normalized coordinate ξ along the r direction is defined as:

$$\xi = (r-a)/(b-a); 0 \le \xi \le 1. \tag{5.13}$$

Following Ritz method, the mid-plane displacements $\left\{u_0, w_0\right\}$ are discretized as finite linear combinations of one-dimensional (1D) orthogonal admissible functions $\left\{\phi_j^u, \phi_j^w\right\}$ and unknown coefficients c_j as:

$$u_0(\xi) = \sum_{j=1}^{n} c_j \phi_j^u(\xi), \tag{5.14a}$$

$$w_0(\xi) = \sum_{j=1}^{n} c_{n+j} \phi_j^w(\xi), \tag{5.14b}$$

where n is the total number of terms for each displacement field. Considering the clamped-free boundary condition of the disk, the lowest-order admissible functions for $\{\phi_j^u, \phi_j^w\}$ are selected as follows:

$$\phi_1^u(\xi) = \xi, \tag{5.15a}$$

$$\phi_1^w(\xi) = \xi^2. \tag{5.15b}$$

Thereafter, the remaining (n-1) number of functions for each displacement field are numerically generated employing Gram-Schmidt orthogonalization scheme.

Substituting Eqs. (5.10)-(5.12) into Eq. (5.9), and further substituting the approximate displacement fields given by Eqs. (5.14a)-(5.14b), the set of governing equations are obtained in algebraic form, which in matrix form can be written as follows:

$$[\mathbf{S}]\{\mathbf{c}\} = \{\mathbf{P}\}. \tag{5.16}$$

In the above equation, $[\mathbf{S}]$ is the total stiffness matrix (of dimension $2n \times 2n$) given by $[\mathbf{S}] = [\mathbf{S}^{cl}] + [\mathbf{S}^{ncl}]$ where $[\mathbf{S}^{cl}]$ and $[\mathbf{S}^{ncl}]$ are the classical and non-classical stiffness matrix respectively; $\{\mathbf{c}\}$ is the vector of unknown coefficients c_j to be determined; $\{\mathbf{P}\}$ is the load vector. The details of $[\mathbf{S}^{cl}]$, $[\mathbf{S}^{ncl}]$ and $\{\mathbf{P}\}$ are provided in Appendix 5A. The system of non-linear algebraic equations given by Eq. (5.16) is solved employing Broyden's method. The solution of Eq. (5.16), when substituted back into Eqs. (5.14a)-(5.14b), determines the displacement fields for the deformed configuration of the micro-disk under combined effects of centrifugal loading, transverse pressure and thermal loading.

5.2.2 Determination of Free Vibration Response of Deformed Micro-Disk

To derive the governing equations for this step involving free vibration of the deformed micro-disk about its deformed configuration, Hamilton's principle is employed which is given as follows:

$$\delta\left(\int_{\tau_1}^{\tau_2}\left(T_k - U\right)d\tau\right) = 0, \tag{5.17}$$

where T_k is the kinetic energy of the micro-disk, U is the total strain energy and τ is time. The expression of T_k is derived to the following form:

$$T_k = 2\pi\int_a^b\left[\frac{\rho_A}{2}\left\{\left(\frac{\partial u_0}{\partial\tau}\right)^2 + \left(\frac{\partial w_0}{\partial\tau}\right)^2\right\} + \frac{\rho_I}{2}\left(\frac{\partial^2 w_0}{\partial\tau\partial r}\right)^2\right] rdr. \tag{5.18}$$

In Eq. (5.18), $\{\rho_A, \rho_I\}$ is the set of inertia coefficients where ρ_A is given as defined in Eq.(2.27i) and ρ_I is defined as given in Eq. (2.38).

The dynamic displacement fields are discretized following Ritz method using the same set of functions $\{\phi_j^u, \phi_j^w\}$ that are used for determining the deformed configuration of the micro-disk but with the combination of a new set of unknown coefficients d_j as follows:

$$u_0(\xi,\tau) = \sum_{j=1}^{n}\left(d_j e^{\mathbf{i}\omega\tau}\right)\phi_j^u(\xi), \tag{5.19a}$$

$$w_0(\xi,\tau) = \sum_{j=1}^{n}\left(d_{n+j} e^{\mathbf{i}\omega\tau}\right)\phi_j^w(\xi). \tag{5.19b}$$

Here ω is the frequency of vibration and $\mathbf{i}=\sqrt{-1}$.

As the micro-disk executes small amplitude free vibration about its deformed configuration, its tangent stiffness is responsible for free vibratory motion that would occur in the neighborhood of the deformed configuration. The elements of the tangent stiffness matrix $\left([\mathbf{K}]\right)$ are derived considering the following relation:

$$[K_{ik}] = \frac{\partial\left\{\sum_{j=1}^{2n}[S_{ij}]\{c_j\}\right\}}{\partial c_k} \text{ for } \begin{vmatrix} i = 1,2,.....,2n, \\ k = 1,2,.....,2n. \end{vmatrix} \tag{5.20}$$

It must be noted that $[\mathbf{K}]$ is contributed by the classical $\left([\mathbf{K}^{cl}]\right)$ and non-classical $\left([\mathbf{K}^{ncl}]\right)$ parts. It is already discussed that the non-classical part of the tangent stiffness is linear, and hence equal to the non-classical part of the total stiffness matrix, i.e., $[\mathbf{S}^{ncl}] = [\mathbf{K}^{ncl}]$.

However the components of the classical part of the tangent stiffness matrix $\left(\left[\mathbf{K}^{cl}\right]\right)$ are non-linear and are provided in Appendix 5B.

Using Eqs. (5.19a) and (5.19b), substituting Eq. (5.18) into Eq. (5.17), and using the components of the tangent stiffness into Eq. (5.17), the governing equations are derived in the following form:

$$\left[\left[\mathbf{K}\right]-\omega^2\left[\mathbf{M}\right]\right]\left\{\mathbf{d}\right\}=0. \tag{5.21}$$

Here $\left[\mathbf{M}\right]$ is the mass matrix, the components of which are given in Appendix 5C; $\left\{\mathbf{d}\right\}$ is the set of unknown coefficients representing the dynamic displacements during the free vibration. Eq. (5.21) represents an eigenvalue problem, which is solved using a standard eigen-solver. Eq. (5.21) is nonlinear but is linearized using the solution parameters $\left\{\mathbf{c}\right\}$ of the previous step to take into the effect of pre-stress induced due to centrifugal loading, transverse pressure and thermal loading. The square roots of the eigenvalues $\left(\omega^2\right)$ signify the frequencies of vibration of the deformed micro-disk, and the eigenvectors i.e., $\left\{\mathbf{d}\right\}$ represent the corresponding mode-shapes of vibration. The mode-shapes are obtained by appropriately substituting $\left\{\mathbf{d}\right\}$ into Eqs. (5.19a) and (5.19b).

5.3 Results and Discussion

The non-dimensional speed $\left(\Omega^*\right)$, pressure $\left(p^*\right)$ and frequency of vibration $\left(\omega^*\right)$ for the present problem are defined as follows (Das et al. (2010); Kermani et al. (2016); Shojaeefard et al. (2018b)):

$$\Omega^*=\Omega b^2\sqrt{\rho_c t/D}, \tag{5.22a}$$

$$p^*=q_0 b^4/\left(E_c^0 t^4\right), \tag{5.22b}$$

$$\omega^*=\omega b^2\sqrt{\rho_c t/D}, \tag{5.22c}$$

where $D=E_c^0 t^3\Big/\left\{12\left(1-\left(\nu_c^0\right)^2\right)\right\}$. It is noted that the non-dimensional parameters, presented above, are defined with reference to the property values of the ceramic phase of the FGM

composition at $T_0\left(=300\,\mathrm{K}\right)$. These property values are calculated using the Touloukian model given by Eq. (2.6), and employing the temperature coefficients provided in Table 2.1. The values of the Young's modulus $\left(E_c^0\right)$, Poisson's ratio $\left(\nu_c^0\right)$ and mass density $\left(\rho_c\right)$ for different ceramic constituents at T_0 used in the present analysis are provided in Table 5.1. It is noted that the mass density is independent of temperature.

In the present case of axisymmetric bending vibration, no separate mode numbers are provided with the results. It is understood that the first axisymmetric mode contains no nodal circle, and as the mode number is increased sequentially from second mode onwards, the number of nodal circles also increases by one for each higher mode.

Table 5.1: Material properties of the ceramic constituents at T_0 = 300 K.

Material Property	Silicon Nitride (Si_3N_4)	Zirconia (ZrO_2)	Alumina (Al_2O_3)
E_c^0 (GPa)	322.27	168.06	320.24
ν_c^0	0.240	0.298	0.260
ρ_c (kg/m^3)	2370	3000	3750

The present formulation is quite general in nature and can be applied for a wide variety of problems by properly adjusting certain parameters as follows: the present model can be reduced to a plate model under non-rotating condition by putting the rotational speed $\Omega = 0$; the size-independent behaviour, which is applicable for a macro-size rotating disk, can be investigated by putting $l = 0$; the problem of solid micro-plate clamped at the outer edge can be investigated by putting a =0, $\Omega = 0$, and considering $\phi_1^u = \left(1-\xi\right)$; $\phi_1^w = \left(1-\xi\right)^2$ as the lowest order admissible function for Ritz discretization; a radial-FG micro-disk/plate is obtained by putting $k_t = 0$; a thickness-FG micro-disk/plate is obtained by putting $k_r = 0$.

Unless otherwise mentioned, the numerical results for this chapter are generated for a Stainless Steel/Silicon Nitride BFGM micro-disk using the following values of the parameters: l =17.6×10^{-6} m (Lam et al. (2003); Park and Gao (2006)), t/l =1, b/t = 50, b/a =10.0, $k_r = k_t = 1$, Ω^*=5, p^*=10 and ΔT =200.Accordingly, the dimensions of the BFGM

rotating annular micro-disk become: t=17.6 μm, b=880 μm, a=88 μm. Based on the convergence study reported in Chapter 3, the number of functions for Ritz approximation has been taken as $n=8$ for generation of results.

5.3.1 Validation Study

Fig. 5.2 compares the variation of the axisymmetric vibration frequency with rotational speed for the fundamental mode of a homogeneous $(k_r=0, k_t=0)$ annular clamped-free rotating disk under uniform transverse pressure with Das et al. (2010). The non-dimensional speed $\overline{\Omega}$ in Fig. 5.2 is defined as $\overline{\Omega}=\Omega b\sqrt{\rho/\sigma_y}$, and the results are generated with the following values: l=0, E=210×10^9 N/m^2, ν=0.3, ρ=7850 kg/m^3, σ_y=300×10^6 N/m^2, t=0.006 m, b/t= 50, b/a=12, p^*=0.3571, ΔT=0. The comparison exhibits excellent matching.

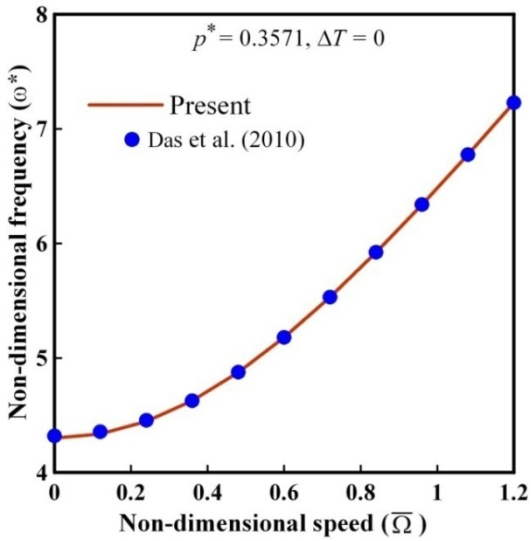

Fig. 5.2: Comparison of non-dimensional speed versus frequency behaviour for the first mode of a homogeneous annular rotating disk under uniform transverse pressure.

Considering different values of k_t, the non-dimensional load-deflection behaviour of a thickness-FG $(k_r=0)$ annular clamped-free micro-plate under uniform transverse pressure has been compared with Reddy et al. (2016) in Fig. 5.3. For this comparison, the normalized deflection (w^*) is defined as $w^*=w_{max}/t$, and the effective Young's modulus is determined

using the following relation: $E_f(z) = E_2 + (E_1 - E_2)\left(\frac{z}{t} + \frac{1}{2}\right)$. The following values are taken for generation of results: E_1=10^6 N/m^2, E_2=10^5 N/m^2, ν_f = 0.25, t=0.1×10^{-6} m, l/t=0.6, b/t= 10, b/a =4, Ω^*=0, ΔT =0. An excellent agreement is observed in Fig. 5.3.

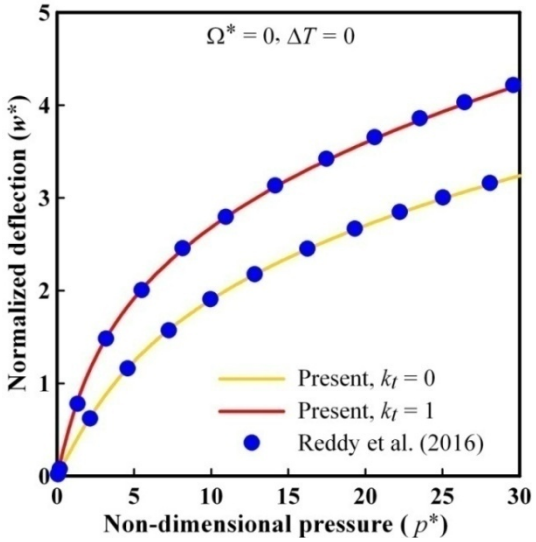

Fig. 5.3: Comparison of non-dimensional pressure versus deflection behaviour of a thickness-FG annular clamped-free micro-plate.

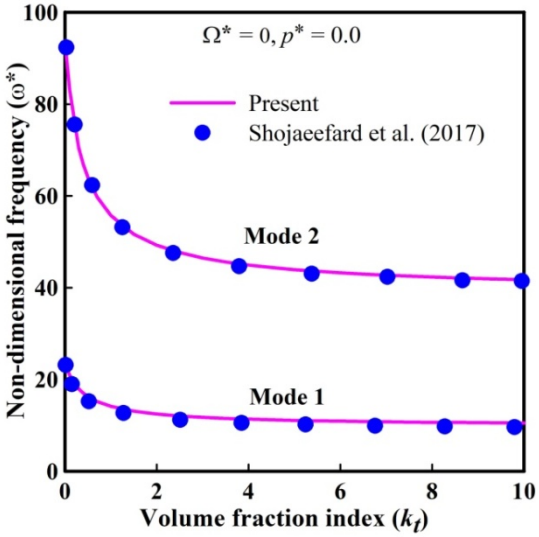

Fig. 5.4: Comparison showing variation of non-dimensional vibration frequency with volume fraction index for the first two modes of a thickness-FG solid circular clamped micro-plate under thermal loading.

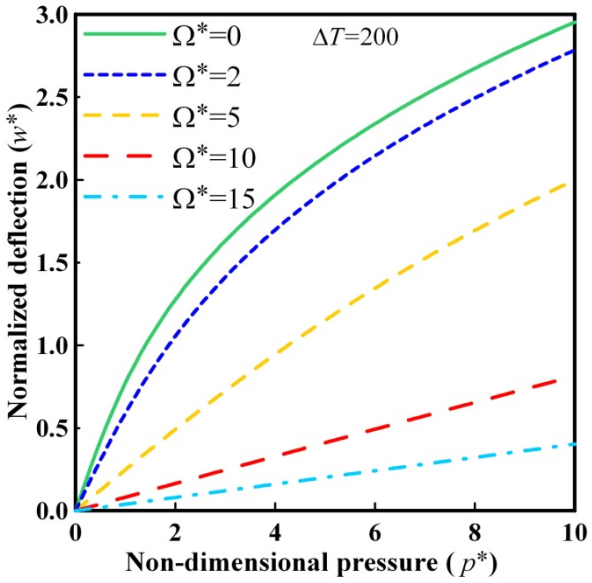

Fig. 5.5: Variation of transverse deflection with applied transverse pressure for different rotational speed under constant thermal loading.

In Fig. 5.4, variations of the vibration frequency with volume fraction index (k_t) for the first two modes of a thickness-FG $(k_r = 0)$ solid circular $(a = 0)$ clamped micro-plate are compared with Shojaeefard et al. (2017). It shows excellent conformity. Fig. 5.4 corresponds to Stainless Steel/Silicon Nitride plate under non-linear through-thickness temperature variation given by $T(z) = 300 + 90\left(\frac{z}{t} + \frac{1}{2}\right)^{0.9}$ K. The results of Fig. 5.4 are generated, considering asymmetric functional gradation, by using the following in Eq. (2.5): $R_f(z,T) = R_m(T) + \{R_c(T) - R_m(T)\}\left(\frac{z}{t} + \frac{1}{2}\right)^{k_t}$, and with the following values: $l = 17.6 \times 10^{-6}$ m, $t/l = 1.0$, $b/t = 20$, $\Omega^* = 0$, $p^* = 0$. The comparisons illustrated through Figs. 5.2-5.4 show excellent matching of the results, and thus validate the present model.

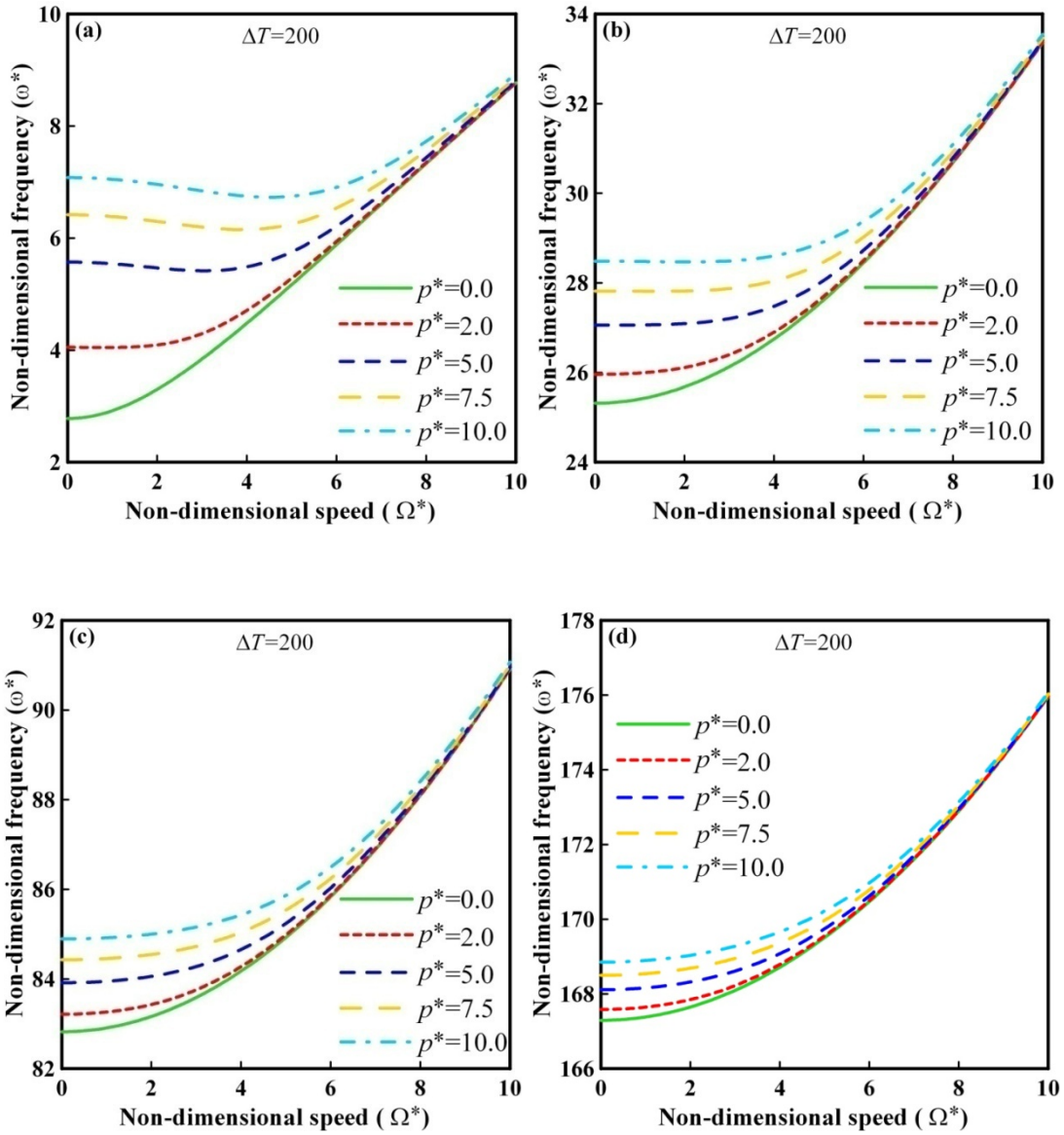

Fig. 5.6: Variation of vibration frequency with rotational speed for different transverse pressure under constant thermal loading: (a) Mode 1, (b) Mode 2, (c) Mode 3, (d) Mode 4.

5.3.2 Numerical Results for Different Parameters

The centrifugal loading due to rotation and the thermal loading are in-plane in nature, and do not induce any bending of the micro-disk. However, it is subjected to static bending due to applied transverse pressure. To illustrate this, the pressure-deflection curves in high-temperature environment are shown in non-dimensional plane in Fig. 5.5 for different rotational speed where the normalized deflection is defined as $w^* = w_{\max}/t$. Fig. 5.5 clearly

shows the hardening type non-linear static behaviour at low to moderate rotational speeds, and almost linear static behaviour at higher values of rotational speed. This non-linearity arises out of the geometric stiffening due to von Kármán type non-linearity. Furthermore, the deflection is found to decrease with increasing rotational speed as a result of enhanced centrifugal stiffening.

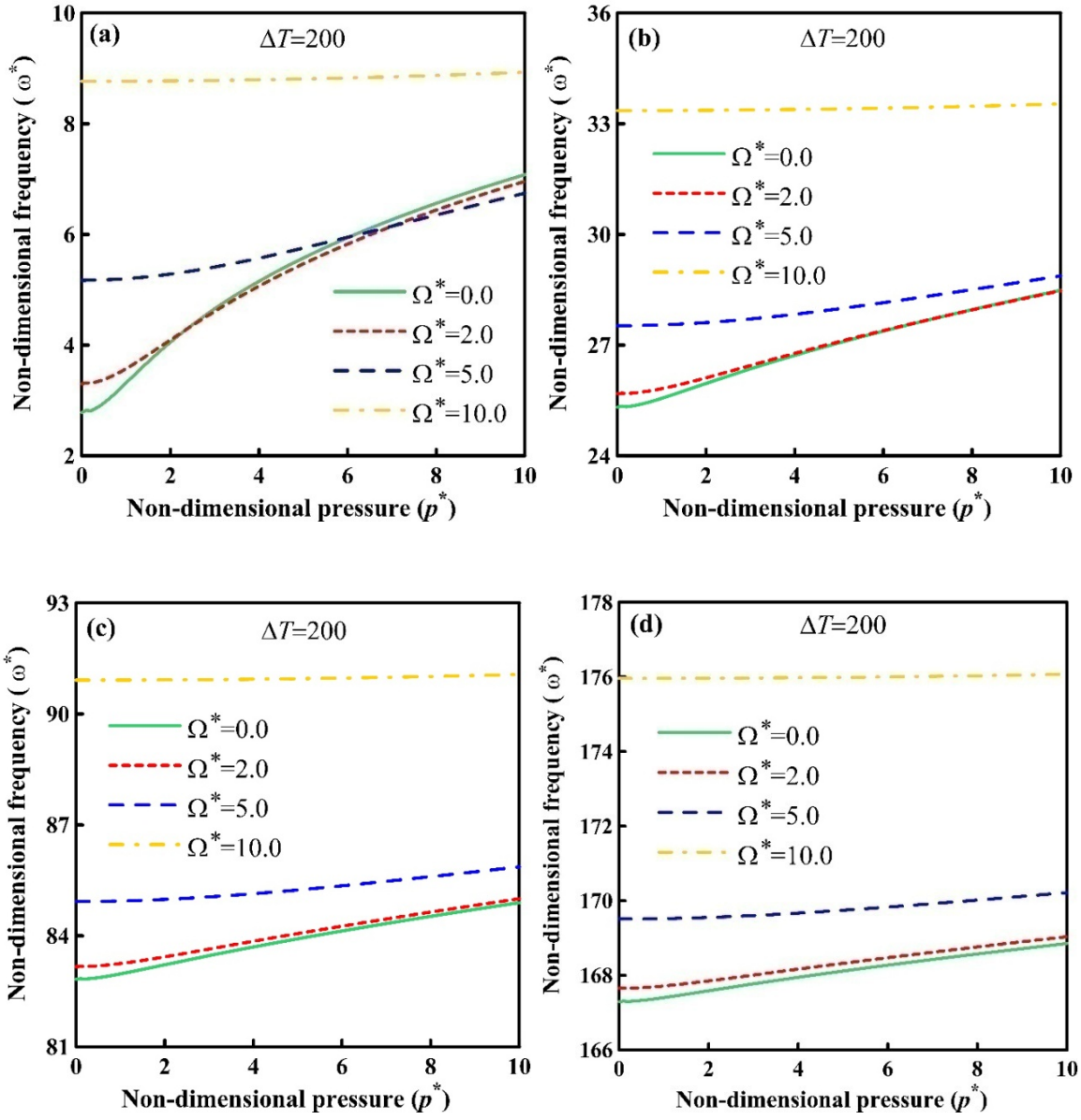

Fig. 5.7: Variation of vibration frequency with transverse pressure for different rotational speed under constant thermal loading: (a) Mode 1, (b) Mode 2, (c) Mode 3, (d) Mode 4.

The non-dimensional speed-frequency behaviour in a high-temperature environment for the first four modes, each for different transverse pressures, is shown in Figs. 5.6(a)-(d). The frequencies are found to increase with speed because of centrifugal stiffening. Further the increase in transverse pressure exhibits increasing frequency values for all the four modes, indicating enhanced geometric stiffening at higher pressure values. However, there is an exception to this for the first and second modes (Figs. 5.6(a) and (b)) for lower speed ranges, and moderate to higher pressure values, where the frequency stays constant or just slightly declines with speed indicating softening effect due to such loading conditions. The impact of transverse pressure decreases with speed, and virtually vanishes at higher rotational speeds for the higher modes of vibration.

Figs. 5.7(a)-(d) show the non-dimensional pressure-frequency behaviour in high-temperature environment for the first four modes, each for different rotational speed. The frequencies are found to increase with pressure because of geometric stiffening but this effect is minute at high speeds. It is found that the effect of centrifugal stiffening plays a crucial role in governing the pressure-frequency behaviour. For the first mode, at higher pressure values, it is found that the stiffening effect due to transverse pressure dominates the centrifugal stiffening. Hence the plots for $\Omega^* = 0.0, 2.0$ and 5.0 shows reverse trend, which is increase in the frequency values with decease in rotational speed.

Tables 5.2-5.4 show the variation of vibration frequencies in high-temperature environment ($\Delta T = 200$) for different size-dependent thickness (t/l) values at different pressure values $p^* = 0,\ 5,\ 10$ respectively, each for the first four modes. The classical theory (i.e., where no size-effect is considered) is restored by putting $l = 0$. It should be noted that the size-effect is greater when the size-dependent thickness is lower and vice versa. For all the modes presented, the frequency values increase as the size-dependent thickness decreases, illustrating enhanced stiffness when the size-effect is increased. Exception to this occurs for the first mode for Table 5.3 and 5.4 at low speed ($\Omega^* = 1$), where the frequency values slightly increase when t/l is increased as 2, 5 up to 10. For all the modes, and any combination of pressure and speed, the classical theory offers the smallest values of frequencies. However, it is found that the difference in the frequency values between the cases of no size effect $(l = 0)$

and highest size effect $(t/l=1)$ varies widely depending on the loading conditions and the mode numbers. The intensity of the size-effect also changes with the mode number since it has been observed that the higher is the mode number, the greater is the decrease in frequency values noticed with an increase in t/l values.

Table 5.2: Effect of size-dependent thickness on vibration frequency for different rotational speed at transverse pressure $p^*=0$ under constant thermal loading ($\Delta T=200$).

Ω^*	t/l	Mode 1	Mode 2	Mode 3	Mode 4
1	1	2.92	25.41	82.91	167.38
	2	2.51	17.17	53.25	106.62
	5	2.19	13.84	41.21	81.84
	10	2.12	13.28	39.17	77.65
	$l=0$ (classical)	2.09	13.08	38.47	76.20
5	1	5.17	27.53	84.93	169.51
	2	4.75	20.22	56.36	109.94
	5	4.47	17.54	45.19	86.13
	10	4.42	17.11	43.35	82.16
	$l=0$ (classical)	4.40	16.96	42.72	80.79
10	1	8.77	33.36	90.92	175.96
	2	8.15	27.73	65.04	119.62
	5	7.83	25.88	55.64	98.15
	10	7.77	25.59	54.15	94.68
	$l=0$ (classical)	7.75	25.49	53.64	93.49

For visualization of the modes, Figs. 5.8(a)–(d) show the mode shapes and associated contour plots of the first four axisymmetric bending vibration modes for $p^*=5$, $\Omega^*=10.0$ and $\Delta T=200$. Fig. 5.8 confirms that the axisymmetric modes contain only nodal circle(s) without any nodal diameter. It is seen that for a clamped-free micro-disk, the first mode contains no nodal circle, and the number of nodal circles increases by one for the next higher mode.

Table 5.3: Effect of size-dependent thickness on vibration frequency for different rotational speed at transverse pressure $p^* = 5$ under constant thermal loading ($\Delta T = 200$).

Ω^*	t/l	Mode 1	Mode 2	Mode 3	Mode 4
1	1	5.54	27.06	83.95	168.16
	2	5.44	19.79	55.35	108.53
	5	5.45	17.20	44.31	84.82
	10	5.46	16.80	42.52	80.88
	$l = 0$ (classical)	3.83	14.56	39.75	77.35
5	1	5.75	27.99	85.24	169.75
	2	5.45	20.95	57.01	110.56
	5	5.31	18.49	46.18	87.14
	10	5.29	18.10	44.42	83.27
	$l = 0$ (classical)	3.92	15.39	40.50	78.09
10	1	8.81	33.40	90.95	175.99
	2	8.21	27.80	65.12	119.70
	5	7.90	25.96	55.75	98.27
	10	7.85	25.68	54.27	94.81
	$l = 0$ (classical)	7.83	25.58	53.77	93.62

Table 5.4: Effect of size-dependent thickness on vibration frequency for different rotational speed at transverse pressure $p^* = 10$ under constant thermal loading ($\Delta T = 200$).

Ω^*	t/l	Mode 1	Mode 2	Mode 3	Mode 4
1	1	7.05	28.48	84.92	168.90
	2	6.93	21.69	57.07	110.17
	5	6.95	19.37	46.57	87.11
	10	6.97	19.01	44.88	83.30
	$l = 0$ (classical)	3.83	14.95	39.75	77.35
5	1	6.75	28.88	85.86	170.22
	2	6.54	22.23	58.21	111.71
	5	6.50	20.01	47.82	88.84
	10	6.50	19.67	46.16	85.09
	$l = 0$ (classical)	6.50	19.56	45.59	83.80
10	1	8.93	33.54	91.07	176.07
	2	8.37	28.00	65.34	119.94
	5	8.10	26.21	56.05	98.62
	10	8.06	25.93	54.59	95.10
	$l = 0$ (classical)	8.04	25.84	54.10	94.01

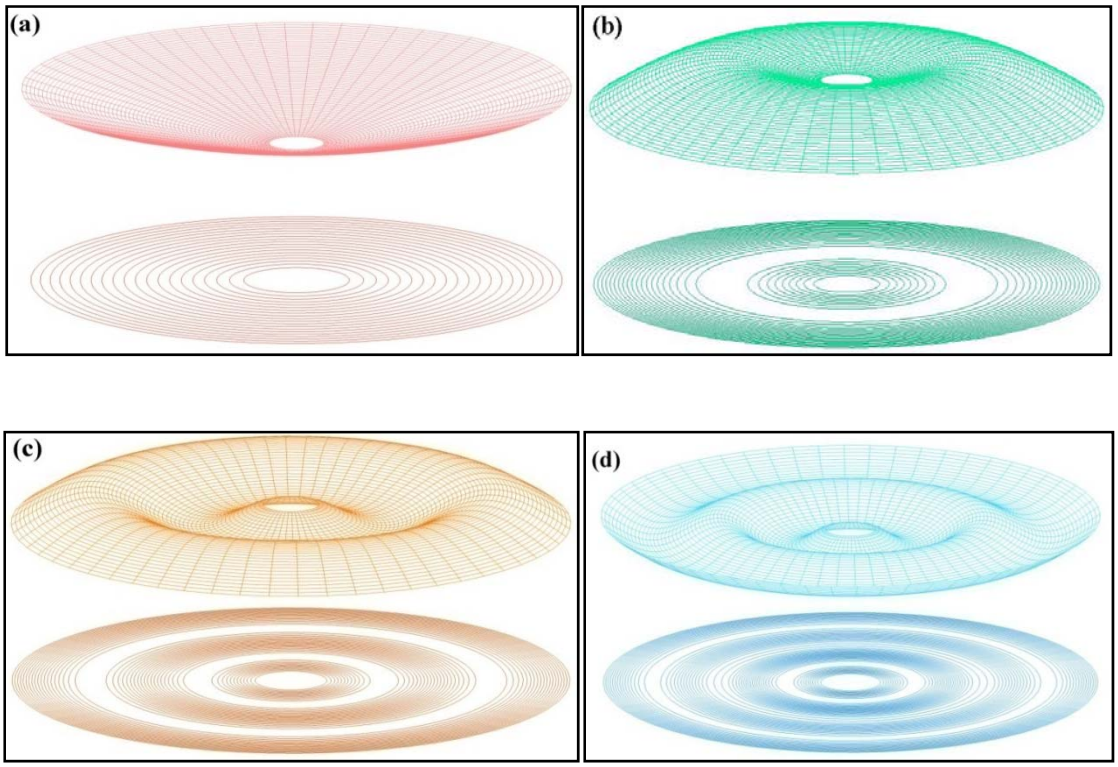

Fig. 5.8: Mode shapes and contour plots of the axisymmetric bending vibration modes: (a) Mode 1, (b) Mode 2, (c) Mode 3, (d) Mode 4.

Figs. 5.9(a)-(d) show the non-dimensional speed-frequency behaviour at a constant transverse pressure for the first four modes, each for different thermal loading. Centrifugal stiffening effect is clearly visible in the plots where the frequency increases with speed. Due to the thermo-elastic degradation of the material properties, it is seen that frequencies decrease as thermal loading increases, and this effect is increased as the mode number increases. For the first mode, at lower speed (up to Ω^* =2.5 approximately), the thermo-elastic degradation is absent, and frequency increases with the increase in the thermal loading.

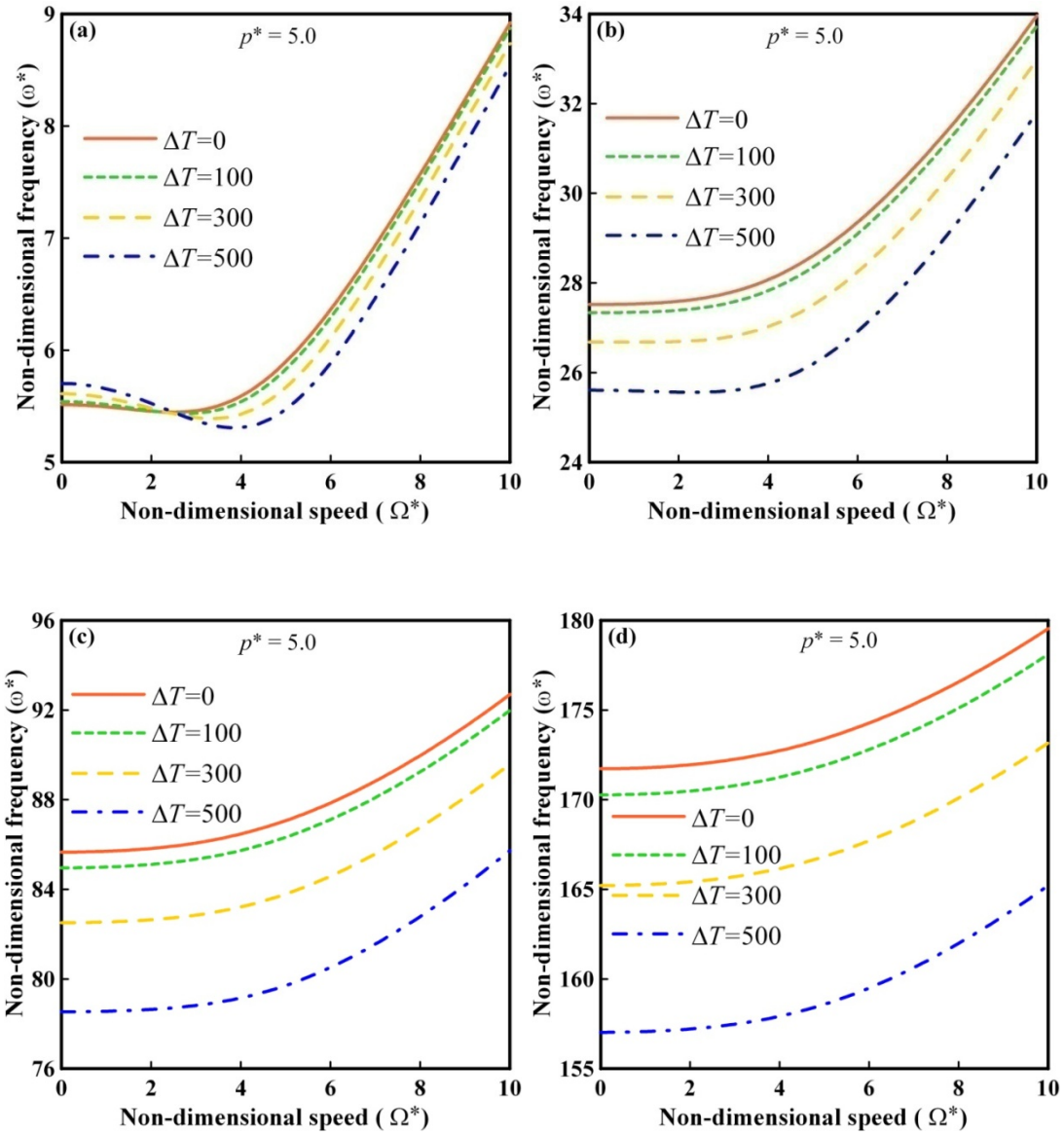

Fig. 5.9: Variation of vibration frequency with rotational speed for different thermal loading under constant transverse pressure: (a) Mode 1, (b) Mode 2, (c) Mode 3, (d) Mode 4.

Figs. 5.10(a)-(d) show the variation of vibration frequency with transverse pressure for different thermal loading under constant rotational speed. In this figure, the influence of pressure on frequency is appreciable for the first modes, but it is not much noticeable for the higher modes. The frequency values decrease as thermal loading increases, indicating thermo-elastic degradation of material properties. With respect to pressure loading, the effect of thermal loading are found to be almost same for all the modes.

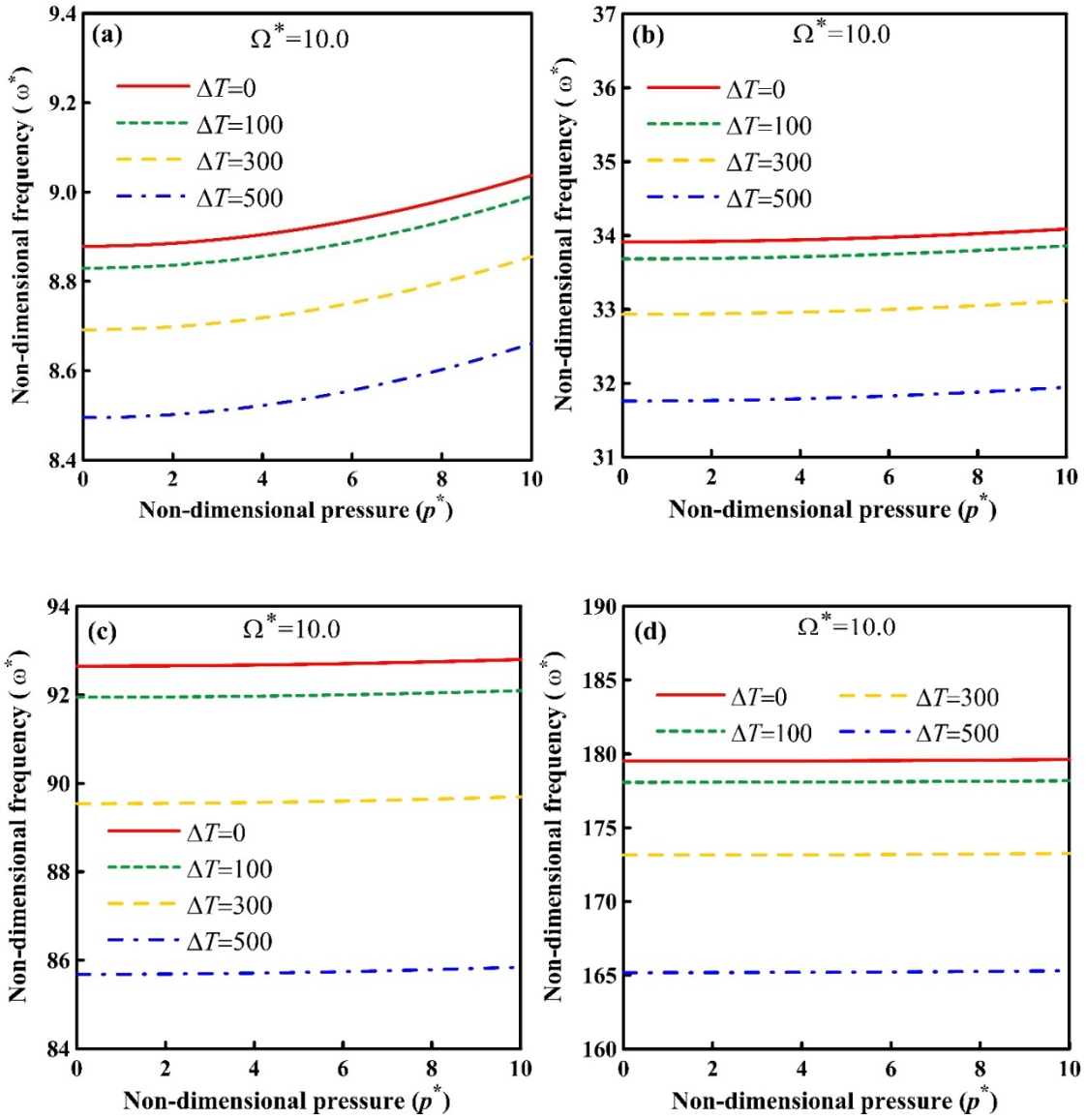

Fig.5.10: Variation of vibration frequency with transverse pressure for different thermal loading under constant rotational speed: (a) Mode 1, (b) Mode 2, (c) Mode 3, (d) Mode 4.

Figs. 5.11(a)-(d) show variation of vibration frequency with rotational speed for different volume fraction indices under constant transverse pressure and thermal loading. For all the values of the volume fraction indices, the frequency values are found to increase with speed, with the exception of the first mode, where they appear to slightly decrease or remain constant in nature at lower speed range. Further the frequencies are found to decrease with increasing values of volume fraction indices. This is due to the fact that increasing of volume fraction indices leads to relative increase of volume proportion of the metal content in the FGM composition, and for Stainless Steel/Silicon Nitride, the metal phase has less elasticity

and more density with respect to the ceramic phase. This effect of volume fraction indices becomes enhanced with increasing mode number.

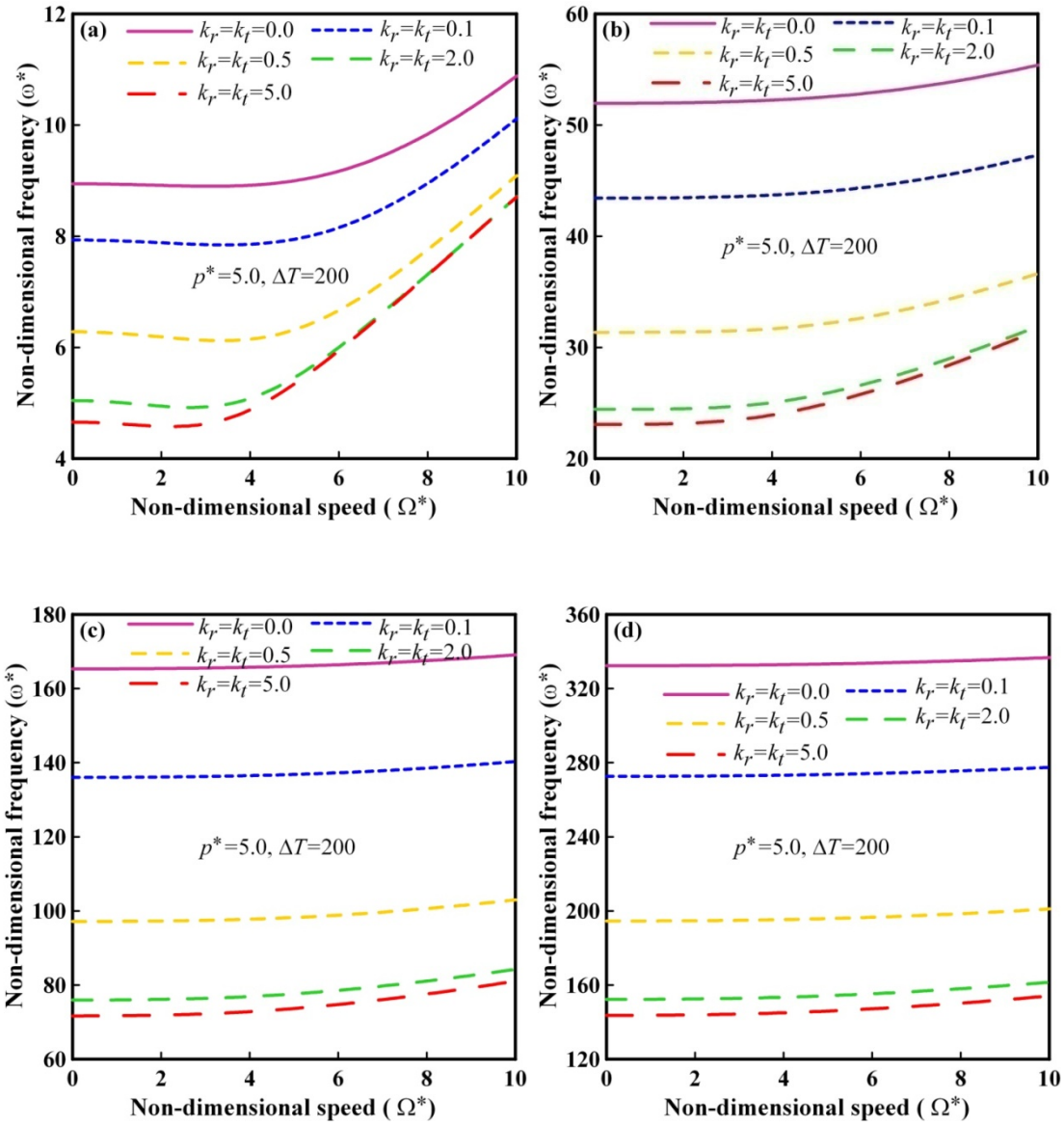

Fig. 5.11: Variation of vibration frequency with rotational speed for different volume fraction indices under constant transverse pressure and thermal loading: (a) Mode 1, (b) Mode 2, (c) Mode 3, (d) Mode 4.

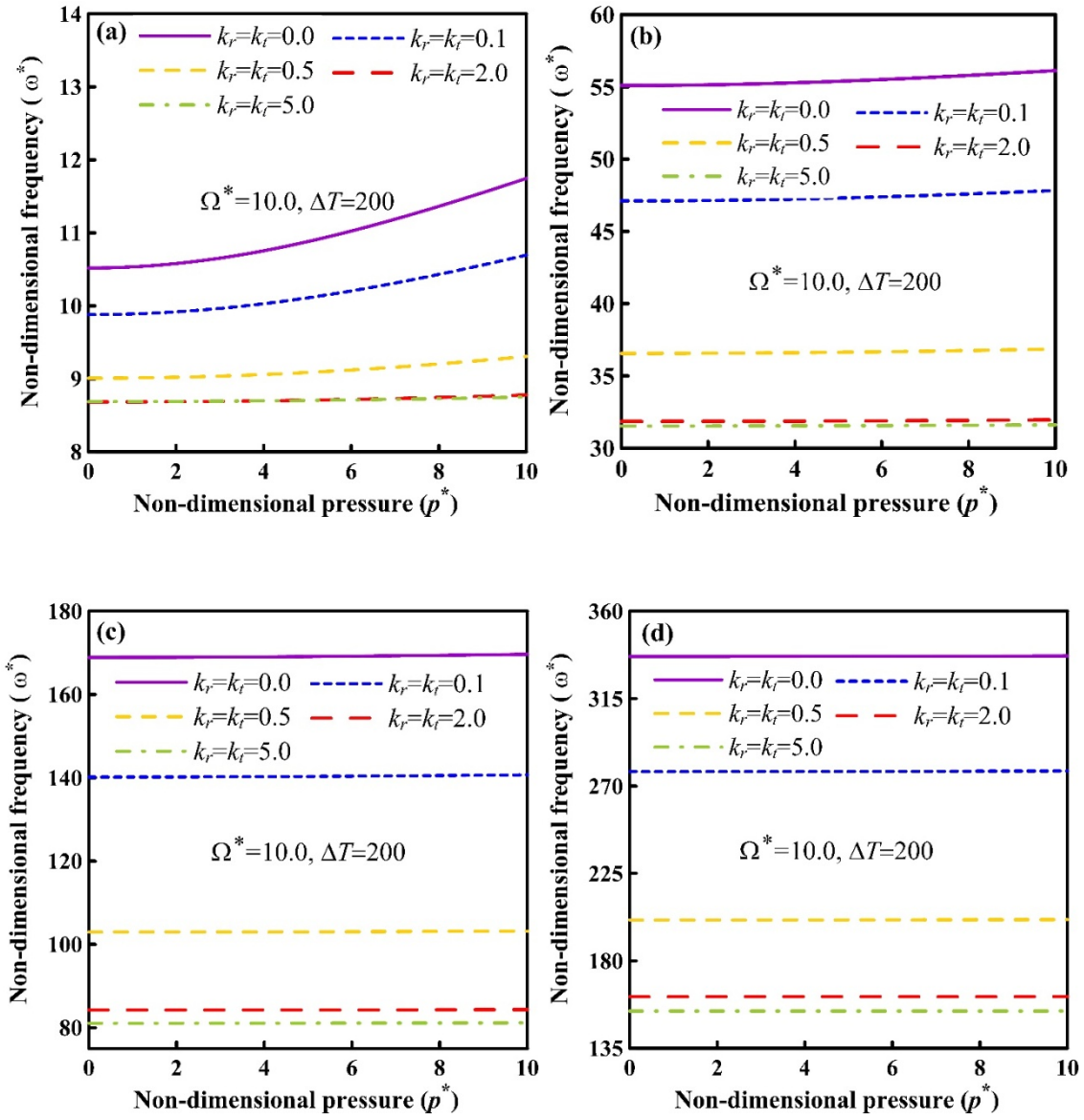

Fig. 5.12: Variation of vibration frequency with transverse pressure for different volume fraction indices under constant rotational speed and thermal loading: (a) Mode 1, (b) Mode 2, (c) Mode 3, (d) Mode 4.

Figs. 5.12(a)-(d) show variation of vibration frequency with transverse pressure for different volume fraction indices under constant rotational speed and thermal loading. The frequency gradually increases with pressure for the first mode, whereas for the higher modes, the frequency remains almost entirely independent of transverse pressure. Further, the frequencies are found to decrease with increasing values of volume fraction indices. This is due to the fact that increasing volume fraction indices leads to relative increase of volume

proportion of the metal content which is less elastic and heavier compared to the ceramic phase.

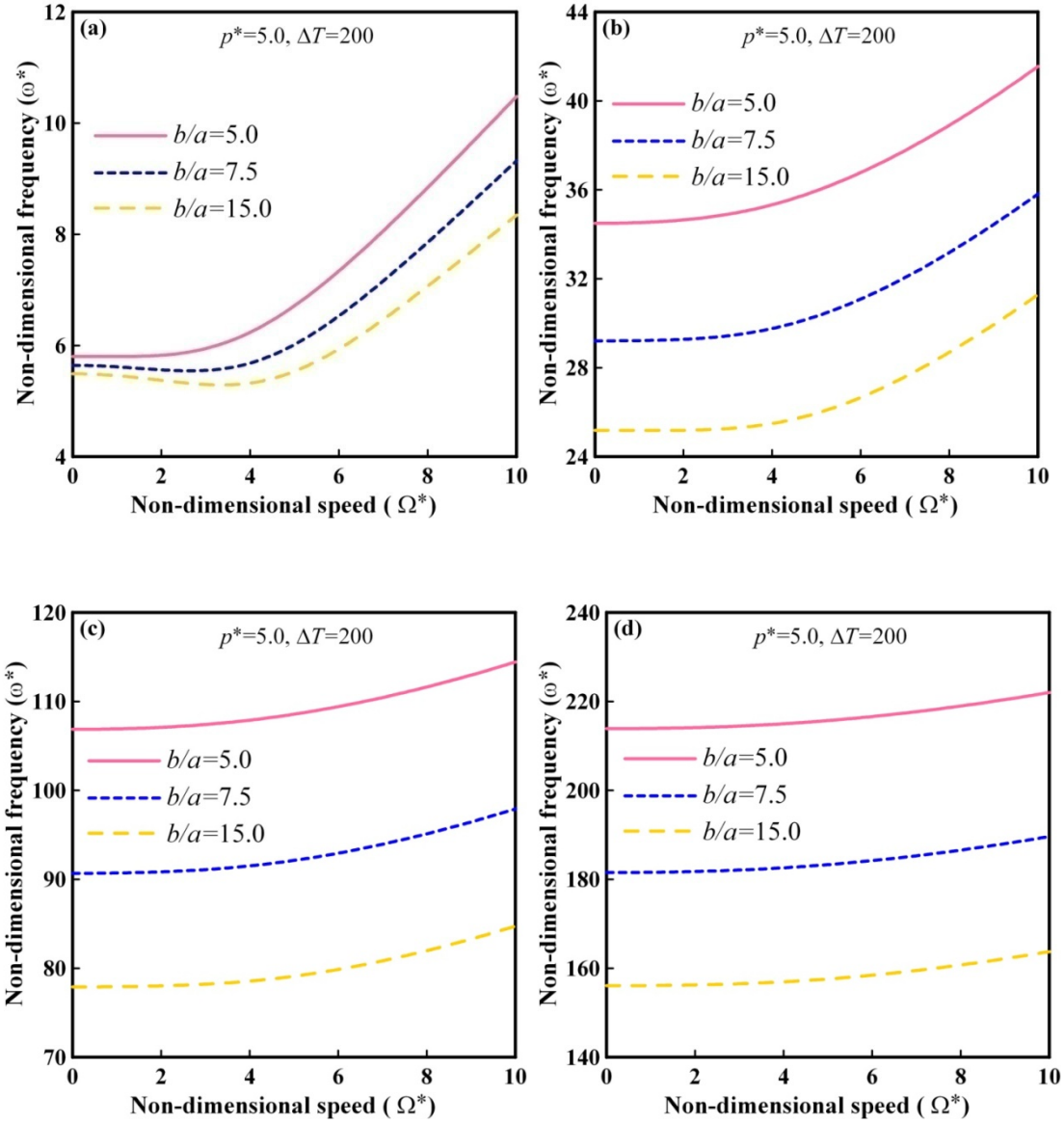

Fig. 5.13: Variation of vibration frequency with rotational speed for different radius ratio under constant transverse pressure and thermal loading: (a) Mode 1, (b) Mode 2, (c) Mode 3, (d) Mode 4.

Figs. 5.13(a)-(d) show the variation of vibration frequency with rotational speed for different radius ratio under constant transverse pressure and thermal loading. In general, the frequency increases with speed. But for the first mode, the frequency slightly decreases or

remains constant with speed at lower speeds, and this is true for all the values of the radius ratio considered. As far as the effect of radius ratio is considered, it shows that the frequencies increase with decreasing radius ratio. This is because the decreasing radius ratio indicates lesser un-supported radial span of the disk which is clamped at the inner radius, and thus stiffness of the disk increases against bending vibration. The effect of radius ratio becomes enhanced with higher modes.

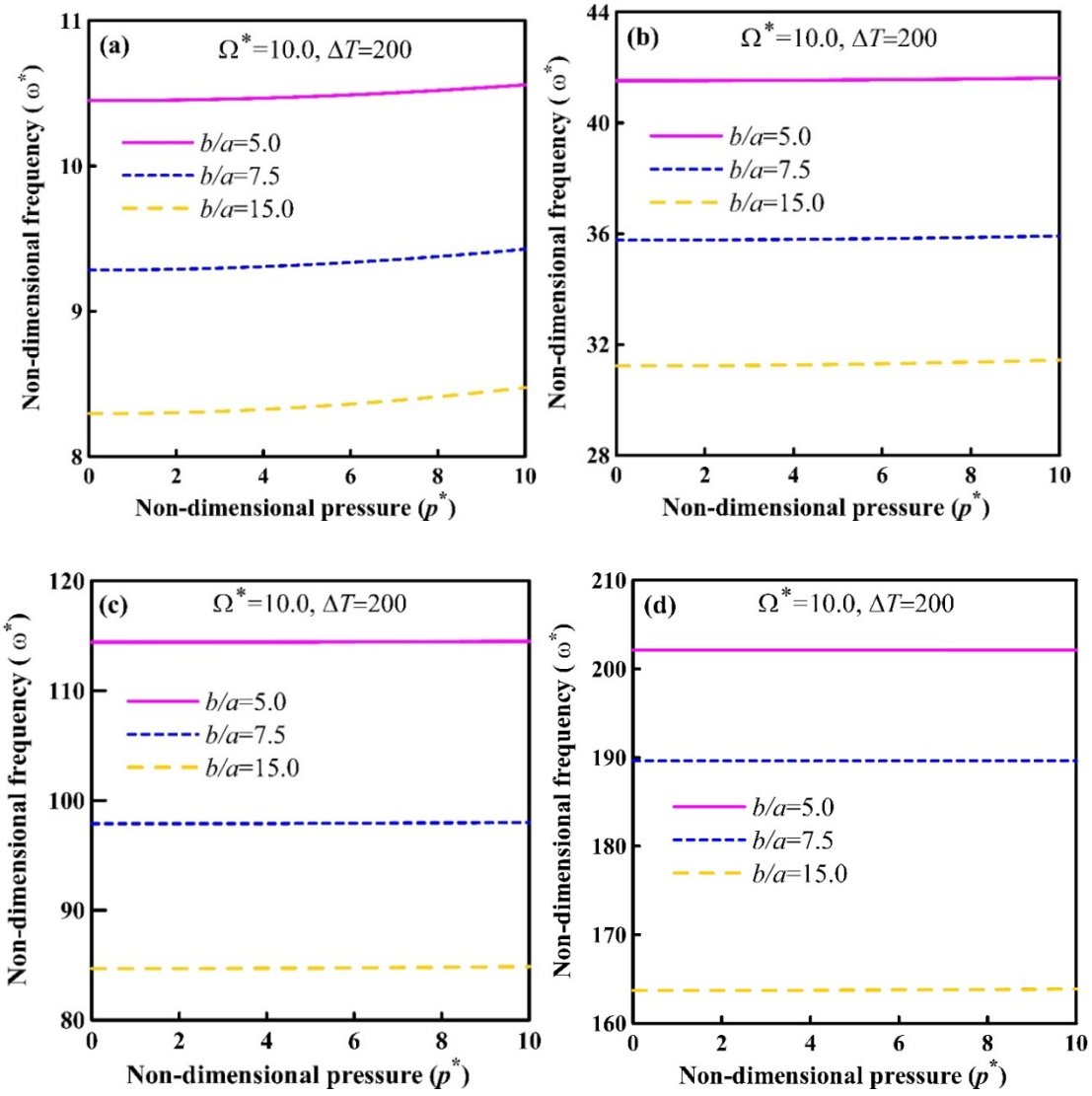

Fig. 5.14: Variation of vibration frequency with transverse pressure for different radius ratio under constant rotational speed and thermal loading: (a) Mode 1, (b) Mode 2, (c) Mode 3, (d) Mode 4.

Figs. 5.14(a)-(d) depicts the variation of vibration frequency with transverse pressure for different radius ratio under constant rotational speed and thermal loading. As already reported, pressure has very little effect on the frequency of vibration. The increasing radius ratio decreases the frequency value of the clamped-free disk as its un-supported radial span increases, and thus making the disk less stiff to bending. This effect seems higher for the higher modes.

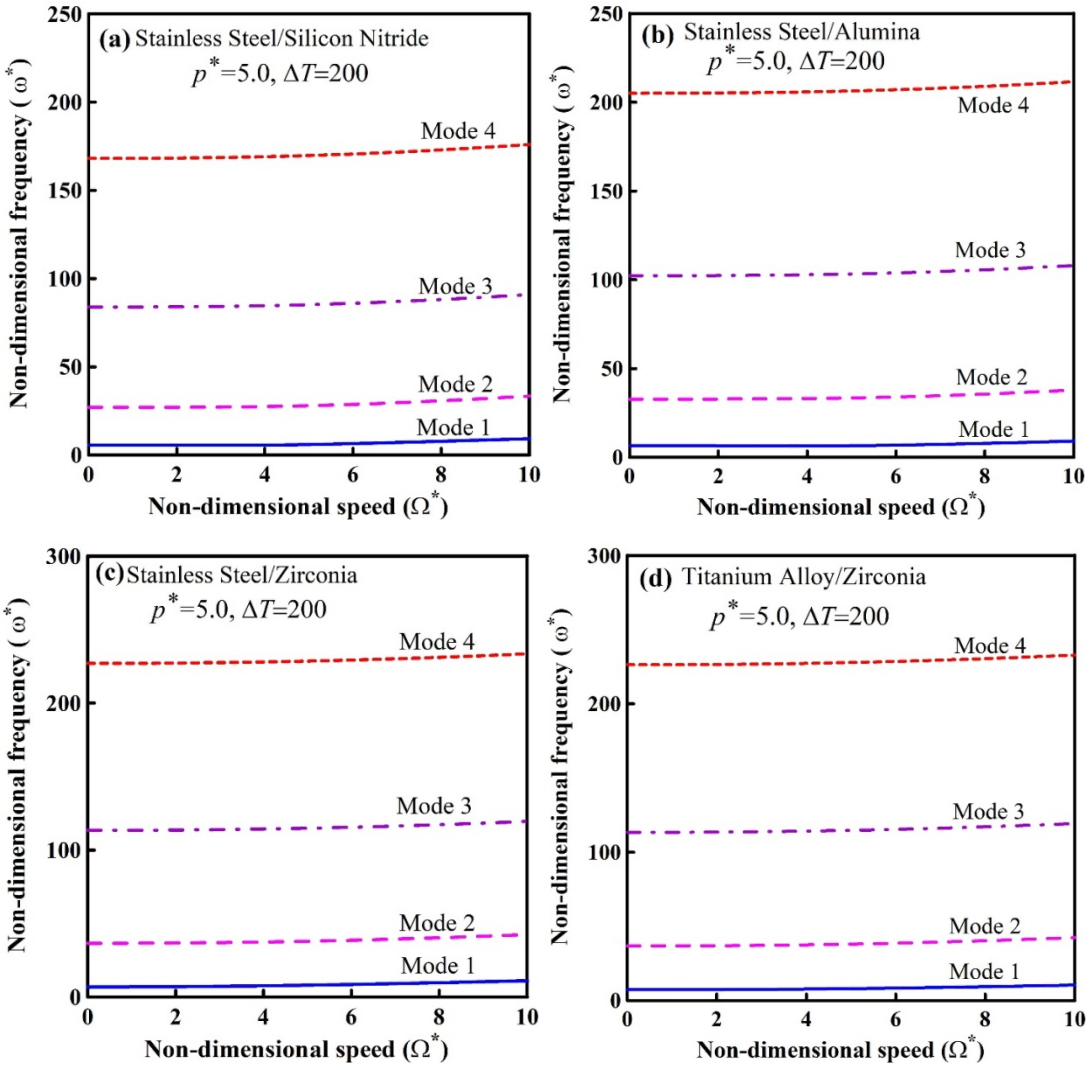

Fig. 5.15: Variation of vibration frequency with rotational speed for different material composition under constant transverse pressure and thermal loading: (a) Stainless Steel/Silicon Nitride, (b) Stainless Steel/Alumina, (c) Stainless Steel/Zirconia, (d) Titanium Alloy/Zirconia.

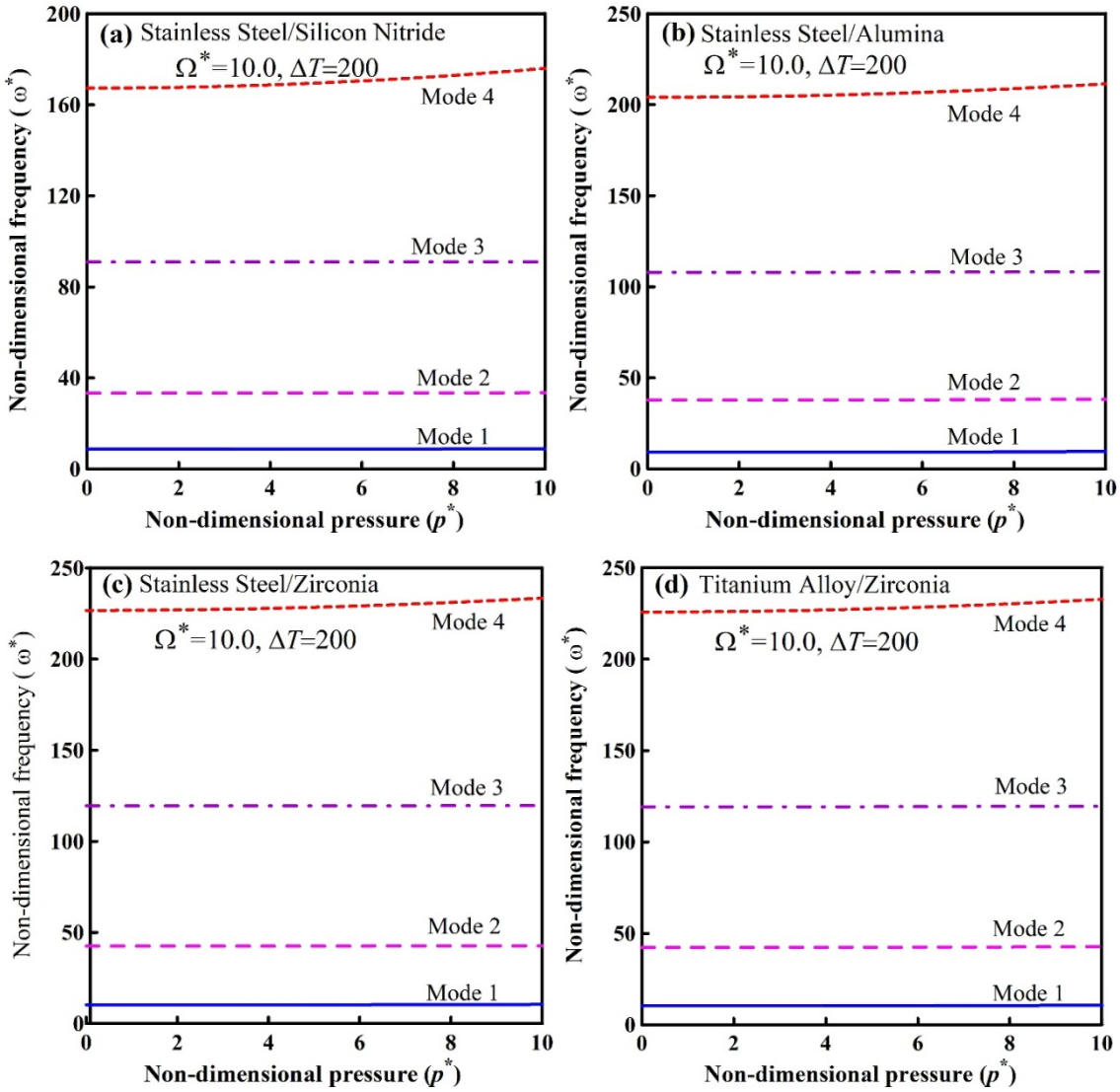

Fig. 5.16: Variation of vibration frequency with transverse pressure for different material composition under constant rotational speed and thermal loading: (a) Stainless Steel/Silicon Nitride, (b) Stainless Steel/Alumina, (c) Stainless Steel/Zirconia, (d) Titanium Alloy/Zirconia.

All the previous results are presented considering Stainless Steel/Silicon Nitride composition. To illustrate the impact of variation of FGM compositions, Figs. 5.15(a)-(d) show speed-frequency behaviour at constant pressure and thermal loading, and Figs. 5.16(a)-(d) show pressure-frequency behaviour at constant speed and thermal loading. Results for Figs. 5.15 and 5.16 are presented for Stainless Steel/Silicon Nitride, Stainless Steel/Alumina, Stainless Steel/Zirconia and Titanium Alloy/Zirconia compositions, each for the first four axisymmetric bending modes. Fig. 5.15 shows that speed-frequency behaviour for all four

compositions are identical, and differs in the relative values. For all the compositions in Fig. 5.15, the frequency increases slightly with increase in speed for all the four modes. Fig. 5.16 shows that the pressure-frequency behaviour for all four compositions are identical, and differs in the relative values. In Fig. 5.16, the increase in frequency with pressure is observed only for the fourth mode, whereas the frequency values for the other modes remain almost constant over the range of pressure considered.

5.4 Chapter Summary

With the objective of studying the free axisymmetric bending vibration behaviour of rotating micro-disks operating in high-pressure and high-temperature environment, a mathematical model has been developed exclusively for the axisymmetric problem. In this chapter, the important problem parameters are defined, and the governing equations are provided in a concise manner, maintaining the overall methodology discussed in Chapter 2. Using Kirchhoff plate theory and the MCST, an energy-based mathematical model is developed. The model is successfully validated by comparing it with several simplified problems. For a wide range of parametric values, the effects of speed, transverse pressure, thermal loading, size-dependent thickness, radial and thickness gradation indices, radius ratio and FGM composition on the frequencies of vibration of the first four modes have been discussed through extensive sets of numerical results. Some mode-shape plots along with their contour have been presented for visualization of the axisymmetric vibration modes. The mathematical model is a novel one. The presented results are the first of their kind and will act as a benchmark for further study in this domain. The key findings of this chapter are summarized below:

- The micro-disk experiences non-linear static bending as a result of the transverse pressure, particularly at low to moderate rotating speeds.
- The effect of centrifugal stiffening is observed clearly at moderate to high speed. For the first and second modes, at lower speed ranges and for moderate and higher-pressure values, the frequency either remains constant or slightly decreases with speed, showing dominance of softening.

- The influence of pressure is observed to diminish with increasing speed. But the increase in pressure results in a mild rise in vibration frequency for all four modes due to enhanced geometric stiffening.
- Under higher thermal loading, the frequency values generally decrease due to thermo-elastic degradation of the micro-disk.
- The size-effect is found to have a considerable impact, where the greatest size-dependent stiffening of the micro-disk is illustrated by the smallest size-dependent thickness, yielding higher frequency values.
- Due to the presence of greater metal content than its ceramic counterpart, increasing the volume fraction indices results in lower frequency values and vice versa.
- Increased radius ratio gives decreased frequency value of the disk due to reduced bending stiffness as a result of increased unsupported radial span of the disk.
- It is found that the speed-frequency and pressure-frequency behaviours are identical for all the FGM four compositions considered, and they only differ in their relative values.

Appendix 5A

Classical Part of Total Stiffness Matrix

The sub-matrices of $\left[\mathbf{S}^{cl}\right]$, each of dimension $n\times n$, are as follows:

$$\left[\mathbf{S}^{cl}\right]=\begin{bmatrix}\left[\mathbf{S}_{\mathbf{11}}^{cl}\right] & \left[\mathbf{S}_{\mathbf{12}}^{cl}\right]\\ \left[\mathbf{S}_{\mathbf{21}}^{cl}\right] & \left[\mathbf{S}_{\mathbf{22}}^{cl}\right]\end{bmatrix}. \tag{5A.1}$$

The components of these sub-matrices are given below:

$$\left[\mathbf{S}_{\mathbf{11}}^{cl}\right]=2\pi\left(b-a\right)\int_0^1\left[E_A\left\{r\frac{\partial\phi_i^u}{\partial r}\frac{\partial\phi_j^u}{\partial r}+\frac{1}{r}\phi_i^u\phi_j^u\right\}+E_{PA}\left\{\phi_i^u\frac{\partial\phi_j^u}{\partial r}+\frac{\partial\phi_i^u}{\partial r}\phi_j^u\right\}\right]d\xi, \tag{5A.2}$$

$$\left[\mathbf{S}_{\mathbf{12}}^{cl}\right]=2\pi\left(b-a\right)\int_0^1\left[\frac{E_A}{2}r\left(\frac{\partial w_0}{\partial r}\right)\frac{\partial\phi_i^u}{\partial r}\frac{\partial\phi_j^w}{\partial r}+\frac{E_{PA}}{2}\left(\frac{\partial w_0}{\partial r}\right)\phi_i^u\frac{\partial\phi_j^w}{\partial r}\right]d\xi, \tag{5A.3}$$

$$\left[\mathbf{S}_{\mathbf{21}}^{cl}\right]=0, \tag{5A.4}$$

$$\begin{aligned}\left[\mathbf{S}_{\mathbf{22}}^{cl}\right]=2\pi\left(b-a\right)\int_0^1\Bigg[&E_A\left\{r\left(\frac{\partial u_0}{\partial r}\right)\frac{\partial\phi_i^w}{\partial r}\frac{\partial\phi_j^w}{\partial r}+\frac{r}{2}\left(\frac{\partial w_0}{\partial r}\right)^2\frac{\partial\phi_i^w}{\partial r}\frac{\partial\phi_j^w}{\partial r}\right\}\\&+E_I\left\{r\frac{\partial^2\phi_i^w}{\partial r^2}\frac{\partial^2\phi_j^w}{\partial r^2}+\frac{1}{r}\frac{\partial\phi_i^w}{\partial r}\frac{\partial\phi_j^w}{\partial r}\right\}+E_{PA}\left(u_0\right)\frac{\partial\phi_i^w}{\partial r}\frac{\partial\phi_j^w}{\partial r}+E_{PI}\left\{\frac{\partial\phi_i^w}{\partial r}\frac{\partial^2\phi_j^w}{\partial r^2}+\frac{\partial^2\phi_i^w}{\partial r^2}\frac{\partial\phi_j^w}{\partial r}\right\}\\&-E_{TA}r\frac{\partial\phi_i^w}{\partial r}\frac{\partial\phi_j^w}{\partial r}\Bigg]d\xi.\end{aligned} \tag{5A.5}$$

Non-classical Part of Total Stiffness Matrix

The sub-matrices of $\left[\mathbf{S}^{ncl}\right]$, each of dimension $n\times n$, are as follows:

$$\left[\mathbf{S}^{ncl}\right]=\begin{bmatrix}\left[\mathbf{S}_{\mathbf{11}}^{ncl}\right] & \left[\mathbf{S}_{\mathbf{12}}^{ncl}\right]\\ \left[\mathbf{S}_{\mathbf{21}}^{ncl}\right] & \left[\mathbf{S}_{\mathbf{22}}^{ncl}\right]\end{bmatrix}. \tag{5A.6}$$

The components of these sub-matrices are given below:

$$\left[\mathbf{S}_{\mathbf{11}}^{ncl}\right]=0, \tag{5A.7}$$

$$\left[\mathbf{S}_{\mathbf{12}}^{ncl}\right]=0, \tag{5A.8}$$

$$\left[\mathbf{S}_{\mathbf{21}}^{ncl}\right]=0, \tag{5A.9}$$

$$\left[\mathbf{S}_{\mathbf{22}}^{ncl}\right]=2\pi\left(b-a\right)l^2\int_0^1 G_A\left[-\frac{\partial\phi_i^w}{\partial r}\frac{\partial^2\phi_j^w}{\partial r^2}-\frac{\partial^2\phi_i^w}{\partial r^2}\frac{\partial\phi_j^w}{\partial r}+r\frac{\partial^2\phi_i^w}{\partial r^2}\frac{\partial^2\phi_j^w}{\partial r^2}+\frac{1}{r}\frac{\partial\phi_i^w}{\partial r}\frac{\partial\phi_j^w}{\partial r}\right]d\xi. \tag{5A.10}$$

Elements of Load Vector

The sub-vectors of $\left[\mathbf{P}\right]$, each of dimension $n\times 1$, are as follows:

$$\left\{\mathbf{P}\right\}=\begin{Bmatrix}\left\{\mathbf{P_1}\right\}\\ \left\{\mathbf{P_2}\right\}\end{Bmatrix}. \tag{5A.11}$$

The components of these sub-vectors are given below:

$$\left\{\mathbf{P_1}\right\}=2\pi\left(b-a\right)\left[\Omega^2\int_0^1\rho_A r^2\phi_i^u d\xi+\int_0^1 E_{TA}\left(\phi_i^u+r\frac{\partial\phi_i^u}{\partial r}\right)d\xi\right], \tag{5A.12}$$

$$\left\{\mathbf{P_2}\right\}=2\pi\left(b-a\right)p_0\int_0^1 r\phi_i^w d\xi. \tag{5A.13}$$

Appendix 5B

Classical Part of Tangent Stiffness Matrix

The sub-matrices of $\left[\mathbf{K}^{\mathbf{cl}}\right]$, each of dimension $n \times n$, are as follows:

$$\left[\mathbf{K}^{cl}\right] = \begin{bmatrix} \left[\mathbf{K}_{\mathbf{11}}^{cl}\right] & \left[\mathbf{K}_{\mathbf{12}}^{cl}\right] \\ \left[\mathbf{K}_{\mathbf{21}}^{cl}\right] & \left[\mathbf{K}_{\mathbf{22}}^{cl}\right] \end{bmatrix}. \tag{5B.1}$$

The components of these sub-matrices are given below:

$$\left[\mathbf{K}_{\mathbf{11}}^{cl}\right] = 2\pi\left(b - a\right)\int_a^b \left[E_A \left\{ r \frac{\partial \phi_i^u}{\partial r}\frac{\partial \phi_k^u}{\partial r} + \frac{1}{r}\phi_i^u \phi_k^u \right\} + E_{PA}\left\{ \phi_i^u \frac{\partial \phi_k^u}{\partial r} + \frac{\partial \phi_i^u}{\partial r}\phi_k^u \right\} \right] d\xi, \tag{5B.2}$$

$$\left[\mathbf{K}_{\mathbf{12}}^{cl}\right] = 2\pi\left(b - a\right)\int_a^b \left[E_A r \left(\frac{\partial w_0}{\partial r} \right) \frac{\partial \phi_i^u}{\partial r}\frac{\partial \phi_k^w}{\partial r} + E_{PA}\left(\frac{\partial w_0}{\partial r} \right) \phi_i^u \frac{\partial \phi_k^w}{\partial r} \right] d\xi, \tag{5B.3}$$

$$\left[\mathbf{K}_{\mathbf{21}}^{cl}\right] = 2\pi\left(b - a\right)\int_a^b \left[E_A r \left(\frac{\partial w_0}{\partial r} \right) \frac{\partial \phi_i^w}{\partial r}\frac{\partial \phi_k^u}{\partial r} + E_{PA}\left(\frac{\partial w_0}{\partial r} \right) \frac{\partial \phi_i^w}{\partial r} \phi_k^u \right] d\xi, \tag{5B.4}$$

$$\begin{aligned} \left[\mathbf{K}_{\mathbf{22}}^{cl}\right] = 2\pi\left(b - a\right)\int_a^b \Bigg[& E_A \left\{ r \left(\frac{\partial u_0}{\partial r} \right) \frac{\partial \phi_i^w}{\partial r}\frac{\partial \phi_k^w}{\partial r} + \frac{3r}{2}\left(\frac{\partial w_0}{\partial r} \right)^2 \frac{\partial \phi_i^w}{\partial r}\frac{\partial \phi_k^w}{\partial r} \right\} \\ & + E_I \left\{ r \frac{\partial^2 \phi_i^w}{\partial r^2}\frac{\partial^2 \phi_k^w}{\partial r^2} + \frac{1}{r}\frac{\partial \phi_i^w}{\partial r}\frac{\partial \phi_k^w}{\partial r} \right\} + E_{PA}\left(u_0 \right) \frac{\partial \phi_i^w}{\partial r}\frac{\partial \phi_k^w}{\partial r} + E_{PI}\left\{ \frac{\partial \phi_i^w}{\partial r}\frac{\partial^2 \phi_k^w}{\partial r^2} + \frac{\partial^2 \phi_i^w}{\partial r^2}\frac{\partial \phi_k^w}{\partial r} \right\} \\ & - E_{TA} r \frac{\partial \phi_i^w}{\partial r}\frac{\partial \phi_k^w}{\partial r} \Bigg] d\xi. \end{aligned} \tag{5B.5}$$

Appendix 5C

Elements of Mass Matrix

The sub-matrices of $[\mathbf{M}]$, each of dimension $n \times n$, are as follows:

$$[\mathbf{M}] = \begin{bmatrix} [\mathbf{M}_{11}] & \mathbf{0} \\ \mathbf{0} & [\mathbf{M}_{22}] \end{bmatrix}. \tag{5C.1}$$

The components of these sub-matrices are given below:

$$[\mathbf{M}_{11}] = 2\pi(b-a)\int_a^b \left[\rho_A r \phi_i^u \phi_j^u\right] d\xi, \tag{5C.2}$$

$$[\mathbf{M}_{22}] = 2\pi(b-a)\int_a^b \left[\left(\rho_A r \phi_i^w \phi_j^w\right) + \left(\rho_I r \frac{\partial \phi_i^w}{\partial r}\frac{\partial \phi_j^w}{\partial r}\right)\right] d\xi. \tag{5C.3}$$

Chapter 6

FREE VIBRATION & STATIC BUCKLING BEHAVIOURS OF BFGM ROTATING MICRO-DISKS FOR DIFFERENT BOUNDARY CONDITIONS

6.1 Introduction

The literature survey shows that the free vibration behaviour of rotating BFGM micro-disks has not yet been studied for annular configuration under different boundary conditions. Though studies on rotating FGM micro-size plates are available (Mahinzare et al. (2018a), Mahinzare et al. (2018b), Shojaeefard et al. (2018a) and Shojaeefard et al. (2018b)), they are conducted for rotating solid micro-plates under clamped and hinged boundary conditions. For rotating annular micro-disks, no research work dealing with their vibration behaviour is available in the literature. Hence there exists a research gap. The BFGM micro-disk for which the free vibration behaviour has been studied in the preceding three chapters, is essentially considered as clamped-free, i.e., its inner radius is rigidly mounted on a shaft and its outer radius is free.To acquire a comprehensive understanding of rotating disk dynamics, it is essential to study the free vibration behaviour of rotating annular micro-disks under different boundary conditions. Hence, to fill up the research gap, and for thematic development of the present thesis, another problem has been undertaken in this chapter, which studies the free vibration behaviour of BFGM rotating annular micro-disks under four different boundary conditions namely, simply supported-simply supported (SS), clamped-simply supported (CS), simply supported-clamped (SC) and clamped-clamped (CC). Here ‘S’ and ‘C’ stand for clamped and simply supported boundary condition respectively. The first letter of each boundary condition corresponds to the inner radius and the second letter corresponds to the outer radius.

Unlike the previous two chapters, the present problem is studied for a micro-disk, which is subjected to centrifugal loading due to rotational speed and thermal loading due to high-temperature environment, i.e., the effect of transverse pressure has not been considered

in this case. Another striking feature of this problem is that the critical condition leading to static buckling of the BFGM micro-disk, when the vibration frequency becomes zero, has been identified and reported. While considering different boundary conditions mentioned above, the micro-disk is assumed radially immovable due to constraints both at the inner and outer radii. This induces compressive axial force due to both centrifugal and thermal loading, resulting in softening of the micro-disk. As a result, the vibration frequency becomes zero at a particular higher value of the rotating speed, making the disk statically unstable. This particular speed is termed as the critical buckling speed.

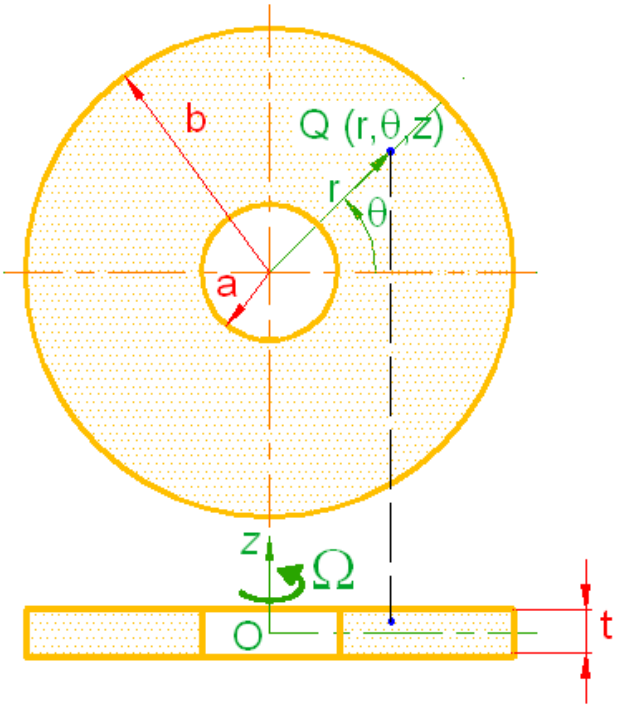

Fig. 6.1: Two-dimensional schematic diagram of a rotating disk.

The mathematical model for this problem has been successfully validated with appropriate problems pertaining to different boundary conditions. The effects on the first four frequencies of vibration for different parameters such as rotating speed, size-dependent thickness, gradation indices and radius ratio have been presented. Some representative mode-shapes along with their contour have been presented. As far as the critical buckling speed is considered, the effects of size-dependent thickness and gradation indices have been depicted. The present model can be obtained from the generalized mathematical model discussed in Chapter 2. The outline of the mathematical formulation has been briefly discussed in the

following section, to maintain continuity and to have a better understanding of the numerical results.

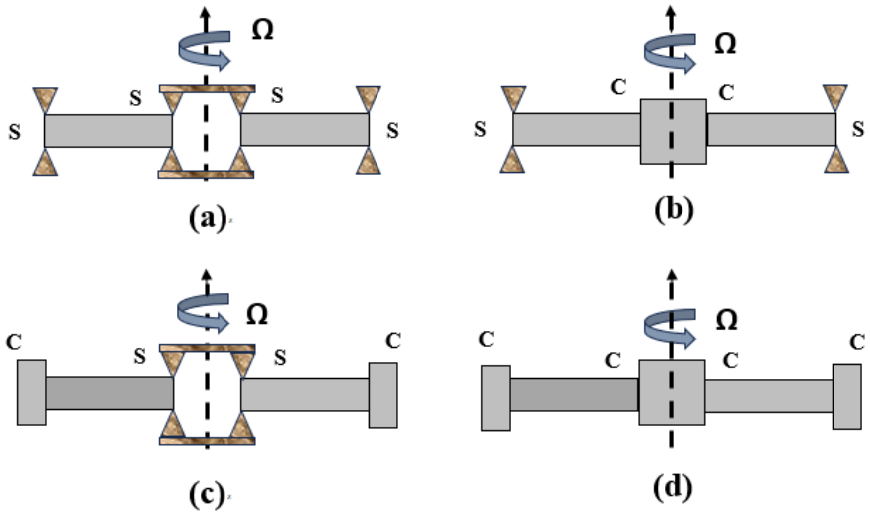

Fig. 6.2: Schematic diagram showing different boundary configurations: (a) SS, (b) CS, (c) SC, (d) CC.

6.2 Mathematical Background

A rotating micro-disk having inner radius a, outer radius b and constant thickness t is considered as shown in Fig. 6.1. Figs. 6.2(a)-(d) have been presented to show the cross-sectional view of the micro-disk for SS, CS, SC and CC boundary conditions respectively. The disk is made of metal-ceramic BFGM, which is graded along the radial and transverse directions, following Voigt rule involving power law. The parameters k_r and k_t symbolize the gradation indices along the radial and thickness directions respectively. The material properties are determined using Eq. (2.5).The model is developed using two steps. In the first step, the deformed configuration of the BFGM micro-disk under centrifugal loading due to constant rotational speed (Ω) and thermal loading $(\Delta T = T - T_0)$ due to uniform temperature rise has been determined. In the second step, the free vibration response of the deformed BFGM micro-disk about its deformed configuration has been determined. Thereafter, the critical buckling speed at which the frequency of vibration of the first bending mode becomes zero has been determined by tracking the speed-frequency behaviour.

For the first step, the governing equations remain same as Eq. (2.34), which is again given below:

$$\left[\mathbf{S}\right]\left\{\mathbf{c}\right\}=\left\{\mathbf{P}\right\}. \tag{6.1}$$

In Eq. (6.1), $\left[\mathbf{S}\right]$ is the total stiffness matrix (of dimension $3n\times 3n$, where n is the number of functions to discretize each of the displacement fields $\left\{u_0, v_0, w_0\right\}$) having classical $\left(\left[\mathbf{S}^{cl}\right]\right)$ and non-classical $\left(\left[\mathbf{S}^{ncl}\right]\right)$ parts; $\left\{\mathbf{c}\right\}$ is the vector of unknown coefficients c_j to be determined with reference to Eqs. (2.31a)-(2.31c); $\left\{\mathbf{P}\right\}$ is the load vector due to rotational speed and thermal loading. The components of $\left[\mathbf{S}^{cl}\right]$ and $\left[\mathbf{S}^{ncl}\right]$ remain same as given in Appendix 2A. In the absence of transverse pressure, the components of the load vector $\left\{\mathbf{P}\right\}=\left\{\left\{\mathbf{P}_1\right\}\ \left\{\mathbf{P}_2\right\}\ \left\{\mathbf{P}_3\right\}\right\}^T$ for the present problem are derived to the following form:

$$\left\{\mathbf{P}_1\right\}=\Omega^2\int_0^1\int_0^1\rho_A r^2\phi_i^u\left|\mathbf{J}\right|d\xi d\mu+\int_0^1\int_0^1 E_{TA}\left[\phi_i^u+r\frac{\partial\phi_i^u}{\partial r}\right]\left|\mathbf{J}\right|d\xi d\mu, \tag{6.2a}$$

$$\left\{\mathbf{P}_2\right\}=\int_0^1\int_0^1 E_{TA}\frac{\partial\phi_i^v}{\partial\theta}\left|\mathbf{J}\right|d\xi d\mu, \tag{6.2b}$$

$$\left\{\mathbf{P}_3\right\}=0. \tag{6.2c}$$

The governing equations for the second step have already been derived as an eigenvalue problem in Eq. (2.42), which is again given below:

$$\left[\left[\mathbf{K}\right]-\omega^2\left[\mathbf{M}\right]\right]\left\{\mathbf{d}\right\}=0. \tag{6.3}$$

In Eq. (6.3), $\left[\mathbf{K}\right]$ is the tangent stiffness matrix, the components of which are given in Appendix 2C; $\left[\mathbf{M}\right]$ is the mass matrix, the components of which are given in Appendix 2D; $\left\{\mathbf{d}\right\}$ is the set of unknown coefficients representing the dynamic displacements. With respect to Eq. (6.3), the square roots of the eigenvalues $\left(\omega^2\right)$ signify the frequencies of vibration of the deformed micro-disk, and the eigenvectors i.e., $\left\{\mathbf{d}\right\}$ provide the corresponding mode-shapes of vibration. The mode-shapes are obtained by appropriately substituting $\left\{\mathbf{d}\right\}$ into Eqs. (2.39a)-(2.39c).

6.3 Results and Discussion

The non-dimensional speed $\left(\Omega^*\right)$ and frequency of vibration $\left(\omega^*\right)$ are defined as follows (Das et al. (2010); Kermani et al. (2016); Shojaeefard et al. (2018b)):

$$\Omega^* = \Omega b^2 \sqrt{\rho_c t / D}, \tag{6.4a}$$

$$\omega^* = \omega b^2 \sqrt{\rho_c t / D}, \tag{6.4b}$$

where $D = E_c^0 t^3 \Big/ \left\{12\left(1-\left(\upsilon_c^0\right)^2\right)\right\}$. The non-dimensional parameters defined above are defined with reference to the property values of the ceramic phase of the FGM composition at $T_0\left(=300\,\mathrm{K}\right)$. The numerical results for this chapter are presented for Stainless Steel/Silicon Nitride composition. Based on the Touloukian model given by Eq. (2.6), the Young's modulus $\left(E_c^0\right)$, Poisson's ratio $\left(\upsilon_c^0\right)$ and mass density $\left(\rho_c\right)$ of Silicon Nitride (ceramic) are calculated, and their values are obtained as 322.27 GPa, 0.240 and 2370 kg/m^3 respectively. If not mentioned otherwise, the numerical results are generated for the following parameter values: $l = 17.6\times10^{-6}$ m (Lam et al. (2003); Park and Gao (2006)), $t/l = 1$, $b/t = 50$, $b/a = 4.0$, $k_r = k_t = 1$, $\Delta T = 0$.Accordingly, the dimensions of the BFGM rotating annular micro-disk become: $t = 17.6$ μm, $b = 880$ μm, $a = 220$ μm. Based on the convergence study reported in the third chapter, the number of functions for Ritz approximation has been taken as $n = 8\times 8$ for generation of results. The mode number of any vibration frequency is denoted by $\left(p,q\right)$ where p and q signify the number of nodal circles and nodal diameters respectively. It must be mentioned that $q = 0$ signifies an axisymmetric vibration mode, and the presence of one or more nodal diameters generates an asymmetric mode $\left(q \neq 0\right)$.

The present formulation is quite general in nature and can be applied for a wide variety of problems by properly adjusting certain parameters as follows: the present model can be reduced to a plate model under non-rotating condition by putting the rotational speed $\Omega = 0$; the size-independent behaviour for a macro-size rotating disk can be investigated by substituting $l = 0$; the problem of solid micro-plate clamped at the outer edge can be

investigated by putting a=0, $\Omega = 0$, and considering $\psi_1^u = \psi_1^v = \xi(1-\xi)$; $\psi_1^w = (1-\xi)^2$ as the lowest order admissible function for Ritz discretization; the problem of solid micro-plate simply supported at the outer edge can be investigated by putting a=0, $\Omega = 0$ and considering $\psi_1^u = \psi_1^v = \xi(1-\xi)$; $\psi_1^w = \sin\{0.5\pi(1-\xi)\}$ as the lowest order admissible function for Ritz discretization; a radial-FG micro-disk/plate is obtained by putting $k_t = 0$; a thickness-FG micro-disk/plate is obtained by putting $k_r = 0$.

Table 6.1: Comparison of the free bending vibration frequencies (ω^*) for the first four modes of homogeneous annular plate for different boundary conditions and radius ratios.

Boundary Condition	Mode	b/a=2.5		b/a=5.0	
		Present	Zhou et al. (2011)	Present	Zhou et al. (2011)
SS	1st (0,0)	28.086	28.183	16.734	16.733
	2nd (0,1)	30.079	30.079	19.197	19.432
	3rd (0,2)	36.139	36.143	27.248	27.285
	4th (0,3)	46.311	46.321	40.330	40.340
CS	1st (0,0)	41.242	41.261	22.755	22.767
	2nd (0,1)	42.529	42.548	24.309	24.322
	3rd (0,2)	46.678	46.699	30.118	30.088
	4th (0,3)	54.307	54.332	41.353	41.329
SC	1st (0,0)	44.931	44.932	26.626	26.619
	2nd (0,1)	46.732	46.735	29.160	29.158
	3rd (0,2)	52.345	52.353	37.573	37.579
	4th (0,3)	62.135	62.148	51.670	51.685
CC	1st (0,0)	61.846	61.872	34.593	34.609
	2nd (0,1)	62.968	62.996	36.085	36.103
	3rd (0,2)	66.640	66.672	41.797	41.820
	4th (0,3)	73.592	73.630	53.361	53.388

6.3.1 Validation Study

Based on the classical plate theory (l=0), the free bending vibration frequencies (ω^*) for the first four modes of a homogeneous ($k_r = k_t = 0$) annular plate are compared with Zhou et al.

(2011) in Table 6.1, and the comparison study is conducted for four boundary conditions which are SS, CS, SC and CC, each for two different radius ratio such as b/a = 2.5 and 5.0. These results are generated considering ν =1/3, b/t =100 and ΔT =0. The comparison shows excellent agreement.

Based on the classical plate theory (l =0), free bending vibration frequencies $\left(\omega^*\right)$ for the first four modes of a radial-FG annular rotating disk with CS boundary condition are compared with Kermani et al. (2016) and presented in Table 6.2 for both rotating as well as non-rotating condition. The comparison study is carried out considering the following values and relations: b/t =100, b/a =5, $E_f = 3800e^{\lambda r/b}$ GPa, $\rho_f = 380e^{\lambda r/b}$ kg/m^3, $\nu_f = 0.3$ (constant)with λ =1.The comparison shows excellent matching of results.

Table 6.2: Comparison of the free bending vibration frequencies $\left(\omega^*\right)$ for the first four modes of a CS radial-FG annular rotating disk.

Mode	Ω = 0 rpm		Ω = 2000 rpm	
	Present	Kermani et al. (2016)	Present	Kermani et al. (2016)
1st (0,0)	21.48	21.53	19.39	19.43
2nd (0,1)	23.29	23.34	21.42	21.54
3rd (0,2)	29.63	29.67	28.39	28.49
4th (0,3)	41.24	41.28	40.46	40.52

Table 6.3: Comparison of the free bending vibration frequencies (kHz) for the first three axisymmetric modes of a homogeneous simply supported solid circular micro-plate.

t/l	Reference	Mode		
		1st	2nd	3rd
1	Present	1.2051	13.3244	34.1734
	Eshraghi et al. (2015)	1.2051	13.3263	34.1874
2	Present	1.1565	8.6926	22.0047
	Eshraghi et al. (2015)	1.1566	8.6939	22.0136

Based on the MCST, the free bending vibration frequencies (kHz) for the first three axisymmetric modes of a homogeneous ($k_r = k_t = 0$) simply supported solid circular micro-plate ($k_r = k_t = 0$) are compared with Eshraghi et al. (2015)and presented in Table 6.3. The

results for this comparison study are generated using the following values: $t = 100 \times 10^{-6}$ m, $b/t = 50$, $E = 1.44$ GPa, $\nu = 0.38$, $\rho = 1220$ kg/m^3. The comparison shows excellent agreement. The comparisons shown through Tables 6.1-6.3establish the validity of the present model.

6.3.2 Numerical Results for Different Parameters

The variation of the free vibration frequencies with rotational speed is shown in Figs. 6.3(a)-(d) for the first four modes respectively, where each figure shows results for all the four boundary conditions namely, SS, CS, SC and CC. All the modes shown in the plots are bending in nature where the first mode is an axisymmetric one ((0,0)),and the other three modes are ((0,1), (0,2) and (0,3)) are asymmetric for all the boundary condition stated above. The micro-disks for different boundary conditions can be arranged in increasing sequence of vibration frequency for all four modes as follows: SS, CS, SC and CC. Both the SS and CS micro-disks demonstrate a softening behaviour across all the four modes indicating a gradual initial decrease in frequency with speed followed by a more rapid decline at higher speeds. In this case, as the mode number increases, the rate at which the frequency decreases with speed gradually diminishes. It is worth mentioning that in contrast to the other two boundary conditions, the speed-frequency behaviours for SC and CC micro-disks show a distinct pattern. For all four modes, the SC micro-disk exhibits hardening-type speed-frequency behaviour, where the frequency increases with speed first slowly and afterward quite rapidly. This rate also increases with the mode number. For the CC micro-disk, the first two modes show a moderate softening type speed-frequency behaviour, where the frequency slowly drops with speed, which is more visible for the first mode. However, for the third and fourth modes of the CC micro-disk, the speed-frequency behaviour changes to a hardening type, with the fourth mode having a considerably larger rate of frequency rise with speed. The instability condition associated with static buckling is expected to occur at greater rotating speeds when the micro-disk's frequency becomes zero because of the radial immovability of the disk. This is valid for all the boundary conditions including those that initially display a hardening kind of speed-frequency behaviour. Figs. 6.4(a)-(d) provide visual understanding of the vibrating CS micro-disk with $b/a = 10$, illustrating the mode-shapes and contour plots indicating deformation patterns for the first four modes.

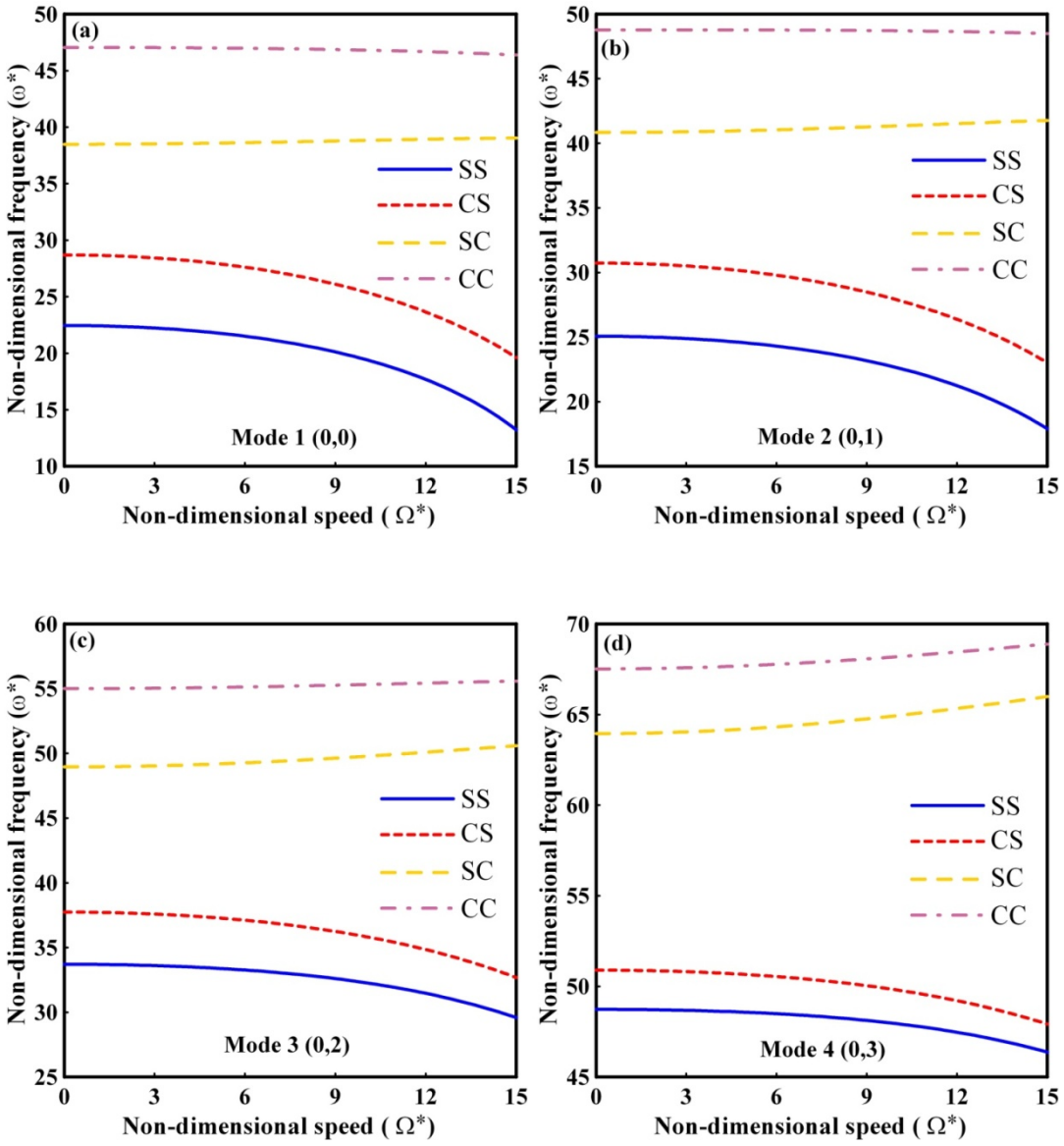

Fig. 6.3: Non-dimensional speed versus frequency behaviour for different boundary conditions: (a) Mode 1 (0,0), (b) Mode 2 (0,1), (c) Mode 3 (0,2), (d) Mode4 (0,3).

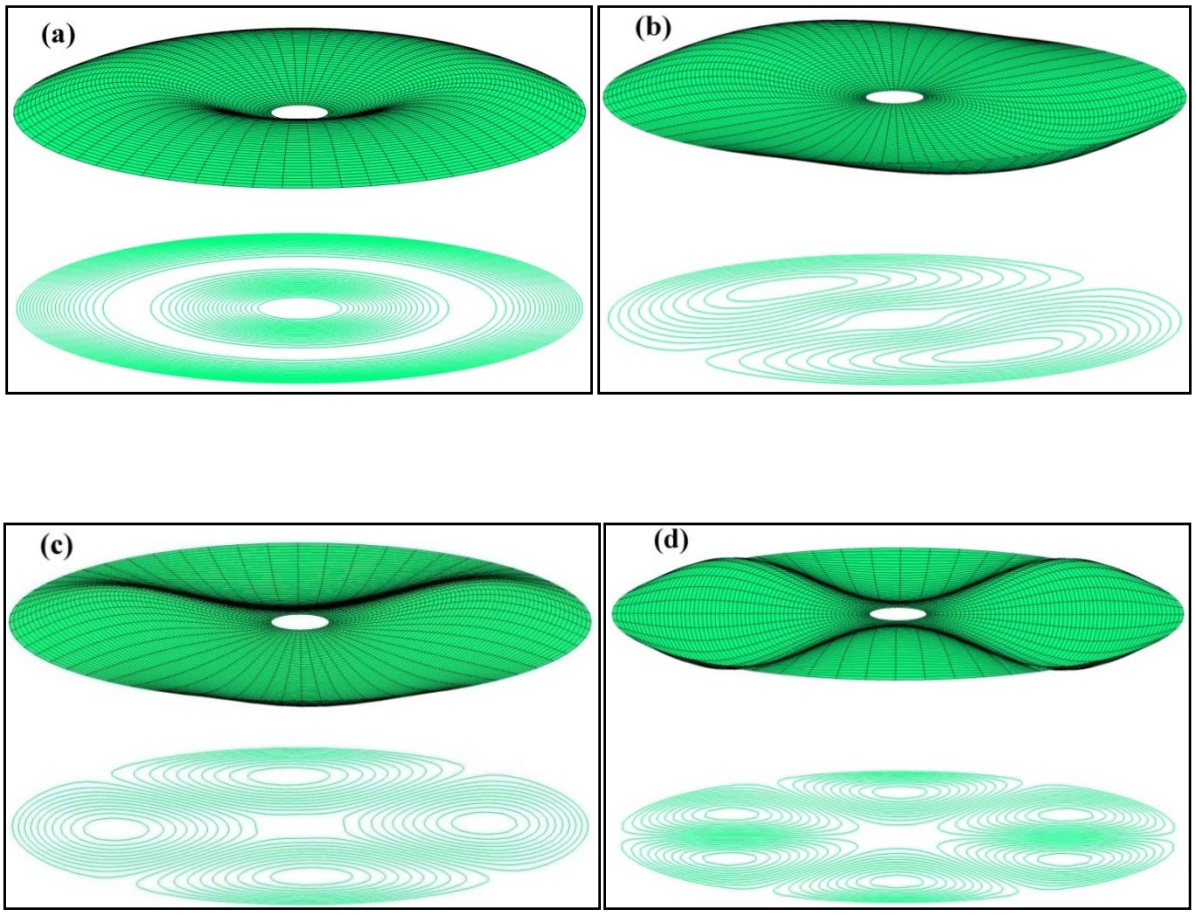

Fig. 6.4: Mode shape and contour plots for a CS micro-disk for b/a=10: (a) Mode 1 (0,0), (b) Mode 2 (0,1), (c) Mode 3 (0,2), (d) Mode 4 (0,3).

Table 6.4: Effect of size-dependent thickness on the free vibration frequencies of the first four modes for different boundary conditions and rotational speeds.

t/l	BC**	$\Omega^*=5$				$\Omega^*=10$				$\Omega^*=15$			
		Mode				Mode				Mode			
		1st	2nd	3rd	4th	1st	2nd	3rd	4th	1st	2nd	3rd	4th
1	SS	21.82 (0,0)	24.55 (0,1)	33.41 (0,2)	48.57 (0,3)	19.46 (0,0)	22.64 (0,1)	32.29 (0,2)	47.94 (0,3)	13.23 (0,0)	17.91 (0,1)	29.59 (0,2)	46.38 (0,3)
	CS	27.96 (0,0)	30.09 (0,1)	37.31 (0,2)	50.66 (0,3)	25.42 (0,0)	27.89 (0,1)	35.85 (0,2)	49.81 (0,3)	19.63 (0,0)	23.01 (0,1)	32.68 (0,2)	47.92 (0,3)
	SC	38.59 (0,0)	40.98 (0,1)	49.18 (0,2)	64.21 (0,3)	38.83 (0,0)	41.35 (0,1)	49.78 (0,2)	64.94 (0,3)	39.04 (0,0)	41.77 (0,1)	50.59 (0,2)	65.99 (0,3)
	CC	47.00 (0,0)	48.77 (0,1)	55.09 (0,2)	67.70 (0,3)	46.81 (0,0)	48.71 (0,1)	55.32 (0,2)	68.19 (0,3)	46.39 (0,0)	48.49 (0,1)	55.58 (0,2)	68.89 (0,3)
2	SS	13.34 (0,0)	15.22 (0,1)	21.10 (0,2)	30.87 (0,3)	8.35 (0,0)	11.40 (0,1)	18.91 (0,2)	29.60 (0,3)	-*	-*	9.57 (0,2)	24.99 (0,3)
	CS	17.60 (0,0)	19.00 (0,1)	23.70 (0,2)	32.23 (0,3)	12.75 (0,0)	14.89 (0,1)	20.99 (0,2)	30.63 (0,3)	-*	-*	11.55 (0,2)	25.63 (0,3)
	SC	23.87 (0,0)	25.51 (0,1)	30.94 (0,2)	40.66 (0,3)	24.19 (0,0)	26.01 (0,1)	31.79 (0,2)	41.70 (0,3)	23.93 (0,0)	26.08 (0,1)	32.49 (0,2)	42.82 (0,3)
	CC	29.60 (0,0)	30.76 (0,1)	34.86 (0,2)	42.93 (0,3)	29.21 (0,0)	30.57 (0,1)	35.12 (0,2)	43.60 (0,3)	28.08 (0,0)	29.78 (0,1)	35.09 (0,2)	44.25 (0,3)
5	SS	9.61 (0,0)	11.22 (0,1)	16.00 (0,2)	23.63 (0,3)	-*	3.08 (0,1)	12.30 (0,2)	21.49 (0,3)	-*	-*	-*	8.27 (0,3)
	CS	13.30 (0,0)	14.42 (0,1)	18.11 (0,2)	24.70 (0,3)	3.83 (0,0)	7.28 (0,1)	13.79 (0,2)	22.14 (0,3)	-*	-*	-*	8.71 (0,3)
	SC	17.59 (0,0)	18.96 (0,1)	23.38 (0,2)	30.99 (0,3)	17.90 (0,0)	19.51 (0,1)	24.33 (0,2)	32.18 (0,3)	16.55 (0,0)	18.64 (0,1)	24.37 (0,2)	32.83 (0,3)
	CC	22.42 (0,0)	23.35 (0,1)	26.56 (0,2)	32.79 (0,3)	21.74 (0,0)	22.93 (0,1)	26.74 (0,2)	33.51 (0,3)	19.43 (0,0)	21.10 (0,1)	25.96 (0,2)	33.65 (0,3)
10	SS	8.93 (0,0)	10.50 (0,1)	15.12 (0,2)	22.40 (0,3)	-*	-*	10.91 (0,2)	19.99 (0,3)	-*	-*	-*	-*
	CS	12.56 (0,0)	13.64 (0,1)	17.16 (0,2)	23.43 (0,3)	-*	5.15 (0,1)	12.33 (0,2)	20.58 (0,3)	-*	-*	-*	-*
	SC	16.48 (0,0)	17.82 (0,1)	22.07 (0,2)	29.35 (0,3)	16.78 (0,0)	18.36 (0,1)	23.05 (0,2)	30.56 (0,3)	15.02 (0,0)	17.15 (0,1)	22.82 (0,2)	31.01 (0,3)
	CC	21.19 (0,0)	22.08 (0,1)	25.15 (0,2)	31.07 (0,3)	20.43 (0,0)	21.60 (0,1)	25.30 (0,2)	31.79 (0,3)	17.70 (0,0)	19.40 (0,1)	24.25 (0,2)	31.73 (0,3)
l=0	SS	8.69 (0,0)	10.25 (0,1)	14.81 (0,2)	21.97 (0,3)	-*	-*	10.39 (0,2)	19.45 (0,3)	-*	-*	-*	-*
	CS	12.30 (0,0)	13.37 (0,1)	16.83 (0,2)	22.99 (0,3)	-*	4.18 (0,1)	11.78 (0,2)	20.03 (0,3)	-*	-*	-*	-*
	SC	16.09 (0,0)	17.42 (0,1)	21.62 (0,2)	28.78 (0,3)	16.39 (0,0)	17.96 (0,1)	22.60 (0,2)	30.00 (0,3)	14.45 (0,0)	16.60 (0,1)	22.26 (0,2)	30.36 (0,3)
	CC	20.77 (0,0)	21.64 (0,1)	24.66 (0,2)	30.48 (0,3)	19.97 (0,0)	21.13 (0,1)	24.79 (0,2)	31.19 (0,3)	17.07 (0,0)	18.79 (0,1)	23.63 (0,2)	31.05 (0,3)

* indicates instability of the micro-disk; ** BC means boundary condition

Table 6.5: Effect of volume fraction indices on the free vibration frequencies of the first four modes for different boundary conditions and rotational speeds.

$k_r = k_t$	BC**	Ω^*=5				Ω^*=10				Ω^*=15			
		Mode				Mode				Mode			
		1st	2nd	3rd	4th	1st	2nd	3rd	4th	1st	2nd	3rd	4th
0.0	SS	44.06 (0,0)	48.98 (0,1)	65.34 (0,2)	93.62 (0,3)	42.92 (0,0)	48.04 (0,1)	64.74 (0,2)	93.25 (0,3)	40.83 (0,0)	46.30 (0,1)	63.64 (0,2)	92.56 (0,3)
	CS	55.88 (0,0)	59.66 (0,1)	72.76 (0,2)	97.39 (0,3)	54.62 (0,0)	58.56 (0,1)	71.99 (0,2)	96.91 (0,3)	52.37 (0,0)	56.58 (0,1)	70.61 (0,2)	96.06 (0,3)
	SC	76.63 (0,0)	81.20 (0,1)	96.92 (0,2)	125.71 (0,3)	76.75 (0,0)	81.38 (0,1)	97.21 (0,2)	126.06 (0,3)	76.92 (0,0)	81.65 (0,1)	97.67 (0,2)	126.63 (0,3)
	CC	92.91 (0,0)	96.21 (0,1)	108.11 (0,2)	132.02 (0,3)	92.80 (0,0)	96.16 (0,1)	108.22 (0,2)	132.26 (0,3)	92.61 (0,0)	96.08 (0,1)	108.38 (0,2)	132.65 (0,3)
0.5	SS	25.75 (0,0)	28.79 (0,1)	38.90 (0,2)	56.53 (0,3)	23.86 (0,0)	27.26 (0,1)	38.01 (0,2)	56.05 (0,3)	19.58 (0,0)	23.87 (0,1)	36.03 (0,2)	54.93 (0,3)
	CS	32.83 (0,0)	35.25 (0,1)	43.53 (0,2)	59.05 (0,3)	30.75 (0,0)	33.44 (0,1)	42.33 (0,2)	58.36 (0,3)	26.44 (0,0)	29.75 (0,1)	39.90 (0,2)	56.94 (0,3)
	SC	44.80 (0,0)	47.50 (0,1)	56.89 (0,2)	74.42 (0,3)	45.02 (0,0)	47.83 (0,1)	57.43 (0,2)	75.08 (0,3)	45.26 (0,0)	48.26 (0,1)	58.21 (0,2)	76.07 (0,3)
	CC	54.55 (0,0)	56.57 (0,1)	63.88 (0,2)	78.60 (0,3)	54.39 (0,0)	56.53 (0,1)	64.09 (0,2)	79.05 (0,3)	54.05 (0,0)	56.37 (0,1)	64.36 (0,2)	79.71 (0,3)
2.0	SS	19.42 (0,0)	21.94 (0,1)	29.97 (0,2)	43.51 (0,3)	16.55 (0,0)	19.62 (0,1)	28.58 (0,2)	42.69 (0,3)	7.02 (0,0)	13.08 (0,1)	25.01 (0,2)	40.57 (0,3)
	CS	24.92 (0,0)	26.87 (0,1)	33.39 (0,2)	45.29 (0,3)	21.92 (0,0)	24.28 (0,1)	31.65 (0,2)	44.24 (0,3)	14.21 (0,0)	17.96 (0,1)	27.62 (0,2)	41.81 (0,3)
	SC	34.97 (0,0)	37.16 (0,1)	44.57 (0,2)	58.01 (0,3)	35.22 (0,0)	37.55 (0,1)	45.21 (0,2)	58.78 (0,3)	35.37 (0,0)	37.92 (0,1)	46.01 (0,2)	59.84 (0,3)
	CC	42.49 (0,0)	44.10 (0,1)	49.78 (0,2)	61.01 (0,3)	42.28 (0,0)	44.02 (0,1)	50.02 (0,2)	61.54 (0,3)	41.76 (0,0)	43.73 (0,1)	50.25 (0,2)	62.24 (0,3)
5.0	SS	18.22 (0,0)	20.54 (0,1)	27.97 (0,2)	40.49 (0,3)	14.87 (0,0)	17.83 (0,1)	26.32 (0,2)	39.47 (0,3)	-*	9.01 (0,1)	21.82 (0,2)	36.77 (0,3)
	CS	23.31 (0,0)	25.10 (0,1)	31.11 (0,2)	42.09 (0,3)	19.90 (0,0)	22.14 (0,1)	29.09 (0,2)	40.84 (0,3)	9.84 (0,0)	14.22 (0,1)	24.19 (0,2)	37.83 (0,3)
	SC	33.17 (0,0)	35.20 (0,1)	42.10 (0,2)	54.61 (0,3)	33.41 (0,0)	35.59 (0,1)	42.76 (0,2)	55.41 (0,3)	33.50 (0,0)	35.92 (0,1)	43.55 (0,2)	56.47 (0,3)
	CC	40.14 (0,0)	41.62 (0,1)	46.89 (0,2)	57.32 (0,3)	39.91 (0,0)	41.54 (0,1)	47.14 (0,2)	57.87 (0,3)	39.32 (0,0)	41.19 (0,1)	47.34 (0,2)	58.56 (0,3)

* indicates instability of the micro-disk; ** BC means boundary condition

Table 6.6: Effect of radius ratio on the free vibration frequencies of the first four modes for different boundary conditions and rotational speeds.

b/a	BC**	Ω^*=5				Ω^*=10				Ω^*=15			
		Mode				Mode				Mode			
		1st	2nd	3rd	4th	1st	2nd	3rd	4th	1st	2nd	3rd	4th
2.0	SS	47.60 (0,0)	49.68 (0,1)	55.94 (0,2)	66.51 (0,3)	46.66 (0,1)	48.79 (0,0)	55.22 (0,2)	65.97 (0,3)	44.70 (0,0)	46.97 (0,1)	53.72 (0,2)	64.84 (0,3)
	CS	67.75 (0,0)	69.31 (0,1)	74.11 (0,2)	82.54 (0,3)	66.21 (0,0)	67.82 (0,1)	72.79 (0,2)	81.43 (0,3)	63.39 (0,0)	65.11 (0,1)	70.37 (0,2)	79.41 (0,3)
	SC	79.65 (0,0)	81.29 (0,1)	86.37 (0,2)	95.30 (0,3)	80.29 (0,0)	81.93 (0,1)	87.01 (0,2)	95.95 (0,3)	81.24 (0,0)	82.89 (0,1)	87.99 (0,2)	96.95 (0,3)
	CC	106.06 (0,0)	107.25 (0,1)	111.01 (0,2)	117.80 (0,3)	105.99 (0,0)	107.20 (0,1)	110.99 (0,2)	117.86 (0,3)	105.82 (0,0)	107.06 (0,1)	110.94 (0,2)	117.91 (0,3)
5.0	SS	19.43 (0,0)	22.27 (0,1)	31.84 (0,2)	48.06 (0,3)	16.72 (0,0)	20.18 (0,1)	30.71 (0,2)	47.43 (0,3)	8.65 (0,0)	14.71 (0,1)	27.92 (0,2)	45.82 (0,3)
	CS	24.10 (0,0)	26.38 (0,1)	34.36 (0,2)	49.09 (0,3)	21.33 (0,0)	24.07 (0,1)	32.98 (0,2)	48.32 (0,3)	14.42 (0,0)	18.64 (0,1)	29.82 (0,2)	46.53 (0,3)
	SC	34.77 (0,0)	37.33 (0,1)	46.46 (0,2)	63.07 (0,3)	34.89 (0,0)	37.64 (0,1)	47.09 (0,2)	63.84 (0,3)	34.89 (0,0)	37.95 (0,1)	47.94 (0,2)	64.93 (0,3)
	CC	41.26 (0,0)	43.19 (0,1)	50.41 (0,2)	64.88 (0,3)	41.04 (0,0)	43.15 (0,1)	50.76 (0,2)	65.50 (0,3)	40.56 (0,0)	42.96 (0,1)	51.19 (0,2)	66.38 (0,3)
10.0	SS	16.10 (0,0)	18.92 (0,1)	30.18 (0,2)	48.18 (0,3)	12.68 (0,0)	16.60 (0,1)	29.13 (0,2)	47.52 (0,3)	-*	9.64 (0,1)	26.31 (0,2)	45.80 (0,3)
	CS	18.28 (0,0)	20.78 (0,1)	30.84 (0,2)	48.27 (0,3)	14.97 (0,0)	18.35 (0,1)	29.69 (0,2)	47.60 (0,3)	1.60 (0,0)	11.68 (0,1)	26.74 (0,2)	45.86 (0,3)
	SC	29.38 (0,0)	32.06 (0,1)	43.55 (0,2)	62.96 (0,3)	29.23 (0,0)	32.33 (0,1)	44.31 (0,2)	63.76 (0,3)	28.79 (0,0)	32.57 (0,1)	45.33 (0,2)	64.87 (0,3)
	CC	32.54 (0,0)	34.77 (0,1)	44.64 (0,2)	63.13 (0,3)	32.27 (0,0)	34.86 (0,1)	45.29 (0,2)	63.90 (0,3)	31.65 (0,0)	34.83 (0,1)	46.15 (0,2)	64.99 (0,3)

* indicates instability of the micro-disk; ** BC means boundary condition

The size-effect has been illustrated in Table 6.4 where the free vibration frequencies for the first four modes at three different rotational speeds are presented for different values of size-dependent thickness values (t/l) such as 1, 2, 5 and 10, and that without the size-effect (l=0). It is noted that higher is the size-dependent thickness, lower will be the size-effect and vice-versa. Table 6.4 omits frequency values at Ω^*=10 and 15 for specific combinations of mode and size-dependent thickness. This exclusion is due to the fact that the instability condition, leading to static buckling, occurs at speeds equal to or lower than those specified

values (i.e., Ω^* = 10 and 15). Within the range of speed considered, the instability has been observed to reach for SS and CS boundary conditions. The first mode is consistently seen to be (0,0), whereas its following three modes are recognized as (0,1), (0,2), and (0,3), respectively, regardless of the boundary conditions and t/l values. An evident trend is observed where the frequency values decrease as the t/l values increase. In other words, a greater size-effect leads to higher frequencies of vibration. This relationship holds true across all the modes and boundary conditions that have been considered. The observed correlation provides clear evidence that the size-effect results in a stiffening response into the micro-disks. The absence of instability in the SC and CC micro-disks within the speed Ω^*=15 indicates their higher stiffness compared to the SS and CS micro-disks. Due to the increased stiffness, it is anticipated that instability for these boundary conditions would manifest at higher rotational speeds (i.e., $\Omega^* > 15$). The size-effect reaches a state of near-saturation around t/l=10, as evidenced by the frequency values at t/l=10, being nearly equal to or slightly greater than those predicted by the classical theory (l=0).

Table 6.5 displays the frequencies of free vibrations for the first four modes at three different rotational speeds and considering four distinct values of volume fraction indices which are: $k_r = k_t = 0.0$, 0.5, 2.0 and 5.0. The table aims to illustrate how these different volume fraction indices affect the vibration frequencies of the system. Regardless of the boundary conditions, Table 6.5 consistently reveals that the first mode corresponds to (0,0), while the subsequent three modes are identified as (0,1), (0,2), and (0,3) respectively. This pattern remains unchanged across the different values of the volume fraction indices considered in the table. The instability condition is observed to manifest in the first mode of the SS micro-disk for $k_r = k_t = 5.0$, occurring at a speed equal to or lower than 15. It is observed that, across all the four modes and four boundary conditions considered, the frequencies exhibit a decreasing trend with an increase in k_r and/or k_t values. As the value of k_r and/or k_t increases, the rate of frequency reduction becomes less pronounced, resulting in a more gradual decrease in the frequency values. According to Eq. (2.5), $k_r = k_t = 0$ indicates that the disk is fully ceramic, and as k_r and/or k_t increases, the metal fraction increases. As for the present FGM composition, the metal constituent (Stainless Steel) is less elastic and denser

compared to its ceramic counterpart (Silicon Nitride), the frequency values decrease with increase in the values of k_r and/or k_t.

Table 6.7: Effect of thermal load on the free vibration frequencies of the first four modes for different boundary conditions and rotational speeds.

ΔT	BC**	Ω^*=5				Ω^*=10				Ω^*=15			
		Mode				Mode				Mode			
		1st	2nd	3rd	4th	1st	2nd	3rd	4th	1st	2nd	3rd	4th
100	SS	14.38 (0,0)	17.06 (0,1)	25.98 (0,2)	41.28 (0,3)	9.99 (0,0)	13.86 (0,1)	24.39 (0,2)	40.48 (0,3)	-*	-*	20.27 (0,2)	38.44 (0,3)
	CS	21.56 (0,0)	23.48 (0,1)	30.36 (0,2)	43.54 (0,3)	17.88 (0,0)	20.37 (0,1)	28.41 (0,2)	42.48 (0,3)	6.16 (0,0)	12.12 (0,1)	23.94 (0,2)	40.08 (0,3)
	SC	34.46 (0,0)	36.47 (0,1)	43.86 (0,2)	58.26 (0,3)	34.75 (0,0)	36.90 (0,1)	44.56 (0,2)	59.09 (0,3)	35.00 (0,0)	37.38 (0,1)	45.49 (0,2)	60.27 (0,3)
	CC	43.19 (0,0)	44.63 (0,1)	50.16 (0,2)	61.97 (0,3)	42.99 (0,0)	44.56 (0,1)	50.42 (0,2)	62.53 (0,3)	42.52 (0,0)	44.32 (0,1)	50.71 (0,2)	63.30 (0,3)
200	SS	-*	-*	13.74 (0,2)	31.32 (0,3)	-*	-*	-*	30.15 (0,3)	-*	-*	-*	27.02 (0,3)
	CS	10.39 (0,0)	12.44 (0,1)	20.00 (0,2)	33.96 (0,3)	-*	-*	16.59 (0,2)	32.48 (0,3)	-*	-*	-*	28.96 (0,3)
	SC	29.16 (0,0)	30.64 (0,1)	37.05 (0,2)	50.78 (0,3)	29.53 (0,0)	31.18 (0,1)	37.91 (0,2)	51.77 (0,3)	29.83 (0,0)	31.77 (0,1)	39.03 (0,2)	53.15 (0,3)
	CC	38.44 (0,0)	39.44 (0,1)	43.97 (0,2)	54.86 (0,3)	38.21 (0,0)	39.37 (0,1)	44.28 (0,2)	55.50 (0,3)	37.67 (0,0)	39.09 (0,1)	44.62 (0,2)	56.39 (0,3)
400	SS	-*	-*	-*	-*	-*	-*	-*	-*	-*	-*	-*	-*
	CS	-*	-*	-*	-*	-*	-*	-*	-*	-*	-*	-*	-*
	SC	8.10 (0,1)	9.75 (0,0)	11.99 (0,2)	27.50 (0,3)	10.26 (0,1)	11.03 (0,0)	14.71 (0,2)	29.46 (0,3)	11.90 (0,0)	12.09 (0,1)	17.63 (0,2)	32.01 (0,3)
	CC	23.89 (0,1)	24.43 (0,0)	25.04 (0,2)	33.84 (0,3)	23.80 (0,1)	24.07 (0,0)	25.64 (0,2)	34.96 (0,3)	23.15 (0,0)	23.31 (0,1)	26.26 (0,2)	36.44 (0,3)

* indicates instability of the micro-disk; ** BC means boundary condition

Table 6.6 presents the free vibration frequencies for the first four modes at three distinct rotational speeds, considering three different values of the radius ratio b/a, which are: 2.0, 5.0 and 10.0. The purpose of the table is to illustrate how varying the radius ratio

impacts the vibration frequencies of the system across different modes and rotational speeds. Regardless of the boundary conditions and the values of the b/a ratio, the first mode corresponds to (0,0), while the subsequent three modes are identified as (0,1), (0,2), and (0,3) respectively. It is observed that the instability condition occurs in the system for the first mode of the SS micro-disk for b/a=10 at a speed equal to or less than 15. Across all the four modes and four boundary conditions considered, it has been found that the frequencies decrease as the values of the b/a ratio increase. This consistent trend can be attributed to the fact that an increase in the radius ratio implies a larger span of the disk in both the radial and circumferential directions, subsequently resulting in a decrease in the bending resistance. Consequently, the frequency values exhibit a decline nature as the b/a values increase.

Table 6.7 presents the free vibration frequencies for the first four modes at three distinct rotational speeds, considering three different values of thermal load, specifically ΔT = 100, 200, and 400. The purpose of the table is to present how the vibration frequencies of the system vary with different thermal loads. For all the four boundary conditions up to ΔT = 200, this table demonstrates that the first mode is (0,0) and the next three modes are (0,1), (0,2) and (0,3) respectively. At ΔT = 400, it has been observed that a mode switching phenomenon takes place between the first two modes for the SC and CC boundary conditions at speed values of Ω^*=5 and 10. As a result, the order of occurrence of the first four modes is changed, and they are observed to be (0,1), (0,0), (0,2) and (0,3) respectively. For the ranges of speed and thermal load examined, it has been observed that the instability condition arises for all the modes under the SS and CS boundary conditions at various combinations of loads. The property-temperature relationship shown in Eq. (2.6) shows that when ΔT increases, the components of the disk material degrade thermo-elastically, thus softening the micro-disk, and causing the frequency values to decline. Similarly, an increase in the value of ΔT also signifies the development of compressive forces due to the immovable nature of the radial boundary conditions. This development of compressive force induces a geometric softening effect in the micro-disk, which ultimately leads to a decrease in the frequency values. This observation highlights the influence of thermal load on the free vibration behaviour of the micro-disk, as higher temperature can significantly impact its stability and lead to static buckling of the disk, particularly for the SS and CS boundary conditions.

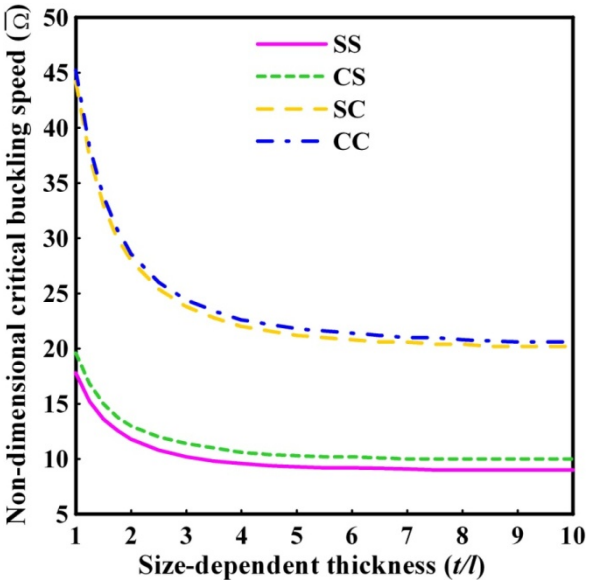

Fig. 6.5: Variation of non-dimensional critical buckling speedwith size-dependent thickness for the fundamental mode for different boundary conditions.

It is mentioned that $\overline{\Omega}$ is used to denote the non-dimensional critical buckling speed for which the same non-dimensional scheme, as used in Eq. (6.4a), is considered. Fig. 6.5 represents the variation of the non-dimensional critical buckling speed ($\overline{\Omega}$) with size-dependent thickness (t/l) for all the four boundary conditions. In the present study, only the fundamental (first) buckling mode has been considered. The results indicate that variations of critical buckling speed with t/l are almost identical for the SS and CS micro-disks, and also for the SC and CC micro-disks. It means the critical buckling speed is nearly unaffected by the nature of the inner boundary condition, resulting in the SS and CS micro-disks to demonstrate nearly identical behaviour, while the SC and CC micro-disks exhibit almost indistinguishable behaviour in this regard. For all the boundary conditions, the critical buckling speed is found to be maximum at t/l=1 and decreases rapidly with increase in the t/l values. This plot implies that increasing the size-effect increases the critical buckling speed. The critical buckling speed becomes almost invariant of the size-dependent thickness for SS and CS micro-disks beyond t/l=5, and for SC and CC micro-disks beyond t/l=9. To have an idea on the value of t/l, at which the critical buckling speed saturates to the value of a classical disk (l=0), Table 6.8 shows the non-dimensional critical buckling speed of the

BFGM rotating annular disk considering classical theory (l=0). The results are shown for all the four boundary conditions in Table 6.8.

Table 6.8: Non-dimensional critical buckling speed for the fundamental mode based on the classical theory (l=0) for different boundary conditions.

Boundary Condition	Non-dimensional Critical Buckling Speed($\overline{\Omega}$)
SS	8.80
CS	9.80
SC	19.80
CC	20.20

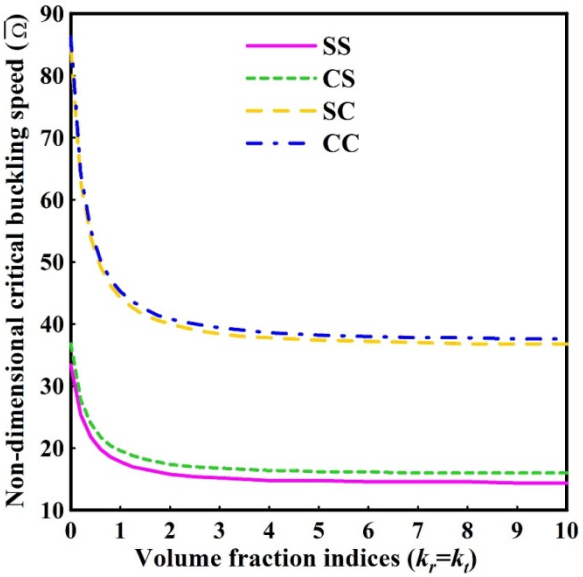

Fig. 6.6: Variation of the non-dimensional critical buckling speed with volume fraction indices for the fundamental mode for different boundary conditions.

Fig. 6.6 shows the variation of the non-dimensional critical buckling speed ($\overline{\Omega}$)with volume fraction indices ($k_r = k_t$)for the fundamental mode for all the four boundary conditions considered. The observed results demonstrate that the inner boundary condition has minimal influence on the critical buckling speed. As a result, the behaviours of SS and CS micro-disks are remarkably similar, while the behaviours of SC and CC micro-disks are virtually indistinguishable in relation to this aspect. The critical buckling speed is found to be

maximum at $k_r = k_t = 0$,and decreases rapidly with increase in the values of k_r and k_t. The critical buckling speed remains almost invariant of the size-dependent thickness beyond $k_r = k_t = 7$ for SS and CS micro-disks, and beyond $k_r = k_t = 9$ for SC and CC micro-disks.

6.4 Chapter Summary

To fill up the research gap and to acquire a comprehensive understanding on the thematic problem of BFGM rotating micro-disks, the present chapter studied the free vibration behaviour of a BFGM rotating annular micro-disk under four different boundary conditions. They are simply supported-simply supported (SS), clamped-simply supported (CS), simply supported-clamped (SC) and clamped-clamped (CC). This problem essentially reveals a softening type behaviour of the rotating annular micro-disk. Hence tracking the speed-frequency behaviour, the critical buckling speed pertaining to instability of the micro-disk has been determined and reported. In the present problem, the BFGM micro-disk has been considered to be subjected to centrifugal and thermal loading, and the effect of transverse pressure has been assumed to be zero. The important problem parameters are defined, and the governing equations are provided in a concise manner, maintaining the overall methodology discussed in Chapter 2. Using Kirchhoff plate theory and the MCST, an energy-based mathematical model is developed. The validity of the model has been established through a number of comparison studies. The free vibration behaviour has been reported for the first four modes to study the effects of speed, thermal loading, size-dependent thickness, radial and thickness gradation indices and radius ratio. Some illustrative mode-shape plots along with their contour have been presented for visualization of the bending vibration modes. The effects of size-dependent thickness, and radial and thickness gradation indices on the critical buckling speed of the fundamental mode have been discussed. The key findings of this chapter are summarized below:

- For all the parameters considered, except for the thermal load, the first mode has been found to be of axisymmetric bending ((0,0)), while the next three modes exhibit asymmetric bending characteristics ((0,1), (0,2), (0,3)). For the entire range of parameters, no torsional mode has been observed to appear within the first four modes.

- Arranging the micro-disks in ascending order based on the frequency values, the sequence is as follows: SS, CS, SC, and CC for all four modes.
- For SS and CS micro-disks, the frequency of vibration decreases with an increase in speed across all four modes. In contrast, for CC micro-disks, the frequency increases with speed for all modes, and for SC micro-disks, the frequency slightly decreases with speed for the first two modes but increases for the next two modes.
- The size-dependent thickness has significant stiffening effect for all the four modes. The frequency values approach to those of the classical theory when the size-dependent thickness reaches approximately the value of 10.
- The volume fraction indices exert a significant influence on the vibration frequency, with an increase in the indices resulting in a decrease in frequency values for all the four modes considered.
- Increasing the radius ratio causes a decrease in the vibration frequency for all the four modes.
- Thermal loading induces softening in the micro-disks, resulting in a significant decrease in the frequency values.
- Some of the frequency values for the above parametric variations have not been reported due to reaching of the instability condition.
- Decreasing the size-dependent thickness increases the critical buckling speed and vice-versa. The effect is sharp at lower values of the size-dependent thickness values.
- The critical buckling speed decreases rapidly with increasing volume fraction indices.

Chapter 7

CONCLUSIONS

7.1 Problems of the Thesis

With the thematic objective of studying the free vibration behaviour of functionally graded rotating micro-disks, the following four problems have been investigated in the present thesis work:

- First Problem: Free vibration behaviour of a BFGM annular clamped–free micro-disk, which is rotating at constant angular speed, and operating in high-temperature environment.
- Second Problem: Free vibration behaviour of a BFGM annular clamped–free micro-disk, which is rotating at constant angular speed, subjected to uniform transverse pressure, and operating in high-temperature environment.
- Third Problem: Free axisymmetric bending vibration behaviour of a BFGM annular clamped–free micro-disk, which is rotating at constant angular speed, subjected to uniform transverse pressure, and operating in high-temperature environment.
- Fourth Problem: Free vibration and static buckling behaviours of a BFGM annular micro-disk under different boundary conditions, which is rotating at constant angular speed, and operating in high-temperature environment.

All the above problems that have been successfully solved and discussed in the thesis were defined based on the research gaps found through an extensive literature review. These problems have been studied for the first time through this thesis work, and hence they contribute to the novelty of the thesis.

7.2 Mathematical Model

The salient features of the developed mathematical model are summarized below:

- A BFGM micro-size rotating disk has been considered, which is assumed to be functionally graded along the radial and thickness directions. The through-thickness gradation has been assumed symmetrical to avoid bending due to centrifugal loading.
- The mechanical properties of the metal-ceramic BFGM constituents have been considered temperature-dependent based on the Touloukian model. The effective material properties of the BFGM have been calculated using the rule-of-mixtures (Voigt model) and following the power law.
- The mathematical model has been formulated based on the mid-plane displacements of the micro-disk. The model has been built employing Kirchhoff plate theory coupled with von Kármán nonlinearity for circular plates using polar coordinates. The small size-effect in the micron level has been addressed within the framework of the MCST, and assuming linear elastic material behaviour.
- The problem is formulated using two steps.
- In the first step, the deformed configuration of the BFGM micro-disk under time-invariant centrifugal loading due to rotational speed, mechanical loading due to uniform transverse pressure and thermal loading due to uniform temperature rise has been determined employing the principle of minimum total potential energy. The thermal effect due to high-temperature operating environment has been incorporated into the mathematical model through thermo-elastic constitutive relations. The set of governing equations for this step is nonlinear due to the presence von Kármán type nonlinearity, and is solved employing Broyden's algorithm.
- In the second step, the free vibration response of the micro-disk about its deformed configuration has been determined employing Hamilton's principle. The tangent stiffness of the deformed micro-disk has been determined and used in the governing equations. The set of governing equations for this step, which is an eigenvalue problem, has been linearized using the solution parameters of the first step, and solved using a standard eigen-solver.

- The governing equations for both the steps have been discretized following Ritz method with the help of admissible orthogonal functions, and employing Gram-Schmidt orthogonalization scheme.
- A general formulation embracing all the four problems of the thesis has been presented such that a reduced model can be obtained by retaining the problem specific relevant terms, and neglecting or omitting the out-of-the problem terms, maintaining the base of the considered problem.
- The present model is capable of investigating both the axisymmetric and asymmetric bending vibration behaviours as well as the torsional vibration behaviour.
- The convergence of the results with increasing number of terms for the assumed admissible orthogonal functions has been successfully exhibited, and it thus establishes the validity of the Ritz technique.
- The validity of the model as a whole, and for the problems of the thesis in specific, has been established through a number of comparison studies with the standard available results for some reduced problems.
- As mentioned earlier, the first step of the problem determines the deformed configuration of the micro-disk under centrifugal, mechanical and thermal loading. It implies that the present model is capable of studying the static behaviour of the micro-disk under any of the, or combination of the loadings.
- The critical buckling speeds of the rotating micro-disk under various boundary conditions have been determined by numerically tracking the speed-frequency behaviour. It implies that the present model is capable of determining the critical buckling load under any particular loading which imparts softening effect into the micro-disk.
- The developed formulation is quite general in nature, and can be applied for a wide variety of problems, apart from the specific problems of the thesis, by properly adjusting certain parameters as follows:
  - The present model can be reduced to a circular micro-disk/plate under non-rotating condition by putting the rotational speed $\Omega = 0$.
  - The present model can be reduced to a solid circular micro-disk/plate by making the inner radius $a = 0$.

- The classical theory representing the size-independent behaviour of a macro-size disk/plate can be restored by substituting $l = 0$.
- The present model can be used to represent any classical boundary conditions by properly selecting the lowest order admissible functions for the mid-plane displacement fields.
- The present model can be reduced to that of a radial-FG micro-disk/plate by putting $k_t = 0$, and a thickness-FG micro-disk/plate by putting $k_r = 0$.

That the present model successfully solved the four research problems of the thesis clearly justifies the novelty of the model. Additionally, the fact that the model can be employed to solve a wide variety of problems related to mechanical behaviour of micro-disks/plates is a testament of the robustness of the present model.

7.3 Observations and Findings through the Numerical Results

The problems of the thesis have been studied for a variety of physical parameters, each for a wide range of values/variants. All the numerical results, except the thermal loading, have been presented in non-dimensional form. The present thesis has been undertaken to study the free vibration behaviour of the micro-disk in the frequency domain. Hence, all the results are generated and presented to investigate the effects of various loading parameters and problem parameters on the vibration frequencies of the first few modes. Through extensive sets of numerical results, some important observations and findings have been noted with regard to different parameters. These are briefly summarized below:

- **Rotational Speed:**

For CF micro-disks, the rotational speed imparts centrifugal stiffening, which leads to an increase in the bending vibration frequencies, in general, for all the modes. However, under moderate to high transverse pressure, the effect of rotational speed almost vanishes for the lower bending modes. Further, the torsional vibration frequency is found to be indifferent with the change of speed.

For SS and CS micro-disks, the frequency of vibration decreases with speed for the first four bending modes, indicating a softening type effect. In contrast, for CC micro-disks, the frequency increases with speed for the first four bending modes. However, for SC micro-

disks, the frequency slightly decreases with speed for the first two bending modes but increases with speed for the next two bending modes. The softening type effect of the rotational speed leads the vibration frequency to become zero, making the disk unstable.

- **Transverse Pressure:**

For CF micro-disks, the increase in transverse pressure results in a mild rise in the vibration frequency for all the bending modes due to enhanced geometric stiffening. Further, the transverse pressure affects the bending modes within low to moderate speed ranges, and its effect is observed to diminish with increasing speed. On the other hand, the rotational speed has a substantial impact on the bending vibration frequencies over the entire range of pressure values. However, the torsional frequency is found to be independent of the transverse pressure.

- **Thermal Loading:**

Under thermal loading due to uniform temperature rise, the bending frequency values generally decrease due to thermo-elastic degradation of the CF micro-disks. The speed-frequency and pressure-frequency behaviours are found to be significantly affected by the high operating temperature only for the higher modes. However the effect of thermal loading is found to be more prominent on the axisymmetric bending modes compared to the asymmetric bending modes. Furthermore, the thermal loading significantly reduces the torsional vibration frequency. It has been observed that the effect of thermal loading is more pronounced on the torsional mode compared to the bending modes.

For the micro-disks other than CF configuration, the thermal loading induces softening due to both thermo-elastic degradation and development of compressive thermal stress due to radial restraint at the boundaries. This results in significant decrease in the bending frequency values.

- **Size-dependent Thickness:**

When the material length scale parameter approaches the representative dimension (thickness) of the micro-disk, it implies enhanced size-effect. Hence, less is the size-dependent thickness, more is the small-size effect. For all the boundary conditions considered, including the CF

micro-disks, the small-size effect shows significant stiffening effect on both the axisymmetric and asymmetric bending modes of vibration, resulting in enhanced frequencies of vibration. However, the small-size effect has very insignificant influence on the torsional vibration frequency. For the bending modes, the frequency values approach to those of the classical theory when the size-dependent thickness reaches approximately the value of 10.

Decreasing the size-dependent thickness increases the critical buckling speed and vice-versa. The effect of size-dependent thickness on the critical buckling speed has been observed to be sharp at lower values of the size-dependent thickness. As far as the effect of size-dependent thickness is concerned, the critical buckling speed is nearly unaffected by the nature of the inner boundary condition, resulting in the SS and CS micro-disks to demonstrate nearly identical behaviour, while the SC and CC micro-disks exhibit almost indistinguishable behaviour in this regard.

- **Gradation Indices:**

The radial and thickness gradation indices exert a significant influence on the vibration frequencies for the axisymmetric and asymmetric modes as well as for the torsional mode. To be specific, the increase in the gradation indices results in a decrease in the frequency values for all the modes considered. Furthermore, the influences of these indices are found to be more prominent on the higher bending modes. Increasing the gradation indices results in more volume proportion of the metallic phase compared to its ceramic counterpart, and for the FGM compositions considered, the metallic phase is less elastic and lighter compared to the ceramic phase. That is why increasing gradation indices results in decrease in the vibration frequencies.

The critical buckling speed decreases rapidly with increase in the volume fraction indices. The effect is sharp for lower values of the gradation indices. As far as the effect of gradation indices is concerned, the critical buckling speed is almost unaffected by the nature of the inner boundary condition, resulting in the SS and CS micro-disks to demonstrate nearly similar behaviour, while the SC and CC micro-disks exhibit almost indistinguishable behaviour.

- **Radius Ratio:**

The vibration frequencies for the bending modes are found to increase with decrease in the radius ratio for the first two modes. But it exhibits reverse trend for the higher bending modes, especially at the higher values of the radius ratio. This observation is true for the CF micro-disks and for the asymmetric modes. However for the other boundary conditions and for the axisymmetric modes, the vibration frequencies are found to increase with decrease in the radius ratio for all the modes. It is known that increased radius ratio increases the radial and circumferential span of the micro-disk, making it less stiff for bending.

- **FGM Composition:**

Although the overall trend of the influence is same for various FGM compositions, different FGM compositions exhibit different extent of influence on the speed-frequency and pressure-frequency behaviours. It is observed that, as a whole, Stainless Steel/Silicon Nitride and Stainless Steel/Alumina compositions exhibit almost similar behaviour, whereas the behaviours of Stainless Steel/Zirconia and Titanium Alloy/Zirconia compositions are close to each other.

Apart from the above-mentioned observations and findings, various mode-shapes along with their contour have been presented. The representative mode-shapes are shown for the first few axisymmetric and asymmetric bending modes, and also for the torsional mode. The problem-specific results presented in specific chapters as well as the overall summary of the results presented above are new of its kind. These results and the corresponding findings will definitely serve as benchmark for further study in the domain of dynamics of rotating micro-disks.

7.4 Future Scope of Work

In view of the present thesis, the following can be considered for further research study in the field of dynamics of rotating micro-disks:

(i) The free vibration behaviour of rotating micro-disks can be studied employing other size-dependent continuum theories such as nonlocal theory, strain gradient theory etc.

(ii) The free vibration behaviour of rotating micro-disks can be studied by considering tridirectional functionally graded micro-disks, for which the material gradation can be considered along the circumferential direction apart from the radial and thickness directions.

(iii) An experimental study involving free vibration behaviour of micro-size rotating disks, though extremely challenging, will reveal many important aspects of the problem.

BIBLIOGRAPHY

Adamou A, Turner J, Costall A, Jones A and Copeland C (2021) Design, simulation, and validation of additively manufactured high temperature combustion chambers for micro gas turbines. *Energy Conversion and Management* 248: 114805.

Afsar AM and Go J (2010) Finite element analysis of thermoelastic field in a rotating FGM circular disk. *Applied Mathematical Modelling* 34: 3309–3320.

Ahmadi AR (2015) Free vibration analysis of annular vibration analysis of annular flexural micro-plates using C2 quadrilateral finite elements. *Journal for Multiscale Computational Engineering* 13: 311–319.

Akour SN, Al-Heymari M, Ahmed T and Khalil KA (2018) Experimental and theoretical investigation of micro wind turbine for low wind speed regions. *Renewable Energy* 116: 215–223.

Al-Furjan MSH, Sohrforozani ES, Habibi M, Jung DW and Safarpour H (2021) Vibrational characteristics of a higher-order laminated composite viscoelastic annular microplate via modified couple stress theory. *Composite Structures* 257: 113152.

Amrani I, Cheriet A and Feliachi M (2018) Design and experimental investigation of a bi-directional valveless electromagnetic micro-pump. *Sensors and Actuators A: Physical* 272: 310–17.

Anjomshoa A and Tahani M (2016) Vibration analysis of orthotropic circular and elliptical nano-plates embedded in elastic medium based on nonlocal Mindlin plate theory and using Galerkin method. *Journal of Mechanical Science and Technology* 30: 2463-2474.

Anjomshoa A, Shahidi AR, Shahidi SH and Nahvi H (2015) Frequency analysis of embedded orthotropic circular and elliptical micro/nano-plates using nonlocal variational principle. *Journal of Solid Mechanics* 7: 13-27.

Ansari R and Norouzzadeh A (2016) Nonlocal and surface effects on the buckling behavior of functionally graded nanoplates: An isogeometric analysis. *Physica E*: 84–97.

Ansari R, Gholami R, Shojaei MF, Mohammadi V and Sahmani S (2015) Bending, buckling and free vibration analysis of size-dependent functionally graded circular/annular microplates based on the modified strain gradient elasticity theory. *European Journal of Mechanics A/Solids* 49: 251-267.

Ansari R, Mohammadi V, Shojaei MF, Gholami R and Sahmani S (2014) Surface stress effect on the postbuckling and free vibrations of axisymmetric circular Mindlin nanoplates subject to various edge supports. *Composite Structures* 112: 358–367.

Arshid E, Amir S and Loghman A (2021) Bending and buckling behaviors of heterogeneous temperature-dependent micro annular/circular porous sandwich plates integrated by FGPEM nano-Composite layers. *Journal of Sandwich Structures and Materials* 23: 3836–3877.

Asemi SR and Farajpour A (2014) Decoupling the nonlocal elasticity equations for thermo-mechanical vibration of circular graphene sheets including surface effects. *Physica E* 60: 80–90.

Asghari M and Ghafoori E (2010) A three-dimensional elasticity solution for functionally graded rotating disks. *Composite Structures* 92: 1092–1099.

Ashoori AR and Vanini SAS (2016a) Thermal buckling of annular microstructure-dependent functionally graded material plates resting on an elastic medium. *Composites Part B* 87: 245-255.

Ashoori AR and Vanini SAS (2016b) Nonlinear thermal stability and snap-through behavior of circular microstructure-dependent FGM plates. *European Journal of Mechanics A/Solids* 59: 323-332.

Babamiri BB, Shahrjerdi A and Bayat M (2020) Effect of geometrical imperfection on the thermomechanical behavior of functionally graded material rotating disk. *Journal of the Brazilian Society of Mechanical Sciences and Engineering* 42: 271.

Baddour N and Zu JW (2007) Nonlinearly coupled in-plane and transverse vibrations of a spinning disk. *Applied Mathematical Modelling* 31: 54–77.

Baghani M, Heydarzadeh N and Roozbahani MM (2016) Stress analysis of a functionally graded micro/nanorotating disk with variable thickness based on the strain gradient theory. *International Journal of Applied Mechanics* 8: 1650020.

Bagheri E and Asghari M (2021) Elasticity formulation for motion equations of couple stress based micro-rotating disks with varying speeds. *Mechanics Based Design of Structures and Machines* 49: 1-19.

Bagheri E and Jahangiri V (2019) Analysis of in-plane vibration and critical speeds of the functionally graded rotating disks. *International Journal of Applied Mechanics* 11: 1950020.

Bagheri E, Asghari M and Danesh V (2019) Analytical study of micro-rotating disks with angular acceleration on the basis of the strain gradient elasticity. *Acta Mechanica* 230: 3259–3278.

Bagheri E, Jahangiri M and Asghari M (2020) Effects of couple stresses on the in-plane vibration of micro-rotating disks. *Journal of Vibration and Control* 26: 1246-1259.

Bashmal S, Bhat R and Rakheja S (2009) In-plane free vibration of circular annular disks. *Journal of Sound and Vibration* 322: 216–226.

Bauer HF and Eidel W (2007) Transverse vibration and stability of spinning circular plates of constant thickness and different boundary conditions. *Journal of Sound and Vibration* 300: 877–895.

Bayat M, Rahimi M, Saleem M, Mohazzab AH, Wudtke I and Talebi H (2014) One-dimensional analysis for magneto-thermo-mechanical response in a functionally graded annular variable-thickness rotating disk. *Applied Mathematical Modelling* 38: 4625-4639.

Bayat M, Sahari BB, Saleem M, Ali A and Wong SV (2009a) Bending analysis of a functionally graded rotating disk based on the first order shear deformation theory. *Applied Mathematical Modelling* 33: 4215–4230.

Bayat M, Sahari BB, Saleem M, Hamouda AMS and Reddy JN (2009b) Thermo elastic analysis of functionally graded rotating disks with temperature-dependent material properties: uniform and variable thickness. *International Journal of Mechanics and Materials in Design* 5: 263–279.

Bayat M, Saleem M, Sahari BB, Hamouda AMS and Mahdi E (2008) Analysis of functionally graded rotating disks with variable thickness. *Mechanics Research Communications* 35: 283–309.

Bedroud M, Nazemnezhad R, Hashemi SH and Valixani M. (2016) Buckling of FG circular/annular Mindlin nano plates with an internal ring support using nonlocal elasticity. *Applied Mathematical Modelling* 40: 3185–3210.

Benazouz K, Bechir H and Djema A (2022) Modeling nonlinear bending of axisymmetric circular nanoplates in framework of Ru's surface stress elasticity theory. *Journal of Engineering Mathematics* 132: 6.

Çallioglu H, Bektaş NB and Sayer M (2011) Stress analysis of functionally graded rotating discs: analytical and numerical solutions. *Acta Mechanica* 27: 950–955.

Chen J, Ding H and Chen W (2007) Three-dimensional analytical solution for a rotating disc of functionally graded materials with transverse isotropy. *Archive of Applied Mechanics* 77: 241–251.

D'Angelo C and Mote CD Jr (1993) Natural frequencies of a thin disk, clamped by thick collars with friction at the contacting surfaces, spinning at high rotation speed. *Journal of Sound and Vibration* 168: 1-14.

Dai T and Dai HL (2015) Investigation of mechanical behavior for a rotating FGM circular disk with a variable angular speed. *Journal of Mechanical Science and Technology* 29: 3779-3787.

Dai T and Dai HL (2016) Thermo-elastic analysis of a functionally graded rotating hollow circular disk with variable thickness and angular speed. *Applied Mathematical Modelling* 40: 7689–7707.

Dai T, Dai HL and Lin ZY (2019) Multi-field mechanical behavior of a rotating porous FGMEE circular disk with variable thickness under hygrothermal environment. *Composite Structures* 210: 641-656.

Danesh V and Asghari M. (2014) Analysis of micro-rotating disks based on the strain gradient elasticity. *Acta Mechanica* 225: 1955-1965.

Das D (2018) A new tangent stiffness-based formulation to study the free vibration behavior of a transversely loaded Timoshenko beam with geometric nonlinearity. *Journal of Vibration and Control* 24: 1716-1727.

Das D, Sahoo P and Saha K (2009) Nonlinear vibration analysis of clamped skew plates by a variational method. *Journal of Vibration and Control* 15: 985-1017.

Das D, Sahoo P and Saha K (2010) Free vibration analysis of a rotating annular disc under uniform pressure loading. *Proceedings of the Institution of Mechanical Engineers Part C: Journal of Mechanical Engineering Science* 224: 615–634.

Das D, Sahoo P and Saha K (2011) A numerical analysis of large amplitude beam vibration under different boundary conditions and excitation patterns. *Journal of Vibration and Control* 18: 1900-1915.

Dastjerdi S and Akgöz B (2018) New static and dynamic analyses of macro and nano FGM plates using exact three-dimensional elasticity in thermal environment. *Composite Structures* 192: 626-641.

Dastjerdi S and Jabbarzadeh M (2016) Nonlocal bending analysis of bilayer annular/circular nano plates based on first order shear deformation theory. *Journal of Solid Mechanics* 8: 645-661.

Dastjerdi S and Jabbarzadeh M (2017) Non-linear bending analysis of multi-layer orthotropic annular/circular graphene sheets embedded in elastic matrix in thermal environment based on non-local elasticity theory. *Applied Mathematical Modelling* 41: 83–101.

Duan WH and Wang CF (2007) Exact solutions for axisymmetric bending of micro/nanoscale circular plates based on nonlocal plate theory. *Nanotechnology* 18: 385704.

Durodola JF and Attia O (2000) Deformation and stresses in functionally graded rotating disks. *Composites Science and Technology* 60: 987-995.

Eid H and Adams GG (2006) Critical speeds and the response of a spinning disk to a stationary load using Mindlin plate theory. *Journal of Sound and Vibration* 290: 209–222.

Eldeeb AM, Shabana YM and Elsawaf A (2021) Influences of angular deceleration on the thermoelastoplastic behaviors of nonuniform thickness multilayer FGM discs. *Composite Structures* 258: 113092.

Epstein AH and Senturia SD (1997) Macro power from micro machinery. *Science* 276: 1211.

Eraslan AN and Orcan Y (2002) On the rotating elastic–plastic solid disks of variable thickness having concave profiles. *International Journal of Mechanical Sciences* 44: 1445–1466.

Eringen AC (1967) Theory of micropolar plates. *Journal of Applied Mathematics and Mechanics* 18: 12–30.

Eringen AC (1983) On differential equations of nonlocal elasticity and solutions of screw dislocation and surface waves. *Journal of Applied Physics* 54: 4703–4710.

Eshraghi I, Dag S and Soltani N (2015) Consideration of spatial variation of the length scale parameter in static and dynamic analyses of functionally graded annular and circular micro-plates. *Composites Part B* 78: 338-348.

Eshraghi I, Dag S and Soltani N (2016) Bending and free vibrations of functionally graded annular and circular micro-plates under thermal loading. *Composite Structures* 137: 196-207.

Fleck NA and Hutchinson JW (1997) Strain gradient plasticity. In: Hutchinson JW and Wu TY (Eds.) *Advances in Applied Mechanics* 33: 295–361, New York: Academic Press.

Fleck NA and Hutchinson JW (2001) A reformulation of strain gradient plasticity. *Journal of the Mechanics and Physics of Solids* 49: 2245–2271.

Fleck NA, Muller GM, Ashby MF and Hutchinson JW (1994) Strain gradient plasticity: theory and experiments. *Acta Metallurgica et Materialia* 42: 475–487.

Ghadiri M, Mahinzare M, Shafiei N and Ghorbani K (2017) On size‐dependent thermal buckling and free vibration of circular FG micro-plates in thermal environments. *Microsystem Technologies* 23: 4989–5001.

Gheshlaghi B and Hasheminejad SM (2013) Size dependent damping in axisymmetric vibrations of circular nanoplates. *Thin Solid Films* 537: 212–216.

Giostri A, Binotti M, Sterpos C and Lozza G (2020) Small scale solar tower coupled with micro gas turbine. *Renewable Energy* 147: 570–583.

Golmakani ME and Kadkhodayan M (2014) An investigation into the thermoelastic analysis of circular and annular functionally graded material plates. *Mechanics of Advanced Materials and Structures* 21: 1–13.

Golmakani ME and Vahabi H (2017) Nonlocal buckling analysis of functionally graded annular nanoplates in an elastic medium with various boundary conditions. *Microsystem Technologies* 23: 3613-3628.

Gurtin ME and Murdoch AI (1978) Surface stress in solids. *International Journal of Solids and Structures* 14: 431–440.

Güven U (2019) Inertial elastic instability of rotating nano disks. *Journal of Theoretical and Applied Mechanics* 57: 853-858.

Hassani A, Hojjati MH, Farrahi G and Alashti RA (2011) Semi-exact elastic solutions for thermo-mechanical analysis of functionally graded rotating disks. *Composite Structures* 93: 3239–3251.

Hosseini M, Shishesaz M and Hadi A (2019) Thermoelastic analysis of rotating functionally graded micro/nanodisks of variable thickness. *Thin-Walled Structures* 134: 508-523.

Hosseini M, Shishesaz M, Tahan KN and Hadi A (2016) Stress analysis of rotating nano-disks of variable thickness made of functionally graded materials. *International Journal of Engineering Science* 109: 29-53.

Hosseini-Hashemi S, Bedroud M and Nazemnezhad R (2013) An exact analytical solution for free vibration of functionally graded circular/annular Mindlin nanoplates via nonlocal elasticity. *Composite Structures* 103: 108–118.

Hu YD and Wang T (2016) Nonlinear free vibration of a rotating circular plate under the static load in magnetic field. *Nonlinear Dynamics* 85: 1825–1835.

Jacobson SA and Epstein AH (2003) An informal survey of power mems. In: *Proceedings of international symposium on micro-mechanical engineering*. Tsukuba, Japan, Paper No: ISMME2003-K18.

Jahangiri M, Asghari M and Bagheri E (2020) Torsional vibration induced by gyroscopic effect in the modified couple stress based micro-rotors. *European Journal of Mechanics/A Solids* 81: 103907.

Jalali MH, Shahriari B, Zargar O, Baghani M and Baniassadi M (2018) Free vibration analysis of rotating functionally graded annular disc of variable thickness using generalized differential quadrature method. *Scientia Iranica Transactions B: Mechanical Engineering* 25: 728-740.

Ji X, Li A and Zhou S (2017) A comparison of strain gradient theories with applications to the functionally graded circular micro-plate. *Applied Mathematical Modelling* 49: 124–143.

Jomehzadeh E, Noori HR and Saidi AR (2011) The size-dependent vibration analysis of micro-plates based on a modified couple stress theory. *Physica E* 43: 877–883.

Kahrobaiyan MH, Vardi I, Ahmadian MT and Henein MT (2015) Investigating the size-dependent static and dynamic behavior of circular micro-plates subjected to capillary force. *Proceedings of the ASME 2015 International Design Engineering Technical Conferences & Computers and Information in Engineering Conference*. Massachusetts, USA, Paper No: DETC2015-46487.

Ke LL, Yang J, Kitipornchai S and Bradford MA (2012) Bending, buckling and vibration of size-dependent functionally graded annular microplates.. *Composite Structures* 94: 3250–3257.

Ke LL, Yang J, Kitipornchai S, Bradford MA and Wang YS (2013) Axisymmetric nonlinear free vibration of size-dependent functionally graded annular microplates. *Composites: Part B* 53: 207–217.

Kermani ID, Ghayour M and Mirdamadi HR (2012) Free vibration analysis of multi-directional functionally graded circular and annular plates. *Journal of Mechanical Science and Technology* 26: 3399-3410.

Kermani ID, Mirdamadi HR and Ghayour M (2016) Nonlinear stability analysis of rotational dynamics and transversal vibrations of annular circular thin plates functionally graded in radial direction by differential quadrature. *Journal of Vibration and Control* 22: 2482–2502.

Khorasany RMH and Hutton SG (2010) An analytical study on the effect of rigid body translational degree of freedom on the vibration characteristics of elastically constrained rotating disks. *International Journal of Mechanical Sciences* 52: 1186–1192.

Kim CK and Yoon JY (2016) Performance analysis of bladeless jet propulsion micro-steam turbine for micro-CHP (combined heat and power) systems utilizing low-grade heat sources. *Energy* 101: 411–420.

Kim K, Guo J, Xu X and Fan D (2015) Micromotors with step-motor characteristics by controlled magnetic interactions among assembled components. *ACS Nano* 9: 548–554.

Koç H, Genel ÖE, Tüfekci M and Tüfekci E (2023) Analysis of the dynamical behaviour of spinning annular disks with various boundary conditions. *Mechanics Based Design of Structures and Machines* 51: 5427-5451.

Koiter WT (1964) Couple stresses in the theory of elasticity: I and II. *Philosophical Transactions of the Royal Society of London B* 67: 17–44.

Kordkheili SAH and Naghdabadi R (2007) Thermoelastic analysis of a functionally graded rotating disk. *Composite Structures* 79: 508–516.

Lam DCC, Yang F, Chong ACM, Wang J and Tong p (2003) Experiments and theory in strain gradient elasticity. *Journal of the Mechanics and Physics of Solids* 51: 1477–1508.

Lei J, He Y, Guo S, Li Z and Liu D (2016) Size-dependent vibration of nickel cantilever microbeams: Experiment and gradient elasticity. *AIP Advances* 6: 105202.

Leissa AW and Narita Y (1980) Natural frequencies of simply supported circular plates. *Journal of Sound and Vibration* 70: 221-229.

Li S, Chen S and Xiong P (2018) Thermoelastic damping in functionally graded material circular micro plates. *Journal of Thermal Stresses* 41: 1396–1413.

Li Z, He Y, Lei J, Han S, Guo S and Liu D (2019) Experimental investigation on size dependent higher mode vibration of cantilever microbeams. *Microsystem Technologies* 25: 3005–3015.

Liebold C and Muller WH (2016) Comparison of gradient elasticity models for the bending of micromaterials. *Computational Materials Science* 116: 52–61.

Liu H, Pan CH and Liu P (2008) Dimension effect on mechanical behavior of silicon micro-cantilever beams. *Measurement* 41: 885–95.

Mahinzare M, Alipour MJ, Sadatsakkak SA and Ghadiri M. (2019) A nonlocal strain gradient theory for dynamic modeling of a rotary thermo piezo electrically actuated nano FG circular plate. *Mechanical Systems and Signal Processing* 115: 323–337.

Mahinzare M, Ranjbarpur H and Ghadiri M (2018a) Free vibration analysis of a rotary smart two directional functionally graded piezoelectric material in axial symmetry circular nanoplate. *Mechanical Systems and Signal Processing* 100: 188-207.

Mahinzare M, Barooti MM and Ghadiri M (2018b) Vibrational investigation of the spinning bi-dimensional functionally graded (2-FGM) micro plate subjected to thermal load in thermal environment. *Microsystem Technogies* 24: 1695-1711.

Malekzadeh P and Farajpour A (2012) Axisymmetric free and forced vibrations of initially stressed circular nanoplates embedded in an elastic medium. *Acta Mechanica* 223: 2311–2330.

Manzione P and Nayfeh AH (2001) Combination resonance of a centrally clamped rotating circular disk. *Journal of Vibration and Control* 7: 979-1011.

Maretic R and Glavardanov V (2008) Impact of mounting with an overlap on vibration and stability of a rotating annular plate. *Journal of Sound and Vibration* 313: 308–324.

Mindlin RD and Tiersten HF (1962) Effects of couple-stresses in linear elasticity. *Archive for Rational Mechanics and Analysis* 11: 415–448.

Mohammadi V, Ansari R, Shojaei MF, Gholami R and Sahmani S (2013) Size-dependent dynamic pull-in instability of hydrostatically and electrostatically actuated circular microplates. *Nonlinear Dynamics* 73: 1515–1526.

Mohammadimehr M, Emdadi M, Afshari H and Navi BR (2018) Bending, buckling and vibration analyses of MSGT microcomposite circular-annular sandwich plate under hydro-thermo-magneto-mechanical loadings using DQM. *International Journal of Smart and Nano Materials* 9: 233–260.

Nejad MZ, Rastgoo A and Hadi A (2014) Exact elasto-plastic analysis of rotating disks made of functionally graded materials. *International Journal of Engineering Science* 85: 47-57.

Norouzzadeh A and Ansari R (2018) Isogeometric vibration analysis of functionally graded nanoplates with the consideration of nonlocal and surface effects. *Thin-Walled Structures* 127: 354–372.

Okuizumi N (2009) Vibration mode analysis of a rotating circular membrane under transverse distributed load. *Journal of System Design and Dynamics* 3: 95-106.

Pardoen GC (1973) Static, vibration and buckling analysis of axisymmetric circular plates using finite elements. *Computers & Structures* 3: 355-375.

Park SK and Gao XL (2006) Bernoulli-Euler beam model based on a modified couple stress theory. *Journal of Micromechanics and Microengineering* 16: 2355-2359.

Pei YC (2012) Thermo elastic damping in rotating flexible micro-disk. *International Journal of Mechanical Sciences* 61: 52-64.

Pei YC, Wang JH and Yang F (2018) Dynamics comparison of rotating flexible annular disk under different edge boundary conditions. *International Journal of Mechanical Sciences* 137: 121-132.

Peng XL and Li XF (2010) Thermal stress in rotating functionally graded hollow circular disks. *Composite Structures* 92: 1896–1904.

Pourabdy M, Shishehsaz M, Shahrooi S and Roknizadeh SAS (2021) Analysis of axisymmetric vibration of functionally-graded circular nano-plate based on the integral form of the strain gradient model. *Journal of Applied and Computational Mechanics* 7: 2196–2220.

Presas A, Egusquiza E, Valero C, Valentin D and Seidel U (2014) Feasibility of using PZT actuators to study the dynamic behavior of a rotating disk due to rotor-stator interaction *Sensors* 14: 11919-11942.

Presas A, Valentin D, Egusquiza E, Valero C and Seidel U (2015a) Influence of the rotation on the natural frequencies of a submerged-confined disk in water. *Journal of Sound and Vibration* 337: 161–180.

Presas A, Valentin D, Egusquiza E, Valero C and Seidel U (2015b) On the detection of natural frequencies and mode shapes of submerged rotating disk-like structures from the casing. *Mechanical Systems and Signal Processing* 60-61: 547–570.

Press WH, Teukolsky SA, Vetterling WT and Flannery BP (1992) *Numerical Recipes in Fortran 77: The Art of Scientific Computing.* Second Edition, New York: Cambridge University Press.

Raman A and Mote CD Jr (1999) Non-linear oscillations of circular plates near a critical speed resonance. *International Journal of Non-Linear Mechanics* 34: 139-157.

Ravari MRK and Shahidi AR (2013) Axisymmetric buckling of the circular annular nanoplates using finite difference method. *Meccanica* 48: 135–144.

Reddy JN (2002) *Energy Principles and Variational Methods in Applied Mechanics*. USA: John Wiley & Sons, Inc.

Reddy JN (2007) *Theory and Analysis of Elastic Plates and Shells*. Second Edition, Boca Raton: CRC Press, Taylor & Francis group.

Reddy JN (2008) *An Introduction to Continuum Mechanics With Applications*. New York: Cambridge University Press.

Reddy JN and Berry J (2012) Nonlinear theories of axisymmetric bending of functionally graded circular plates with modified couple stress. *Composite Structures* 94: 3664–3668.

Reddy JN and Chin CD (1998) Thermomechanical analysis of functionally graded cylinders and plates. *Journal of Thermal Stresses* 21: 593–626.

Reddy JN, Romanoff J and Loya JA (2016) Nonlinear finite element analysis of functionally graded circular plates with modified couple stress theory. *European Journal of Mechanics A/Solids* 56: 92-104.

Saha KN, Misra D, Pohit G and Ghosal S (2004) Large amplitude free vibration study of square plates under different boundary conditions through a static analysis. *Journal of Vibration and Control* 10: 1009-1028.

Sahmani S and Bahrami M (2015) Nonlocal plate model for dynamic pull-in instability analysis of circular higher-order shear deformable nanoplates including surface stress effect. *Journal of Mechanical Science and Technology* 29: 1151-1161.

Sajadi B, Alijani F, Goosen H and Keulen FV (2018) Effect of pressure on nonlinear dynamics and instability of electrically actuated circular micro-plates. *Nonlinear Dynamics* 91: 2157–2170.

Schneider U, Olofsson B, Sörnmo O, Drust M, Robertsson A, Hägele M and Johansson R (2014) Integrated approach to robotic machining with macro/micro-actuation. *Robotics and Computer Integrated Manufacturing* 30: 636–47.

Shahab AAS (1993) Finite element analysis for the vibration of variable thickness discs. *Journal of Sound and Vibration* 162: 67-88.

Shahriari B, Jalali M and Ravari MRK (2017) Vibration analysis of a rotating variable thickness bladed disk for aircraft gas turbine engine using generalized differential quadrature method. *Proceedings of the Institution of Mechanical Engineers Part G: Journal of Aerospace Engineering* 231: 2739-2749.

Shahrokhi M, Jomehzadeh E and Rezaeizadeh M (2019) Size-dependent Green's function for bending of circular micro plates under eccentric load. *Journal of Solid Mechanics* 11: 14-22.

Shames IH and Dym CL (2009) *Energy and Finite Element Methods in Structural Mechanics*. Delhi: New Age International Publishers.

Sharafkhani N, Rezazadeh G and Shabani R (2012) Study of mechanical behavior of circular FGM micro-plates under nonlinear electrostatic and mechanical shock loadings. *Acta Mechanica* 223: 579–591.

Shariati M, Shishehsaz M, Mosalmoni R and Roknizadeh SAS (2022) Size effect on the axisymmetric vibrational response of functionally graded circular nano-plate based on the nonlocal stress-driven method. *Journal of Applied and Computational Mechanics* 8: 962-980.

Sharma D, Kaur R and Sharma H (2021) Investigation of thermo-elastic characteristics in functionally graded rotating disk using finite element method. *Nonlinear Engineering* 10: 312-322.

Sharma JN, Sharma D and Kumar S (2013) Vibration analysis of a rotating FGM thermoelastic axisymmetric circular disk using FEM. *International Journal for Computational Methods in Engineering Science and Mechanics* 14: 262–270.

Shen HS (2004) Thermal postbuckling behavior of functionally graded cylindrical shells with temperature-dependent properties. *International Journal of Solids and Structure* 41: 1961-1974.

Shishesaz M, Hosseini M, Tahan KN and Hadi (2017) Analysis of functionally graded nanodisks under thermoelastic loading based on the strain gradient theory. *Acta Mechanica* 228: 4141-4168.

Shishesaz M, Shariati M and Yaghootian A (2020) Nonlocal elasticity effect on linear vibration of nano-circular plate using adomian decomposition method. *Journal of Applied and Computational Mechanics* 6: 63-76.

Shojaeefard MH, Googarchin HS, Ghadiri M and Mahinzare M (2017) Micro temperature-dependent FG porous plate: Free vibration and thermal buckling analysis using modified couple stress theory with CPT and FSDT. *Applied Mathematical Modelling* 50: 633-655.

Shojaeefard MH, Googarchin HS, Mahinzare M and Ghadiri M (2018a) Free vibration and critical angular velocity of a rotating variable thickness two-directional FG circular microplate. *Microsystem Technologies* 24: 1525-1543.

Shojaeefard MH, Googarchin HS, Mahinzare M and Eftekhari SA (2018b) Magnetic field effect on free vibration of smart rotary functionally graded nano/microplates: A comparative study on modified couple stress theory and nonlocal elasticity theory. *Journal of Intelligent Material Systems and Structures* 29: 2492-2507.

Tang C and Alici G (2011a) Evaluation of length-scale effects for mechanical behaviour of micro- and nanocantilevers: I. Experimental determination of length-scale factors. *Journal of Physics D: Applied Physics* 44: 335501.

Tang C and Alici G (2011b) Evaluation of length-scale effects for mechanical behaviour of micro- and nanocantilevers: II. Experimental verification of deflection models using atomic force microscopy. *Journal of Physics D: Applied Physics* 44: 335502.

Tang Q, Li C, She H and Wen B (2021) Analysis of frequency and mode shape of rotating-flexible disk-drum coupled structure with non-continuous connections. *International Journal of Mechanical Sciences* 190: 106004.

Thai HT, Vo TP, Nguyen TK and Lee J (2014) A nonlocal sinusoidal plate model for micro/nanoscale plates. *Proceedings of the Institution of Mechanical Engineers Part C: Journal of Mechanical Engineering Science* 228: 2652–2660.

Touloukian YS (1967) *Thermophysical Properties of High Temperature Solid Materials*. New York: Macmillan.

Toupin RA (1962) Elastic materials with couple stresses. *Archive for Rational Mechanics and Analysis* 11: 385–414.

Tutuncu N and Temel B (2013) An efficient unified method for thermoelastic analysis of functionally graded rotating disks of variable thickness. *Mechanics of Advanced Materials and Structures* 20: 38–46.

Wang YG, Lin WH and Liu N (2013) Large amplitude free vibration of size-dependent circular microplates based on the modified couple stress theory. *International Journal of Mechanical Sciences* 71: 51–57.

Wang YG, Song HF, Lin WH and Xu L (2017) Large deflection analysis of functionally graded circular micro-plates with modified couple stress effect. *Journal of the Brazilian Society of Mechanical Sciences and Engineering* 39: 981–991.

Yamanouchi M, Koizumi M, Hirai T and Shiota I (eds.) (1990) *Proceedings of the First International Symposium on Functionally Gradient Materials*. Sendai, Japan.

Yan Z (2016) Size-dependent bending and vibration behaviors of piezoelectric circular nanoplates. *Smart Materials and Structures* 25: 035017.

Yang F, Chong ACM, Lam DCC and Tong P (2002) Couple stress based strain gradient theory for elasticity. *International Journal of solids and Structures* 39: 2731–43.

Yang Y, Zou J, Lee YK and Li XF (2018) Bending of circular nanoplates with consideration of surface effects. *Meccanica* 53: 985–999.

Yang YB and Kang JH (2018) Vibration and buckling analysis of a rotating annular plate subjected to a compressive centrifugal body force. *International Journal of Structural Stability and Dynamics* 18: 185009.

Zandekarimi S, Asadi B and Rahaeifard M (2018) Size dependent thermal buckling and postbuckling of functionally graded circular microplates based on modified couple stress theory. *Journal of Thermal Stresses* 41: 1–16.

Zarei M, Faghani GR, Ghalami M and Rahimi GH (2018a) Buckling and vibration analysis of tapered circular nano plate. *Journal Applied and Computer Mechanics* 4: 40-54.

Zarei M, Choobar MG, Rahimi GH and Faghani GR (2018b) Free vibration analysis of non-uniform circular nanoplate. *Journal of Solid Mechanics* 10: 400-415.

Zenkour AM (2005) Analytical solutions for rotating exponentially-graded annular disks with various boundary conditions. *International Journal of Structural Stability and Dynamics* 5: 557–577.

Zenkour AM (2007) Elastic deformation of the rotating functionally graded annular disk with rigid casing. *Journal of Materials and Science* 42: 9717–9724**.**

Zhang B, He Y, Liu D, Lei J, Shen L and Wang L (2015) A size-dependent third-order shear deformable plate model incorporating strain gradient effects for mechanical analysis of functionally graded circular/annular microplates. *Composites Part B* 79: 553-580.

Zhang XQ, Wang XL, Liu R and YY Zhang (2013) Modeling and analysis of micro hybrid gas spiral-grooved thrust bearing for microengine. *Journal of Engineering for Gas Turbines and Power* 135: 122508.

Zheng Y, Bahaloo H, Mousanezhad D, Mahd E, Vaziri A and Hashemi HN (2016) Stress analysis in functionally graded rotating disks with non-uniform thickness and variable angular velocity. *International Journal of Mechanical Sciences* 119: 283-293.

Zhou SS and Gao XL (2014) A nonclassical model for circular Mindlin plates based on a modified couple stress theory. *Journal of Applied Mechanics* 81: 51014.

Zhou ZH, Wong KW, Xu XS and Leung AYT (2011) Natural vibration of circular and annular thin plates by Hamiltonian approach. *Journal of Sound and Vibration* 330: 1005–1017.

Suman Pal
29/04/2024